FACULTY OF ELECTRICAL ENGINEERING
DEPARTMENT OF RADIOELECTRONICS

Ing. TOMÁŠ LUKEŠ

SUPER-RESOLUTION MICROSCOPY LIVE CELL IMAGING AND IMAGE ANALYSIS

DOCTORAL THESIS

PRAGUE, JANUARY 2017

Ph.D. PROGRAMME:	ELECTRICAL ENGINEERING AND INFORMATION TECHNOLOGY
BRANCH OF STUDY:	RADIOELECTRONICS
SUPERVISOR:	Prof. Ing. MILOŠ KLÍMA, CSc.
SUPERVISOR-SPECIALIST:	Ing. KAREL FLIEGEL, Ph.D.
EXTERNAL ADVISOR:	Prof. THEO LASSER, Ph.D.

CONTACT

TOMAS LUKES

MULTIMEDIA TECHNOLOGY GROUP
FACULTY OF ELECTRICAL ENGINEERING
CTU IN PRAGUE,
CZECH REPUBLIC
LUKESTOM@FEL.CVUT.CZ
MMTG.FEL.CVUT.CZ

&

LABORATOIRE D'OPTIQUE BIOMEDICALE
INSTITUTE OF BIOENGINEERING
EPFL,
SWITZERLAND
TOMAS.LUKES@EPFL.CH
LOB.EPFL.CH

Acknowledgements

My thesis would not be accomplished without the help and close collaboration with many colleagues from various research laboratories. First of all, I would like to express my deepest gratitude to Prof. Theo Lasser. I contacted him three years ago with an idea for a cooperation. Few hours later, Theo responded with many more ideas, we had a Skype meeting, I was invited to Lausanne, caught the first plane and in two days we had a complete draft of a joint research project for the Swiss SCIEX programme. We received the grant and I started to work in between both EPFL in Switzerland and CTU in Prague ever since. This story is just one of many examples of Theo's great passion for work, exceptional ability to motivate his co-workers, and huge enthusiasm. He promoted my PhD research to an international level and guided me through my whole PhD studies as a mentor and a friend.

I am especially grateful to my adviser Prof. Miloš Klíma and co-adviser Karel Fliegel for their constant support, the great trust and the freedom they gave me for my research. I know both of them since my bachelor thesis. Without their help and kindness, maybe I would not even start my PhD studies. I also would like to thank Karel for his help in fighting the administration with his never ending positive attitude. I am in a great depth of gratitude to Guy M. Hagen who introduced me to super-resolution microscopy and pointed me towards this fascinating field which then became the topic of my doctoral thesis. I am very glad that I had the opportunity to collaborate with him and his research team at the Charles University and later at the University of Colorado Colorado Springs.

I would like to express my thanks to Marcel Leutenegger and Stefan Geissbuehler for teaching me the super-resolution optical fluctuation imaging method and the fun we had during the process. Many thanks belong also to my colleague Azat Sharipov for all the samples he prepared and provided me. For the projects on PALM and SOFI, I had a great pleasure to work closely with Hendrik Deschout and Prof. Aleksandra Radenovic. I would like to thank them for the numerous fruitful discussions and the great collaboration. I am very grateful that I had an opportunity to collaborate with Guy M. Hagen, Pavel Křížek, Martin Ovesný and Zdeněk Švindrych and Jakub Pospíšil on the structured illumination microscopy projects MAP-SIM and SIMToolbox. I was lucky that I could supervise two master thesis of brilliant students Arik Girsault and Vojtěch Terš. I would like to express my many thanks to my old friend, theoretical physicist Jakub Benda. No matter what kind of a mathematical problem I encountered, he was always willing to help and solve it in a record time. I am deeply grateful to Marek Cebecauer and his team especially to Daniela Glatzová, Zuzana Kvíčalová and Tomáš Chum for the great collaboration and help in applying SOFI. I thank to Jochem Deen and Kristin Grußmayer for

the proof reading of my thesis. I would like to thank to all my colleagues and co-workers in Prague, Lausanne, Colorado, and Leuven who cooperated with me during my PhD and who are the co-authors in our joint publications. It has been a great pleasure.

Last and above all, my most profound thanks go to my parents and family for their unconditional love and support. I would like to express my deepest gratitude to my father Ivo Lukes for all the joyful discussions, encouragement and motivation to pursue the PhD study. I would like to dedicate this work to the memory of my beloved grandfather Vlastimil Lukes who was always so interested in my work and shared with me his priceless life experiences.

Prague, 9 January 2017 Tomáš Lukeš

Declaration

I hereby declare that I worked out the presented thesis independently and I quoted all the sources used in this thesis in accord with Methodical instructions about ethical principles for writing academic thesis.

Prague, 9 January 2017

Funding

Projects in the thesis were partially funded by the Swiss National Science Foundation (SNSF, http://www.snf.ch/) under grants 200020-159945 and 205321-138305, by the Czech Science Foundation under grants P102/10/1320, GA304/09/1047 and P205/12/P392, and by COST CZ LD12018. I acknowledge a SCIEX scholarship (13.183) and Czech Technical University student grants (SGS14/148/OHK3/2T/13, SGS16/167/OHK3/2T/13).

Abstract

Novel fundamental research results provided new techniques going beyond the diffraction limit. These recent advances known as super-resolution microscopy have been awarded by the Nobel Prize as they promise new discoveries in biology and live sciences. All these techniques rely on complex signal and image processing. The applicability in biology, and particularly for live cell imaging, remains challenging and needs further investigation.
Focusing on image processing and analysis, the thesis is devoted to a significant enhancement of structured illumination microscopy (SIM) and super-resolution optical fluctuation imaging (SOFI) methods towards fast live cell and quantitative imaging. The thesis presents a novel image reconstruction method for both 2D and 3D SIM data, compatible with weak signals, and robust towards unwanted image artifacts. This image reconstruction is efficient under low light conditions, reduces phototoxicity and facilitates live cell observations. We demonstrate the performance of our new method by imaging long super-resolution video sequences of live U2-OS cells and improving cell particle tracking. We develop an adapted 3D deconvolution algorithm for SOFI, which suppresses noise and makes 3D SOFI live cell imaging feasible due to reduction of the number of required input images. We introduce a novel linearization procedure for SOFI maximizing the resolution gain and show that SOFI and PALM can both be applied on the same dataset revealing more insights about the sample. This PALM and SOFI concept provides an enlarged quantitative imaging framework, allowing unprecedented functional exploration of the sample through the estimation of molecular parameters. For quantifying the outcome of our super-resolution methods, the thesis presents a novel methodology for objective image quality assessment measuring spatial resolution and signal to noise ratio in real samples. We demonstrate our enhanced SOFI framework by high throughput 3D imaging of live HeLa cells acquiring the whole super-resolution 3D image in 0.95 s, by investigating focal adhesions in live MEF cells, by fast optical readout of fluorescently labelled DNA strands and by unraveling the nanoscale organization of CD4 proteins on a plasma membrane of T-cells. Within the thesis, unique open-source software packages SIMToolbox and SOFI simulation tool were developed to facilitate implementation of super-resolution microscopy methods.

Key words: Super-resolution microscopy, image reconstruction, image analysis, image processing, fluorescent microscopy, live cell imaging, quantitative imaging

Abstrakt

Nové výsledky základního výzkumu poskytují techniky schopné překonat difrakční limit. Tyto nedávné pokroky, známé pod názvem super-resolution mikroskopie, slibují nové objevy v biologii a vědách o živé přírodě. Všechny tyto techniky spoléhají na komplexní zpracování signálu a obrazu. Jejich aplikovatelnost v biologii, a to zejména pro zobrazování živých buněk, zůstává stále velmi náročná a vyžaduje další zkoumání.
Práce se soustředí na zpracování a analýzu obrazu pro rozvoj metod structured illumination microscopy (SIM) a super-resolution optical fluctuation imaging (SOFI) vstříc super-resolution, kvantitativnímu zobrazování živých buněk. Práce představuje novou metodu rekonstrukce obrazu pro 2D i 3D SIM data, která je kompatibilní se slabými signály a robustní vůči nežádoucím obrazovým artefaktům. Tato rekonstrukční metoda je efektivní v podmínkách slabého osvětlení, redukuje fototoxicitu a usnadňuje pozorování živých buněk. Výkonnost této naší nové metody je demonstrována snímáním dlouhých super-resolution videí živých U2-OS buněk, kde zlepšuje navazující úlohu sledování částic buňky. V práci je vyvinut nový algoritmus 3D dekonvoluce adaptovaný pro SOFI, jež potlačuje šum a umožňuje 3D SOFI snímání živých buněk díky redukci počtu požadovaných vstupních snímků. Je představen nový proces linearizace pro SOFI umožňující maximalizovat zlepšení rozlišení. Je ukázáno, že SOFI a PALM metody lze aplikovat na stejná data a získat tak více informací o zkoumaném vzorku. Tento koncept rozšiřuje možnosti kvantitativního zobrazování a umožňuje bezprecedentní funkční zkoumání vzorků pomocí odhadu molekulárních parametrů. Práce představuje novou metodiku hodnocení kvality obrazu měřením rozlišení a poměru signálu k šumu v reálných buněčných vzorcích Za účelem kvantifikace výsledků našich super-resolution metod. Možnosti vylepšené SOFI metody jsou demonstrovány na rychlém 3D zobrazování živých HeLa buněk dosažením snímacího času 0.95 s pro jeden celý super-resolution 3D snímek, zkoumáním fokálních adhezí v živých MEF buňkách, rychlým optických čtením fluorescenčně obarvené DNA a pozorováním prostorového uspořádání CD4 proteinů na membráně T-buněk v nano měřítku. V rámci práce byly vytvořeny open-source softwary SIMToolbox a SOFI simulation tool, které jsou první svého druhu a kladou si za cíl usnadnit použití super-resolution mikroskopie.

Klíčová slova: Super-resolution mikroskopie, rekonstrukce obrazu, analýza obrazu, zpracování obrazu, fluorescenční mikroskopie, snímání živých buněk, kvantitativní zobrazování

Contents

1 Introduction

Research of cells very much depends on the ability to directly visualize their structure and dynamics. For this purpose, fluorescence microscopy is a widely used technique due to its two major advantages. First, specific molecules of the cell can be labeled with a fluorescent dye in order to make them visible so that cellular components can be studied. Second, living cells can be observed in real time. Compared to electron microscopy, the spatial resolution of conventional fluorescence microscopy is relatively low due to the diffraction limit of light. In practice even with large numerical apertures, perfect lenses and optimal alignment, the spatial resolution of optical microscopes is limited to approximately half of the wavelength of the light used. It is about 200–300 nm in the lateral direction and 500–700 nm in the axial direction [1].

Innovations including fluorescence and confocal laser scanning microscopy have become powerful tools in cell biology. A large number of sub-cellular structures are smaller than the wavelength of light. The diffraction limit in light microscopy becomes an obstacle for studying these structures in detail. Therefore, it is necessary to develop techniques that improve the spatial resolution of light microscopy while keeping its major advantages for biological research. The recent invention of super-resolution microscopy, awarded by the Nobel Prize, overcomes the diffraction limit and promises new discoveries in biological research.

The goal of the thesis is to extend selected super-resolution microscopy methods and facilitate super-resolution live-cell imaging for applications in cell biology. The thesis focuses on the structured illumination microscopy (SIM) and super-resolution optical fluctuation imaging (SOFI). These methods represent a low cost extension of the standard widefield microscope and are well suited for live cell imaging. At the beginning, major super-resolution methods are introduced (chapter 1) followed by the state of the art (chapter 2). Results and new algorithms for SIM and SOFI are presented in chapters 3 and 4. Chapter 5 describes applications of the new algorithms in cell biology. Chapter 6 is devoted to objective image quality assessment measuring spatial resolution and signal to noise ratio (SNR) of super-resolution images. At the end of the thesis, a brief outlook for future work is discussed.

1.1 Image resolution in optical microscopy

The fundamental resolution limit of light microscopy is governed by the physical nature of light, which is a wave phenomenon and is subject to diffraction as visible light wavefront pass through the circular aperture of the rear focal plane of the objective. This resolution limitation imposed by the wave nature of light is often referred to as the diffraction limit.

Abbe's law defines the resolving capability of an optical microscope in the lateral image plane as

$$d_{xy} = \frac{\lambda}{2NA}, \tag{1.1}$$

where λ is the average wavelength of light used, NA is the numerical aperture of the objective defined as

$$NA = n\sin(\phi), \tag{1.2}$$

where n is the refractive index of the imaging medium and ϕ denotes the maximal half-angle of the cone of light that can be gathered by the objective. The axial resolution of the optical microscope is given by

$$d_z = \frac{2\lambda}{NA^2}. \tag{1.3}$$

According to Abbe's theory, the only mechanism for maximizing the spatial resolution is an increase in numerical aperture, using an imaging medium with a higher refractive index, or decrease the wavelength of illumination. As a result of diffraction, a point source in the sample plane will appear in the image plane as an Airy pattern with a finite central disk broader than the original object. The three-dimensional intensity distribution of the Airy disk is called the point spread function (PSF) which is an important characteristics of the microscope. Spatial resolution is often defined as the smallest separation distance between two nearby point sources at which they are still distinguishable. Therefore, resolution criteria based on this definition are directly related to properties of the PSF. The size of the PSF determines the resolution of the microscope.

According to the Rayleigh criterion, the spatial resolution of the optical microscope is given as [2]:

$$d_{xy} = 0.61\lambda/NA. \tag{1.4}$$

Two point sources observed in the microscope are regarded as being resolved when their mutual distance is larger then the distance between principal diffraction maximum from one point source and the first diffraction minimum from the other point source.

The resolution of an image captured by a digital camera mounted on an optical microscope is

affected not only by the PSF of the optical system, but also by the pixel size of an image sensor in the camera i.e. by the sampling frequency (see Figure 1.1). The condition of being resolved explained above assumes that the image is projected onto an image sensor with adequate spatial sampling. The projected pixel size given by the physical size of the pixels on the image sensor and the magnification of the lens system has to be small enough to meet the Nyquist sampling limit in order to preserve the diffraction-limited resolution of the microscope. The sampling frequency must be at least two times higher than the maximal frequency of the signal to avoid pixelation and unwanted aliasing. Stated in other words, preservation of the spatial resolution of the optics requires that a FWHM be covered by a minimum of two adjacent pixels on the camera sensor.

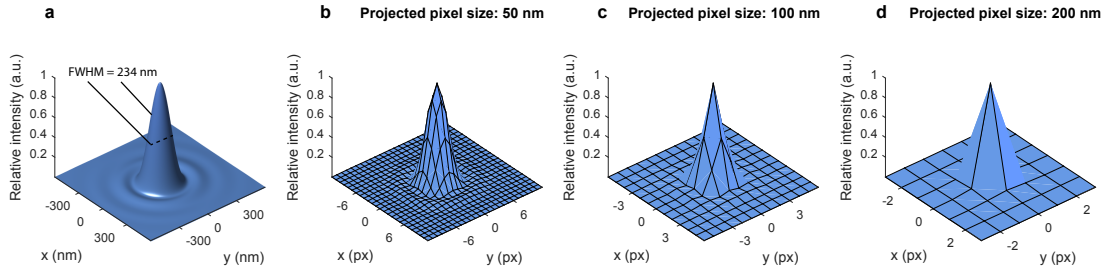

Figure 1.1: Point spread function (PSF) of a diffraction limited microscope and sampling on the camera sensor. (a) Theoretical PSF in xy plane without aberrations for NA = 1.3, λ = 500 nm. (b) Oversampled PSF. FWHM is covered by approx. 4 pixels. (c) Sampling limit. FWHM is covered by approx. 2 pixels. (d) Undersampled PSF. FWHM is covered by approx. 1 pixel. Image resolution is limited by sampling to approx. 400 nm.

1.2 Fluorescence microscopy

Fluorescence microscopy allows visualization of specific molecules that fluoresce when excited by a light source. Typically, molecules are tagged with a fluorescent dye or fluorochrome in order to make them visible. Fluorescence microscopes employ a unique method of illumination to produce images of fluorescent light emitted from excited molecules in the sample. Shorter excitation wavelengths are illuminating the sample, while longer fluorescence wavelengths emitted from the sample form the image. In the epi-fluorescence microscope, the fluorescently labelled sample is illuminated through the objective. Illuminated specimen emits light into all directions. The emitted light is partly collected by the objective, separated from the excitation light by an emission filter and acquired by the camera. Fluorescence microscopy provides high specificity, contrast and sensitivity which makes it an essential tool in biomedical and biological research for studies of the intracellular distribution, dynamics and molecular mechanisms. Conventional fluorescence microscopy has a diffraction limited resolution which prevents observation of important sub-cellular structures.

1.3 Super-resolution light microscopy methods

Development of super-resolution imaging techniques is driven by the effort to examine subcellular structures smaller than the resolution limit of the conventional fluorescent light microscopes. The methods to improve spatial resolution can be divided on near-field and far-field methods. In the case of near-field methods, the light propagates through a distance shorter than the wavelength of light. Besides these rather specialized near-field approaches, several new, more generally applicable, far-field methods have been developed recently to overcome the diffraction limit of optical microscopes. These techniques include methods employing non-linear effects to sharpen the point-spread function of the microscope, such as stimulated emission depletion [3] (STED), techniques based on the localization of individual fluorescent molecules such as photoactivated localization microscopy [4, 5] (PALM) and stochastic optical reconstruction microscopy [6] (STORM), techniques exploiting higher order statistics of blinking fluorophores like super-resolution optical fluctuation imaging [7] (SOFI), as well as several types of structured illumination microscopy [8, 9, 10] (SIM) based on patterned excitation light and image scanning microscopy (ISM) using properties of the confocal microscope.

The thesis is devoted to a substantial extension of SIM and SOFI methods, which are both very promising for fast live cell imaging due to their robustness, simplicity, low hardware requirements and relatively high photon efficiency. Broader use of super-resolution fluorescence microscopy promises an observation of previously unresolved details of cellular structures. It may facilitate new progress in many research fields like for instance cell biology, neurobiology, and immunology.

1.3.1 STED

In STED microscopy, the PSF is engineered to be considerable smaller, allowing higher resolution (typically 30 - 80nm [3]). The shaping of PSF is performed using two superimposed laser beams. First laser provides the excitation light and a second laser (STED laser) suppresses the fluorescence emission from the fluorophores located off the center of the excitation. The STED laser needs to have a mode pattern with zero intensity at the center of the excitation laser focus and nonzero intensity at the periphery. STED is based on two key factors: non-linear emission depletion and fluorescent molecules that can be switched between bright and dark states by stimulated emission depletion. The combination of the linear process of dye excitation and the nonlinear exponential response to emission depletion allows to produce very small scanning spot. Consequently, the fluorescence signal can be observed only in a small region around the focal point, reducing the effective width of the PSF. The resolution is then determined mainly by the spot size of remaining excited fluorophores. In practice, attention needs to be paid to the correct timing, duration of the STED pulse, and a good quality of the zero intensity in the center of the STED beam.

1.3.2 PALM, STORM

This approach is usually referred to as single-molecule localization super-resolution microscopy (SMLM). A biological structure is marked by fluorescent molecules. The fluorescence image is generated by fluorophores and thus defined by their spatial coordinates. Therefore, super-resolution microscopy can also be achieved by determining the precise position of fluorophores in a sample. The image of one fluorophore is a spot of a finite size. Observing the sample through time, more photons from one fluorophore can be collected. Resulting N photons can be viewed as N measurements of the fluorophore localisation, each with an uncertainty determined by the PSF. This information is further used to determine the fluorophore position with higher precision. Fluorescently labeled biological samples, however, contains thousands or even millions of fluorophores at a high density, making them difficult to resolve by the single-molecule localization approach. Using fluorescent probes that can be switched between a fluorescent and a dark state, a recent invention overcomes this barrier by separating in the time domain the otherwise spatially overlapping fluorophores. In this approach, molecules within a diffraction limited region can be activated at different time so that they can be individually localized. Massively parallel localization is achieved through wide-field imaging, so that the coordinates of many fluorophores can be mapped and a super-resolution images reconstructed. This concept has been independently developed and implemented by three labs, and it was given the names STORM [6], PALM [11], and FPALM [12], respectively.

1.3.3 ISM

ISM represents a microscopy technique which combines conventional confocal-laser scanning microscopy with fast wide-field CCD detection to achieve two fold improvement in lateral resolution. Confocal microscope behaves as an imaging system in which the effective point spread function (PSF) is given by the product of the excitation and emission PSFs. A confocal microscope with an almost closed pinhole can produce the effective PSF $\sqrt{2}$ narrower in the lateral direction compared to widefiled [13], but the almost-closed pinhole rejects too much of the emission light. ISM [14] uses a widefield detection and a CCD camera, where the pixels of the camera detector act as micropinholes . The final image is reconstructed by detecting signal by an array of these micropinholes for each position of the focused laser spot scanning across a sample, and reassigning the collected signal to different image bins using interpolation [14]. If the excitation and emission PSFs are nearly equal, the resulting PSF is effectively the square of the widefield PSF, improving lateral resolution by $\sqrt{2}$ and doubling the frequency content in the Fourier domain [13]. Implying a deconvolution algorithm or a Fourier weighting, a full two fold lateral resolution improvement can be achieved compared to widefield microscopy [14].

Several alternative approaches have been introduced which use various kinds of patterned illumination bringing the ISM method closer to SIM [15, 16]. In multifocal structured illumination microscopy (MSIM) [15] a 2D array of focused laser spots is scanned across a sample, and subsequent image processing is used to achieve an image with improved resolution.

1.3.4 SIM

Another approach to increase the spatial resolution of optical microscopy is to apply a patterned illumination to the sample. In this approach, the spatial frequencies of the illumination pattern mix with those of the sample features. It causes aliasing and shifts the high-frequency features to lower frequencies that are detectable by the microscope. By acquiring multiple images with illumination patterns of different phases and orientations, high frequency information can be restored from the aliased parts of the image and a high-resolution image is reconstructed doubling the resolution in all three spatial dimensions [17]. A resolution of approximately 100 nm in the lateral direction and approximately 300 nm in the axial direction has been achieved [17]. SIM approach is attractive because it does not require expensive hardware changes in the system and conventional fluorescent dyes can be applied. In section 2.1, SIM methods are discussed in detail.

1.3.5 SOFI

Super-resolution optical fluctuation imaging (SOFI) is a microscopy technique that achieves resolution beyond the diffraction limit by computing higher order statistics (cumulants) of time series of stochastically blinking fluorophores [7]. Instead of localizing each individual fluorophore, the resolution improvement in SOFI results from properties of spatio-temporal cross cumulants calculated from the entire image sequence. In contrast to localization microscopy techniques, SOFI is compatible with a wide range of blinking conditions and high labeling densities [18]. SOFI is descibed in details in section 2.2. The main part of the thesis is devoted to an enhancement of the current SOFI method and its applications.

1.4 Thesis objectives

Several optical super-resolution techniques have been developed overcoming the diffraction limit by up to an order of magnitude. Nevertheless, their usability in biological research and in particular for live-cell investigations still remains challenging. These state of the art super-resolution techniques come along with high technical complexity and generally slow acquisition rates. In addition, phototoxicity may distort the cellular dynamics and processes.

The aim of the thesis is to improve and further enhance SIM and SOFI imaging towards fast and robust super-resolution multidimensional live cell imaging. Although SIM is limited to two fold resolution improvement, high photon efficiency, widefield illumination, low costs and high acquisition rates reveal an interesting potential for SIM methods. Additionally, nearly any fluorescent dye or fluorescent protein can be used, making the method useful for a broad range of studies in cell biology. SOFI enables n-fold resolution improvement in all three spatial dimensions growing with n-order cumulant analysis. The compatibility with low fluorescence signals and the ability to simultaneously acquire a 3D super-resolved image at increased frame rates, makes SOFI an attractive imaging method. SIM can be used for fast 2D and 3D imaging if a conventional fluorescent dye is preferred. Multiplane SOFI [19] is able to acquire a whole 3D image simultaneously and offers high throughput imaging of live cells compatible with blinking fluorescent emitters. Additionally, SOFI provides more than two fold resolution improvement and allows one to extract molecular parameters of the sample.

The goal of the thesis is to facilitate super-resolution live-cell imaging for applications in cell biology. It involves:

- New algorithms for SIM towards robust image reconstruction and low phototoxicity live cell observations (chapter 3).
- New algorithms for SOFI towards fast 3D live cell imaging and molecular parameter extraction (chapter 4).
- Applications of super-resolution microscopy in cell biology (chapter 5).
- Quantitative image analysis of super-resolution images and videos (chapters 5 and 6).

2 State of the art

Parts of the following chapter were published in:
Lukeš et al., Comparison of image reconstruction methods for structured illumination microscopy, Proc. SPIE, Biophotonics, 2014 [20]

2.1 Structured illumination microscopy (SIM)

SR-SIM uses illumination patterns with high spatial frequency (close to the resolution limit of the microscope) to illuminate the sample. High frequency information contained in the sample is encoded, through aliasing, into the acquired images. By acquiring multiple images with illumination patterns of different phases and orientations, aliased components can be separated and a high-resolution image reconstructed [10, 8]. Two-dimensional SR-SIM enables a twofold resolution improvement in the lateral dimension [8, 21, 22], but does not provide optical sectioning. If a three-dimensional illumination pattern is used, resolution can also be improved in the axial direction [17, 23]. Structured illumination microscopy has also been used for optical sectioning, but without lateral resolution enhancement (OS-SIM) [24]. Optically sectioned images can be calculated by taking the root mean square of the differences of the acquired images (square-law method), or by a form of homodyne detection [24].

Recently, new concepts in structured illumination have appeared such as combining OS-SIM and SR-SIM by weighting Fourier space image components [25], or use of random speckle patterns for illumination the sample (blind-SIM) [26]. Orieux et al. suggested a framework for SR-SIM based on Bayesian estimation for 2D image reconstruction [27]. We previously showed that Bayesian estimation methods have several advantages over the square-law method and can achieve a performance comparable to SR-SIM methods [20].

2.1.1 Optical Sectioning SIM (OS-SIM)

In 1997 Neil et al. [24] proposed a simple fringe projection method which can be used to obtain an optically sectioned image from the three separate images captured using patterned

illumination and widefield detection. Neil's method is simple in principle and computationally inexpensive. Optically sectioned images can also be processed by applying maximum minus minimum projection [28] or by a form of homodyne detection [24]. If the illumination pattern position in the acquired images is precisely known, scaled subtraction of the out of focus light can be performed. Křížek et al. have shown that scaled subtraction provides better results (higher signal to noise ratios and better rejection of out-of-focus fluorescence) than other detection methods [29]. When combined with optimized illumination patterns, OS-SIM can achieve axial resolution of cca 300 nm, about two to three fold better than is achievable in confocal laser scanning microscopy (CLSM) [30, 29]. Neil et al. [24] used an incoherently illuminated mask, which is imaged onto the sample. The intensity of the final fluorescence image recorded by CCD camera in the image plane is defined as follows:

$$g_i(\mathbf{x}) = (m_i(\mathbf{x}) f(\mathbf{x})) * h(\mathbf{x}), \tag{2.1}$$

where $*$ is a convolution operator and $\mathbf{x} = (x, y)$ is a vector in the image plane. The point spread function (PSF) for the detection path is denoted h, $m(\mathbf{x})$ represents the illumination mask and $f(\mathbf{x})$ is the distribution of fluorescence in the observed sample. The i-th illumination mask is given as:

$$m_i(\mathbf{x}) = 1 + \alpha\cos(2\pi(\mathbf{px} + \varphi_i)), \tag{2.2}$$

where α is the modulation depth, $\mathbf{p}$ is the modulation vector and φ_i is an arbitrary spatial phase. To remove the grid pattern from the resulting image of the specimen, three images are taken (g_1, g_2, g_3) with spatial phases $\varphi_1 = 0, \varphi_2 = 2\pi/3, \varphi_3 = 4\pi/3$, respectively. The reconstructed image can be obtained according to a square-law method:

$$I = [(g_1 - g_2)^2 + (g_1 - g_3)^2 + (g_2 - g_3)^2]^{(1/2)}. \tag{2.3}$$

The conventional wide field image can be recovered by summing g_1, g_2, g_3. Optically-sectioned image can also be reconstructed by a method in a form of Homodyne detection [24]. For equally spaced phase-shifted illumination patterns the final image can be obtained according to

$$I(x) = |\sum_{n=1}^{N} g_n(\mathbf{x}) e^{-\varphi_n}|. \tag{2.4}$$

It can be shown that for three images (g_1, g_2, g_3) taken with spatial phases $\varphi_1 = 0, \varphi_2 = 2\pi/3, \varphi_3 = 4\pi/3$, the result is identical to the above square-law method [31]. Additionally, this method can be easily extended to any number of phase-shifted images. Another method for extracting an optically sectioned image is scaled subtraction. For this method it is necessary to know the position of the illumination mask in the acquired data. Subtraction of out of

focus light is then defined as:

$$I(x) = \frac{\sum_{i=1}^{N} g_i(\mathbf{x}) m_i(\mathbf{x})}{\sum_{i=1}^{N} m_i(\mathbf{x})} - \frac{\sum_{i=1}^{N} g_i(\mathbf{x})(1 - m_i(\mathbf{x}))}{\sum_{i=1}^{N}(1 - m_i(\mathbf{x}))}, \tag{2.5}$$

where $m_i \in [0,1]$ is the intensity of the illumination pattern at the image plane for a given i-th image.

2.1.2 Super-resolution SIM (SR-SIM)

Super-resolution structured illumination microscopy (SR-SIM) utilizes patterns of excitation light to encode usually unobservable information into the observed image. An optical system can be characterized by its optical transfer function (OTF), which describes the capability of the optical system to transfer a signal at various spatial frequencies. The OTF equals zero for all frequencies beyond the cutoff frequency. Any frequencies outside the support of the transfer function cannot be observed and the information is lost. The idea of SIM is to move information contained at high frequencies inside the support of the transfer function using spatially modulated illumination. The spatial frequencies of the illumination pattern mix with those of the sample features. This causes aliasing and shifts the high-frequency features to lower frequencies that are detectable by the microscope. By acquiring multiple images with illumination patterns of different phases and orientations, high frequency information can be restored from the aliased parts of the image and a high-resolution image can be reconstructed. High frequency information can be recovered by shifting appropriate regions in the frequency domain and then combining the images using a generalized Wiener filter. The method was developed and experimentally demonstrated by Gustafsson et al.[8, 32] and by Heintzmann et al. [10, 22]. Let us denote the true fluorophore density of the specimen $f(x)$ and its Fourier transform $F(k)$. The observed images $g_i(x)$ under structured illumination are given by Eq. (2.1). After Fourier transformation, this equation can be rewritten as:

$$G(\mathbf{k}) = H(\mathbf{k})[F(\mathbf{k}) * M(\mathbf{k})]. \tag{2.6}$$

In the standard setup, the structured illumination is a sinusoidal pattern of parallel stripes. The illumination pattern can then be described by Eq. (2.2). The Fourier transform of this pattern is

$$M_n(\mathbf{k}) = \delta(\mathbf{k}) + \frac{\alpha}{2}\delta(\mathbf{k}-\mathbf{p})e^{2i\pi\varphi_n} + \frac{\alpha}{2}\delta(\mathbf{k}+\mathbf{p})e^{-2i\pi\varphi_n}. \tag{2.7}$$

Substitution Eq. (2.6) into Eq. (2.7) leads to the following formula

$$G_i(\mathbf{k}) = H(\mathbf{k})(F(\mathbf{k}) + \frac{\alpha}{2}F(\mathbf{k}-\mathbf{p})e^{2i\pi\varphi} + \frac{\alpha}{2}F(\mathbf{k}+\mathbf{p})e^{-2i\pi\varphi}), \tag{2.8}$$

where $H(\mathbf{k})$ is the optical transfer function (OTF).

The spectrum $F(k)$ of the original image is replicated three times with spectral components

centered on (**0**), (**p**), and (−**p**). This mixes frequencies that are outside the region of support of the optical transfer function $H(\mathbf{k})$ with lower observable frequencies. If the same process is repeated with different orientations of the illumination pattern, the images can be reconstructed with nearly isotropic resolution. To separate the spectral components of Eq. (2.8) at least three images with different phase shifts of the illumination pattern need to be acquired [8]. With equally separated phase shifts $(0, 2\pi/3, -2\pi/3)$, the following system of equations can be solved for each pattern orientation:

$$\begin{bmatrix} G_1(\mathbf{k}) \\ G_2(\mathbf{k}) \\ G_3(\mathbf{k}) \end{bmatrix} = \begin{bmatrix} 1 & 1 & 1 \\ 1 & e^{2i\pi/3} & e^{-2i\pi/3} \\ 1 & e^{-2i\pi/3} & e^{2i\pi/3} \end{bmatrix} \times \begin{bmatrix} H(\mathbf{k})F(\mathbf{k}) \\ \frac{\alpha}{2}H(\mathbf{k})F(\mathbf{k}-\mathbf{p}) \\ \frac{\alpha}{2}H(\mathbf{k})F(\mathbf{k}+\mathbf{p}) \end{bmatrix} \tag{2.9}$$

The solutions $C_n(\mathbf{k})$ represent the shifted spectra multiplied by non-shifted OTFs:

$$\begin{bmatrix} C_1(\mathbf{k}) \\ C_2(\mathbf{k}) \\ C_3(\mathbf{k}) \end{bmatrix} = \begin{bmatrix} 1 & 1 & 1 \\ 1 & e^{-2i\pi/3} & e^{2i\pi/3} \\ 1 & e^{2i\pi/3} & e^{-2i\pi/3} \end{bmatrix} \times \begin{bmatrix} G_1(\mathbf{k}) \\ G_2(\mathbf{k}) \\ G_3(\mathbf{k}) \end{bmatrix} \tag{2.10}$$

These three separated components then need to be shifted:

$$\begin{aligned} CS_1(\mathbf{k}) &= C_1(\mathbf{k}) \\ CS_2(\mathbf{k}) &= C_2(\mathbf{k}+\mathbf{p}) \\ CS_3(\mathbf{k}) &= C_3(\mathbf{k}-\mathbf{p}) \end{aligned} \tag{2.11}$$

and combined e.g. through a generalized Wiener filter

$$S(\mathbf{k}) = \frac{\sum_{n=1}^{N} OTF_n(\mathbf{k})^* CS_n(\mathbf{k})}{\sum_{n=1}^{N} |OTF_n(\mathbf{k})|^2 + w}, \tag{2.12}$$

where $S(\mathbf{k})$ is the reassembled image in reciprocal space, OTF_n is the n^{th} shifted OTF of the imaging system (in analogy to Eq. (2.11)), N is the total number of image components (i.e. number of acquired patterned illumination images) and w is a small constant that controls the noise of the reconstructed image. The reassembled image is then apodized with the desired OTF profile to decrease ringing artifacts caused by sharp edges of the new reassembled Fourier spectrum. The resulting image is finally transformed back to real space. Here we note that due to the linearity and shifting properties of the Fourier transform, the spectral decomposition (Eq. (2.10)) and the frequency shifts (Eq. (2.11)) can be performed in real space.

2.1.3 Statistical approach

The Bayesian theory with various noise models and regularization forms is widely used for microscopy image deconvolution [33],[34],[35]. Vermolen et al. [36] have demonstrated a

restoration technique that simultaneously uses a confocal and a widefield image. An algorithm that is able to estimate the sample fluorescence density from low resolution images obtained under unknown speckle patterns has been proposed (blind-SIM) by Mudry et. al. [26]. Orieux et al. presented a framework for SIM based on Bayesian estimation of an inverse problem[27]. Their method achieves similar performance as SR-SIM method but using a reduced number of acquired images. Orieux et al. uses the mean of the joint posterior law which leads to an integration problem. We introduced a simpler Bayesian estimation approach based on the maximum a posteriori (MAP) estimator and performed a comparison of different SIM algorithms [20]. Recently, we have presented a new 3D reconstruction method for SIM based on maximum a posteriori probablity (MAP-SIM)[37]. Theoretical bacground and performance of this new method is discussed in details in chapter 3.

2.2 Super-resolution optical fluctuation imaging (SOFI)

SOFI is based on spatio-temporal cross-cumulants calculated from a time series of images of stochastically blinking emitters. Cumulants are a statistical measure used to describe a probability distribution [38]. The resolution improvement is given by the properties of these cumulants and described in a seminal paper by J. Enderlein and coworkers [7].

Based on a second order cumulant analysis, SOFI achieved a two-fold resolution improvement with quantum dots [7], small organic fluorophores [39] and reversibly photoswitchable fluorescent proteins [40]. As shown by Dertinger et al. [7] and Geissbüehler et al. [18] a further resolution improvement can be achieved by increasing the cumulant order. P. Dedecker et al. [40] imaged HeLa cells co-expressing Lyn-Dronpa. Gallina et al. [41] applied bicolor SOFI to co-localize hDcp1a, a processing body protein, and the tubulin cytoskeletal network in cells. Recently, Geissbüehler et al. conceived a multi-plane setup allowing parallel acquisition of multiple depth planes and super-resolved three-dimensional imaging without mechanical scanning [19]. This methodology significantly reduced the overall acquisition time for 3D imaging and has been applied to the imaging of the mitochondrial network in fixed C2C12 cells with 3-fold resolution improvement in all three spatial dimensions. SOFI exhibits a nonlinear response to brightness and blinking heterogeneities in the sample, which restricts in practice the achievable resolution improvement. Geissbüehler et al. introduced an extension of the SOFI concept (the so-called balanced SOFI (bSOFI) [42]) that enables to cancel the non-linear response to brightness. Several cumulant orders can be combined to extract spatial maps of photo-physical parameters such as the blinking rates of the fluorescent markers as well as their molecular brightness and densities. STORM improves the resolution by precisely localizing individual fluorophores (usually frame by frame). To distinguish densely packed single fluorophores in time, the off state of the fluorophores have to be significantly longer than the on state. It puts more demands to the blinking statistics of the fluorescent dyes. In contrast to localization microscopy, SOFI analysis processes the whole input image stack at once and is compatible with weakly emitting fluorophores, higher labeling densities and a wide range of blinking conditions [18].

2.2.1 SOFI principle and theory

SOFI applies high order statistics to exploit the temporal blinking sequence of fluorescent emitters [7, 44]. More precisely, SOFI is based on calculating spatio-temporal cross-cumulants to obtain a super-resolved, background-free and noise-reduced image using a conventional widefield microscope. As stated by Dertinger et al. [7], the fluctuating emitters should fulfill the following conditions:

1. The markers should switch between at least two optically distinguishable states, e.g. a dark and a bright state.

2. Each emitter switches between the states repeatedly and independtly in a stochastic manner.

3. The point-spread image of each emitter has to extend over several camera pixels.

As shown in Figure 2.1a, images of stochastically blinking emitters are recorded such that the point-spread function (PSF) is spread over several camera pixels. By acquiring a stack of images over time, one obtains a time trace for each pixel (Figure 2.1b). The time trace contains the sum of the contributions of every fluorophore whose PSF reaches the pixel. Assuming N independently fluctuating emitters, the detected intensity can be described as

$$I(\mathbf{r},t) = \sum_{k=1}^{N} \epsilon_k U(\mathbf{r}-\mathbf{r}_k) s_k(t) + b(\mathbf{r}) + n(\mathbf{r},t), \tag{2.13}$$

where ϵ_k is the molecular brightness, $U(\mathbf{r}-\mathbf{r}_k)$ is the PSF of the optical system, $s_k(t)$ denotes a switching function (normalized fluctuation sequence, $s_k(t) \in \{0,1\}$), $b(\mathbf{r})$ is a constant background, and $n(\mathbf{r},t)$ represents an additive noise. The sample is assumed to be stationary during the image acquisition.

Random blinking of an emitter is spatio-temporally correlated with itself and uncorrelated with neighboring emitters. For each pixel, a measure of correlation in a form of an n^{th} order cumulant is calculated for a better discrimination of emitters inside the PSF volume. Using cross-cumulants, values for virtual pixels in between the physical pixel grid can be also calculated in order to obtain a finer sampling of the image [44]. Figure 2.1c shows a 2^{nd} order cross-cumulant with various time lags calculated for each pixel time trace (Figure 2.1b). Note that the 2^{nd} order cross-cumulant is mathematically equivalent to the 2^{nd} cross-correlation. Cumulants are appropriate for a generalization of SOFI to higher orders, because unlike higher order correlations, n^{th} order cumulants does not contain lower order cross-terms which would hamper the resolution enhancement [7].

Generally, spatio-temporal cumulants can be calculated with various time lags. For reducing the computational complexity and ensuring the maximum of the signal, we used zero time lag. As shown in [44], virtual pixels can be calculated in between the physical pixels acquired

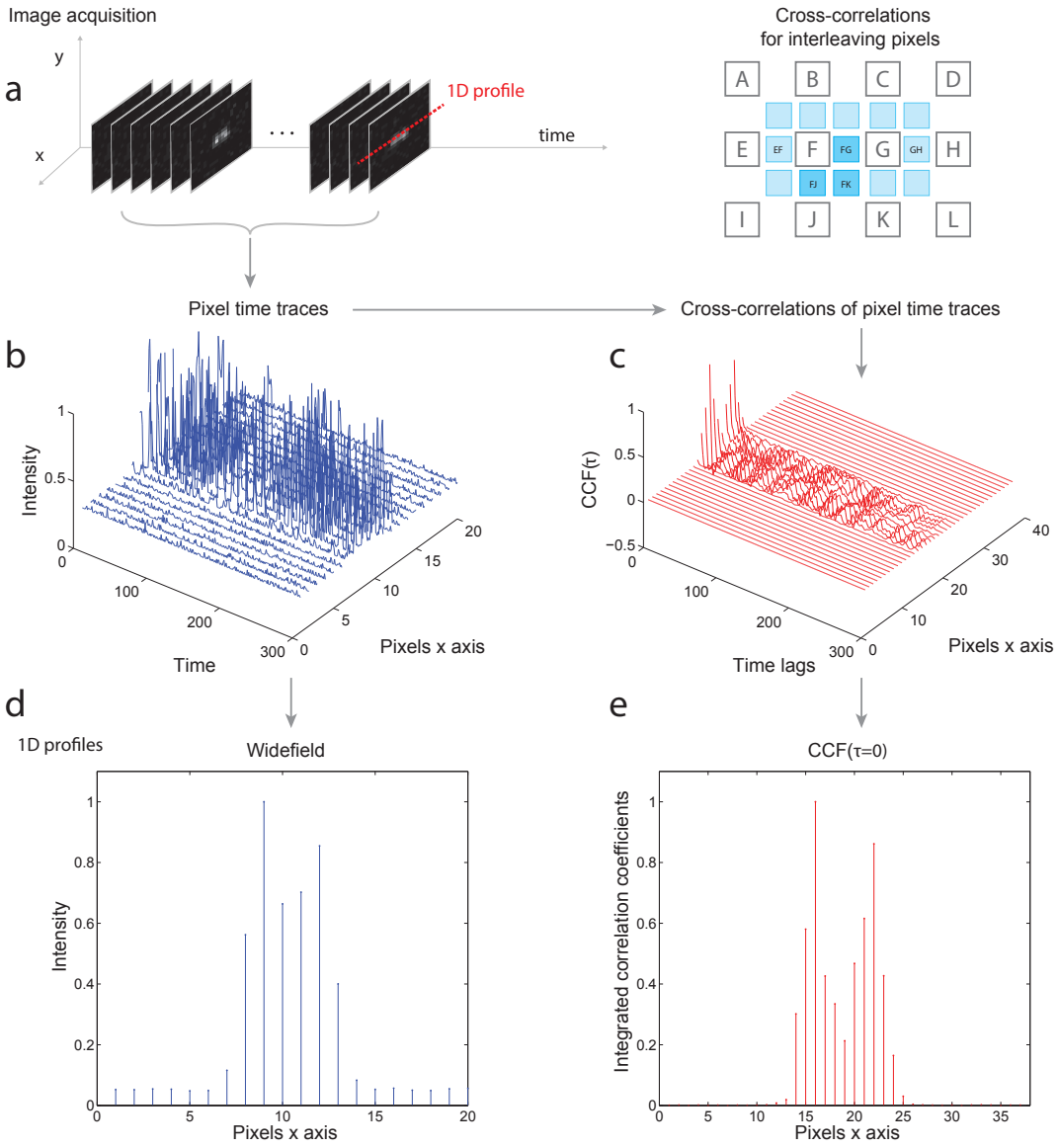

Figure 2.1: The SOFI principle in a one dimensional example. (a) An image sequence of two blinking emitters. (b) Intensity time traces of a line profile shown in (a). (c) 2^{nd} order cross-cumulants calculated from the intensity time traces (b) for all time lags. Using cross-cumulants, the interleaving pixels are also calculated. Note that the 2^{nd} order cross-cumulant is mathematically equivalent to the 2^{nd} cross-correlation. (d) The temporal average of (b) i.e. the widefield image. (e) The 2^{nd} order cross-cumulants for $\tau = 0$. Adjusted from Girsault & Lukeš et al., Plos One, 2016 [43].

by the camera using cross-cumulants and followed by a flattening operation (i.e. assigning proper weights to virtual pixels) [44, 45, 46]. By applying the n^{th} order cumulant to the Eq. (2.13), we obtain

$$\kappa_n\{I(\mathbf{r},t)\}(\tau) = \kappa_n\left\{\sum_{k=1}^{M} \epsilon_k U(\mathbf{r}-\mathbf{r}_k)s_k(t) + b(\mathbf{r}) + n(\mathbf{r},t)\right\}(\tau). \tag{2.14}$$

Using the fundamental properties of cumulants like additivity and semi-invariance [47], the n^{th} order cumulant with zero time lag can be written as

$$\kappa_n\{I(\mathbf{r},t)\} = \sum_{k=1}^{N} \epsilon_k^n U^n(\mathbf{r}-\mathbf{r}_k)\kappa_n\{s_k(t)\} + \kappa_n\{b(\mathbf{r})\} + \kappa_n\{n(\mathbf{r},t)\}. \tag{2.15}$$

For ($n \geq 2$), under the assumption of uncorrelated noise and stationary background, the terms $\kappa\{b(\mathbf{r})\}$ and $\kappa\{n(\mathbf{r},t)\}$ will cancel out. For an n^{th} order cumulant, the PSF is raised to the n^{th} power. In consequence, the spatial resolution is improved by a factor of $\sqrt{n}$ [7]. Therefore, increasing the cumulant order yields an image with an enhanced spatial resolution. Since a multiplication in the spatial domain corresponds to a convolution in the frequency domain, the cut-off frequency of $U^n(\mathbf{r})$ is in principle n-times higher than that of $U(\mathbf{r})$. Consequently, by applying deconvolution and a subsequent rescaling, the n^{th} order cumulant image exhibits up to an n-fold resolution improvement [44].

SOFI usually assumes STORM like blinking model of the fluorohores i.e. the fluorophores reversibly switch between a bright and a dark state. In Deschout & Lukeš et al., we have shown that SOFI can be applied also to PALM data [48]. In the PALM photo-physical model, the emitter activation is assumed as non-reversible, however, since the emitter is activated, it exhibits several quick blinking events prior to be finally bleached [49]. On a shorter time scale (within one subsequence of input dataset), the emitter fluctuates. If the emitter fluctuates between two different states (an on-state S_{on} and a dark state S_{off}), we can define the on-time ratio as

$$\rho = \frac{\tau_{\text{on}}}{\tau_{\text{on}} + \tau_{\text{off}}}, \tag{2.16}$$

where τ_{on} and τ_{off} are the characteristic lifetimes of S_{on} and S_{off} states. The n^{th} order cumulant $\kappa_n\{s_k(t)\}$ is in this model described by a Bernoulli distribution with probability ρ_{on} [42] and approximated by an n^{th} order polynomial function of the on-time ratio (further referred to as a cumulant function)

$$f_n(\rho_{\text{on}}) = \rho_{\text{on}}(1-\rho_{\text{on}})\frac{\partial f_{n-1}}{\partial \rho_{\text{on}}}. \tag{2.17}$$

Under these conditions, the n^{th} order spatio-temporal cross-cumulant can be approximated as [42]:

$$\kappa_n\{I(\mathbf{r},\mathbf{t})\} \approx \epsilon^n f_n(\rho_{\text{on}}) \sum_{k=1}^{N} U^n(\mathbf{r}-\mathbf{r}_k). \tag{2.18}$$

As a characteristic of SOFI, any stationary background is strongly suppressed, uncorrelated noise is reduced and signals of several blinking emitters can be discriminated beyond the diffraction limit [7, 44].

The nonlinear response to molecular brightness ϵ^n in Eq. (2.18) represents a limitation in practice for 3^{rd} and higher orders where most of the structural details are hidden in the background due to a few brightest spots. Geissbuehler et al. [42] proposed a reformulation of the original SOFI concept called balanced SOFI (bSOFI). First step is a deconvolution in order to correct the non-linear response to brightness without compromising the resolution improvement. Assuming a perfect deconvolution applied to the n^{th} order cumulant in Eq. (2.18), the deconvolved cumulant image can be expressed as

$$\hat{\kappa}_n\{I(\mathbf{r},\mathbf{t})\} \approx \epsilon^n f_n(\rho_{\text{on}}) \sum_{k=1}^{N} \delta(\mathbf{r}-\mathbf{r}_k). \tag{2.19}$$

In the next step, a linearization of the brightness response is performed by taking the n-th root. The result is then reconvolved with the n-times size-reduced PSF to limit the final resolution to a physically reasonable value [42]. Figure 2.2b shows 2D SOFI images up to the 4^{th} cumulant order after flattening and linearization. Cumulants are proportional to the n^{th} order polynomial of the on-time ratio $f_n(\rho_{\text{on}})$. Close to the roots of the polynomial, the SNR of the cumulant drops. These roots in the interval $\rho_{on} = [0,1]$ are at different positions for different cumulant orders. Once the cumulants are linearized by the aforementioned procedure, it is possible to combine linearized cumulant of order n with a linearized cumulant of order $n-1$ using an on-time ratio map $\rho_{on}(\mathbf{r})$ to restore the badly defined areas with low SNR [42]. On-time ratio estimation is discussed in section 4.3.3.

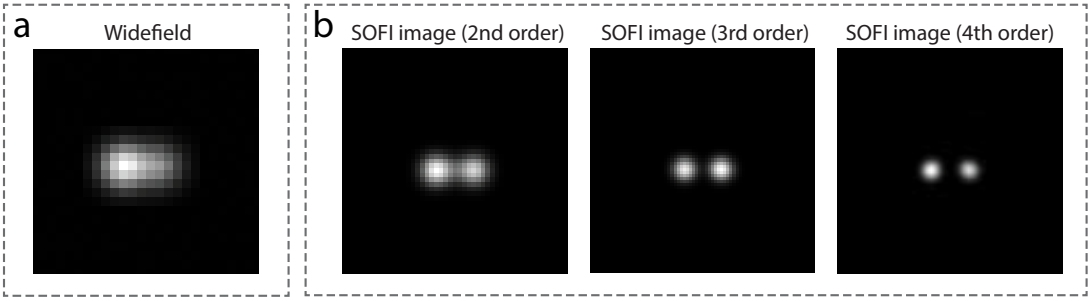

Figure 2.2: SOFI example. (a) Widefield image (temporal average of the input image sequence shown in 2.1a). (b) Linearized 2D SOFI images up to the 4^{th} order cumulant.

3 SIM imaging

Parts of the following chapter were published in:
Lukeš et al., Three-dimensional super-resolution structured illumination microscopy with maximum a posteriori probability image estimation, Optics Express 2014 [37]

We developed a new high performance image reconstruction method for super-resolution structured illumination microscopy based on maximum a posteriori probability estimation (MAP- SIM). [37]. Imaging performance was demonstrated on a variety of fluorescent samples of different thickness, labeling density and noise levels. The method provides good suppression of out of focus light, improves spatial resolution, and allows reconstruction of both 2D and 3D images of cells even in the case of weak signals. The method can be used to process both optical sectioning and super-resolution structured illumination microscopy data to create high quality super-resolution images. We used a microscope setup (Figure 3.1) in which the illumination pattern is generated by a spatial light modulator together with incoherent illumination. Details about the microscope setup can be found in [29, 37]. MAP-SIM does not require precise knowledge of the point spread function (PSF) which must be carefully measured in most SR-SIM approaches.

3.1 Three-dimensional super-resolution SIM with Bayesian image reconstruction

SR-SIM requires one to precisely shift the separated spectral components to their proper positions in reciprocal space. High noise levels in the raw data can cause inaccuracies in the shifts of the spectral components which degrade the super-resolved image. The method is also sensitive to imprecise knowledge of the illumination pattern. Therefore, the aim is to provide more robust and efficient reconstruction algorithm compatible with weak signals. We have shown that the Bayesian estimation is more robust to changes in noise level and illumination pattern frequency compared to SR-SIM [20]. We propose a new image reconstruction method for SIM which provides resolution improvement in all three dimensions using two-dimensional illumination patterns. Our method, maximum a posteriori probability

SIM (MAP-SIM) [37] is based on combining, via spectral merging in the frequency domain, maximum a posteriori probability estimation (for resolution improvement) and homodyne detection (for optical sectioning).

3.1.1 Maximum a posteriori probability estimation

An image acquired by the microscope can be modeled as a convolution of an ideal image of a real sample with the point spread function (PSF) of the microscope (see section 1.1). The additional noise is composed of different noise sources (e.g., photon noise, read out noise) and can be modeled by additive Gaussian noise with zero mean [34, 50]. Image acquisition in structured illumination microscopy can then be described as

$$y_k = HM_k x + n_k, \tag{3.1}$$

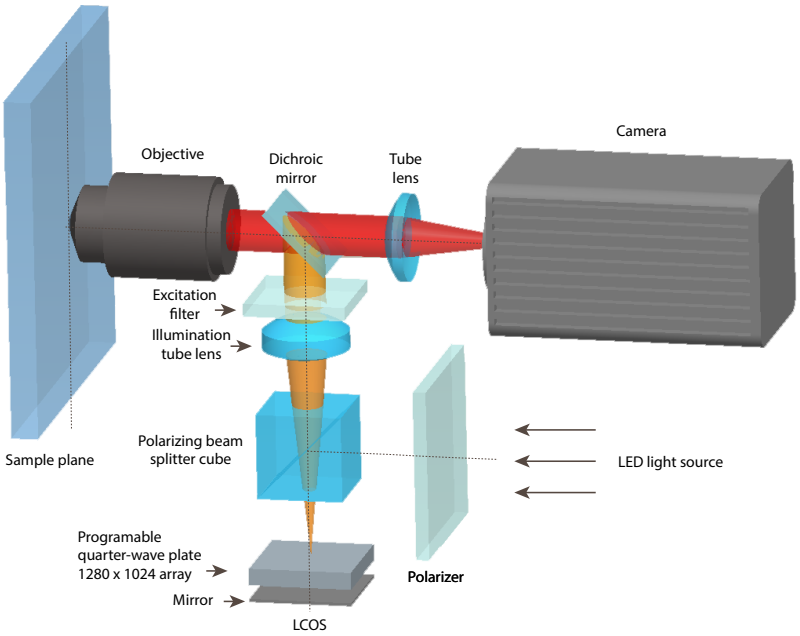

Figure 3.1: Our structured illumination microscope setup. The desired illumination patterns are produced by a high speed ferroelectric liquid crystal on silicon (LCOS) microdisplay. The LCOS microdisplay used here can be configured with a variety of timing schemes. With the timing program that we used, the microdisplay can display an illumination pattern and switch to the next pattern in the sequence in 1.14 ms. Given a bright enough light source, fast enough camera, and appropriate sample, acquisition of raw SIM images at rates exceeding 800 Hz would therefore be possible. More details about the setup can be found in our publication [37].

where $k = 1,\ldots,K$ indexes the sequence of illumination patterns, y_k denotes a vectorized (matrix converted into a column vector by stacking the columns of the matrix on top of one another) diffraction limited low-resolution (LR) image acquired by the camera using the k-th illumination pattern, x represents an unknown, vectorized high-resolution (HR) image, and n_k is a vectorized image containing additive noise. All of these vectors contain m elements. Toeplitz matrix H is an $m \times m$ matrix which models the convolution between the HR image and the PSF of the system, and M_k is an $m \times m$ diagonal matrix in which the elements represent the k-th illumination pattern. We model the PSF of the microscope as an Airy function, see section 2.2.

The reconstruction of the HR image x can be performed using a Bayesian approach [27, 33, 51]. The maximum a posteriori estimator of x is given by maximizing the probability of the HR image represented by the observed LR images

$$\hat{x} = \arg\max_{\mathrm{x}} \left[P\left(x|y_1, y_2, \ldots, y_K\right) \right]. \tag{3.2}$$

Applying Bayes' theorem to the conditional probability in Eq. (3.2) and by taking the logarithm, we obtain

$$\hat{x} = \arg\max_{\mathrm{x}} \left[\log P\left(y_1, y_2, \ldots, y_K|x\right) + \log P\left(x\right) \right]. \tag{3.3}$$

Because the LR images y_k are independent measurements, we can write

$$P\left(y_1, y_2, \ldots, y_K|x\right) = \prod_{k=1}^{K} P\left(y_k|x\right). \tag{3.4}$$

The additive noise n_k in Eq. (3.1) is modeled as white Gaussian noise with a mean of zero and variance σ^2. The density function in Eq. (3.4) can be expressed as

$$P\left(y_k|x\right) \propto \exp\left(-\frac{\left\| y_k - HM_k x \right\|^2}{2\sigma^2} \right). \tag{3.5}$$

Because of the presence of noise, the inversion of Eq. (3.1) is an ill-posed problem and some form of regularization is needed to ensure uniqueness of the solution. The regularization term in Eq. (3.3), provided by the density function $P(\mathrm{x})$, reflects prior knowledge about the HR image, such as a positivity constraint and image smoothness. Several kinds of priors and regularization techniques have been proposed within the Bayesian framework [52]. To impose a smoothness condition and to ensure that a cost function is simple to minimize, we have adopted a term composed of finite difference approximations of the first order derivatives at each pixel location [53]

$$\log P(\mathrm{x}) = \Gamma(\mathrm{x}) = \sum_i \left[(\Delta_h \mathrm{x})_i^2 + (\Delta_v \mathrm{x})_i^2 \right], \tag{3.6}$$

where Δ_h and Δ_v are the finite difference operators along the horizontal and vertical direction of an image, and $(\cdot)_i$ denotes the i-th element of a vector. Substituting Eq. (3.5) and Eq. (3.6) into Eq. (3.3), the image reconstruction can be expressed as a minimization of the following cost function

$$\hat{x} = \arg\min_{x} \left[\sum_{k=1}^{K} \left\| y_k - HM_k x \right\|^2 + \lambda \Gamma(x) \right]. \tag{3.7}$$

The cost function in Eq. (3.7) consists of two terms. The first term describes the mean square error between the estimated HR image and the observed LR images. The second term is the regularization term and its contribution is controlled by the parameter λ which is a small positive constant defining the strength of the regularization. After substituting Eq. (3.5) and (3.6) into Eq. (3.3) and further treatment, λ absorbs the variance of the noise (σ^2). Lambda can be also expressed as $\lambda = 2\sigma^2\lambda'$, where λ' is a small positive constant. Eq. (3.7) is minimized by gradient descent optimization methods and the estimate of the unknown image x at the $(n+1)^{\text{th}}$ iteration is obtained as

$$x^{(n+1)} = x^{(n)} - \alpha^{(n)} g^{(n)}. \tag{3.8}$$

Here $\alpha^{(n)}$ is the step size, $\mathrm{g}^{(n)}$ is the gradient of the cost function, and $n = 0, 1, 2, \ldots$ is an iteration step. Computation iteratively continues until $\left\| \alpha^{(n+1)} \mathrm{g}^{(n+1)} \right\| / \left\| \alpha^{(n)} \mathrm{g}^{(n)} \right\| < \varepsilon$, where $\varepsilon > 0$ is a user-defined stopping criterion. This enables one to stop the algorithm very quickly after only a few aggressive steps towards minimum.

3.1.2 OTF modeling

The spatial frequency f_c at which the optical transfer function (OTF) reaches zero determines the achievable resolution of a microscope, see Figure 1(a) . We model the PSF as an Airy disk which in Fourier space leads to an OTF

$$OTF(\mathbf{f}) = \frac{1}{\pi} \left[2\cos^{-1}\left(\frac{\mathbf{f}}{f_c} \right) - \sin\left(2\cos^{-1}\left(\frac{\mathbf{f}}{f_c} \right) \right) \right], \tag{3.9}$$

where $\mathbf{f}$ is the spatial frequency. The cut off frequency f_c is estimated by calculating the radial average of the power spectral density (PSD) of a widefield image, see Figure 3.2(b).

3.1.3 Spectral merging

MAP estimation of a high resolution image obtained with structured illumination microscopy enables reconstruction of images (HR-MAP) with details unresolvable in a widefield microscope. However, MAP estimation as described here does not suppress the out of focus light.

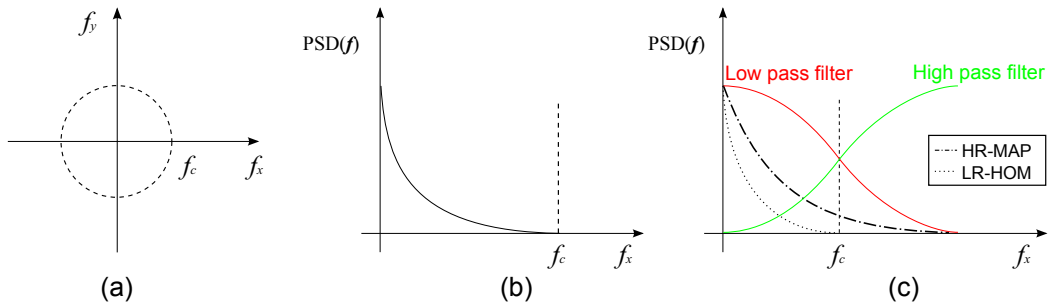

Figure 3.2: Schematic of spectral merging (a) Spatial frequencies in Fourier space, where f_c is the cut off frequency. (b) Power spectral density (PSD) in relation to the spatial frequency. (c) Blending frequency spectra of HR-MAP estimation and LR homodyne detection using low and high pass filters.

On the other hand, the homodyne detection method

$$\mathrm{x}_{\text{LR-HOM}} = \left| \sum_{k=1}^{K} \mathrm{y}_k \exp\left(2\pi \mathrm{i} \frac{k}{K}\right) \right|, \tag{3.10}$$

used in OS-SIM [24] provides images (LR-HOM) with optical sectioning but without resolution improvement. Noting that the unwanted out of focus light is dominantly present at low spatial frequencies, we merge both LR-HOM and HR-MAP images in the frequency domain, see (Figure 3.2(c)) to obtain the final HR image (MAP-SIM). Low pass filtering is applied to the LR-HOM image and a complementary high pass filter is applied to the HR-MAP image. O'Holleran and Shaw [25] used Gaussian weights with empirically adjusted standard deviations for weighting frequency components obtained by SR-SIM. We verified that Gaussian functions are well suited for our case. We applied a weighting scheme which can be described by

$$\begin{aligned} \mathrm{x}_{\text{MAP-SIM}} = \mathscr{F}^{-1}\Bigg\{ & (1-\beta)\mathscr{F}\{\mathrm{x}_{\text{LR-HOM}}\} \exp\left(-\frac{\mathbf{f}^2}{2\rho^2}\right) \\ & + \beta\mathscr{F}\{\mathrm{x}_{\text{HR-MAP}}\}\left(1-\exp\left(-\frac{\mathbf{f}^2}{2\rho^2}\right)\right)\Bigg\}, \end{aligned} \tag{3.11}$$

where $\mathscr{F}, \mathscr{F}^{-1}$ denotes Fourier transform operator and its inverse, respectively, $\mathbf{f}$ is the spatial frequency, ρ is the standard deviation of the Gaussian filter, and β is a positive weighting coefficient. The use of these variables and application of Eq. (3.11) are described in more detail in our publication devoted to MAP-SIM method [37].

3.1.4 3D MAP-SIM imaging

To demonstrate the optical sectioning characteristics of MAP-SIM, we imaged a relatively thick biological sample, a fluorescent pollen grain about 50 μm thick, see Figure 3.3. The images were acquired using a 60 x /1.35 NA oil immersion objective. In this case an illumination

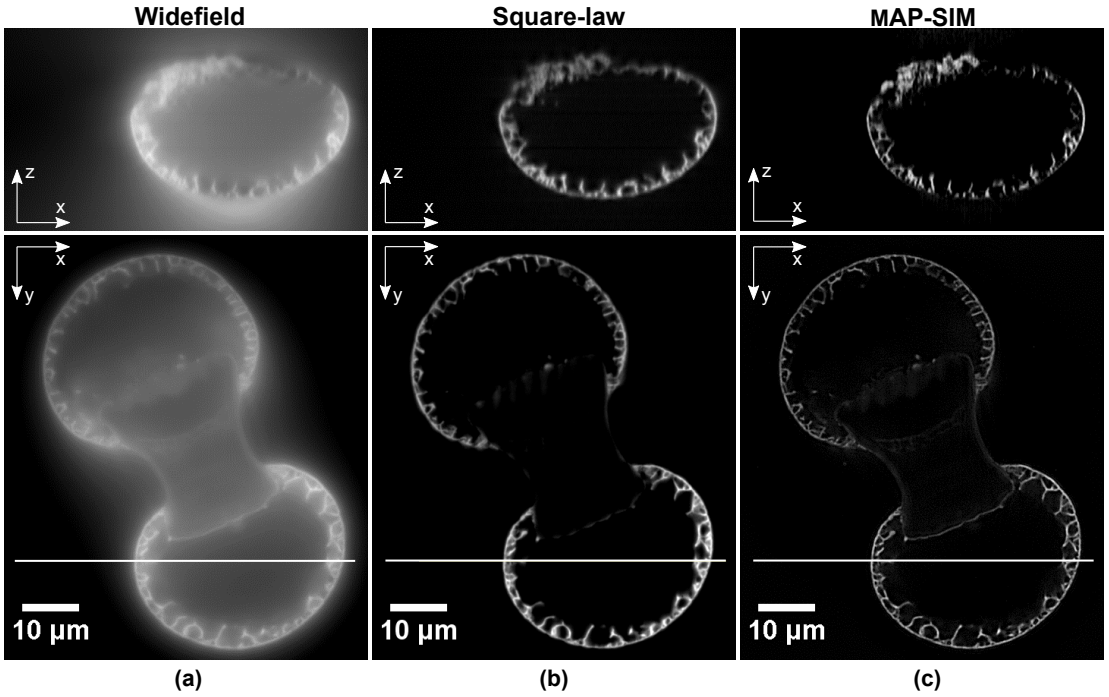

Figure 3.3: Image of an autofluorescent pollen grain acquired using a 60 x /1.35 NA oil immersion objective. (a) Widefield image. (b) square-law method. (c) MAP-SIM. Shown are also XZ projections taken along the pixel row indicated by the white line. Published in Lukeš et al., Optics Express, 2014 [37].

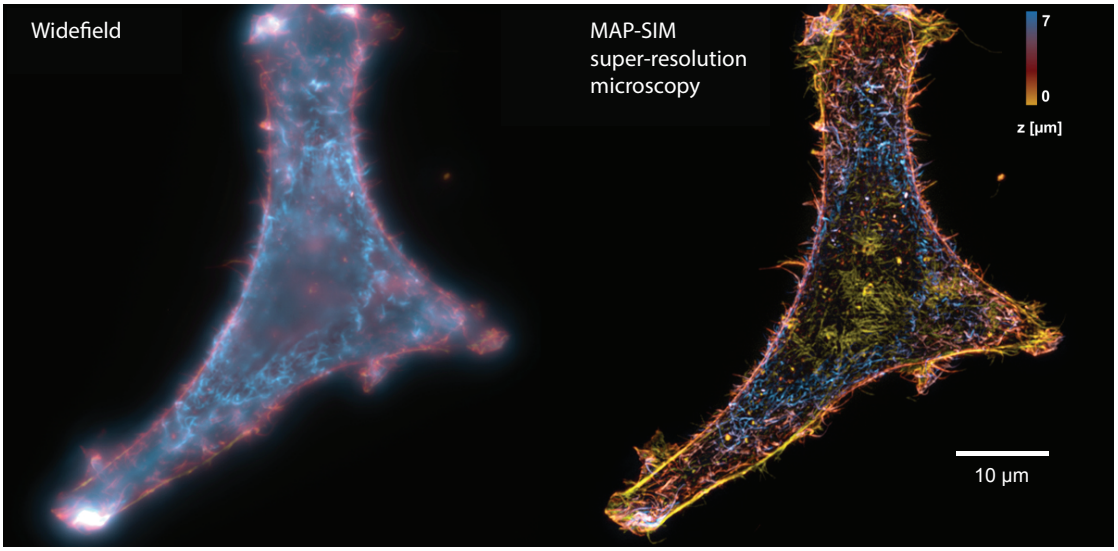

Figure 3.4: Atto-532 Phalloidin labeled actin in a HepG2 cell. Maximum intensity projections of the 3D stack - widefield and MAP-SIM. Thickness of the sample is 7 μm. Depth color coding.

pattern with a single orientation was used (orientation: 0°; number of shifts: 10; period: 2.27 μm). Ninety planes along the z-axis were scanned with a spacing of 500 nm. Lateral and axial cross sections of the pollen grain image in Figure 3.3(c) reveal that MAP-SIM provides increased lateral and axial resolution compared to the widefield image. We also imaged Atto-532 phalloidin labeled actin in a HepG2 cell using the same illumination patterns as the pollen grain sample, see Figure 3.4. Depth color coding was applied to the image using the isolum color map [54]. Maximum intensity projections of the color coded 3D MAP-SIM images are shown in Figure 3.4. MAP-SIM is robust towards imperfections of illumination patterns at the sample plane even in the case of week signals. In our paper [37], we have tested a variety of SNR conditions and the MAP-SIM reconstruction was successful even in the presence of high noise levels, where the SNR of the corresponding widefield images was about 5.9 dB.

3.1.5 Iterative deconvolution compared to MAP-SIM

We imaged Alexa Fluor 488 phalloidin labeled actin in BPAE cells using a 100 × /1.40 NA oil immersion objective and 460 nm LED. For MAP-SIM reconstruction, 14 illumination patterned images were used (3 line illumination patterns at 0° and 90°, 4 illumination patterns at 45° and 135°). The widefield image was deconvolved using Huygens software (Hilversum, The Netherlands) with the maximum likelihood estimation algorithm. The difference between deconvolved image and MAP-SIM image is visible in Figure 3.5. Deconvolution emphasized the edges, but the deconvolved image does not contain more details. Fine cytoskeletal features are better resolved in the MAP-SIM image as can be seen in the region of interest in Figure 3.5.

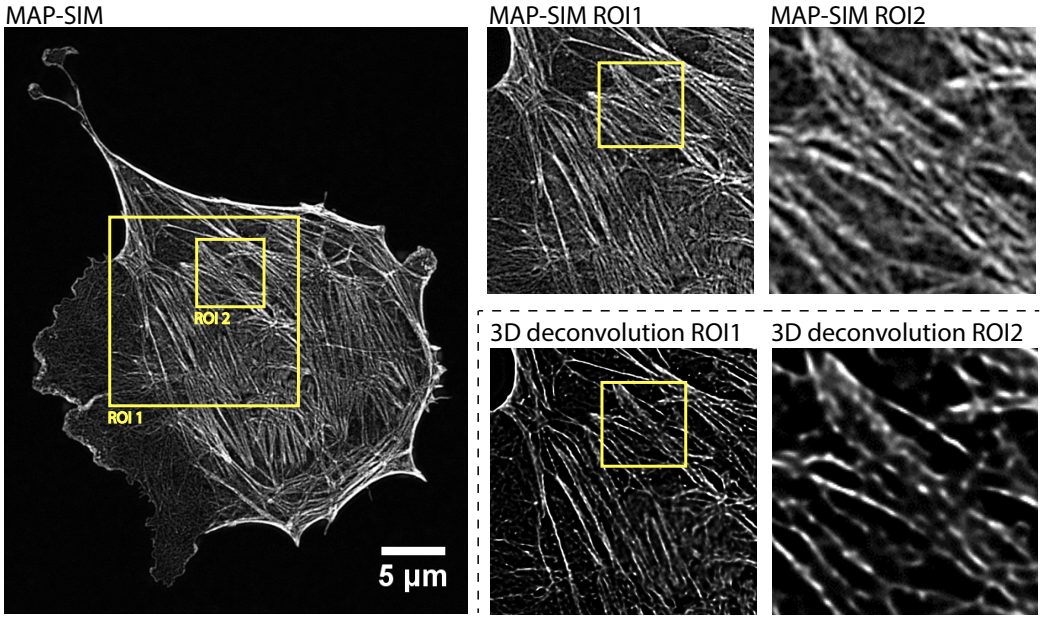

Figure 3.5: Comparison between a state of the art 3D deconvolution using Huygens software and MAP-SIM. Maximum intensity projections of the deconvolved image and the the MAP-SIM image correspond the the regions of interest indicated by the yellow box.

3.2 SIMToolbox: a MATLAB toolbox for SIM

We have published the first open-source software for SIM called SIMToolbox [55]. Our goal is to offer a collection of processing methods, developed based on extensive testing with real data, to facilitate image reconstruction for researchers developing their own SIM microscopes and to accelerate progress in image processing tasks. SIMToolbox is an open-source, modular set of functions for MATLAB equipped with a user friendly graphical interface and designed for processing both OS-SIM and SR-SIM data according to a variety of methods including our new MAP-SIM method. This allows researchers building their own systems to process their data using a unique set of tools and concepts. The software also offers features not currently present in commercially available software, making it a useful choice for reconstructing super-resolution images acquired with commercial equipment, however some of the tools and documentation provided are meant for researchers developing their own systems. In addition to the software, we provide example data, a user's guide, and a detailed description of the implemented methods and algorithms on the website of the journal [55] and on the project website [56].

3.3 Imaging live cells with MAP-SIM

Imaging live cells with super-resolution structured illumination microscopy (SR-SIM) for more than a few time points remains a challenge due to the requirement to acquire multiple images to reconstruct a single high resolution image, and also due to inflexibility in acquisition protocols present in the currently available commercialized instruments for SR-SIM. Live cell SR-SIM has been demonstrated in several applications, including 2D [21, 22], and 3D imaging [23, 57, 58]. Structured illumination methods have also been combined with light sheet excitation, a method ideally suited for imaging live cells [59, 60, 61, 62, 63].

Here we demonstrate super-resolution imaging of live cells using MAP-SIM method descsribed in section 3.1. We imaged U2-OS cells (an osteosarcoma cell line) that had been transfected with GFP-tagged lysosomal associated membrane protein (LAMP1-GFP). Figure 3.6 shows widefield, OS-SIM (homodyne detection), and MAP-SIM images of U2-OS cells expressing LAMP1-GFP. We found that, in addition to lysosomal expression, LAMP1-GFP is also present in high concentrations in the plasma membrane of U2-OS cells. In this experiment (Figure 3.6), we acquired SIM image sequences with an exposure time of 25 ms, a raw imaging rate of 40 Hz. We used a SIM pattern with 11 phases (pattern period in the sample plane $1.5\mu m$) and a single angle (0 deg with respect to the camera), acquiring 5192 total frames, resulting in 472 processed frames. The imaging rate of processed result frames was therefore 3.6 Hz. The pattern we used was chosen based on our earlier publication [29]. An optimal illumination pattern depends on the sample in question. Having particle tracking application in mind, we aimed at the best possible optical sectioning and image quality in terms of signal to noise ratio (SNR). The frequency spectrum of the pattern contains several higher harmonics, the highest of which is positioned close to the resolution limit of the objective. As in conventional

SR-SIM, this allows aliasing of high resolution information into the passband of the objective. The particle tracking applied to this video sequence is analyzed in details in chapter 5.4.

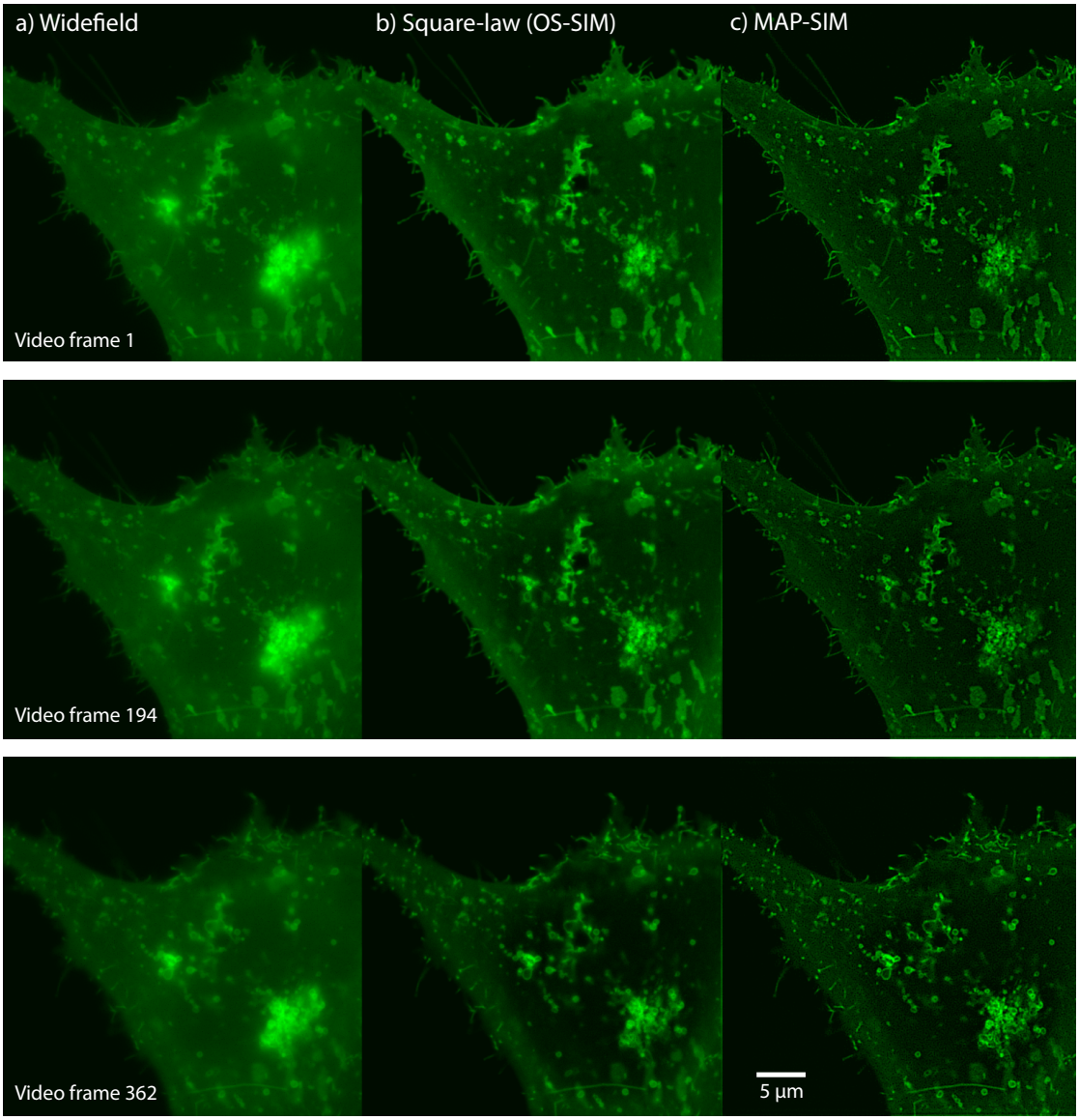

Figure 3.6: Several frames of 362 frames video sequence of LAMP1-GFP expressed in a U2-OS cell. (a) Widefield, (b) Square-law method (OS-SIM), (c) MAP-SIM. Overall acquisition time for one super-resolved frame 275ms.

4 SOFI imaging

Parts of the following chapter were published in:
H. Deschout & T. Lukeš* et al., Complementarity of PALM and SOFI for super-resolution live cell imaging of focal adhesions, Nature Communications, 2016 [48]*

A. Girsault & T. Lukeš* et al., SOFI Simulation Tool: A Software Package for Simulating and Testing Super-Resolution Optical Fluctuation Imaging, Plos One, 2016 [43]*
**Equal contribution.*

Aiming for super-resolved 3D live cell imaging, our efforts are driven towards a reduction of the acquisition time. We developed an adapted 3D deconvolution algorithm described in section (4.1) and incorporated it into the bSOFI method. This improved algorithm can handle the peculiarities of multidimensional cumulant images and increase the signal to noise ratio. As a consequence, the overall image quality is improved and the acquisition time is reduced. We developed a novel linearization procedure for SOFI maximizing the available resolution improvement (section 4.3). Focusing on quantitative imaging, we investigate molecular parameter estimation and generalize this procedure for higher order cumulants (section 4.3.3). We show that SOFI can be applied on the same dataset as PALM. We perform a comprehensive spatio-temporal analysis of PALM and SOFI which reveals the complementarity of both methods (section 4.5). Applying both PALM and SOFI on the same dataset can provide more information about the sample.

4.1 3D deconvolution for SOFI

The bSOFI data processing demands a deconvolution in order to restore a linear image contrast. bSOFI uses the classical Lucy-Richardson (LR) deconvolution [64, 65] which does not suppress noise and assumes a non-negativity constraint for the image data. This condition is met for classical imaging, but violated for bSOFI which may lead to image artifacts. Here, we present SOFI image analysis integrating a new 3D deconvolution algorithm suitable for cumulant images.

Several deconvolution algorithms regularizing noise were introduced like statistical methods [51], wavelet based restoration [66] and augmented Lagrangian methods [67] using the non-negativity assumption, which is violated for cumulants of higher orders. Augmented Lagrangian and Bregman iterative methods [67, 68, 69] (both methods lead to the mathematically equivalent algorithm) allow splitting the minimization problem into several sub-problems. These sub-problems are easier to solve and possible stable solutions may be provided. Therefore, we adopted the split Bregman iterative method and adjust it to 3D SOFI conditions.

In SOFI, the super-resolved image is given by a cumulant calculated over several hundreds time frames. The cumulant order n leads to an n-fold resolution enhancement [44, 42]. The cumulant of order n of a pixel set $\mathbf{P} = \{\mathbf{r_1}, \mathbf{r_2}, ..., \mathbf{r_n}\}$ with time lags $\tau = \{\tau_1, \tau_2, ..., \tau_n\}$ is given as [38]

$$\kappa_n\left(\mathbf{r} = \frac{1}{n}\sum_{i=1}^{n}\mathbf{r}_i; \tau\right) = \sum_P (-1)^{|P|-1}(|P|-1)\prod_{p\in P}\left\langle \prod_{i\in p} I(\mathbf{r}_i, t-\tau_i)\right\rangle_t, \tag{4.1}$$

where $\langle ... \rangle_t$ stands for averaging over time t. P runs over all partitions of a set $\mathbf{S} = \{1, 2, ..., n\}$, which means all possible divisions of $\mathbf{S}$ into non-overlapping and non-empty subsets or parts that cover all elements of $\mathbf{S}$. $|P|$ denotes the number of parts of partition P and p runs over these parts. $I(\mathbf{r}_i)$ denotes the intensity distribution measured over time on a detector pixel $\mathbf{r}_i$.

To obtain a good signal to noise ratio (SNR), high number of image frames is preferred. Due to the photobleaching, fluorescence signal decreases in time, which limits the maximum number of frames for cumulant calculation. SNR can be improved by dividing the whole sequence of images into subseqeunces, calculate cumulants for each subsequence and than average over multiple raw cumulants.

Assuming discrete n-th order cumulant image $\kappa_{n,k}$ that has been calculated from k-th subsequence of input images, a discrete observation model for a fluorescence microscope is

$$\kappa_{n,k} = \mathcal{N}(\mathbf{Hf} + \mathbf{b}), \tag{4.2}$$

where $\mathbf{f}, \mathbf{b}$ are vectors that denotes the ideal image of the object, and the background, respectively. In Eq. (4.2) $\kappa_{n,i}, \mathbf{f}, \mathbf{b}$ are written in vectorized form (columnwise). $\mathbf{H}$ is a convolution matrix of size M x M where M denotes a number of pixels of the image. Function $\mathcal{N}(.)$ represents a noise process with Gaussian or Poisson distribution. To get a deconvolved cumulant image i.e. image $\mathbf{f}$, inversion of Eq. (4.2) is required. In the presence of noise, this inversion becomes unstable and a regularization is necessary. The total variation (TV) based regularization introduced by Rudin et. al. [70] is often preferred for image reconstruction tasks due to its ability to preserve edges. The isotropic TV takes the form

$$\|\mathbf{f}\|_{TV} = \sum_i \sqrt{[\mathbf{D}_x\mathbf{f}]_i^2 + [\mathbf{D}_y\mathbf{f}]_i^2 + [\mathbf{D}_z\mathbf{f}]_i^2}, \tag{4.3}$$

where the operators $\mathbf{D}_x, \mathbf{D}_y, \mathbf{D}_z$ are the finite difference operators with respect to x, y, and z coordinates. Solving Eq. (4.2) for a Gaussian noise case then becomes the following optimization problem

$$\min_{\mathbf{f}} \|\mathbf{Hf} - \kappa_{n,k}\| + \|\mathbf{f}\|_{TV} \,. \tag{4.4}$$

Bregman iterative algorithm has been shown to be efficient for image restoration based on the Eq. (4.4) [68]. This iterative method has several advantages over the traditional methods, such as fast convergence rate, flexibility of parameters, and prominent stability. Goldstein and Osher [69] introduced the split Bregman iterative method to solve more general L_1 regularized optimization problem. It was shown that the Eq. (4.4) can be solved efficiently by split augmented Lagrangian shrinkage algorithm (SALSA) [67]. Chan et. al. [71] employed augmented lagrangian method with split Bregman iterations for video restoration. Sroubek & Milanfar [72] applied it to multichannel blind deconvolution of 2D images. Multichannel deconvolution approaches benefit from the assumption that more observations (images) of the same scene are known. In our case, one super-resolved, cumulant image is known for each of the k-th subsequences. We have previously showed, that SOFI can be extended into 3D [19] where each of these cumulants represents a different 3D observation of the same sample. In the following, we present a multichannel 3D deconvolution based on Bregman iterative method. Using the full norm for regularization [73] and assuming K subsequences, the minimization task becomes

$$\min_{\mathbf{f}} \left\{ \|\mathbf{Df}\|_1 + \frac{\alpha}{2}\|\mathbf{f}\|_2^2 + \frac{\mu}{2}\sum_{k=1}^{K} \|\mathbf{Hf} - \mathbf{g}_k\|_2^2 \right\} \text{ s.t. } \mathbf{g}_k = \kappa_{n,k}. \tag{4.5}$$

Using split Bregman iteration to solve Eq. (4.5), we replace $\mathbf{Df} \rightarrow \mathbf{u}$. Considering an unconstrained problem, this yields to an augmented Lagrangian of the form

$$\mathscr{L}(\mathbf{f},\mathbf{u}) = \|\mathbf{u}\|_1 + \frac{\alpha}{2}\|\mathbf{f}\|_2^2 + \frac{\mu}{2}\sum_{k=1}^{K} \|\mathbf{Hf} - \mathbf{g}_k\|_2^2 + \frac{\lambda}{2}\|\mathbf{u} - \mathbf{Df}\|_2^2. \tag{4.6}$$

The split Bregman iterative algorithm for solving Eq. (4.6) takes the form

$$\mathbf{f}^{(i+1)} = \underset{\mathbf{f}^{(i)}}{\operatorname{argmin}} \left\{ \frac{\alpha}{2}\|\mathbf{f}^{(i)}\|_2^2 + \frac{\mu}{2}\sum_{k=1}^{K} \|\mathbf{Hf}^{(i)} - \mathbf{g}_k\|_2^2 + \frac{\lambda}{2}\|\mathbf{Df}^{(i)} - \mathbf{u}^{(i)} + \mathbf{a}^{(i)}\|_2^2 \right\}, \tag{4.7}$$

$$\mathbf{u}^{(i+1)} = \underset{\mathbf{u}^{(i)}}{\operatorname{argmin}} \left\{ \|\mathbf{u}\|_1^{(i)} + \frac{\lambda}{2}\|\mathbf{u}^{(i)} - \mathbf{Df}^{(i+1)} - \mathbf{a}^{(i)}\|_2^2 \right\}, \tag{4.8}$$

$$\text{with the update formula for } \mathbf{a}^{(i+1)} \tag{4.9}$$

$$\mathbf{a}^{(i+1)} = \mathbf{a}^{(i)} + (\mathbf{Df}^{(i+1)} - \mathbf{u}^{(i+1)}). \tag{4.10}$$

The f-subproblem can be solved as

$$\mathbf{f}^{(n+1)} = \frac{\sum_{k=1}^{K} \mu \mathbf{H}^T \mathbf{g}_k + \lambda \mathbf{D}^T (\mathbf{u}^{(n)} - \mathbf{a}^{(\mathbf{n})})}{(\alpha \mathbf{I} + K\mu \mathbf{H}^T \mathbf{H} + \lambda \mathbf{D}^T \mathbf{D})}. \tag{4.11}$$

The u-subproblem can be solved by using the generalized shrinkage formula [69]

$$\mathbf{u}^{(n+1)} = \frac{\mathbf{D}\mathbf{f}^{(n+1)} + \mathbf{a}^{(n)}}{\|\mathbf{D}\mathbf{f}^{(n+1)} + \mathbf{a}^{(n)}\|_2} \max\left\{ \|\mathbf{D}\mathbf{f}^{(n+1)} + \mathbf{a}^{(n)}\|_2 - \frac{1}{\lambda}, 0 \right\}. \tag{4.12}$$

The whole f-subproblem can be efficiently solved in Fourier domain.

4.2 Time lapse live cell imaging using 3D SOFI

We adopted the split Bregman iterative method for 3D SOFI deconvolution and used it to process consecutive frames of a video sequence. This approach leads towards the video sequence or time lapse 3D SOFI. Figure 4.1 shows the ground lying framework for video SOFI. An individual super-resolved image of the output video sequence is in fact a 3D image reconstructed from a subsubsequence of input frames. At each time point, our new multiplane SOFI microscope simultaneously acquires two frames, each of them containing four z planes as indicated in Figure 4.2. The field stop limits the lateral field such that the image frames do not overlap. A unique, custom made prism splits the fluorescence into 8 optical paths with various focal length and thus the system can acquire 8 focal planes by two cameras at one time point. This allows us to calculate spatio-temporal cross-cumulants also along the axial direction and obtain virtual z planes in between the physically acquired planes. This ability translates to 15 z planes (the 2^{nd} order 3D SOFI) and 22 z planes (the 3^{rd} order 3D SOFI) acquired in one shot without moving the microscope stage, which increases the throughput of the method in terms of voxel/s.

Due to the new deconvolution algorithm described in the previous section, smaller number of input images is required for a SOFI reconstruction and super-resolved 3D image sequences of moving cell structures become feasible. We demonstrated the performance of this algorithm by imaging live HeLa cells expressing vimentin-Dreiklang (Figure 4.3). In this experiment, 300 frames (with acquisition rate 316 f.p.s.) were used for the reconstruction. The acquisition time for one super-resolved 3D image was 0.95s. Charts in Figure 4.3 show circular averaged power spectral density and line profiles of the widefield, SOFI and SOFI with the new deconvolution algorithm. The widefield image is given as an average over the input image sequence. Figure 4.4 shows the first frame of a super-resolved 3D video sequence of live Hela cells expressing Vimentin-Dreiklang reconstructed from 100 frames of the input image sequence. Overall acquisition for one super-resolved 3D image was 2 s. In total, 50 super-resolution images were acquired with a time lapse of 1 min after each 5 super-resolved frames.

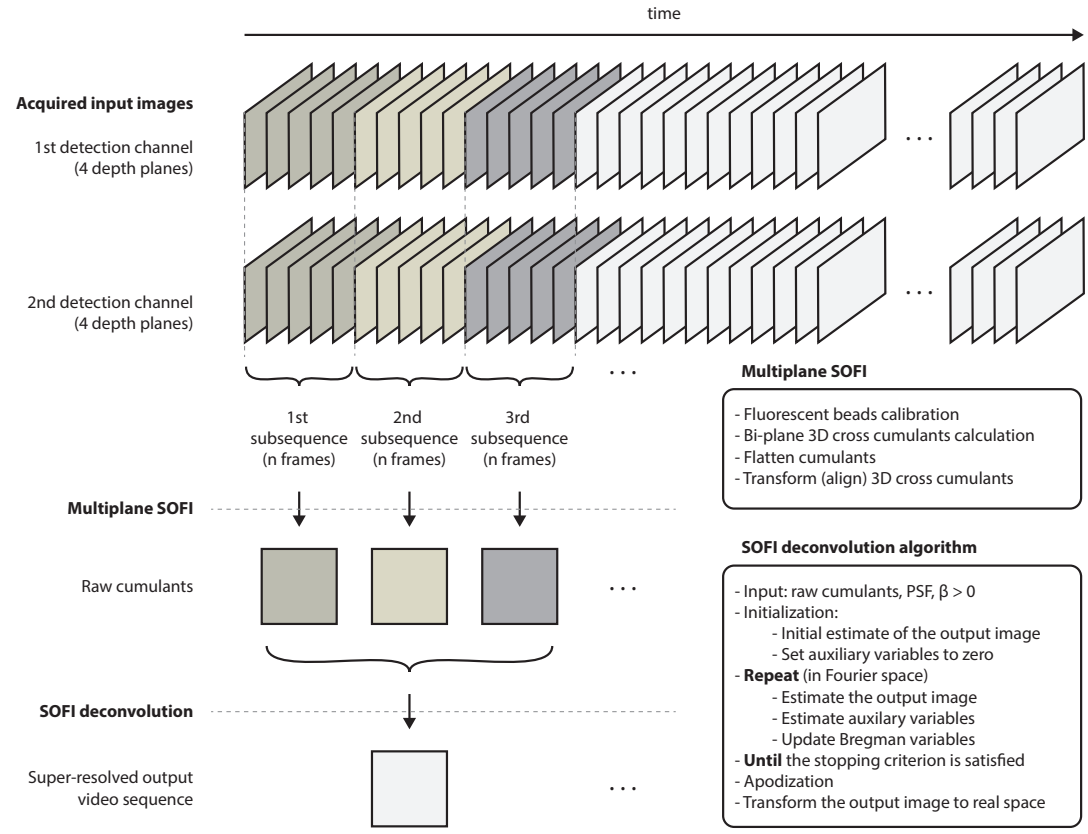

Figure 4.1: Video SOFI diagram. Input image sequence is divided into subsequences (for each channel). 3D SOFI cumulant images are calculated from the subsequences and deconvolved.

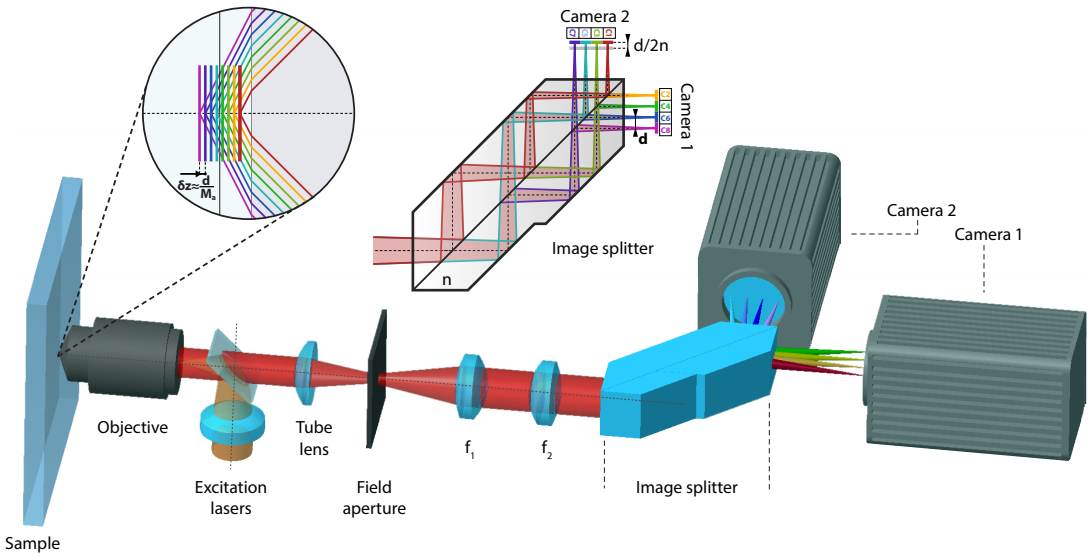

Figure 4.2: New generation of the multiplane SOFI microscope setup with the novel image splitter. The sample planes are imaged on two camera sensors as interleaved image frames C1-C8.

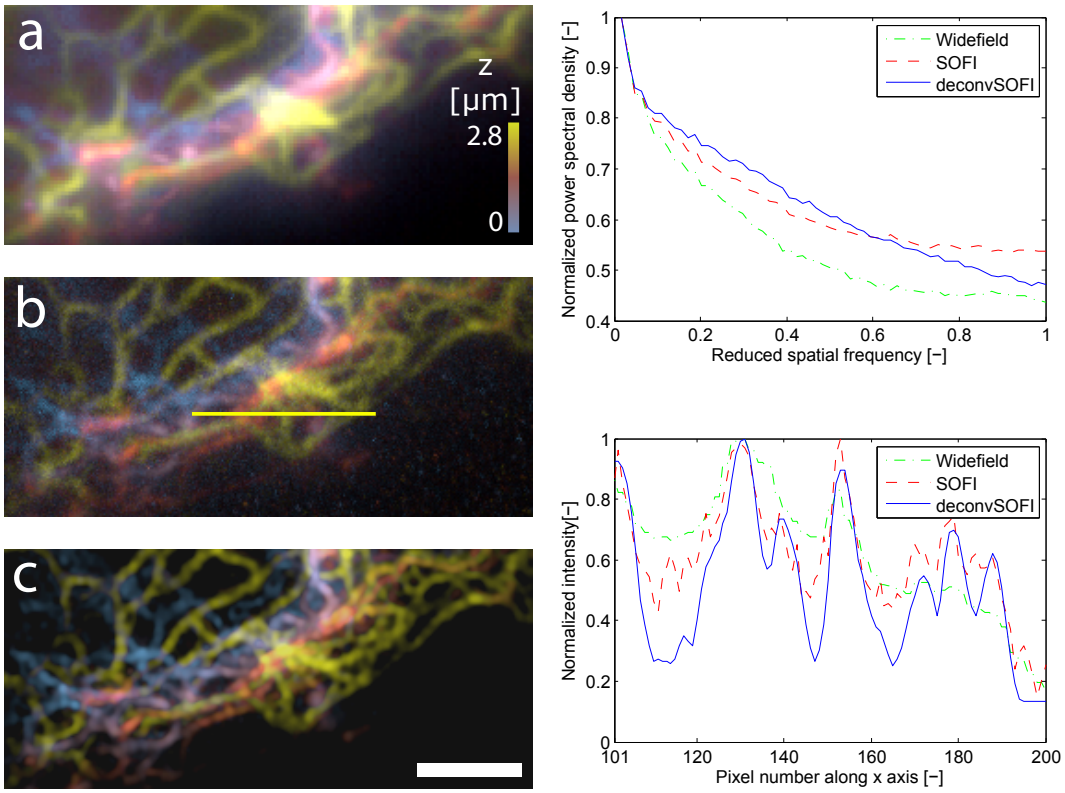

Figure 4.3: Live HeLa cells expressing vimentin-Dreiklang. 300 frames (with acquisition rate 316 Hz) were used for the reconstruction. Depth color coded maximum intensity projections of the 3D stack of (a) 8-plane widefield image given as an average over the input image sequence, (b) 15-plane SOFI image, and (c) 15-plane SOFI image deconvolved by our new algorithm. Thickness of the sample is 2.8 μm. Scale bar (a,b,c) 2 μm. Charts show circular averaged power spectral density and line profiles of all three images. Line profile of the images is indicated by the yellow line in (b).

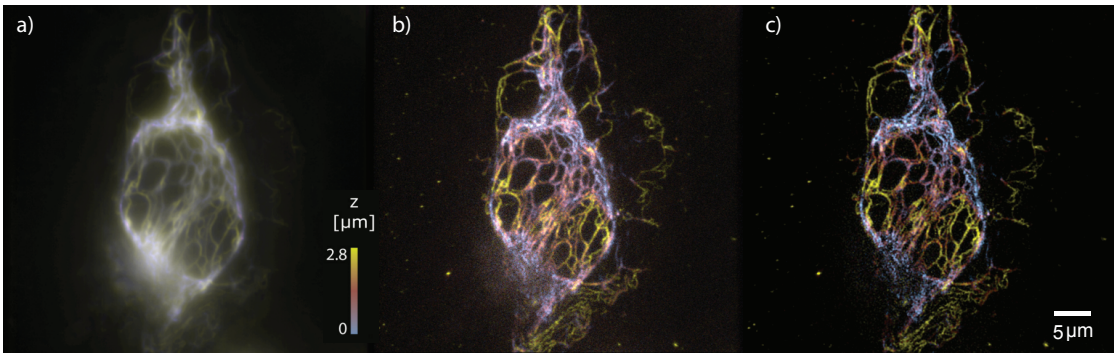

Figure 4.4: First frame of a super-resolved 3D video sequence of live Hela cells expressing Vimentin-Dreiklang. Maximum intensity projections of a 3D image of (a) widefield, (b) SOFI with adjusted dynamic range, (c) improved bSOFI algorithm. Depth color coding. Only 100 images were used for the SOFI reconstruction. Image acquisition for one super-resolved 3D image 2 s.

4.3 Optimized high order bSOFI

We have achieved for the first time SOFI up to the 6th order. Besides a gain in resolution we also addressed the impact on contrast. Using bSOFI up to the sixt order translates into a decrease in contrast necessitating to readdress this question to fully exploit the potential of bSOFI imaging.

We modified the bSOFI algorithm [42] by introducing a linearization for a better compensation of the intrinsic nonlinearity of SOFI. Additionally, this takes into account the on-time ratio and linearizes the response to detected intensity. In summary, we show that this step improves the attainable resolution assessed by the sFRC (Figure 4.5).

4.3.1 Linearization and higher order SOFI

The molecular brightness as described in Eq. (2.18) is raised to the n-th power. High order cumulant images exhibit fluorescent spots of high brightness which are masking less bright structural details. The non-linear response to molecular brightness limits the use of high order cumulants with consequences on resolution enhancement and contrast. Geissbuehler et al. [42] proposed balanced SOFI (bSOFI) which allows one to linearize the nonlinear brightness response. Firstly, the n-th order cumulant image is deconvolved. Secondly, the brightness response is linearized by taking the n-th root of the deconvolved cumulant image. This approach has proven efficient for 2D and 3D super-resolution imaging [42, 19].

When using SOFI up to the sixth order, we need to readdress the linearization by taking into account the contribution of $f_n(\rho_{\text{on}})$ in Eq. (2.18). Figure 4.6 shows the cumulant function dependence on the on-time ratio ρ_{on} for different orders. In the case of a 4^{th} order cumulant and $\rho_{\text{on}} = 0.2$, the cumulant function decreases. Under these conditions, the contrast of the 4^{th} cumulant image is attenuated. The resulting image is flat and the dynamic range is reduced strongly which leads to a loss of signal-to-noise ratio (SNR). In general, the SNR drops with increasing orders limiting the maximum available resolution enhancement. To overcome this problem, we introduced a novel linearization procedure which takes into account the influence of the cumulant function and linearizes the response to the detected intensity.

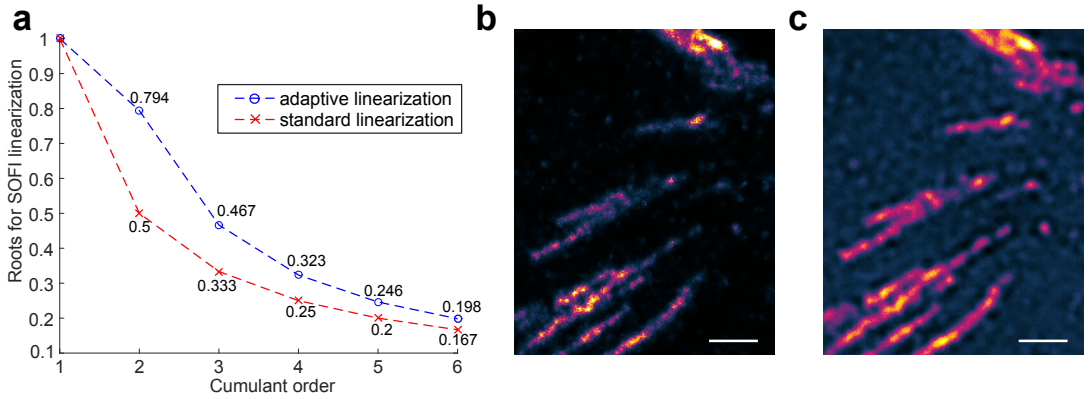

Figure 4.5: Enhanced bSOFI. Images of fixed MEF cells expressing paxillin labeled with mEos2 obtained from a raw image sequence of 20,000 frames. (a) Roots for SOFI standard and adaptive linearization. (b) 4^{th} order bSOFI using a novel linearization (sFRC=134 nm). (c) 4^{th} order bSOFI using standard linearization (sFRC=166 nm). Dynamic range is reduced too much which leads to lower SNR and deconvolution artifacts in the low SNR background regions. Scale bars: 1 μm. Published in Supplementary Deschout & Lukeš et al., Nature Comm., 2016 [48].

The first four cumulants can be written as

$$\begin{aligned}
g_1 &\approx \epsilon(\mathbf{r}) f_1(\rho_{\text{on}}) \sum_{k=1}^{N} U(\mathbf{r}-\mathbf{r}_k) + \kappa_1\{b(\mathbf{r})\} + \kappa_1\{n(\mathbf{r},t)\} \\
g_2 &\approx \epsilon^2(\mathbf{r}) f_2(\rho_{\text{on}}) \sum_{k=1}^{N} U^2(\mathbf{r}-\mathbf{r}_k) \\
g_3 &\approx \epsilon^3(\mathbf{r}) f_3(\rho_{\text{on}}) \sum_{k=1}^{N} U^3(\mathbf{r}-\mathbf{r}_k) \\
g_4 &\approx \epsilon^4(\mathbf{r}) f_4(\rho_{\text{on}}) \sum_{k=1}^{N} U^4(\mathbf{r}-\mathbf{r}_k)
\end{aligned} \tag{4.13}$$

and the on-time ratio polynomials up to the sixth order are

$$f_1(\rho_{\text{on}}) = \rho_{\text{on}} \tag{4.14}$$
$$f_2(\rho_{\text{on}}) = \rho_{\text{on}}(1-\rho_{\text{on}}) \tag{4.15}$$
$$f_3(\rho_{\text{on}}) = \rho_{\text{on}}(1-\rho_{\text{on}})(1-2\rho_{\text{on}}) \tag{4.16}$$
$$f_4(\rho_{\text{on}}) = \rho_{\text{on}}(1-\rho_{\text{on}})(1-6\rho_{\text{on}}+6\rho_{\text{on}}^2) \tag{4.17}$$
$$f_5(\rho_{\text{on}}) = \rho_{\text{on}}(1-\rho_{\text{on}})(1-2\rho_{\text{on}})(12\rho_{\text{on}}^2-12\rho_{\text{on}}+1) \tag{4.18}$$
$$f_6(\rho_{\text{on}}) = \rho_{\text{on}}(1-\rho_{\text{on}})(120\rho_{\text{on}}^4-240\rho_{\text{on}}^3+150\rho_{\text{on}}^2-30\rho_{\text{on}}+1) \tag{4.19}$$

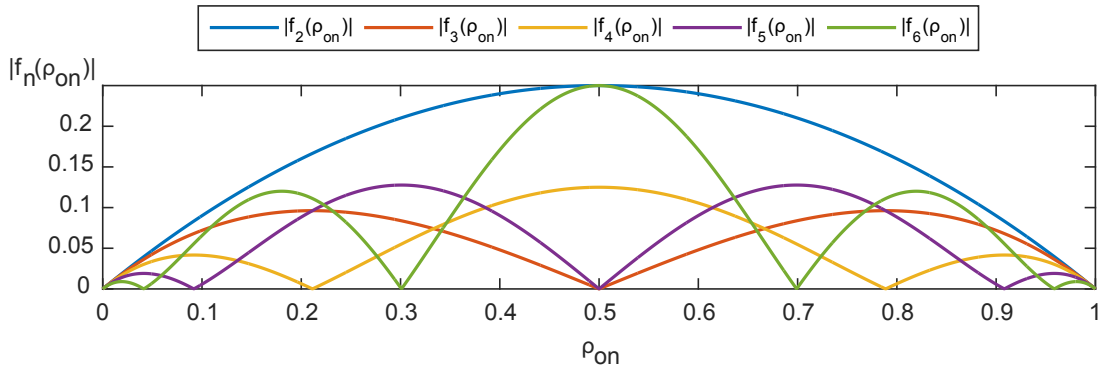

Figure 4.6: On-time ratio polynomial of 2nd to 6th order as a function of the on-time ratio.

Once the on-time ratio is estimated (as described in the next section), the value of the on-time ratio polynomial for a given cumulant order is calculated by Eq. (4.15) - Eq (4.19). In order to correct for the amplified brightness without compromising the resolution, the cumulants have to be deconvolved first, as shown in [42]. The correction factor for a deconvolved n-th order cumulant image $\hat{g}_n$ is $1/f_n(\rho_{\text{on}})$ and we can write

$$\frac{\hat{g}_n}{f_n(\rho_{\text{on}})} = \hat{g}_n^{\frac{log_{10}(\hat{g}_n/f_n(\rho_{\text{on}}))}{log_{10}(\hat{g}_n)}}. \tag{4.20}$$

Instead of taking the n-th root, the corrected, adaptively linearized cumulant image $\bar{g}_n$ is

$$\bar{g}_n = \hat{g}_n^{\frac{1}{n}\frac{log_{10}(\hat{g}_n/f_n(\rho_{\text{on}}))}{log_{10}(\hat{g}_n)}}. \tag{4.21}$$

The roots for linearization of cumulants up to 6th order (linearization curve) and the difference in the final bSOFI images are shown in Figure 4.5. The red line in Figure 4.5a represents the standard linearization where the n-th order cumulant is linearized by taking the n-th root [54]. The corrected roots for our novel linearization are shown in blue (Figure 4.5a).

4.3.2 On-time ratio estimation

Higher-order cumulants contain information about the photo-physics of the emitters. Combining SOFI images of different cumulant orders, molecular parameter maps can be extracted such as on-time ratio, molecular brightness, and molecular density [42], which we applied to assess the dynamics of cell adhesions. Geissbuehler et al. [42] used three cumulant images (2nd, 3rd, and 4th order) to estimate the on-time ratio. Here, we present an estimation of the on-time ratio using only two cumulant images (2nd and 3rd order).

If we assume spatially varying but locally constant on-time ratios and molecular brightness, the cumulants can be approximated by [42]

$$g_1(\mathbf{r}) \approx \epsilon(\mathbf{r}) f_1(\rho_{\text{on}}) N(\mathbf{r}) \mathscr{E}_V\{U(\mathbf{r})\} + \kappa_1\{b(\mathbf{r})\} + \kappa_1\{n(\mathbf{r},t)\} \tag{4.22}$$

$$g_2(\mathbf{r}) \approx \epsilon^2(\mathbf{r}) f_2(\rho_{\text{on}}) N(\mathbf{r}) \mathscr{E}_V\{U^2(\mathbf{r})\} \tag{4.23}$$

$$g_3(\mathbf{r}) \approx \epsilon^3(\mathbf{r}) f_3(\rho_{\text{on}}) N(\mathbf{r}) \mathscr{E}_V\{U^3(\mathbf{r})\} \tag{4.24}$$

$$g_4(\mathbf{r}) \approx \epsilon^4(\mathbf{r}) f_4(\rho_{\text{on}}) N(\mathbf{r}) \mathscr{E}_V\{U^4(\mathbf{r})\}, \tag{4.25}$$

where $\mathscr{E}_V\{U^n(\mathbf{r})\}$ is the expectation value of $U^n(\mathbf{r})$, $N(\mathbf{r})$ is the number of molecules inside a detection volume V centered at $\mathbf{r}$. Generally for the cumulant order $n > 1$, we may write

$$g_n(\mathbf{r}) \approx \epsilon^n(\mathbf{r}) f_n(\rho_{\text{on}}) N(\mathbf{r}) \mathscr{E}_V\{U^n(\mathbf{r})\}. \tag{4.26}$$

The second (g_2) and third (g_3) order cumulant images can be related as

$$g_3 = \frac{\mathscr{E}_V\{U^3(\mathbf{r})\}}{\mathscr{E}_V\{U^2(\mathbf{r})\}^{3/2}} \frac{1}{N^{1/2}(\mathbf{r})} \frac{f_3(\rho_{\text{on}})}{f_2^{3/2}(\rho_{\text{on}})} g_2^{3/2}. \tag{4.27}$$

Substituting Eq. (4.15) and Eq. (4.16) into Eq. (4.27) leads to

$$g_3 = K \frac{1-2\rho_{\text{on}}}{\sqrt{\rho_{\text{on}}(1-\rho_{\text{on}})}} g_2^{3/2}, \tag{4.28}$$

where $K = \frac{\mathscr{E}_V\{U^3(\mathbf{r})\}}{\mathscr{E}_V\{U^2(\mathbf{r})\}^{3/2}} \frac{1}{N^{1/2}(\mathbf{r})}$.

For the on-time ratio ρ_{on}, we obtain the solution

$$\rho_{\text{on}} = \frac{1}{2}\left(1 \pm \frac{\sqrt{4K^2 g_2^3 g_3^2 + g_3^4}}{4K^2 g_2^3 + g_3^2}\right). \tag{4.29}$$

As shown in Figure 4.6, the on-time ratio polynomial is symmetric around $\rho_{\text{on}} = 0.5$, thus Eq. (4.29) has two possible solutions (see section 4.3.3 for more details). To estimate ρ_{on}, we first determine the constant K. The number of molecules $N(\mathbf{r})$ can be estimated using the second order cumulant and the first order cumulant after background subtraction ($\tilde{g}_1$).

$$N(\mathbf{r}) = \frac{\mathscr{E}_V\{U^2(\mathbf{r})\}}{\mathscr{E}_V\{U^1(\mathbf{r})\}^2} \frac{(1-\rho_{\text{on}})}{\rho_{\text{on}}} \frac{\tilde{g}_1}{g_2}. \tag{4.30}$$

Approximating the imaging PSF by a 3D Gaussian profile, we can write [42]

$$\mathscr{E}_V\{U^n_{\text{3DGauss}}(\mathbf{r})\} = \frac{c(\sigma_{x,y}, \sigma_z)}{n^{3/2}}, \tag{4.31}$$

where $c(\sigma_{x,y},\sigma_z)$ is a constant depending on the spatial extend of the PSF. Analogously, approximating the PSF near the interface in a total internal reflection (TIR) configuration by a lateral 2D Gaussian profile and an axial exponential profile, we obtain

$$\mathscr{E}_V\{U^n_{\mathrm{TIR}}(\mathbf{r})\} = \frac{c(\sigma_{x,y},\sigma_z,d_z)}{n^2}, \tag{4.32}$$

where d_z represents the penetration depth of the TIR illumination [42]. The outcome of this analysis has been implemented into our SOFI code inducing the expected contrast gain.

4.3.3 Estimation of molecular parameter maps

In order to find the molecular parameters ρ_{on},ϵ, and N in Eq. (4.26), Geissbuehler et al. [42] used cumulant images of 2^{nd}, 3^{rd}, and 4^{th} order to build up the ratios

$$K_1(\mathbf{r}) = \frac{\mu_{U,2}g_3}{\mu_{U,3}g_2}(\mathbf{r}) = \epsilon(\mathbf{r})(1-2\rho_{\mathrm{on}}(\mathbf{r})) \tag{4.33}$$

$$K_2(\mathbf{r}) = \frac{\mu_{U,2}g_4}{\mu_{U,4}g_2}(\mathbf{r}) = \epsilon^2(\mathbf{r})(1-6\rho_{\mathrm{on}}(\mathbf{r})+6\rho^2_{\mathrm{on}}(\mathbf{r})), \tag{4.34}$$

where $\mu_{U,n} = \mathscr{E}_V\{U^n(\mathbf{r})\}$. Solving it for molecular brightness ϵ, on-time ratio ρ_{on}, and number of molecules N in the detection volume leads to [42]:

$$\epsilon(\mathbf{r}) = \sqrt{3K_1^2(\mathbf{r})-2K_2(\mathbf{r})} \tag{4.35}$$

$$\rho_{\mathrm{on}}(\mathbf{r}) = \frac{1}{2} - \frac{K_1(\mathbf{r})}{2\epsilon(\mathbf{r})} \tag{4.36}$$

$$N(\mathbf{r}) = \frac{g_2(\mathbf{r})}{\epsilon^2(\mathbf{r})\rho_{\mathrm{on}(\mathbf{r})}(1-\rho_{\mathrm{on}}(\mathbf{r}))}. \tag{4.37}$$

In principle, any three distinct cumulant orders could be used to provide a solution by solving the equation system or using a fitting procedure. Molecular parameters ρ_{on},ϵ, and N can be estimated pixel-wise using distinct cumulant images of three or more orders. For cumulants of two to four order we can write:

$$\frac{g_3}{g_2} = \frac{f_3(\rho_{\mathrm{on}}(\mathbf{r}))}{f_2(\rho_{\mathrm{on}}(\mathbf{r}))}\epsilon(\mathbf{r})\frac{\mu_{U,3}}{\mu_{U,2}} \tag{4.38}$$

$$\frac{g_4}{g_2} = \frac{f_4(\rho_{\mathrm{on}}(\mathbf{r}))}{f_2(\rho_{\mathrm{on}}(\mathbf{r}))}\epsilon^2(\mathbf{r})\frac{\mu_{U,4}}{\mu_{U,2}} \tag{4.39}$$

$$\frac{g_4}{g_3} = \frac{f_4(\rho_{\mathrm{on}}(\mathbf{r}))}{f_3(\rho_{\mathrm{on}}(\mathbf{r}))}\epsilon(\mathbf{r})\frac{\mu_{U,4}}{\mu_{U,3}}. \tag{4.40}$$

From Eq. (4.40) we obtain

$$\epsilon(\mathbf{r}) = \frac{g_4}{g_3}\frac{f_3(\rho_{\mathrm{on}}(\mathbf{r}))}{f_4(\rho_{\mathrm{on}}(\mathbf{r}))}\frac{\mu_{U,3}}{\mu_{U,4}}. \tag{4.41}$$

Substitution $\epsilon(\mathbf{r})$ in Eq. (4.38) leads to

$$\frac{g_4 g_2}{g_3^2} = \frac{f_4(\rho_{\text{on}}) f_2(\rho_{\text{on}}(\mathbf{r}))}{f_3^2(\rho_{\text{on}}(\mathbf{r}))}. \tag{4.42}$$

This calculation can be generalized for any other 3 consecutive cumulant images of orders $n, (n-1), (n-2)$, which results in:

$$\frac{g_n g_{n-2}}{g_{n-1}^2} = \frac{f_n(\rho_{\text{on}}(\mathbf{r})) f_{n-2}(\rho_{\text{on}}(\mathbf{r}))}{f_{n-1}^2(\rho_{\text{on}}(\mathbf{r}))}. \tag{4.43}$$

For cumulants 1, 2, 3, we obtain

$$\frac{g_3 g_1}{g_2^2} = \frac{1-2\rho_{\text{on}}(\mathbf{r})}{1-\rho_{\text{on}}(\mathbf{r})}. \tag{4.44}$$

For cumulants 2, 3, 4, we obtain

$$\frac{g_4 g_2}{g_3^2} = \frac{1-6\rho_{\text{on}}(\mathbf{r})+6\rho_{\text{on}}^2(\mathbf{r})}{(1-2\rho_{\text{on}}(\mathbf{r}))(1-2\rho_{\text{on}}(\mathbf{r}))}. \tag{4.45}$$

For cumulants 3, 4, 5, we obtain

$$\frac{g_5 g_3}{g_4^2} = \frac{(1-2\rho_{\text{on}}(\mathbf{r}))^2(12\rho_{\text{on}}^2(\mathbf{r})-12\rho_{\text{on}}(\mathbf{r})+1)}{(1-6\rho_{\text{on}}(\mathbf{r})+6\rho_{\text{on}}^2(\mathbf{r}))^2}. \tag{4.46}$$

For cumulants 4, 5, 6, we obtain

$$\frac{g_6 g_4}{g_5^2} = \frac{(1-6\rho_{\text{on}}(\mathbf{r})+6\rho_{\text{on}}^2(\mathbf{r}))(120\rho_{\text{on}}^4(\mathbf{r})-240\rho_{\text{on}}^3(\mathbf{r})+150\rho_{\text{on}}^2(\mathbf{r})-30\rho_{\text{on}}(\mathbf{r})+1)}{(1-2\rho_{\text{on}}(\mathbf{r}))^2(12\rho_{\text{on}}^2(\mathbf{r})-12\rho_{\text{on}}(\mathbf{r})+1)^2}. \tag{4.47}$$

The argument on the right hand side of the equation for the on-time ratio ρ_{on} in the range $[0,1]$ takes the values as shown in Figure 4.7. The solution for the on-time ratio is unique only for the first case i.e. the combination of g_1, g_2, g_3, but unlike other cumulant images of higher orders, the g_1 is not known. The cumulant of the first order does not cancel out background and additive noise, so we observe only noisy version of g_1 with an added background. Some of the solutions correspond to negative values for molecular brightness ϵ, which is not physically possible and thus these solutions can be omitted. Using the ratios K_1 and K_2 from the Eq. (4.33) for cumulants of $2^{nd}, 3^{rd}$, and 4^{th} order, we obtain the following two solutions for the on-time ratio ρ_{on}, and molecular brightness ϵ

$$\left\{ \rho_{\text{on}}(\mathbf{r}) = \frac{3K_1^2 \pm K_1\sqrt{3K_1^2-2K_2}-2K_2}{2(3K_1^2-2K_2)}, \epsilon(\mathbf{r}) = \mp\sqrt{3K_1^2-2K_2} \right\}, \tag{4.48}$$

where the first solution corresponds to the negative brightness and can be discarded leaving us one solution equivalent to Eq. (4.35). For cumulants of $3^{rd}, 4^{th}$, and 5^{th} order, the ratios K_1

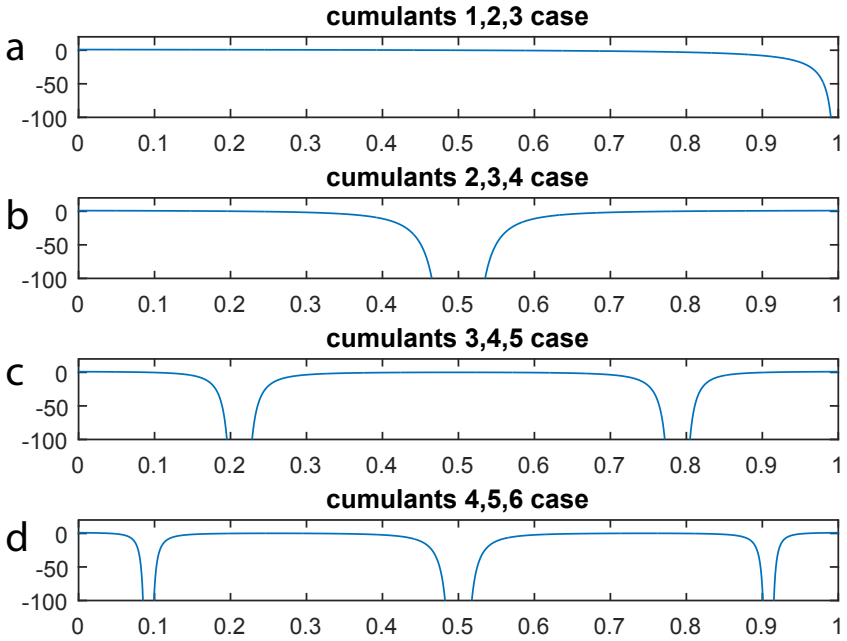

Figure 4.7: Values of the right hand side of (a) Eq. 4.44, (b) Eq. 4.45, (c) Eq. 4.46, (d) Eq. 4.47 (i.e. for different combinations of cumulant orders) for the on-time ratio in the range $[0,1]$.

and K_2 become

$$K_1(\mathbf{r}) = \frac{\epsilon(\mathbf{r})(1-6\rho_{on}+6\rho_{on}^2)}{(1-2\rho_{on}(\mathbf{r}))} \tag{4.49}$$

$$K_2(\mathbf{r}) = \epsilon^2(\mathbf{r})(12\rho_{on}^2-12\rho_{on}+1) \tag{4.50}$$

and we can obtain four solutions. The following two of them correspond to positive molecular brightness

$$\rho_{on}(\mathbf{r})_{1,2} = \frac{12K_1^3 \pm \sqrt{3}\sqrt{K_1^2(4K_1^2-3K_2)}\sqrt{4K_1^2 \mp 2\sqrt{K_1^2(4K_1^2-3K_2)}-3K_2}-9K_1K_2}{6K_1(4K_1^2-3K_2)}, \tag{4.51}$$

$$\epsilon(\mathbf{r})_{1,2} = \frac{\sqrt{4K_1^2 \mp 2\sqrt{K_1^2(4K_1^2-3K_2)}-3K_2}}{\sqrt{3}}. \tag{4.52}$$

Assuming that molecular brightness and on-time ratio maps are locally smooth, the solution closer to the one obtained previously from Eq. (4.48) for the combination of two to four order cumulants will probably describe the best our sample under study. Using a combination of higher order cumulants for molecular parameters can theoretically provide higher spatial resolution of the molecular parameter maps assuming high enough SNR of the cumulant images used. For the combination of $4^{th}, 5^{th}, 6^{th}$ order cumulant, it is also possible to find a

solution in a closed form, but due to its complexity, numerical approach might be preferred.

This pixel-wise estimation is not relevant for image regions which contain only background noise. Therefore, the linearized bSOFI image is used as a transparency mask to cancel out the background regions. The bSOFI image was linearized using our novel adaptive linearization procedure described above.

We performed simulations in order to evaluate the reliability of the SOFI based molecular parameter estimation. Using simulations and the photo-physical model described later in section 4.5.1, we simulated a square of size 1x1μm randomly populated by fluorescent molecules with a given molecular density in the range 100 - 1600 molecules per μm^2. We generated image sequences of these blinking fluorescent molecules of different length (1000 - 5000 frames) and performed pixel-wise SOFI molecular density estimation using two to four order cumulant images. Each combination of the simulated (ground truth) density and the length of the image sequence was repeatedly generated and analyzed 10 times.

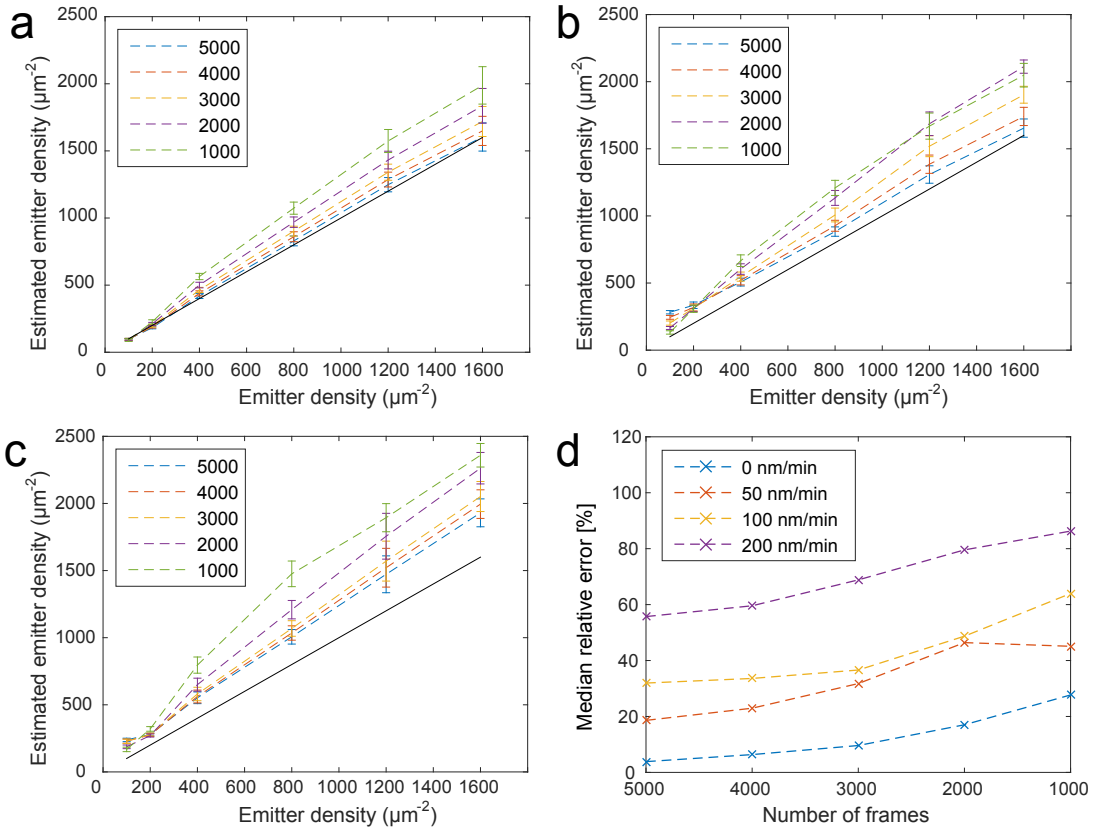

Figure 4.8: SOFI quantitative analysis performed on simulated data. The emitter density estimated by SOFI is shown in function of the ground truth (GT) density for different numbers of simulated frames and velocity of the GT equal to (a) 0 nm/min, (b) 50 nm/min, (c) 100 nm/min. The procedure was repeated 10 times, the error bars represent the standard deviation. (d) Median relative error across the range of tested densities as a function of number of frames. Each curve represents a different velocity of the GT ranging from 0 - 200 nm/min.

To evaluate applicability of this estimation procedure on live cell samples, we further simulated different velocities of the test target (0 nm/min, 50 nm/min, 100 nm/min, 200 nm/min). Figure 4.8 shows the average and the standard deviation calculated over these measurements for various number of frames used for the SOFI reconstruction and parameter estimation. For high number of frames >= 3000 and non moving test target, the median across the whole range of relative errors of estimated densities related to the ground truth is below 10 %. Increasing the velocity of the test target and or decreasing the number of frames cause bias in the estimation towards higher values. SOFI assumes the sample to be stationary during the image acquisition. Introducing significant movement between the first and last frame of the image sequence leads to mismatch of corresponding pixel positions, decrease of correlation and lower SNR.

4.4 A simulation tool for SOFI

Sample preparation for super-resolution imaging and the choice of image acquisition parameters is often a tedious process requiring experience and several trials before a suitable parameter set is found. In order to simplify this task, we developed a simulation tool equipped with a graphical user interface (GUI) allowing a qualitative assessment of SOFI under various conditions [43]. This tool allows the user to generate simulated datasets based on specified optical and molecular parameters, incorporates SOFI and STORM algorithms, displays and describes the SOFI image processing steps, and offers a simple qualitative comparison of the output super-resolved images. Additionally the simulator assists the user to better understand the full chain of processing steps.

The simulator can be used for quick testing of various experimental parameters of the fluorescent sample such as blinking rate, labeling density, as well as system parameters of the microscope and camera prior the experimental work. The software written in MATLAB is freely available together with a user manual at the website of the journal [43] and on the project website [74].

4.4.1 Simulation examples

We simulated various specific situations: standard conditions (i.e. conditions under which STORM is able to resolve individual emitters), short acquisition time, short off-state lifetime of the emitters, low signal-to-noise ratio (SNR), and high-labelling density. Reversibly photoswitchable fluorescent proteins have on-off duty cycles in the order of 0.1 in contrast to organic dyes with on-off duty cycles much smaller (< 0.01) [75]. Figure 4.9 shows the results for widefield, bSOFI, and FALCON STORM. For these simulations, we assumed fluorescent proteins and we set the on-time ratio to 0.1. *Standard conditions* represent a scenario in which the simulator displays comparable performance for FALCON and SOFI in terms of resolution enhancement. All following experimental scenarios deviate from the standard conditions as follows: *Short off-state lifetime*, the sample is composed of emitters with fast off-switching kinetics; *Short acquisition time*, the super-resolution images are generated from an image sequence of only 600 frames; *low SNR*, the number of photons emitted per switching event per emitter is low which results in low signal-to-noise ratios (8 dB). Regarding the various conditions, bSOFI gave reliable results and seems to be well suited for photoswitchable proteins. The dark-state lifetime does not need to exceed the on-state lifetime and only needs to be on the order of the frame exposure time, which is in agreement with previous findings [18].

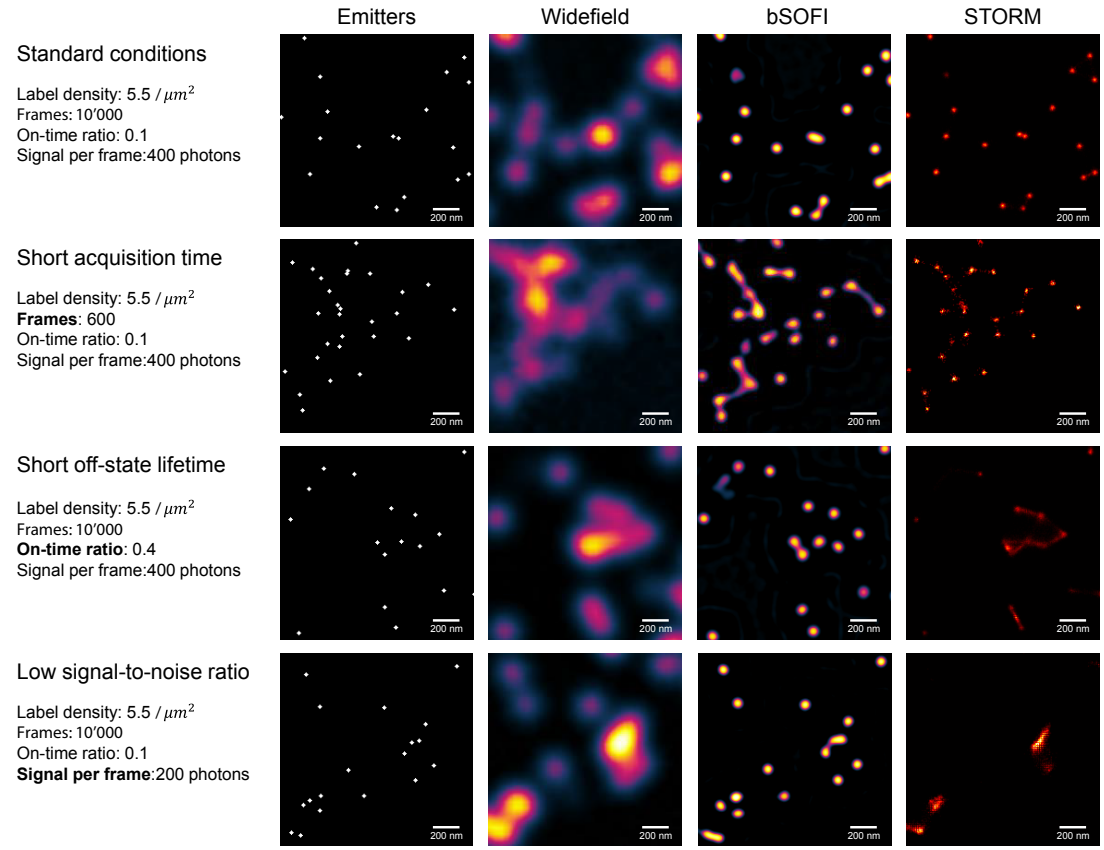

Figure 4.9: Simulation examples. Widefield, SOFI and FALCON STORM images with the generated emitter distributions for different imaging conditions. Emitters shown in the left column are enlarged for the visualization purposes. Published in Girsault & Lukeš et al., Plos One, 2016 [43].

4.5 Complementarity of PALM and SOFI for live cell imaging

Using optimized bSOFI (described in section 4.3), we have achieved a spatial resolution comparable to PALM. Live cell imaging requires a sufficiently high temporal resolution which is truly a challenge for super-resolution microscopy. The spatial super-resolution comes at an expense of temporal resolution. Bleaching, activation or switching rates, camera frame rates, and high number of frames for the image reconstruction limit the achievable temporal resolution. In view of imaging the dynamics of important biological structures like focal adhesions, we are in need of characterizing the difficult balance between lowering spatial super-resolution while enhancing temporal resolution.

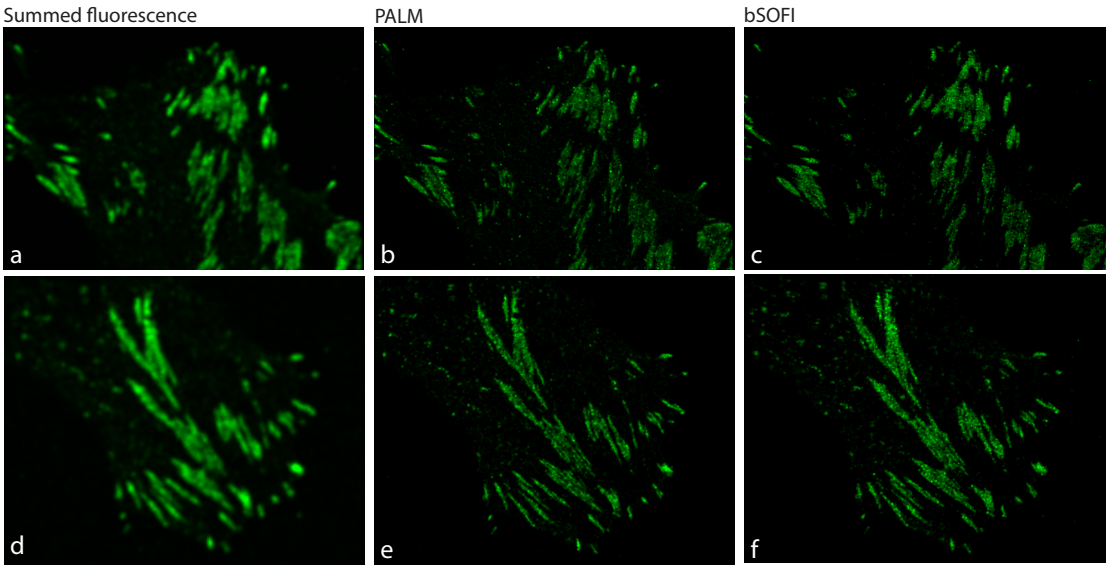

Figure 4.10: CFP labelled paxilin in fixed MEF cells. (a),(d) Sum over the raw image sequence, (b))(e) PALM image, (c),(f) bSOFI image 6th order.

We performed a comprehensive spatio-temporal resolution analysis of both PALM and SOFI by applying them on the same datasets. Comparing PALM and SOFI is challenging due to their very different nature (i.e. a list of localizations vs. higher order statistics calculated across the input image stack). Measures like precision, recall or accuracy are often used when comparing PALM algorithms. In this case, a list of localized emitters is compared with the ground truth data. This approach is not well suited for comparing PALM and SOFI. Although the image resolution improves with increasing SOFI order, SOFI does not provide the localizations of underlying emitters.

In order to objectively characterize the performance of PALM and SOFI under a broader range of conditions, we have introduced a novel approach for assessing contrast and resolution, based on modulation transfer function (MTF) measurements on a simulated test pattern. The MTF allows one to extract the cut-off frequency and the visibility as a function of spatial frequency of an imaging system and is used as a metric for characterizing optical imaging

instruments [28]. We extended the MTF analysis, already well known from classical optics, for application in super-resolution imaging. This MTF analysis on simulated data allowed us to compare the spatio-temporal resolution of PALM and SOFI under controlled conditions close to the real conditions in focal adhesions.

The test pattern is composed of bars with varying width ranging from 500 nm to 20 nm. More precisely, the bars were 500, 400, 300, 200, 150, 120, 100, 90, 80, 70, 60, 50, 40, 30, and 20 nm wide. Repeating every width for three consecutive bars led to the test pattern with 45 bars as shown in Figure 4.12a. Assuming fluorescent labelling, the bars are filled by uniformly distributed emitters according to a predefined labelling density. To approximate the conditions of focal adhesions in a cell, we tested two labeling densities (i.e. 800 and 1200 molecules /μm^2). Our simulation takes into account the photophysics of mEos2 and psCFP2 and parameters of the microscope setup. Based on this test target, we determined the visibility for PALM and SOFI beyond the cut-off frequency of classical widefield microscopy. From each simulated MTF, we extracted the cut-off frequency, resulting in a resolution measure.

4.5.1 Simulations and photo-physical model

The simulation assumes photokinetics typical for fluorescent proteins in PALM measurements. For each fluorophore, a time trace is modelled. The time trace describes the number of photons emitted by a given fluorophore over time. Each fluorophore, once it is in the on-state, shows a "burst" of blinking events before being bleached. The blinking fluorophore randomly switches between the on-state and the dark state (Figure 4.11e). On- and off-times of these blinking events, as well as bleaching of the fluorophore, are governed by an exponential distribution with an average on-time τ_{on}, an average off-time τ_{off}, and an average bleaching lifetime τ_{bl}. The on-time ratio $\tau_{\text{on}}/(\tau_{\text{on}}+\tau_{\text{off}})$ defines the frequency of the blinking in the burst.

Assuming a camera frame rate of 50 Hz, the blinking parameters were set in order to obtain a similar behavior as mEos2 measured in [49]. The average duration of 8 blinking events in one burst takes on average 3.2 s (on-time ratio = 0.05). The exposure time is assumed to be faster than τ_{on} and τ_{off} and the blinking is therefore properly sampled. Figure 4.11a shows time traces of the first 10 fluorophores. Please note that Figure 4.11a shows the time traces before adding noise. The number of blinks per burst is random (in the range 2-10). Figure 4.11c,d shows the statistics of the simulated image stack. The average number of blinks per burst is equal to 5.9. Figure 4.11c shows the number of photons as a function of frame number normalized to one. An exponential decay was fitted to measure the average bleaching lifetime. Bleaching in the simulation was set to match our experimentally measured data.

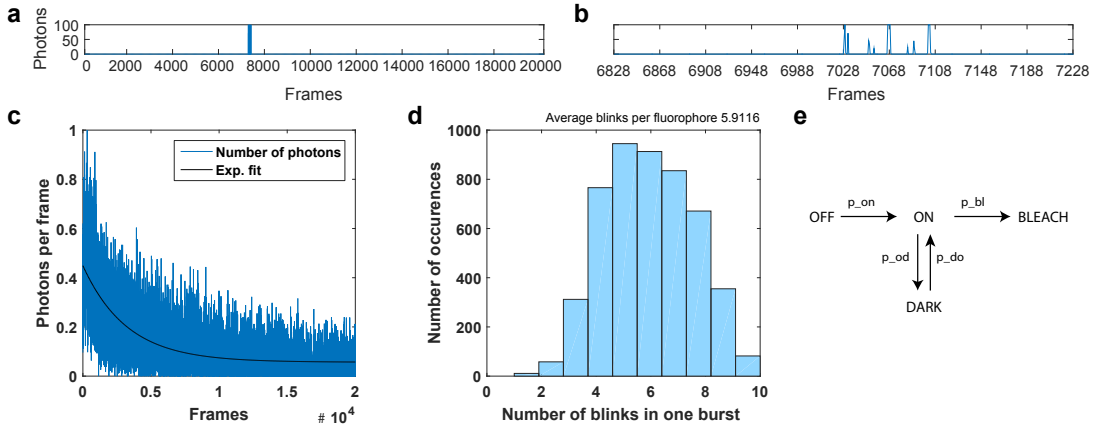

Figure 4.11: Simulation of photophysics of fluorophores. (a) An example of a time traces of one fluorophore. Each fluorophore goes randomly into the on-state and quickly blinks several times, i.e. switches between an on-state (bright) and a dark state. (b) The zoom shows these blinking events in detail. The frequency and duration of these blinks is modeled according to measurements of mEos2 photokinetics in [49]. (c) Number of photons as a function of frames. (d) Number of blinking events in on "burst". During the "burst" each fluorophore blinks several times. (e) A schematic drawing of the four state photophysics model.

4.5.2 Modulation transfer function (MTF) resolution measure

For our MTF analysis, the pattern consists of progressively narrower black and white bars (Figure 4.12a). When imaging this pattern, the bars might still be resolved, but the visibility decreases with increasing spatial frequencies. The visibility is given as

$$M = (F_{\max} - F_{\min})/(F_{\max} + F_{\min}) \tag{4.53}$$

where $F_{\max}$ and $F_{\min}$ are taken as the maximum and minimum intensity values at a given spatial frequency. In classical optics, the microscope is described as a low pass filter. The MTF describes this filtering effect when comparing a periodic object (with a given spatial frequency) to the filtered image. The MTF can be calculated as

$$\text{MTF} = |\mathscr{F}\{P(\mathbf{r})\}| \tag{4.54}$$

where $P(\mathbf{r})$ represents the test pattern composed of the progressively narrower black and white bars as shown in Figure 4.12a and the operator $\mathscr{F}\{\}$ corresponds to the Fourier transform. The modulation depth is associated to the aforementioned visibility and this generalized MTF analysis integrates all contributions starting from the object and ending with the super-resolved image. Assuming no noise, the cut-off frequency f_c corresponds to the spatial frequency where the visibility goes to zero and the limit of resolution is given by $1/f_c$.

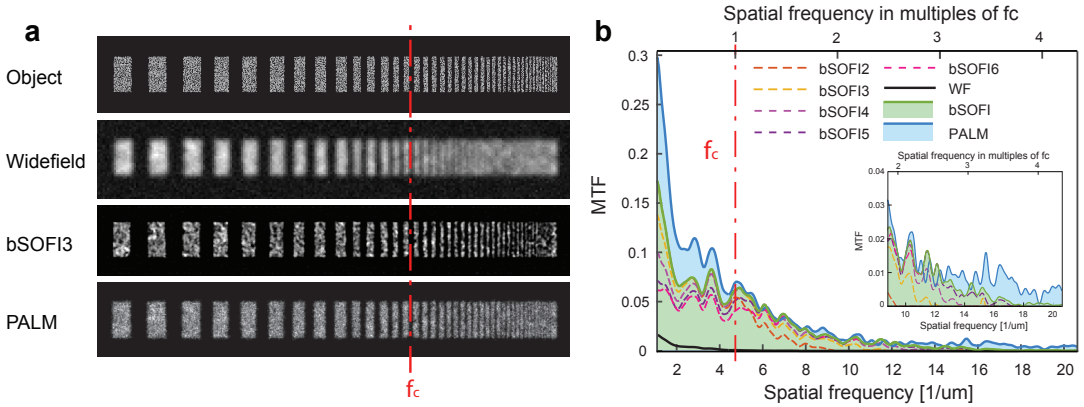

Figure 4.12: (a) MTF test target consisting of single emitters randomly placed inside progressively thinner bars, together with resulting widefield, PALM and third order SOFI image (I_{on} = 100 photons and 20,000 frames). The red line indicates the cutoff frequency f_c for widefield imaging. The PALM images were rendered as localization number histograms with a pixel size equal to the SOFI pixel size. (b) MTF calculated from the simulated SOFI and PALM images in (a). Adjusted from Deschout & Lukeš et al., Nature Comm., 2016 [48]

4.5.3 Spatial-temporal resolution analysis

Figure 4.13 show the simulated cut-off frequency maps for PALM and SOFI based on the same test target, as a function of the number of frames and the number of photons per emitter per frame in an on-state (i.e. I_{on}). Figure 4.13a corresponds to 1200 molecules/μm^2 and the psCFP2 case, whereas Figure 4.13b corresponds to 800 molecules/μm^2 and the mEos2 case. The number of frames ranges from 500 to 20,000. At 20,000 frames, all molecules are detected and the structure of the test pattern is fully described.

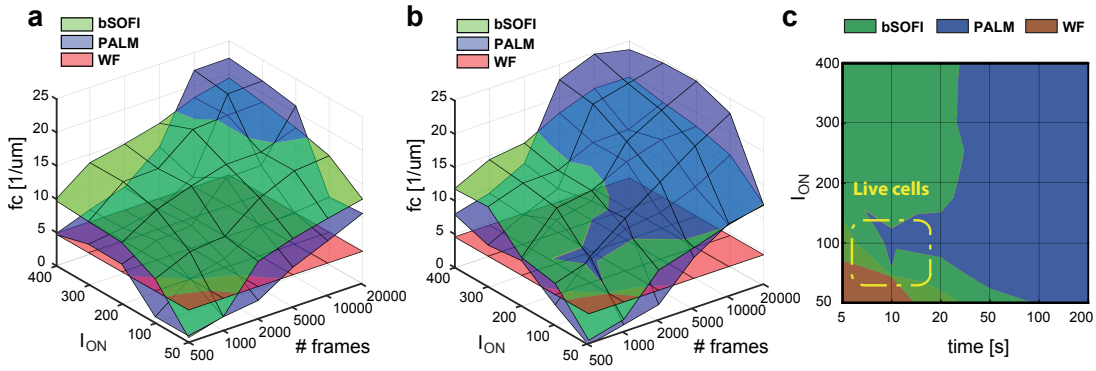

Figure 4.13: (a,b) Cut-off frequencies for PALM and SOFI as a function of I_{on} and the number of frames, with an emitter density of (a) 1,200 μm^{-2} and (b) 800 μm^{-2}. (c) Two-dimensional projection of the chart in (a). The timescale assumes a frame rate equal to 100Hz, which corresponds to the frame rate used for our live-cell measurements. Adjusted from Deschout & Lukeš et al., Nature Comm., 2016 [48]

SOFI shows a slowly growing spatial resolution (i.e. an increase of cut-off frequency) with

increasing I_{on} and the number of frames. The PALM cut-off frequency grows faster, but only outperforms SOFI for a high number of frames (> 10,000 for the higher density case and > 5000 for the lower density case). Note that SOFI requires at least 500 frames before "super-resolution" can be achieved, while PALM needs even more frames (typically > 1000) and depends more strongly on the labeling density. For low frame numbers and low I_{on}, the number of localized emitters and the localization precision are too low for PALM to properly describe the test pattern, which results in low MTF values and corresponding low resolution. Assuming a typical camera frame rate of 100 Hz, Figure 4.13c shows the resolution sub-space where SOFI is dominant over PALM in terms of temporal/spatial resolution, and vice versa the sub-space where PALM outperforms SOFI. This indicates the parameter space where our PALM-SOFI imaging modality can be used for investigating the dynamics of focal adhesions as indicated in Figure 4.13c.

5 Super-resolution imaging applications

Parts of the following chapter were published in:
H. Deschout & T. Lukeš* et al., Complementarity of PALM and SOFI for super-resolution live cell imaging of focal adhesions, Nature Communications, 2016 [48]*
**Equal contribution*

Section 5.2 is a part of a manuscript in preparation:
T. Lukeš, D. Glatzová, Z. Kvíčalová, T. Brdička, T. Lasser & Marek Cebecauer, Determining protein densities in T-cells using super-resolution optical fluctuation imaging

Section 5.4 is a part of a manuscript in preparation:
T. Lukeš, J. Pospíšil, P. Křížek, Z. Švindrych, M. Ovesný, K. Fliegel, K. Spendier, and G. M. Hagen, Imaging live cells with doubled resolution using Bayesian image reconstruction

5.1 Super-resolution live cell imaging of focal adhesions

Using simulations and fixed cell focal adhesion images, we investigated the complementarity between PALM and SOFI in terms of spatial and temporal resolution in section 4.5. We showed that PALM and SOFI can both be independently applied on the same dataset with additional benefit. This PALM-SOFI framework was used to image focal adhesions in living cells, while obtaining a temporal resolution below 10 s. We visualized the dynamics of focal adhesions, and revealed local mean velocities around 190 nm per minute. This PALM and SOFI concept provides an enlarged quantitative imaging framework, allowing unprecedented functional exploration of focal adhesions through the estimation of molecular parameters such as the fluorophore density and the photo-activation and photo-switching rates.

Cell adhesions are essential for cells to adhere to the extracellular matrix for carrying out fundamental tasks such as migration, proliferation, and differentiation [76]. Focal adhesions are composed of dense assemblies of hundreds of proteins [77] forming small structures

close to the cell membrane [78]. These protein assemblies contain transmembrane receptors, such as integrins, binding to the extracellular matrix and recruiting other proteins inside the cytoplasm, such as paxillin and talin. Focal adhesions can thus be seen as the anchor points of the cell onto the extracellular matrix mediating interactions with the actin cytoskeleton. Most focal adhesion proteins have been identified. However, the observation of the spatial organization and dynamics of focal adhesions remains challenging. Focal adhesions evolve over time and they can also undergo translational movement. The mean velocity of focal adhesions in stationary fibroblasts has been reported to be in the order of 100 nm per minute [79]. This translates into a temporal resolution well below one minute in order to capture the fundamental dynamic behavior while avoiding motion blur which would otherwise spoil the anticipated spatial resolution [80].

PALM was used to image the submicron patterns of vinculin in a fixed cell [4] and the dynamic behavior of paxillin [80]. PALM is well suited for live cell imaging of focal adhesions since it uses genetically expressed fluorescent proteins known for being well tolerated in living cells. Although temporal resolutions in the order of seconds are possible, PALM trades temporal resolution for spatial super-resolution, since using less raw images for image reconstruction means less available single molecule localizations. To address the need for quantitative and time-lapse super-resolution imaging of focal adhesions, we enlarged the scope of SMLM by merging PALM with SOFI applied to the same raw image sequence. SOFI tolerates a significant overlap of single molecule images and relaxes the requirements on the activation or switching rates when compared with classical SMLM concepts. This allows one to use fluorescent molecules with a higher activation or switching rate [18], resulting in an improved temporal resolution [19]. When attempting to increase both temporal and spatial resolution, a PALM-SOFI approach based on an identical raw image sequence appears as an interesting imaging modality.

5.1.1 Live cell imaging

We imaged living MEFs expressing paxillin labelled with mEos2 and post-processed the data by both PALM and SOFI algorithms, as shown in Figure 5.1. We obtained a temporal resolution of 10 s, while maintaining an average spatial resolution of 157 nm for SOFI, as determined by the sFRC metric (see section 6.1.1). PALM at this temporal resolution resulted in an average spatial resolution of 145 nm. We determined the mean velocity of one of the focal adhesions, obtained from a kymograph based analysis [81, 82] (see Figure 5.1). PALM and SOFI show similar trends, indicating that the focal adhesion moved with a mean velocity of 190 nm per minute. This mean velocity is in agreement with values reported in [79]. PALM and SOFI can be both applied to the same dataset with no extra cost. The principles of these methods are entirely different (molecule localization by fitting vs calculation of cumulants across the image sequence) and as such are prone to different artifacts. PALM struggles to detect molecules in high density regions where SOFI performs well and exhibits high SNR. On the other hand, PALM achieves high localization precision in sparse regions with only a few molecules where

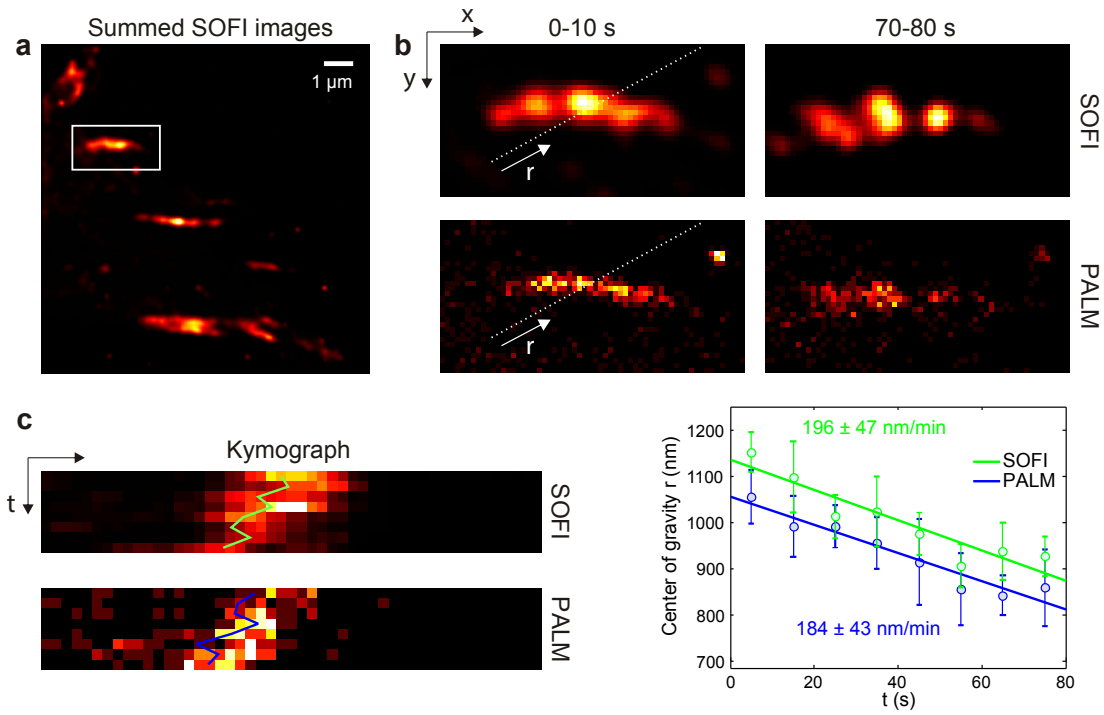

Figure 5.1: Live cell imaging with PALM and SOFI. (a) Sum of 8 SOFI images of a living MEF expressing paxillin labeled with mEos2. Each image is reconstructed from 1000 camera frames with 10 ms exposure time, resulting in a 10 s temporal resolution. The PALM images were rendered as localization number histograms [48] with a pixel size equal to the SOFI pixel size. (b) Region of interest indicated in (a) showing a focal adhesion at different time points for PALM and SOFI. (c) Kymographs along the direction of motion as indicated by the line in (b). The focal adhesion mean velocity is determined by a linear fit to the position of the center of gravity of each line in the kymograph. The procedure was repeated 5 times for parallel kymographs. Adapted from Deschout & Lukeš et al., Nature Comm., 2016 [48].

SOFI exhibits low SNR. Therefore, SOFI image can be used as a control for PALM imaging in high density regions. Carefully assessing both SOFI and PALM images taking into account advantages of both methods helps to better understand the true structure of the sample of interest.

5.1.2 Quantitative imaging

Beyond qualitative imaging, SMLM methods such as PALM allow one to obtain quantitative molecular information, such as the number of localizations. This can be related to the number of fluorescent proteins, but most photoactivatable fluorescent proteins blink, i.e. they can reversibly go to a dark state several times before they bleach. Moreover, this blinking behavior depends on the illumination intensity and the molecular environment of the fluorescent proteins and may give rise to multiple localizations. Simply counting the localizations usu-

ally results in an overestimation of the number of fluorescent proteins. Several methods to correct this over-counting error have been developed for PALM [83, 84]. As these methods require characterization of the blinking behavior, for instance through the calculation of the average time between two emission bursts, they indirectly allow one to probe the molecular environment of the emitters. Focal adhesions are dense assemblies of proteins, making it challenging to avoid merging localizations of different fluorescent proteins, which would lead to an under-counting error. Therefore, as a merging criterion, we assumed a threshold based on a statistical measure called the Hellinger distance [83], which allows one to account for the varying localization precision. We applied this adapted method to our localization data of fixed MEFs expressing paxillin labeled with psCFP2, as shown in Figure 5.2. The corrected localization number and the average time between two blinking events is shown as a function of different thresholds of the Hellinger distance, calculated for three areas with different emitter densities. We determined that a value of 0.9 was a good compromise, but even around this value the number of localizations decreases with increasing threshold values for the densest areas. This indicates that the sample is too dense.

SOFI is an interesting complement to PALM for quantitative imaging, since combining cumulant images of 2nd, 3rd, and 4th order enables to extract molecular parameters such as the on-time ratio, the molecular brightness, and the molecular density [42]. Moreover, as SOFI is superior to PALM in imaging samples with high density regions, this method is of great interest for quantitative imaging of focal adhesions. We used SOFI to determine the on-time ratio and density map of the same localization data used for PALM (see Figure 5.2). As opposed to PALM, SOFI performs well in high density areas. SOFI estimates the molecular parameters pixel-wise. This estimation is relevant only for areas which contain useful signal. Therefore background areas were removed by applying an intensity threshold.

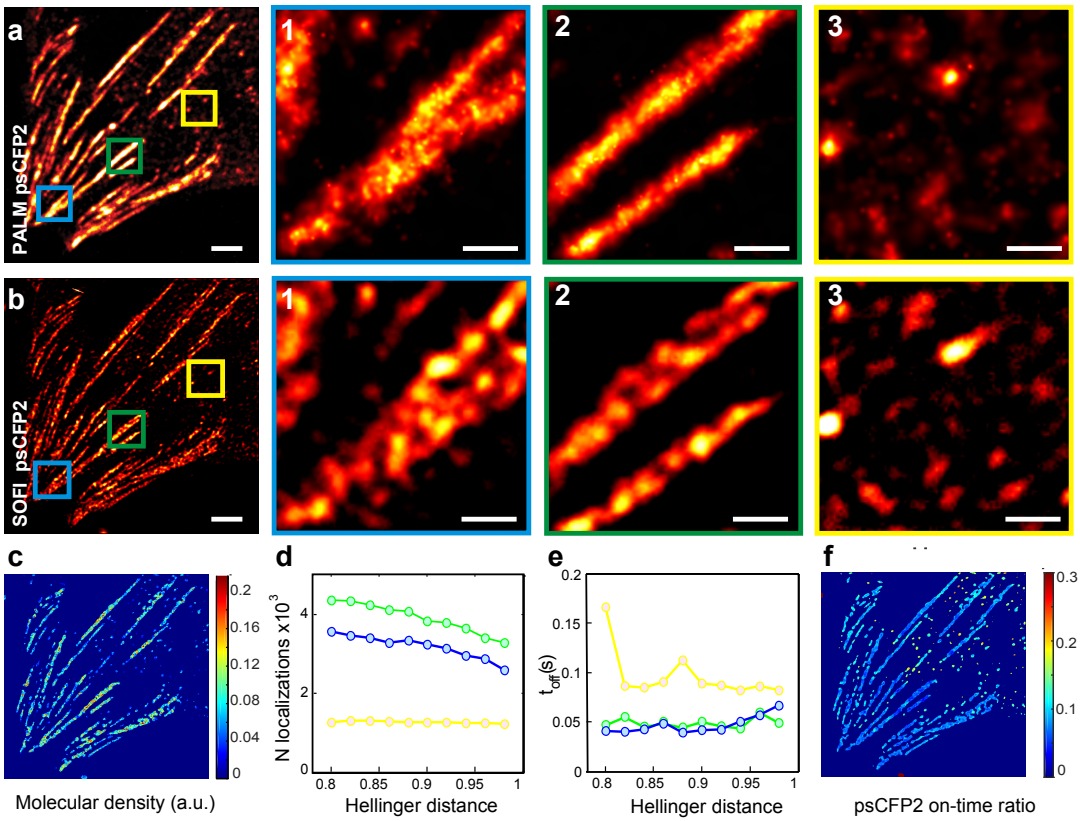

Figure 5.2: Quantitative imaging with PALM and SOFI. (a-b) PALM and SOFI images of a fixed MEF cell expressing paxillin labeled with psCFP2. Panels 1-3 are corresponding zoom-ins for the PALM or SOFI images. (c,f) SOFI analysis yields a fluorophore density and on-time ratio map as described in section 4.3.3 (d,e) Blinking events in PALM data can be detected by merging localizations that are sufficiently close in space and time. This analysis yields the blink corrected number of localizations N and the corresponding average off-time t_{off} between blinks, shown as a function of the distance threshold for merging localizations. The PALM images were rendered as probability maps [48]. Scale bars: (a,b) 2 μm , (1-3) 0.5 μm. Published in Supplementary Deschout & Lukeš et al., Nature Comm., 2016 [48]

.

5.2 Determining protein densities in T-cells using SOFI

Surface proteins are heterogeneously distributed on the plasma membrane of living cells. Dense assemblies and spatial patterns of these proteins may influence the cell function. Therefore, characterization of nanoscale organization of the surface proteins is required for better understanding of cell membrane related processes.

Here, we present a novel method for quantitative evaluation of clustering behaviour of proteins based on molecular density estimation by SOFI. Using this method, we investigate the nanoscale organization of CD4 fluorescent-protein fusion variants on the surface of resting T cells.

5.2.1 Introduction

CD4 is integral membrane glycoprotein essential for T cell development and function. On the surface of T cells, it functions as a co-receptor by increasing sensitivity of TCR interaction with the antigenic ligand present on the surface of antigen-presenting cells. CD4 has single transmembrane domain and requires post-translational modification with palmitates for its full function. We have generated fluorescent-protein fusion variants to investigate the impact of CD4 palmitoylation on its nanoscale distribution on the plasma membrane of resting T cells.

The size of protein clusters is frequently smaller than 200 nm which is the resolution limit of standard fluorescence microscopes. Single molecule localization microscopy (SMLM) techniques such as PALM and STORM rely on temporal separation of otherwise spatially overlapping fluorophores. By fitting a point spread function (PSF) to each separate fluorophore, a precise position of the fluorophore is estimated from the centre of the PSF. SMLM algorithms result in a list of the x and y coordinates of all the localized fluorophores together with estimated localization precision [85, 86, 87, 88].

Several methods for analyzing localizations generated from SMLM have been demonstrated [89, 90, 91, 92, 93, 94, 95]. All these methods rely on the SMLM data. In high density samples, the fitting procedure starts to fail leading to under-counting errors. Additionally, blinking behaviour of fluorescent proteins causes multiple localizations of a single molecule [96]. Multiple blinking introduces a bias into the following quantitative analysis. Few methods have been developed to account for this error [83, 84], but a precise blinking correction is challenging. SOFI is an alternative super-resolution technique based on temporal cumulants of independently fluctuating fluorophores [7, 44]. SOFI can be applied on the same dataset as SMLM algorithms [18, 48]. Instead of localizing each individual fluorophore, SOFI resolution improvement is given by properties of spatio-temporal cross-cumulants calculated from the entire image sequence of 2D [7] or 3D images [19]. The balanced SOFI (bSOFI) [42] linearizes response to brightness and exploits molecular parameters such as molecular state lifetime and molecular density of fluorophores. Multiple blinking of individual fluorophores

improves the SOFI signal and therefore precision of the molecular parameter estimation. SOFI is compatible with wide range of blinking conditions and high labelling densities [18, 48]. Here we employ these advantages of SOFI and present a method for quantitative evaluation of protein distribution based on SOFI molecular density estimation. Using this method, we investigate the nanoscale organization of CD4 variants on the surface of resting T cells.

5.2.2 Algorithm description

Input image sequence is first drift corrected by image registration with sub-pixel precision. Lateral shifts for drift correction are estimated by fluorescent beads drift correction in ThunderSTORM [85]. Drift corrected image sequence is divided into sub-sequences of 500 frames each in order to minimize the effect of photobleaching. In each subsequence, we calculated SOFI images of 2nd, 3rd and 4th order. These SOFI images are then summed across all subsequences. By combining SOFI orders, a system of equation can be established. By solving this equation system, we obtain molecular density map as described in section 4.3.3. As shown in [48, 19], the density estimation can be accurate given long enough input image sequence (>5000 frames). In our experiments, we acquired image sequences of 10 000 frames each.

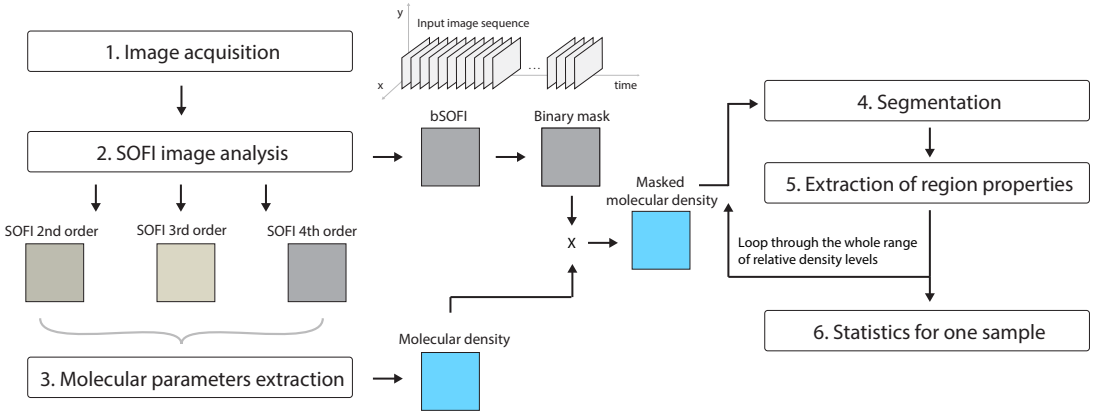

Figure 5.3: Workflow of our clustering analysis based on SOFI density map estimation. SOFI images of different cumulant orders are calculated and used to estimate molecular density map. The background is removed using binary mask estimated from bSOFI image. Molecular density mask without background is segmented with various thresholds which go across the available range of density levels (given as multiples of mean density in the whole region of interest). Properties of the segments are extracted. This routine is then repeated for each sample.

The work flow of our algorithm is shown in Figure 5.3. On-time ratio and density maps are estimated pixel wise. This pixel-wise estimation is reliable only for SOFI image areas where the signal is present. In the image background areas with no useful signal and only noise, the estimated density values are not relevant and might cause a bias to the clustering analysis. To avoid this issue, we perform a binarization step using Sauveola binarization algorithm [97]. This gives us a binary mask which can be used for an effective background removal. In

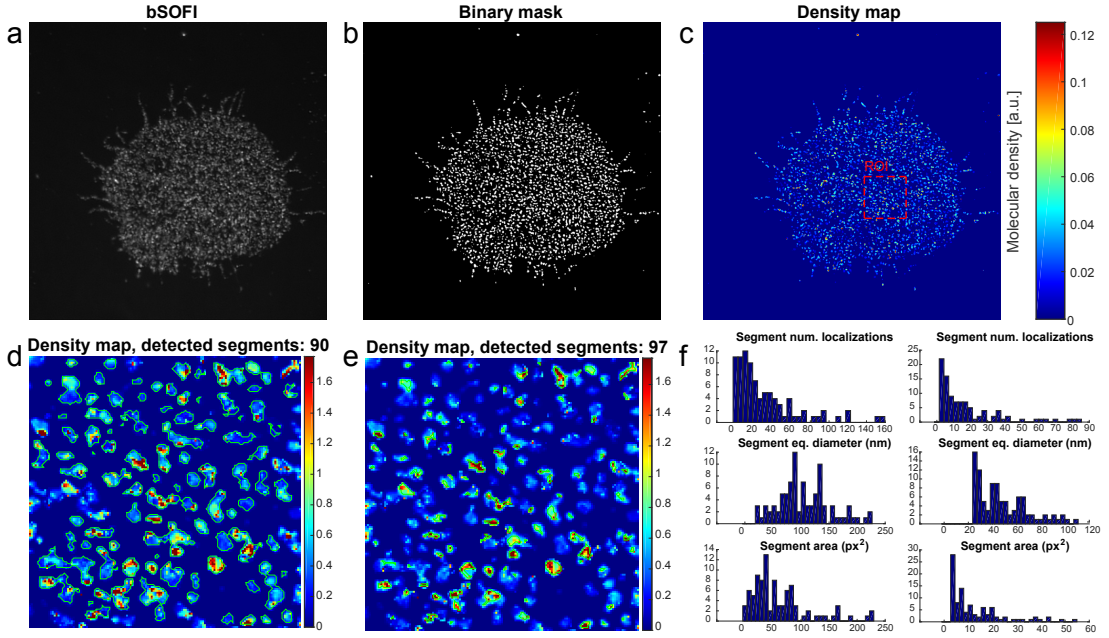

Figure 5.4: Representative image of data processing for a single cell wild-type CD4 labeled with mEos2 fluorescent protein. (a) bSOFI image. (b) Binarized bSOFI image. (c) Molecular density map with removed background using binary mask in **b**. (d),(e) an example of segmentation of the 3 x 3 μm region of interest indicated in **c** by the dashed red line for two relative density thresholds (0.1 and 0.5). (f) Properties of the segmented region in **d** and **e**.

order to investigate clustering behavior and distribution of proteins across a wide range of molecular densities, our algorithm screen through the whole available range of thresholds related to the mean molecular density in the analyzed region instead of applying just one fixed threshold. For each threshold, regions with a high local density are detected and segmented. The number of localizations per segment, area, perimeter and equivalent diameter of the segmented regions are calculated.

5.2.3 Analysis of protein nanoscale organization

We imaged four different variants of CD4 proteins (wt, dCT, dD1D4, CS1) in the plasma membrane of resting T cells labelled with mEOS2. Using TIRF fluorescence microscope, we imaged 20 samples for each CD4 variant (i.e. 80 samples in total). For each sample, 10 000 frames were acquired. We have calculated SOFI images and density maps for each sample as described in section 4.3.3. To evaluate and compare clustering behaviour among different CD4 variants, we selected a 3 x 3 μm region of interest (ROI) in each cell. Figure 5.4 shows a representative data example for a single cell. Cells naturally have various sizes. Taking one ROI for each cell ensure that the larger cells will have the same statistical significance as the smaller cells. In SOFI theory, signals that are constant over time are equal to zero for SOFI 2^{nd} and higher orders. Therefore, SOFI suppress constant background. Beads and vesicles are not

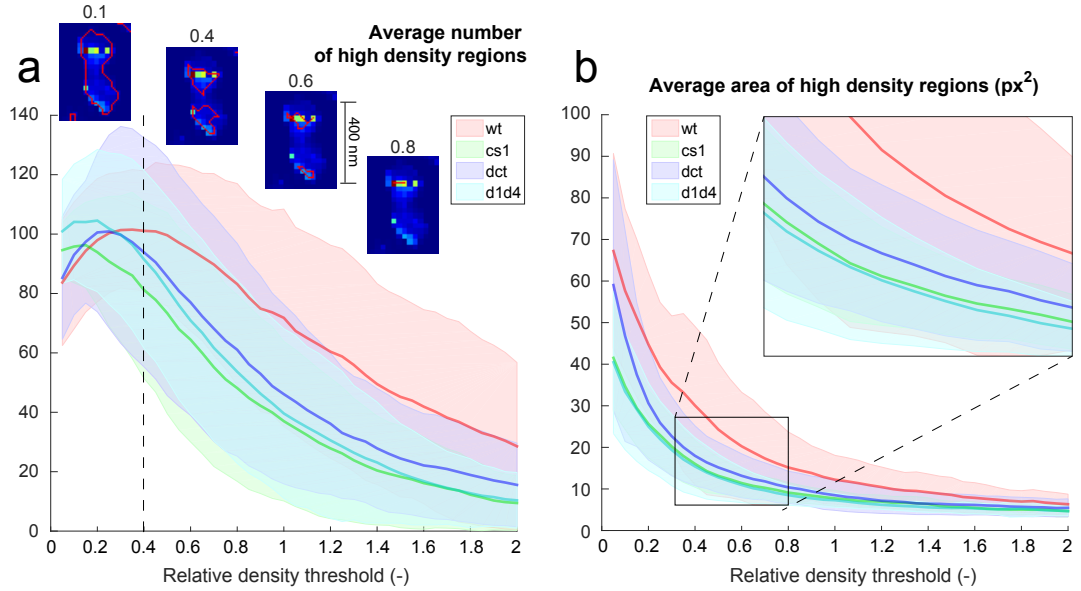

Figure 5.5: SOFI clustering analysis for the whole range of density thresholds related to the mean density in the evaluated 3 x 3 μm region of interest (ROI). (a) Number of high density regions averaged across all samples of one CD4 protein variant. The inset images shows an example of the detection of the segments for various thresholds. (b) Area of high density regions averaged across all samples of one CD4 protein variant in px^2, where pixel size is 25 nm. Semi-transparent color areas represents standard deviation.

blinking and do not appear in the SOFI image when the input image sequence is precisely drift corrected. The absence of beads and vesicles in the SOFI image is convenient for the clustering analysis to avoid misinterpretation of vesicles as high density regions. Each ROI is analyzed as described in section 5.2.2. Calculating average number and area of high density regions across all cells of one CD4 protein variant for the whole range of density thresholds, we obtain curves shown in Figure 5.5a,b. Inset images in 5.5a indicate how the density threshold affect the detection of high density segments. Starting with small thresholds, large regions with low average density are detected. Increasing threshold leads to division of these regions into high density segments which increases the number of detected segments until the threshold is too high and the segments begins to disappear under the high threshold level. With increasing density threshold, the wild-type CD4 distribution exhibits more high density segments of larger size. Average size of the segment as a function of density threshold is shown in Figure 5.5b. Figure 5.6 shows box-plots of the statistics for the density threshold mark by the dashed line in Figure 5.5a.

5.2.4 Discussion

We introduced a novel clustering analysis using SOFI to characterize surface receptors in T cells. The advantage of this method is a shorter acquisition time, no need for a multiple

blinking correction, and a direct access to molecular parameters like the molecular density and the on-time ratio. We demonstrated that the proposed method enables quantitative, model free, clustering analysis of CD4 distribution in the plasma membrane of T-cells on a scale of approx. 50 nm. To our knowledge, this is the first attempt to analyse distribution of CD4 proteins and its variants on the surface of resting T cells in nanoscale using SOFI. The results suggest the importance of palmitoylation for the native distribution of CD4 protein on resting T cells. Currently, we are working on a control experiment in simulated conditions in order to investigate in details the sensitivity and precision of our method and to confirm our preliminary findings.

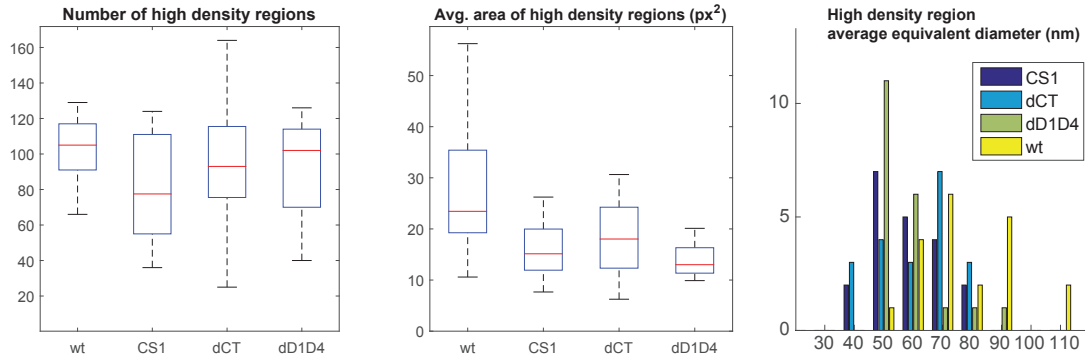

Figure 5.6: SOFI density analysis indicates larger size of high density segments formed by wild-type CD4 and the variant lacking the intracellular part. On the contrary, mutant lacking the extracellular part and non-palmitoylatable mutant were detected in smaller segments.

5.3 SOFI for DNA optical mapping

Metagenomic assessment of the microbial content allow one to detect microbiota changes caused by severe diseases and objectively characterize the impact of treatment. The optical DNA mapping, based on the recently developed "Fluorocode" technology [98, 99], is a promising technique for a fast and cost-effective metagenome analysis. The extracted DNA is subjected to enzymatic labeling, in which a selected methyltransferase enzyme introduces a fluorescent dye at specific sites on the DNA strand. Through the enzymatic sequence specific introduction of fluorophores, a "fluorocode" can be generated for each DNA fragment. Different genomes lead to different distributions of the recognition sites, and therefore different fluorocodes. This enzymatic labeling process provides high density information content, unprecedented by other genomic mapping techniques [100]. The fluorescently labeled DNA is linearized and deposited using a novel rolling droplet method [101]. Following successful labeling and deposition, the next step in the analysis of a raw DNA sample is an optical read out by fluorescent super-resolution microscopy.

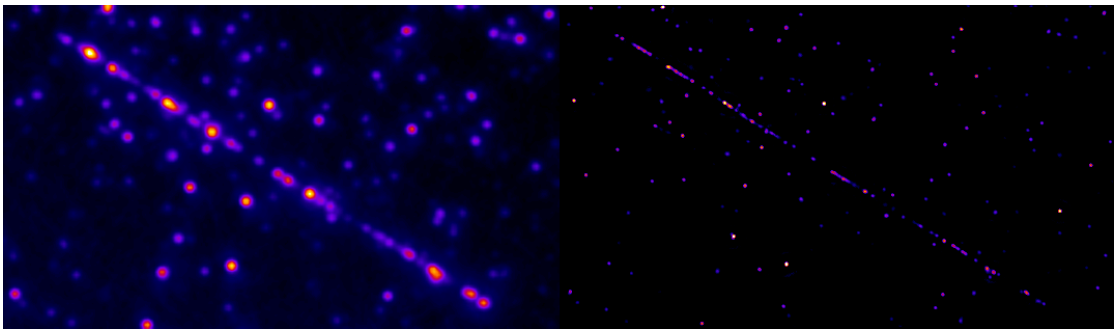

Figure 5.7: DNA images, sample of bacteriophage T7 DNA, 3000 frames a) Average ("Widefield") image (on the left), b) SOFI 3^{rd} order image (on the right), fire colormap.

To accommodate the need for fast and high throughput screening, as required by microbiome diagnostics, high density fluorescent labeling and short off state lifetimes of fluorophores are preferred. These conditions are well suited to SOFI. Therefore, we tested SOFI microscopy for the imaging of the DNA instead of the previously used methods [99]. Images of DNA stretched and deposited to a cover glass labelled with MTaqI and Atto647n were acquired by a standard commercial TIRF microscope and processed by our enhanced bSOFI algorithm. Figure 5.7 shows initial results indicating increase in the resolution obtained by bSOFI.

These images were automatically analysed by the image processing procedure shown in Figure 5.8. Images of DNA strands were segmented using standard Otsu's thresholding method [102]. In the segmented regions, feature points were selected by Harris detector [103] and DNA strand was detected by the random sample consensus (RANSAC) algorithm [104] line fitting. The image was appropriately rotated and the ROI which contains the DNA strand was cropped. Figure 5.9 shows line profiles of the analyzed DNA strand. The widefield image is given as the average image across the input image sequence. The widefiled image was interpolated using bilinear interpolation in order to have the same number of pixels as the

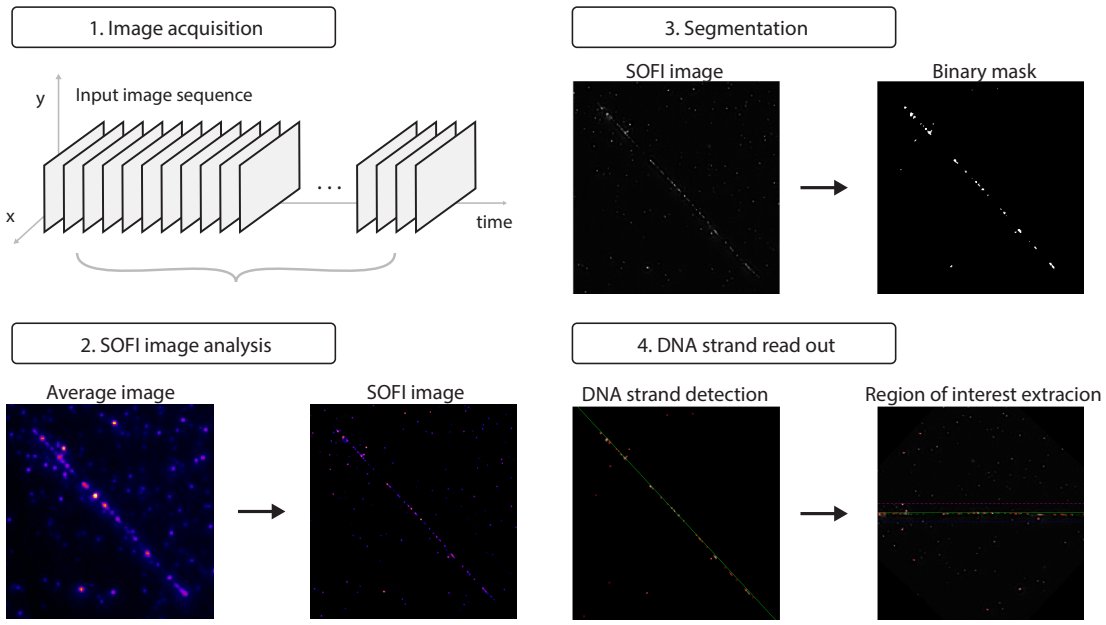

Figure 5.8: Work flow of image processing analyses of fluorescently labeled DNA strands.

SOFI 3^{rd} order cumulant image. The STORM images were calculated using ThunderSTORM [85]. Localized points were rendered into a pixel grid of the same size as the SOFI 3^{rd} order cumulant image. It seems that STORM can localize few separated molecules precisely, but also a lot of molecules are not detected probably due to relatively strong bleaching and the blinking conditions which are not optimal for STORM. SOFI images can be further converted into a list of distances between the locations of fluorophores on DNA, information, which is specific to the organism of origin and can be directly matched to the sequence information. We are currently developing tools to automatically detect stretched DNA molecules from the SOFI image, to extract the vector and list of distances for all DNA strands and perform reliable DNA matching with existing libraries of genome sequences.

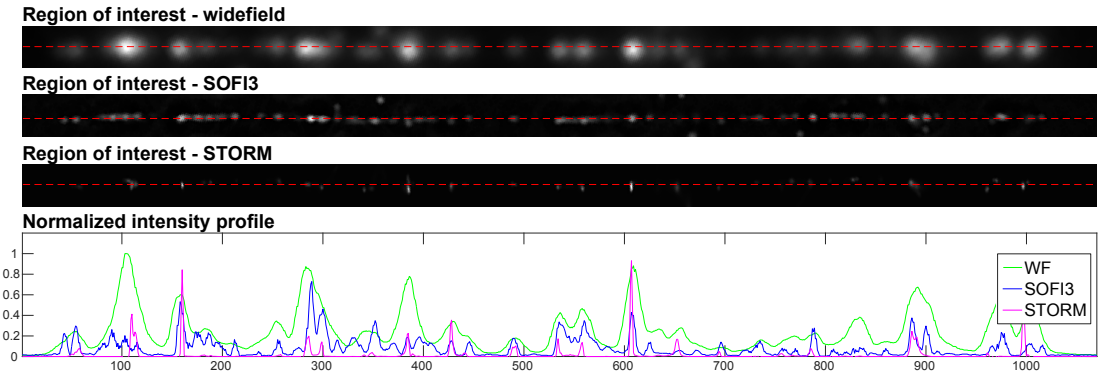

Figure 5.9: Results for the sample of bacteriophage T7 DNA. Region of interest of the widefield image, SOFI image and STORM. Horizontal line profiles (red dashed lines in the images).

5.4 Improved cell particle tracking using MAP-SIM

Single particle tracking (SPT) is a computer enhanced microscopy method used to track the motion of biological molecules or vesicles [105]. In SPT, a particle trajectory is obtained from position coordinates over a series of time steps. There are three basic steps in single particle tracking analysis [106]. The first is detection of the particles in the raw data. This may be regarded as segmentation or feature detection. The second step is localization of the particle, usually accomplished by fitting a small region of interest (7×7 pixels in our case) to a two-dimensional Gaussian function. The third step is to link the localizations together from one frame to the next to create a particle trajectory which is as long as possible. These three steps together determine whether a particle can be successfully tracked. If a particle is not detected in every frame through the sequence, the trajectory will be truncated at the point where the particle was lost. MAP-SIM offers very high axial resolution and optical sectioning ability [37]. Because of this, the signal to background ratio (SBR) of the particles is higher, and the particles are thereby much easier to detect in the raw data. In this experiment, trajectories of single LAMP1-GFP particles (lysosomes, endosomes, or other vesicles containing LAMP1-GFP), were obtained by a SPT algorithm implemented in MATLAB [107]. Briefly, the intensity average of the reconstructed WF or MAP-SIM image stack was subtracted from each individual image within the stack to reduce sCMOS camera-induced fixed pattern noise and for feature enhancement. Initial starting points were selected manually. The particles were tracked for at least 12 up to a maximum of 132 time steps of 250 ms each. After this process of building uninterrupted trajectories, the mean-squared displacement (MSD), was calculated. The MSD is a measure of the average speed a particle travels and is calculated for each time difference Δt in the track. The MSD plot was computed up to $n\Delta t < 1/4$ of the total number of acquired time frames, where n is the number of available displacements of a given duration to $n\Delta t$ in the track record [105, 107].

We tracked 60 LAMP1-GFP particles in the MAP-SIM image sequence taken from Figure 3.6. Figure 5.10(a) depicts the corresponding MSD plots. We attempted to track the same particles in the WF image sequence keeping all the settings the same except for the size of the point spread function, which we took from our previous work [37]. Of the 60 particles tracked in MAP-SIM, 39 (65%) were successfully tracked in the WF data. Figure 5.10(c) depicts the corresponding MSD plots obtained from the WF single particle trajectories. Comparing the MAP-SIM MSD plot, Figure 5.10(a), to the WF MSD plot, Figure 5.10(c), it is evident that fast moving LAMP1-GFP particles, represented by steeper MSD curves, cannot be tracked as successfully in the WF data. Our single particle tracking algorithm [107] is state of the art, however, in this particular case, it is unable to detect dim, faster moving particles in the widefield data consistently enough to be able to build a trajectory longer than a few frames.

As noted above, MAP-SIM increased the signal to background ratio (SBR) of the particles. This is shown in Figures 5.10(b) and 5.10(d). To evaluate the SBR of the particles, we evaluated a region of interest (ROI) around each particle (9x9 pixels). We calculated the local SBR as the ratio between the maximum (average of the 5% of the highest pixel values) and minimum

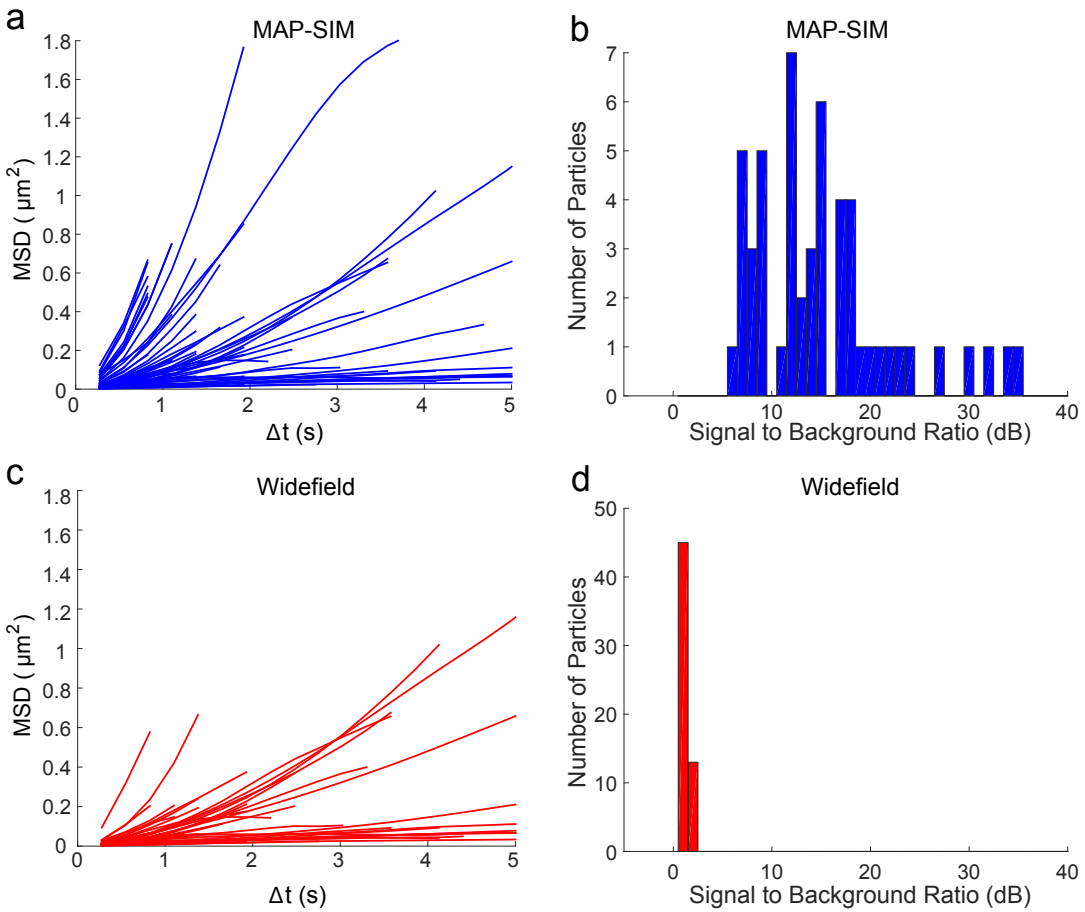

Figure 5.10: MSD plot of (a) 60 LAMP1-GFP particle trajectories obtained from a MAP-SIM image sequence and (d) 39 LAMP1-GFP particle trajectories obtained from WF image sequence. (b) and (e) histograms of particle hop speeds computed for the average distance traveled during the time lag Δt = 250 ms. (c) and (f) histograms of the signal to background ratio calculated for each particle that was tracked in the MAP-SIM (c) and WF (f) data.

(average of the 5% of the lowest pixel values) in the region.

In summary, MAP-SIM allows us to track more particles due to considerable increase of the SBR which makes the particles easier to detect in the raw data. To our knowledge, this is the first demonstration that single particle tracking experiments can be enhanced using SIM.

6 Measuring resolution and image quality in cell samples

Parts of the following chapter were published in:
H. Deschout & T. Lukeš* et al., Complementarity of PALM and SOFI for super-resolution live cell imaging of focal adhesions, Nature Communications, 2016 [48]*
**Equal contribution*

Section 6.1.2 is a part of a manuscript in preparation:
T. Lukeš, J. Pospíšil, P. Křížek, Z. Švindrych, M. Ovesný, K. Fliegel, K. Spendier, and G. M. Hagen, Imaging live cells with doubled resolution using Bayesian image reconstruction

In Abbe's theory, microscopy imaging is conceived as low pass filtering. The generally adopted resolution metric for classical microscopy is a pure instrument parameter independent of the object. Images in super-resolution microscopy are result of complex image processing where the final PSF is synthetic and depends on the performance of the image reconstruction which is largely influenced by sample properties. Therefore, measuring resolution in super-resolution imaging is a challenging task. There is a manifold of sample dependent and difficult to master parameters like labeling density, bleaching and photo-switching kinetics of fluorophores which makes the resolution assessment in the biological sample difficult. The latest development in the super-resolution microscopy field reveals a lack of objective image quality metrics. Automated objective image quality assessment based on image characteristics, i.e. spatial resolution, contrast and signal to noise ratio, is crucial for quantifying the outcome of super-resolution microscopy. Quantitative evaluation of resolution enhancement in a real sample is essential to describe the efficiency of super-resolution microscopy technique. This chapter is devoted to resolution measurements from super-resolution images of biological samples for SOFI, PALM and SIM imaging. Resolution evaluation is further accompanied by signal to noise ratio (SNR) estimation. Measuring both resolution and SNR is important to fully characterize the objective image quality.

6.1 Resolution

6.1.1 Resolution estimation using sectorial Fourier ring correlation

Estimating the resolution in single molecule localization microscopy (SMLM) is challenging, since it depends on several parameters such as the labelling density, the localization precision, and the sample structure. An interesting resolution metric for SMLM is the Fourier ring correlation (FRC) [108, 109]. However, the FRC implicitely assumes that the sample structure is isotropic, while many biological samples like for example focal adhesions often exhibit spatial pattern giving rise to anisotropic Fourier spectra (Figure 6.1,6.2). We have therefore adapted the FRC metric and introduced sectorial Fourier ring correlation (sFRC) to account for the effect of specific patterns of the biological sample.

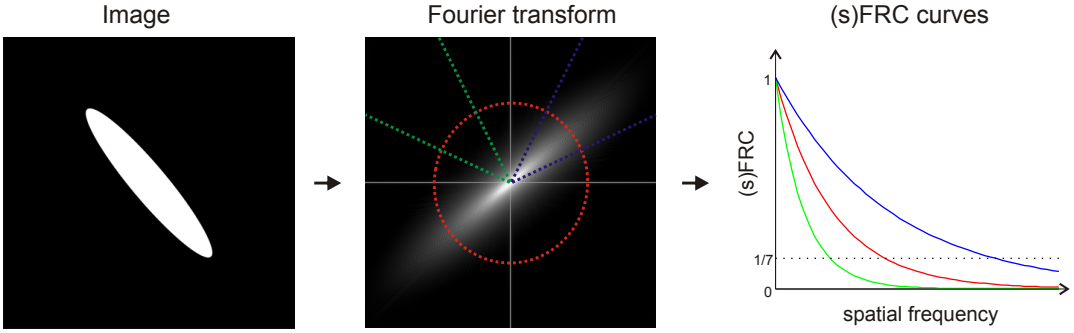

Figure 6.1: Measuring resolution using sFRC metric. Illustration of the sectorial Fourier ring correlation to obtain a measure of the resolution. Sectors contain different amount of information giving variuos FRC curves.

To calculate the FRC, a SMLM dataset is first split into two stochastically independent subsets for generating two SMLM images $I_1(x,y)$ and $I_2(x,y)$. Next, the Fourier transforms $\hat{I}_1(q,\phi)$ and $\hat{I}_2(q,\phi)$ of these two images are calculated (with polar coordinates in frequency space given by magnitude q and phase ϕ). The FRC is then calculated as

$$FRC(q) = \frac{\sum_\phi \hat{I}_1(q,\phi)\hat{I}_2(q,\phi)^*}{\sqrt{\sum_\phi |\hat{I}_1(q,\phi)|^2 \sum_\phi |\hat{I}_2(q,\phi)|^2}} \tag{6.1}$$

correlating $\hat{I}_1(q,\phi)\hat{I}_2(q,\phi)^*$ over a full circular path at a constant magnitude q. For low spatial frequencies, the FRC is close to 1, whereas for high spatial frequencies, the FRC decays to 0. Finally, after applying a smoothing step, the FRC resolution can be calculated as the inverse of the radial frequency for which the curve drops below $1/7$ (i.e. the radial cut-off frequency), as suggested in [109].

Evaluating the cross-correlation of $\hat{I}_1(q,\phi)$ and $\hat{I}_2(q,\phi)$ along a circular path entails an insensitivity to pronounced directional variations in the spatial frequency content, as shown in Figure 6.1. This occurs especially for our images containing specific patterns of cell adhesions,

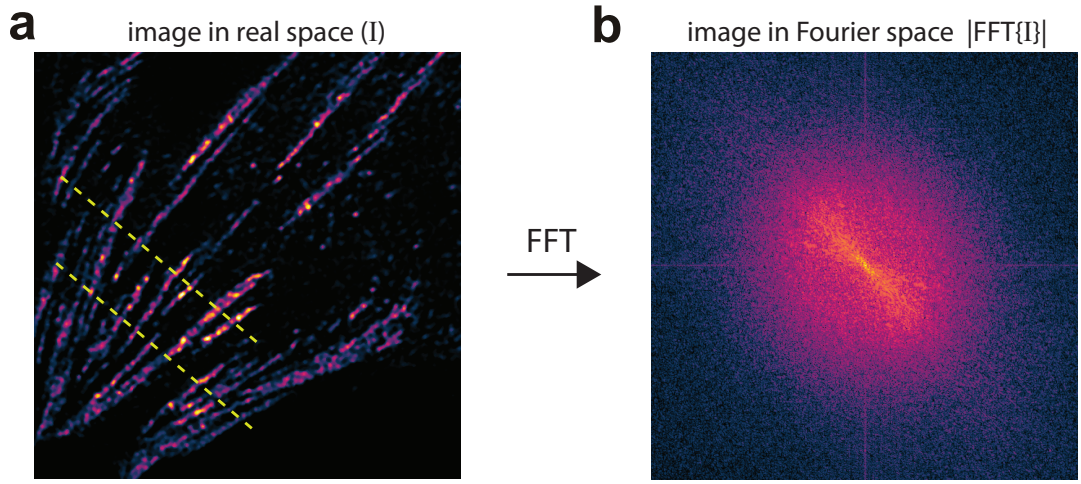

Figure 6.2: Anisotropic frequency content. (a) 4th order bSOFI image of a fixed MEF cell expressing paxillin labeled with psCFP2. The high spatial frequency changes of intensity appear mostly in one direction (marked by the yellow line). (b) Most of the high frequency content in Fourier space appears along the same direction. The color map "morgenstemning" was applied [54]. Published in Supplementary Deschout & Lukeš et al., Nature Comm., 2016 [48]

which have strongly directional imbalanced Fourier spectra (see Figure 6.1a). We therefore introduced the sFRC as a generalization of the FRC. As already suggested in [109], with this generalized metric, the correlation taken over a full circle is replaced by the correlation over a sector with an angular extend of $\Delta\phi$:

$$sFRC(q,\Delta\phi) = \frac{\sum_{\Delta\phi} \hat{I}_1(q,\phi)\hat{I}_2^*(q,\phi)}{\sqrt{\sum_{\Delta\phi}|\hat{I}_1(q,\phi)|^2 \sum_{\Delta\phi}|\hat{I}_2(q,\phi)|^2}} \tag{6.2}$$

This sFRC concept takes into account the major anisotropy of the image spectrum (see Figures 6.1, 6.2). Obviously, the classical FRC metric is easily recovered by calculating the sFRC for a sector with an angular extend of 2π. As a guideline, we suggest to evaluate the sFRC in 12 sectors with an angular extend of $\pi/12$, compromising between an improvement in sampling of the direction and a decrease in the amount of data.

The (s)FRC calculation requires the SMLM data to be split in two stochastically independent subsets, in order to render two stochastically independent SMLM images. First, the full image sequence that consists of N frames is split into K subsequences (containing N/K frames) with K an even number.

Next, K subsequences are split into two subsets of these K subsequences (as shown in Figure 6.3). Each of the two subsets is used to generate one super-resolved image for the (s)FRC calculation. The selection of subsequences into 2 subsets should be done carefully. In case of a

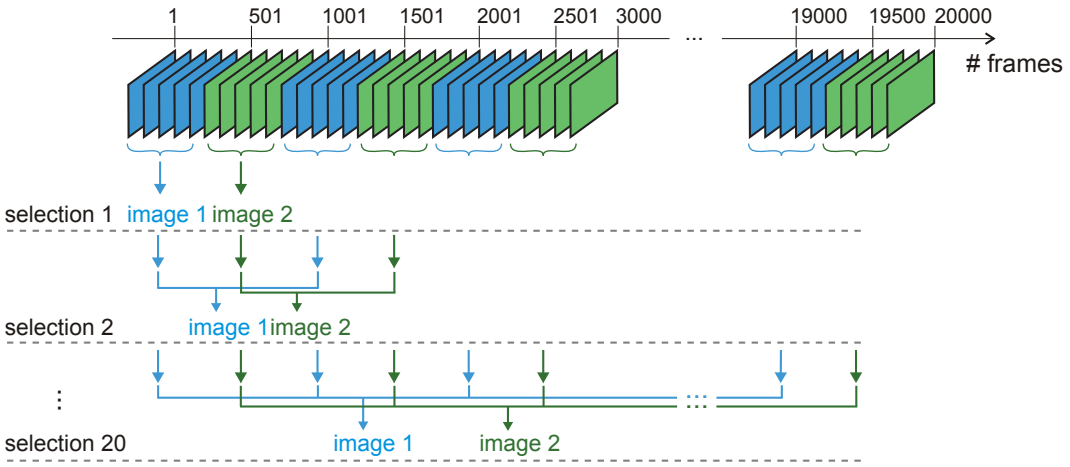

Figure 6.3: Details of the implementation of sFRC metric. Illustration of the frame selection procedure for the sFRC calculation.

random selection, the second subset may contain almost no SMLM data due to photobleaching. This problem can be largely avoided by selection of K subsequences in an alternating way, i.e. creating two subsets of odd and even image subsequences (Figure 6.3).

Although the FRC metric has been conceived for SMLM, we also applied the (s)FRC metric to SOFI images. In order to minimize the effect of photobleaching, a bleaching correction was applied to the input image sequence. The average fluorescence per frame was calculated and fitted by an exponential fit. Images of the input image sequence are then weighted by coefficients given as an inverse of the exponential fit [110]. SOFI processing takes into account temporal relations between consecutive frames, therefore a random division of the input image sequence into two subsets is not possible. We used the alternative approach described above. After splitting the full image sequence into K subsequences (Figure 6.3a), a SOFI image is calculated for each subsequence separately. After selecting a first set of $K/2$ subsequences, a SOFI image is obtained by summing the SOFI images corresponding to these subsequences. Applying the same procedure to the second $K/2$ subsequences yields two SOFI images for the (s)FRC calculation. As the SOFI analysis requires consecutive frames, subsequences with a sufficient number of frames should be chosen. We have chosen subsequences of 500 frames each.

When treated with care, the sFRC can provide a useful information about the sample quality. In our experience with various PALM and SOFI images, the estimated resolution is sometimes lower then theoretically expected. Our simulations also reveal that under tested conditions corresponding to focal adhesions, the (s)FRC values are slightly higher than expected. We attribute this to the fixed threshold used in the calculation of the (s)FRC metric, as suggested in [109]. Selecting an optimal threshold for a precise detection of the true cut-off frequency is very challenging. The closer you are to the true cut-off frequency the lower is the SNR of the curve. We would like to note that the sFRC by definition requires images with a rich

spatial frequency content. When, for instance, a sparse structure in the presence of mostly background is imaged, the sFRC value is unreliable, and this metric is useful for qualitative comparison only. In general sFRC in our experience seems to be rather an objective quality metric than an absolute measure of resolution.

6.1.2 Resolution analysis in SIM live-cell image sequences

Based on our experimental findings, the (s)FRC method is not well suited for measuring resolution of SIM live cell video sequences mainly due to the requirement of two independent observations of the same object and the fixed threshold for the cut-off frequency detection. We introduced a measure based on circular average power spectral density (PSDca) estimated from a single SIM image (one video frame). PSDca describes the distribution of the power of a signal with respect to its frequency. Spatial resolution corresponds to the cut-off frequency f_c in the Fourier domain. In order to estimate the cut-off frequency from a noisy signal, we used a spectral subtraction method for noise suppression.

To estimate image resolution, we evaluated the power spectral density in the reconstructed results. We also evaluated the signal to noise ratio in the reconstructed images with respect to exposure time, providing a quantitative evaluation of realistic imaging rates.

The power spectral density (PSD) describes the distribution of the power of a signal with respect to its frequency. The PSD of an image is the squared magnitude of its Fourier transform, and can be written as

$$PSD(k,l) = 10\log_{10}(|\mathscr{F}\{I(m,n)\}|^2), \tag{6.3}$$

where $\mathscr{F}$ represents the Fourier transform, $I(m,n)$ is the image intensity, and m,n indexes the rows and columns of the 2D image, respectively. In polar coordinates, the circularly averaged PSD (PSD_{ca}) in frequency space with frequency q and angle θ is given as

$$PSD_{ca} = \frac{1}{N_q}\sum_{\theta} I(q,\theta), \tag{6.4}$$

which averages PSD at spatial frequency q. N_q is the number of pixels at a particular frequency q. The resolution limit in real space corresponds to the cut-off frequency in Fourier space. Assuming a noiseless case, the cut-off frequency will be equal to the spatial frequency at which PSD_{ca} drops to zero. In practice, PSD_{ca} contains non-zero values over the whole frequency range caused by noise. The signal to noise ratio (SNR) in Fourier space is generally very low close to the cut-off frequency, which makes precise detection of the cut-off frequency challenging. In order to estimate the cut-off frequency from a noisy PSD_{ca} , we use a spectral subtraction method. Assuming additive noise, in the frequency domain we can write

$$\tilde{X}(k) = Y(k) - E[|N(k)|], \tag{6.5}$$

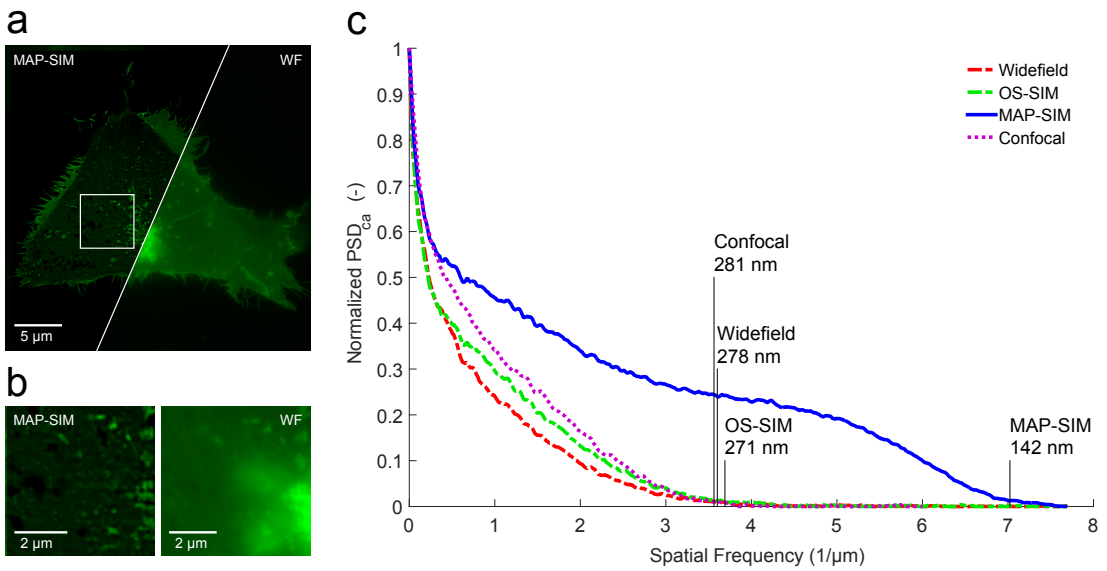

Figure 6.4: Resolution analysis and circular average power spectral density (PSD_{ca}) measured on a selected image (a) from the video sequence. (b) Region of interest of (a). The results indicate a lateral spatial resolution of 278 nm for WF, 271 nm for OS-SIM, and 142 nm for MAP-SIM (c).

where $Y(k)$, $\tilde{X}(k)$ and $E[|N(k)|]$ represent the noisy signal, the desired signal, and the noise spectrum estimate (expected noise spectrum), respectively. The amplitude noise spectrum $|N(k)|$ is estimated from the parts of signal where only noise is present. If the spatial sampling is high enough to fulfill the Nyquist–Shannon criterion and oversamples the resolution limit of SR-SIM, spatial frequencies close to the half of the sampling frequency do not contain useful signal and can be used for noise estimation. We varied the threshold in the range $(0.95 f_{max}–f_{max})$, estimated the level of noise for every threshold value, and obtained the mean and variance of the cut-off frequency (i.e. the resolution estimate). The f_{max} is given by

$$f_{max} = \frac{f_s}{2} = \frac{1}{2p_{xy}}, \tag{6.6}$$

where f_s, p_{xy} are the sampling frequency and the projected pixel size, respectively.

Figure 6.4c shows the PSD_{ca} and corresponding resolution limit measured in the data shown in Figure 6.4a. Using our resolution estimation algorithm, we calculated a lateral spatial resolution of 278 nm for WF, 271 nm for OS-SIM, and 142 nm for MAP-SIM. The measured resolution is in agreement with previously reported results measured on 100 nm fluorescent beads [37]. For comparison, we also imaged LAMP1-GFP cells using a spinning disk confocal microscope, where we measured a resolution of 281 nm.

Figure 6.5 demonstrates the effect of varying the exposure time of the raw data on PSD_{ca} and the effective spatial resolution. We varied the camera exposure time from 10 ms to 100 ms

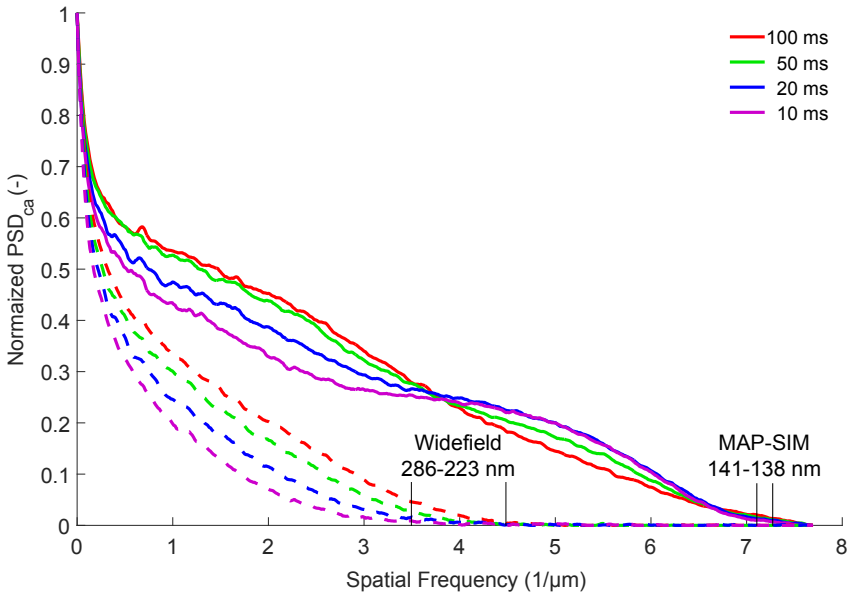

Figure 6.5: Normalized circular average power spectral density (PSDca) measured as a function of exposure time for WF and MAP-SIM.

per SIM sub-image. Low SNR (in this case due to a short exposure time) causes a loss of fine details and therefore a reduction in effective resolution as estimated by our Fourier domain method. These findings are not surprising, but the relationship between SNR (and therefore exposure time and realistic imaging rates) and image resolution is typically not discussed in the SIM literature. This effect can sometimes lead to very high noise and lower effective resolution when trying to push SIM imaging rates.

The lower exposure time data in Figure 6.5 reveals increasing values at the frequencies in the range 4 - 6.8 μ^{-1}. It is a consequence of the spectral merging in MAP-SIM algorithm. With shorter exposure, signal level generally decreases. Most of the signal (in terms of signal power and signal energy) is contained on zero and low spatial frequencies. According to Eq. (3.11), we merge $\mathscr{F}\{x_{\text{LR-HOM}}\}$ (low frequencies) and $\mathscr{F}\{x_{\text{HR-MAP}}\}$ (high frequencies). In this experiment, the weighting coefficient for spectral merging was kept constant ($\beta = 0.85$) in order to compare how the change in the exposure time (i.e. change in SNR) effects the PSD. Low frequency PSD of $x_{\text{LR-HOM}}$ decreases faster compared to high frequency PSD of $x_{\text{HR-MAP}}$. As a result, the high frequency part of the normalized PSD is increasing with shorter exposure time. Balance between low and high frequency part is changing with decreasing SNR. To compensate the effect, a weighting parameter β can be adjusted. In the future, we plan to extend the MAP-SIM algorithm by a procedure which automatically selects the optimal weighting coefficient β taking into account SNR.

6.2 Estimating noise and SNR

Imaging dynamics of cells trades spatial against temporal resolution with an impact on SNR. Therefore, measuring the SNR is important to ensure a sufficient image quality. Standard SNR estimation algorithms are not well suited for SMLM and SOFI images, because in SMLM the final image is rendered from a list of localizations and the SOFI image represents correlations of intensity. For SMLM and SOFI processing, a long sequence of raw images has to be acquired which can be used as an advantage for an SNR estimation based on a statistical approach known as jackknife resampling [46]. We have adopted this general approach and applied it to PALM and SOFI images as described below in section 6.2.1. The jackknife resampling achieves a pixel-wise SNR estimation, but the computational complexity is high and the approach is not applicable on SIM data. On the other hand, simpler and faster SNR estimation methods can be applied on SIM data. In section 6.2.2, we propose a simple algorithm for efficient SNR estimation in SIM video sequences.

6.2.1 Signal-to-noise ratio estimation using statistical resampling

The jackknife method generates N datasets of N-1 camera frames. Each dataset leaves out a single image from the whole sequence of acquired input images (camera frames), as shown in Figure 6.1. Each new dataset is used to generate a new SOFI image, yielding N new SOFI images. For each pixel value $I(x,y)$ of the original SOFI image, N new $I_n(x,y)$ values are generated. As shown in [46], the level of uncertainty associated to each pixel $I(x,y)$ can be quantified using the SNR per pixel, defined as

$$\mathrm{SNR}(x,y) = \frac{I(x,y)}{\sqrt{\mathrm{var}\{I(x,y)\}}} \tag{6.7}$$

The jackknife mean estimator is

$$\bar{I}(x,y) = < I_n(x,y) > \tag{6.8}$$

The jackknife variance estimator is

$$\mathrm{var}\{I(x,y)\} = (N-1) < (I_n(x,y) - \bar{I}(x,y))^2 > \tag{6.9}$$

SNR estimation on PALM data

Although originally introduced for SOFI, the SNR can also be determined for SMLM data, since SMLM images can be rendered in a pixelated fashion (e.g. as a 2D histogram). Moreover, the SMLM localization procedure does not need to be repeated N times. It might be sufficient to localize the molecules only once from the original dataset, and afterwards just rendering N SMLM images by removing the localizations that correspond to the frame that is "deleted".

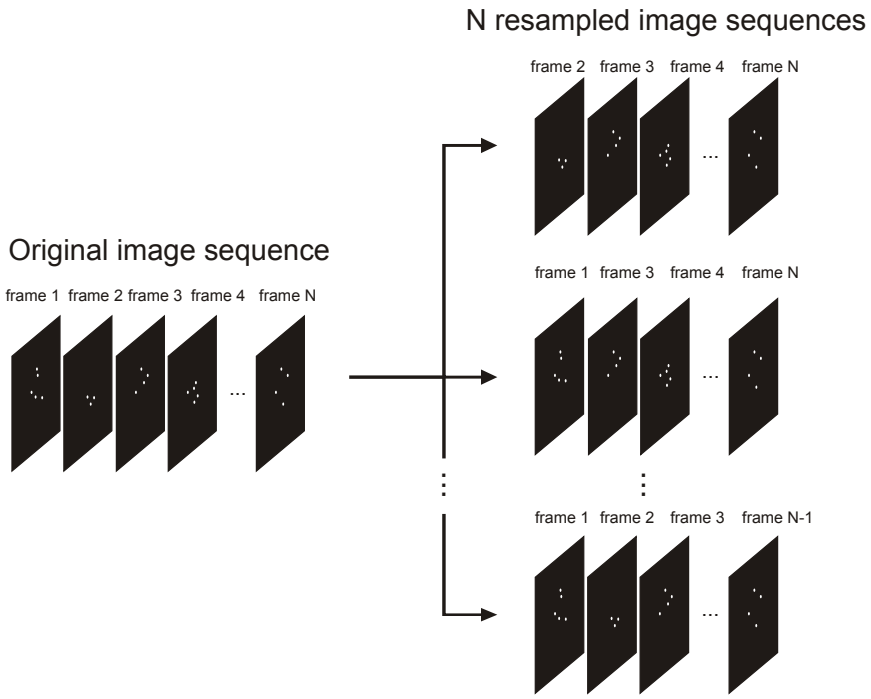

Figure 6.6: The jackknife resampling for SNR estimation generates N data sets of N-1 camera frames. Each resampled dataset is obtained by leaving out one camera frame from the original image sequence.

However, there is a caveat: the same emitter can appear during several consecutive frames. This means that deleting its localization when one of these frames is deleted, is not necessarily correct if one imposes an upper limit on the localization precision. The reason is that the localization precision could still be sufficiently small for the localization to be included, based on the contributions from the other frames that were not deleted. Conversely, new localizations can arise by deleting a frame if an upper limit on the localization precision is imposed (e.g. to exclude bright fiduciary markers). In this case, there is a chance that the localization precision becomes sufficiently large upon deleting one of the frames where it was visible. Both problems can be solved by re-estimating the localization precision after the deletion of one frame, as shown in Figure 6.7. This can be done by making two approximations: (1) the number of photons in each frame is constant, and (2) the localization precision is inversely related to the square root of the amount of photons. An emitter with localization precision σ that appeared in n frames therefore obtains a new localization precision after deleting one frame given by

$$\sigma_{\text{delete-1}} = \sigma\sqrt{n-1} \tag{6.10}$$

After re-calculating the localization precisions and applying the upper and lower limit on the localization precision, the N new SMLM images for the SNR calculation can be rendered. To calculate the variance in Eq. (6.7), a sufficient number of localizations have to be present

inside the pixel area. If not the case, for instance due to a too small pixel size or a too low localization density, the SNR value can become unreliable.

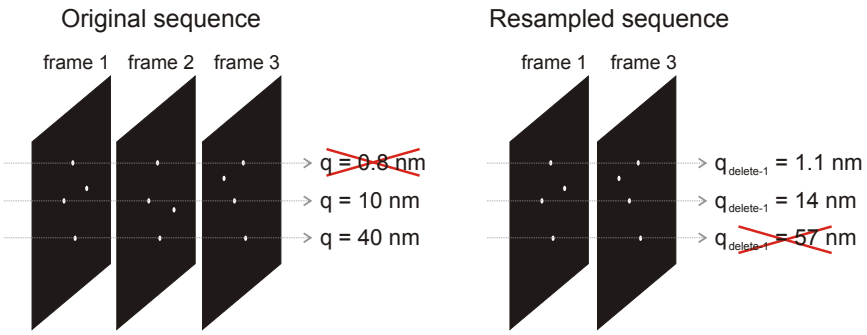

Figure 6.7: Illustration of the effect of leaving out one frame on the localization precision in the SNR estimation.

SNR estimation on SOFI data

When calculating SOFI for long image sequences, photobleaching cannot be neglected. The full image sequence is therefore divided into short subsequences during which the photobleaching effect is insignificant. In our case, each subsequence contained 500 frames. For decreasing the computational burden while evaluating the jackknife resampling, the SOFI image is first pre-calculated for each subsequence. The resampling is always performed within one subsequence, then the pre-calculated SOFI images from the remaining subsequences are added to generate a new resampled SOFI image, as shown in Figure 6.8. At the beginning, the algorithm takes the first subsequence (the first 500 frames) from a total number of K subsequences. The first frame from this subsequence is discarded. A SOFI image s_1 is calculated from the rest of the subsequence (i.e. the following 499 frames). The SOFI image s_1 is summed with the pre-calculated SOFI images from the remaining $K-1$ subsequences which yields a resampled SOFI image $I_1(x,y)$. In the next step, the second frame is discarded, leaving a different subset of 499 frames used to calculate a SOFI image s_2. Combining s_2 with the pre-calculated SOFI images from the remaining $K-1$ subsequences yields a resampled SOFI image $I_2(x,y)$. When the whole first subsequence is resampled, the procedure is repeated step by step for every subsequence to cover the full image sequence (i.e. 20,000 frames in our data).

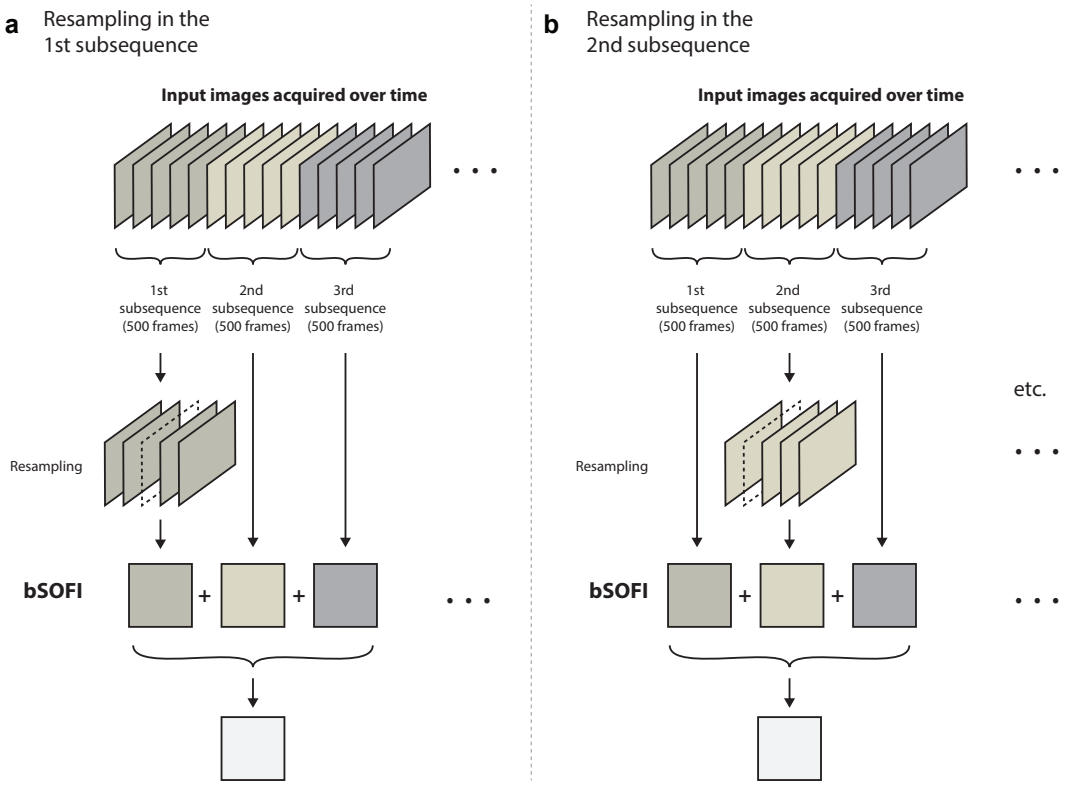

Figure 6.8: Estimating SNR using jackknife resampling. (a) The input image sequence is divided into subsequences. In the first step, the resampling is performed within the first subsequence. Each time one frame of the first subsequence is left out, the bSOFI image is calculated and summed up with the bSOFI images calculated from the remaining subsequences. (b) When all the resampling possibilities are evaluated in the first subsequence, the algorithm starts resampling the second subsequence. Published in Supplementary Deschout & Lukeš et al., Nature Comm., 2016 [48]

6.2.2 Analysis of signal to noise ratios (SNRs) in SIM live-cell image sequences

We evaluated the SNR performance of MAP-SIM using 2D image sequences of live U2-OS cells expressing LAMP1-GFP, acquired at a rate of 1 reconstructed frame per second (10 SIM sub-images with 100 ms exposure time for each). For an approximate comparison with a spinning disk confocal microscope, we acquired a similar image sequence of the same duration and exposure time (100 images, 100 ms exposure). The back-projected pixel size of the spinning disk confocal microscope was 83 nm (slightly larger compared to the SIM set-up, where the back-projected pixel size was 65 nm). The SNR in the live cell image sequence was measured frame by frame. We calculated SNR as

$$SNR = 10\log_{10}(\frac{P_{sn} - P_n}{P_s}) \tag{6.11}$$

according to [111], where P_{sn} is the power of the noise corrupted image and P_n is the power of the noise estimated by the algorithm described in [112]. We used a custom-made MATLAB script to automate the calculation. The results of the SNR measurements are shown in Figure 6.9 together with the results of a new implementation of MAP-SIM in which we have better controlled the scaling of the result images to avoid fluctuations in overall intensity. The new implementation normalizes $x_{\text{LR-HOM}}$ and $x_{\text{HR-MAP}}$ before the merging step (Eq. (3.11)) and then the result is denormalized according to $x_{\text{LR-HOM}}$. This procedure ensures proper average intensity level across the whole super-resolution image sequence. Compared to OS-SIM, the SNR enhancement realized in MAP-SIM is about 8 dB.

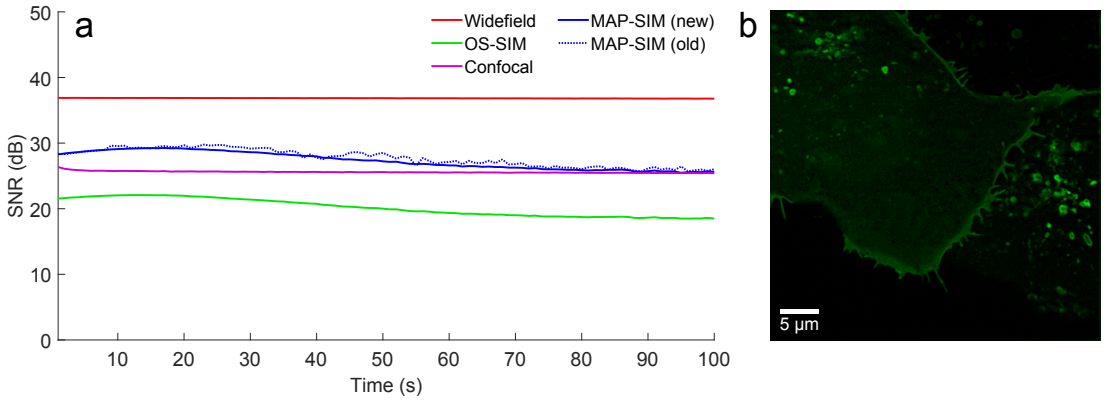

Figure 6.9: SNR measurements trough full length of a live cell image sequence of U2-OS cells expressing LAMP1-GFP. (b) Region of interest from the first frame of the MAP-SIM image sequence.

7 Conclusions and outlook

Images in certain kinds of super-resolution microscopy are the result of complex and highly demanding image processing efforts. The thesis is devoted to image processing and analysis for super-resolution fluorescence microscopy focusing on structured illumination microscopy (SIM) and super-resolution optical fluctuation imaging (SOFI). Both these methods represent relatively simple and inexpensive extensions of a widefield microscope where digital image reconstruction plays an essential role. The thesis substantially enhances the selected super-resolution methods towards super-resolution live cell quantitative imaging and presents applications of these methods for imaging dynamics of focal adhesions, investigation of protein distribution in the plasma membrane of T-cells, optical DNA mapping, and particle tracking in U2-OS cells.

In view of robust SIM image reconstruction and low phototoxicity live cell observations, we developed a new image reconstruction method for SIM based on maximum a posteriori probability estimation (MAP-SIM). The method is suitable for processing both optical sectioning and super-resolution 2D and 3D SIM data to create high quality super-resolution images. Imaging performance was demonstrated on a variety of fluorescent samples of different thickness, labeling density and noise levels. Our image reconstruction was successful even in the presence of high noise levels, where the SNR of the corresponding widefield images was about 5.9 dB. The microscope setup uses a relatively inexpensive microdisplay with no moving parts together with low cost LED illumination and is a simple add-on to conventional widefield fluorescence microscopes. The LED illumination and efficient image reconstruction even in the case of weak signals decreases the phototoxicity and facilitates longer live cell imaging. SIM results sometimes suffer from considerable artifacts related to the illumination pattern due to several factors including illumination pattern phase instability and pattern distortion, because of refractive index mismatch between the sample and the immersion fluid. MAP-SIM is based on a statistical image processing approach. Unlike SR-SIM algorithms, there is no need for precise shifts of the spectral components in Fourier domain. Therefore MAP-SIM is robust towards imperfections of illumination patterns at the sample plane. MAP-SIM processing could also prove useful for other illumination strategies such as TIRF-SIM or emerging

combinations of SIM and light sheet microscopy. Imaging live cells with SR-SIM for more than a few time points remains a challenge due to the requirement to acquire multiple illumination patterned images, and also due to inflexibility in acquisition protocols present in the currently available commercial instruments for SR-SIM. Using MAP-SIM, we demonstrated super-resolution imaging of live U2-OS cells expressing LAMP1-GFP in long image sequences with several hundred of super-resolution images. The LCOS microdisplay we used can switch the illumination patterns at rates approximately 875 Hz. However, such rapid imaging is not useful if the reconstructed SIM images exhibit low SNR limiting the resolution of the structure under study. Specifying the fastest possible acquisition rate is inadequate without consideration of SNR of the results. Therefore, we presented a new resolution measurement and SNR analysis for SIM live cell image sequences to help make realistic conclusions about imaging speeds. We showed that live cell MAP-SIM can enhance common cell biological applications such as the single particle tracking. The optical sectioning ability of MAP-SIM revealed a class of faster moving vesicles which could not be successfully tracked in WF data. Currently, we are further investigating live cell imaging capabilities of MAP-SIM with our unique automatic calibration procedure well suited for SIM systems equipped with a spatial light modulator (SLM) for pattern formation.

Aiming for super-resolution 3D live cell imaging and quantitative imaging of cellular structures, our efforts are driven towards a reduction of the acquisition time and extraction of molecular parameters. We developed and experimentally verified an adapted 3D deconvolution algorithm for SOFI, which allows one to suppress noise and improves signal to noise ratio. Therefore, fewer input images are required for SOFI reconstruction speeding up the overall acquisition. Using our multiplane SOFI setup and multidimensional image processing framework, we are currently able to obtain and process 3D image sequences where the overall acquisition time for one super-resolved frame is less than a second. The resulting four-dimensional data of super-resolved 3D cell structures moving in time represents a good starting point for analysis of cell movement and morphology. We introduced a novel linearization procedure for SOFI which allows one to fully exploit the available dynamic range and maximize the resolution improvement. We have achieved 6th order SOFI images and spatial resolution comparable to PALM. We have shown that SOFI can be applied on PALM data with no extra cost. Performing an extensive analysis on simulations and fixed-cell focal adhesion images, we investigated the complementarity between PALM and SOFI in terms of spatial-temporal resolution. The complementarity of PALM and SOFI was assessed in detail with a novel methodology that integrates a resolution and signal-to-noise ratio metric. Applying both SOFI and PALM on the same dataset reveal more information about the true underlying structure of the sample. Using a combined PALM-SOFI framework, we imaged focal adhesions in living cells, while obtaining a temporal resolution below 10s. We visualized the dynamics of focal adhesions, and revealed local mean velocities around 190 nm/min. This PALM and SOFI concept provides an enlarged quantitative imaging framework, allowing unprecedented functional exploration of focal adhesions through the estimation of molecular parameters such as fluorophore densities and photoactivation or photoswitching kinetics.

Cell adhesion and its dynamics have been assessed for the first time with SOFI. We presented a novel method for quantitative evaluation of clustering behaviour of proteins based on SOFI molecular density estimation. Using this method, we investigated the nanoscale organization of CD4 fluorescent-protein fusion variants on the surface of resting T cells. We have shown that SOFI can also prove useful for fast optical readout of fluorescently labelled DNA. We are currently working on new DNA matching strategies using SOFI images.

The quality of super-resolved images needs to be quantified and measured in order to objectively optimize imaging conditions and distinguish newly resolved sample features from image artifacts. Automated objective image quality assessment based on image characteristics, i.e. spatial resolution, contrast and signal to noise ratio, is crucial for quantifying the outcome of super-resolution microscopy. Our methodology for assessing the image quality integrates an objective evaluation of the resolution and the SNR for super-resolved images. We presented a novel framework for resolution and SNR assessment in real samples. We have presented a new algorithm well suited for resolution estimation in live cell SIM image sequences.

In view of making the super-resolution imaging accessible to a wider audience and facilitate implementation of super-resolution methods in other research labs, we developed open-source software tools in MATLAB. We published the first open-source software for SIM called SIMToolbox. This comprehensive MATLAB toolbox incorporates several SIM algorithms designed for processing two-dimensional and three-dimensional SIM data including wide range of options unavailable in current commercial software. We also published a simulation software package for SOFI. The SOFI software package allows one to test numerous acquisition settings prior to time consuming sample preparation and experimental imaging. The user can quickly investigate the influence of the sample detection and imaging parameters on the final super-resolution image quality. Due to a simple user interface and tutorials which explain the underlying image analysis, the simulation tool makes the SOFI method easily accessible to a wide audience interested in super-resolution microscopy. To our knowledge, the software for simulating SOFI has never been demonstrated before and we believe that this tool will help to implement SOFI.

Super-resolution methods promise to obtain more insights about biological samples, but at the expense of higher complexity and more demands on the user and sample preparation. Super-resolution methods have to be treated with a great care in order to ensure high performance and image quality and to avoid unwanted image artifacts. It seems that none of the recent super-resolution methods is generally superior above others. Advantages of each method depends on the biological application in question. Complementarity of some of these methods naturally motivates new attempts to combine them. Correlating information from multiple methods can provide more insights about the biological sample. In the future, combinations of various super-resolution methods with each other and with different microscopy modalities can be expected like SOFI-SIM, SIM-AFM (Atomic force microscopy) or SIM-OPT (Optical projection tomography). Super-resolution microscopy in general trades temporal resolution for spatial resolution making observation of fast cell processes difficult. The SOFI multiplane

set-up allows to acquire 8 image planes at one time point. These data are compatible with transport of intensity theory which allows one to reconstruct phase images from observations of intensity in two or more planes. In our research lab at EPFL, we are currently developing a system where multidimensional SOFI imaging is accompanied by fast quantitative phase imaging in one set-up. The SOFI image provides high spatial resolution whereas the phase image complement the information with high temporal resolution.

In summary, the thesis provides a novel SIM framework which facilitates live cell imaging under low light conditions robust to reconstruction artifacts and presents, to our knowledge, the first demonstration of cell particle tracking improved by SIM. The novel SOFI framework introduced in this work allows fast multidimensional imaging of live cells, molecular parameter estimation and quantitative cell imaging which was successfully demonstrated by high throughput 3D imaging of live HeLa cells, by investigating focal adhesions in live MEF cells and by unraveling the nanoscale organization of CD4 proteins in the plasma membrane of T-cells. Within the thesis, two separate open-source software packages were developed to facilitate implementation of super-resolution microscopy methods.

Bibliography

[1] B. Huang, M. Bates, and X. Zhuang, "Super resolution fluorescence microscopy," *Annual review of biochemistry*, pp. 993–1016, 2009.

[2] S. Inoue and K. R. Spring, *Video Microscopy: The Fundamentals*. New York: Plenum Press, 2nd ed., 1997.

[3] S. W. Hell and J. Wichmann, "Breaking the diffraction resolution limit by stimulated emission: stimulated-emission-depletion fluorescence microscopy.," *Optics letters*, vol. 19, pp. 780–782, June 1994.

[4] E. Betzig, G. H. Patterson, R. Sougrat, O. W. Lindwasser, S. Olenych, J. S. Bonifacino, M. W. Davidson, J. Lippincott-Schwartz, and H. F. Hess, "Imaging intracellular fluorescent proteins at nanometer resolution.," *Science (New York, N.Y.)*, vol. 313, pp. 1642–5, Sept. 2006.

[5] S. Hess Girirajan T, Mason M, "Ultra-High Resoluion Imaging by Fluorescence Photoactivation Localization Microscopy," *Biophys. J.*, vol. 91, no. 11, pp. 4258–4272, 2006.

[6] M. J. Rust, M. Bates, and X. Zhuang, "Sub-diffraction-limit imaging by stochastic optical reconstruction microscopy (STORM).," *Nature methods*, vol. 3, no. 10, pp. 793–795, 2006.

[7] T. Dertinger, R. Colyer, G. Iyer, S. Weiss, and J. Enderlein, "Fast, background-free, 3D super-resolution optical fluctuation imaging (SOFI).," *Proceedings of the National Academy of Sciences of the United States of America*, vol. 106, no. 52, pp. 22287–92, 2009.

[8] M. G. Gustafsson, "Surpassing the lateral resolution limit by a factor of two using structured illumination microscopy.," *Journal of microscopy*, vol. 198, pp. 82–87, 2000.

[9] M. G. L. Gustafsson, "Nonlinear structured-illumination microscopy: wide-field fluorescence imaging with theoretically unlimited resolution," *Proceedings of the National Academy of Sciences of the United States of America*, vol. 102, pp. 13081–6, Sept. 2005.

[10] R. Heintzmann and C. Cremer, "Laterally Modulated Excitation Microscopy: Improvement of resolution by using a diffraction grating," *Proceedings of SPIE*, vol. 3568, pp. 185–196, 1999.

[11] E. Betzig, G. H. Patterson, R. Sougrat, O. W. Lindwasser, S. Olenych, J. S. Bonifacino, M. W. Davidson, J. Lippincott-Schwartz, and H. F. Hess, "Imaging intracellular fluorescent proteins at nanometer resolution.," *Science (New York, N.Y.)*, vol. 313, pp. 1642–5, 2006.

[12] S. T. Hess, T. P. Girirajan, and M. D. Mason, "Ultra-High Resolution Imaging by Fluorescence Photoactivation Localization Microscopy," *Biophysical Journal*, vol. 91, no. 11, pp. 4258–4272, 2006.

[13] C. J. R. Sheppard, "Super-resolution in Confocal Imaging," *Optik*, vol. 80, no. 2, pp. 53–54, 1988.

[14] C. B. Müller and J. Enderlein, "Image scanning microscopy," *Physical Review Letters*, vol. 104, 2010.

[15] A. G. York, S. H. Parekh, D. D. Nogare, R. S. Fischer, K. Temprine, M. Mione, A. B. Chitnis, C. A. Combs, and H. Shroff, "Resolution doubling in live, multicellular organisms via multifocal structured illumination microscopy," *Nature Methods*, vol. 9, pp. 749–754, 2012.

[16] A. G. York, P. Chandris, D. D. Nogare, J. Head, P. Wawrzusin, R. S. Fischer, A. Chitnis, and H. Shroff, "Instant super-resolution imaging in live cells and embryos via analog image processing.," *Nature methods*, vol. 10, pp. 1122–6, Nov. 2013.

[17] M. G. L. Gustafsson, L. Shao, P. M. Carlton, C. J. R. Wang, I. N. Golubovskaya, W. Z. Cande, D. A. Agard, and J. W. Sedat, "Three-dimensional resolution doubling in widefield fluorescence microscopy by structured illumination," *Biophysical Journal*, vol. 94, no. 12, pp. 4957–4970, 2008.

[18] S. Geissbuehler, C. Dellagiacoma, and T. Lasser, "Comparison between SOFI and STORM.," *Biomedical optics express*, vol. 2, pp. 408–420, Jan. 2011.

[19] S. Geissbuehler, A. Sharipov, A. Godinat, N. L. Bocchio, P. a. Sandoz, A. Huss, N. a. Jensen, S. Jakobs, J. Enderlein, F. Gisou van der Goot, E. a. Dubikovskaya, T. Lasser, and M. Leutenegger, "Live-cell multiplane three-dimensional super-resolution optical fluctuation imaging," *Nature Communications*, vol. 5, Dec. 2014.

[20] T. Lukeš, G. M. Hagen, P. Křížek, Z. Švindrych, K. Fliegel, and M. Klíma, "Comparison of image reconstruction methods for structured illumination microscopy," *Proc. SPIE 9129, Biophotonics: Photonic Solutions for Better Health Care IV, 91293J*, vol. 9129, pp. 1–13, 2014.

[21] P. Kner, B. B. Chhun, E. R. Griffis, L. Winoto, and M. G. L. Gustafsson, "Super-resolution video microscopy of live cells by structured illumination.," *Nature methods*, vol. 6, no. 5, pp. 339–342, 2009.

[22] L. M. Hirvonen, K. Wicker, O. Mandula, and R. Heintzmann, "Structured illumination microscopy of a living cell," *European Biophysics Journal*, vol. 38, pp. 807–812, 2009.

[23] G. M. Shao L, Kner P, Rego EH, "Super-resolution 3D microscopy of live whole cells using structured illumination.," *Nature methods*, vol. 8, pp. 1044–6, 2011.

[24] M. A. Neil, R. Juskaitis, and T. Wilson, "Method of obtaining optical sectioning by using structured light in a conventional microscope.," *Optics letters*, vol. 22, no. 24, pp. 1905–1907, 1997.

[25] K. O'Holleran and M. Shaw, "Optimized approaches for optical sectioning and resolution enhancement in 2D structured illumination microscopy," *Biomedical Optics Express*, vol. 5, p. 2580, July 2014.

[26] E. Mudry, K. Belkebir, J. Girard, J. Savatier, E. L. Moal, C. Nicoletti, M. Allain, and A. Sentenac, "Structured illumination microscopy using unknown speckle patterns," *Nature Photonics*, vol. 6, no. April, pp. 312–315, 2012.

[27] F. Orieux, E. Sepulveda, V. Loriette, B. Dubertret, and J. C. Olivo-Marin, "Bayesian estimation for optimized structured illumination microscopy," *IEEE Transactions on Image Processing*, vol. 21, pp. 601–614, Feb. 2012.

[28] R. Heintzmann, "High-resolution image reconstruction in fluorescence microscopy with patterned excitation," *Appl. Opt.*, vol. 45, no. 20, pp. 5037–5045, 2006.

[29] P. Křížek, I. Raška, and G. M. Hagen, "Flexible structured illumination microscope with a programmable illumination array," *Optics Express*, vol. 20, no. 22, p. 24585, 2012.

[30] F. Chasles, B. Dubertret, and A. C. Boccara, "Optimization and characterization of a structured illumination microscope.," *Optics express*, vol. 15, no. 24, pp. 16130–16140, 2007.

[31] R. Heintzmann, "Structured illumination methods," in *Handbook of Biological Confocal Microscopy* (J. B. Pawley, ed.), pp. 265–279, New York: Springer, 3rd ed., 2006.

[32] M. G. L. Gustafsson, D. A. Agard, and J. W. Sedat, "Doubling the lateral resolution of wide-field fluorescence microscopy using structured illumination," *Proceedings of SPIE*, vol. 3919, pp. 141–150, 2000.

[33] P. J. Verveer, M. J. Gemkow, and T. M. Jovin, "A comparison of image restoration approaches applied to three-dimensional confocal and wide-field fluorescence microscopy," *Journal of microscopy*, vol. 193, no. January, pp. 50–61, 1999.

[34] P. Sarder and a. Nehorai, "Deconvolution methods for 3-D fluorescence microscopy images," *IEEE Signal Processing Magazine*, vol. 23, pp. 32–45, May 2006.

[35] R. Heintzmann, "Estimating missing information by maximum likelihood deconvolution.," *Micron (Oxford, England : 1993)*, vol. 38, pp. 136–44, Jan. 2007.

[36] B. J. Vermolen, Y. Garini, and I. T. Young, "3D restoration with multiple images acquired by a modified conventional microscope," *Microscopy Research and Technique*, vol. 64, pp. 113–125, 2004.

[37] T. Lukeš, P. Křížek, Z. Švindrych, J. Benda, M. Ovesný, K. Fliegel, M. Klíma, and G. M. Hagen, "Three-dimensional super-resolution structured illumination microscopy with maximum a posteriori probability image estimation," *Optics Express*, vol. 22, p. 29805, Nov. 2014.

[38] V. Leonov and A. Shiryaev, "On a method of calculation of semi-invariants," *Theory Probability App*, vol. 4, no. 3, pp. 319–329, 1959.

[39] T. Dertinger, M. Heilemann, R. Vogel, M. Sauer, and S. Weiss, "Superresolution Optical Fluctuation Imaging with Organic Dyes," *Angewandte Chemie*, vol. 122, pp. 9631–9633, 2010.

[40] P. Dedecker, G. C. H. Mo, T. Dertinger, and J. Zhang, "Widely accessible method for superresolution fluorescence imaging of living systems," *Proceedings of the National Academy of Sciences*, vol. 109, no. 27, pp. 10909–10914, 2012.

[41] M. E. Gallina, J. Xu, T. Dertinger, A. Aizer, Y. Shav-Tal, and S. Weiss, "Resolving the spatial relationship between intracellular components by dual color super resolution optical fluctuations imaging (SOFI).," *Optical nanoscopy*, vol. 2, pp. 1–9, 2013.

[42] S. Geissbuehler, N. L. Bocchio, C. Dellagiacoma, C. Berclaz, M. Leutenegger, and T. Lasser, "Mapping molecular statistics with balanced super-resolution optical fluctuation imaging (bSOFI)," *Optical Nanoscopy*, vol. 1, no. 1, 2012.

[43] A. Girsault, T. Lukes, A. Sharipov, S. Geissbuehler, M. Leutenegger, W. Vandenberg, P. Dedecker, J. Hofkens, and T. Lasser, "SOFI Simulation Tool: A Software Package for Simulating and Testing Super-Resolution Optical Fluctuation Imaging," *PLOS ONE*, vol. 11, p. e0161602, 2016.

[44] T. Dertinger, R. Colyer, R. Vogel, J. Enderlein, and S. Weiss, "Achieving increased resolution and more pixels with Superresolution Optical Fluctuation Imaging (SOFI).," *Optics express*, vol. 18, pp. 18875–85, Aug. 2010.

[45] S. C. Stein, A. Huss, D. Hähnel, I. Gregor, and J. Enderlein, "Fourier interpolation stochastic optical fluctuation imaging.," *Optics express*, vol. 23, pp. 16154–63, 2015.

[46] W. Vandenberg, S. Duwé, M. Leutenegger, B. Krajnik, T. Lasser, and P. Dedecker, "Model-free uncertainty estimation in Stochastical Optical Fluctuation Imaging (SOFI) leads to a doubled temporal resolution," vol. 2402, pp. 1347–1355, 2015.

[47] J. M. Mendel, "Tutorial on Higher-Order Statistics (Spectra) in Signal Processing and System Theory: Theoretical Results and Some Applications," *Proceedings of the IEEE*, vol. 79, pp. 278–305, 1991.

[48] H. Deschout, T. Lukes, A. Sharipov, D. Szlag, L. Feletti, W. Vandenberg, P. Dedecker, J. Hofkens, M. Leutenegger, T. Lasser, and A. Radenovic, "Complementarity of PALM and SOFI for super-resolution live-cell imaging of focal adhesions," *Nature Communications*, vol. 7, p. 13693, 2016.

[49] N. Durisic, L. Laparra-Cuervo, A. Sandoval-Álvarez, J. S. Borbely, and M. Lakadamyali, "Single-molecule evaluation of fluorescent protein photoactivation efficiency using an in vivo nanotemplate.," *Nature methods*, vol. 11, pp. 156–62, 2014.

[50] G. M. P. van Kempen, L. J. van Vliet, P. J. Verveer, and H. T. M. van der Voort, "A quantitative comparison of image restoration methods for confocal microscopy," *Journal of Microscopy-Oxford*, vol. 185, pp. 354–365, Mar. 1997.

[51] P. J. Verveer and T. M. Jovin, "Efficient superresolution restoration algorithms using maximum a posteriori estimations with application to fluorescence microscopy," 1997.

[52] P. Milanfar, *Super-Resolution Imaging*. CRC Press, 2011.

[53] S. Chaudhuri, *Super-resolution imaging*. New York: Kluwer Academic Publishers, 2000.

[54] M. Geissbuehler and T. Lasser, "How to display data by color schemes compatible with red-green color perception deficiencies.," *Optics express*, vol. 21, no. 8, pp. 9862–74, 2013.

[55] P. Křížek, T. Lukeš, M. Ovesný, K. Fliegel, and G. M. Hagen, "SIMToolbox: a MATLAB toolbox for structured illumination fluorescence microscopy," *Bioinformatics*, vol. 15, p. btv576, 2015.

[56] T. Lukes, "SIMToolbox Project Website http://mmtg.fel.cvut.cz/simtoolbox/," 2016.

[57] L. Schermelleh, P. M. Carlton, S. Haase, L. Shao, L. Winoto, P. Kner, B. Burke, M. C. Cardoso, D. A. Agard, M. G. L. Gustafsson, H. Leonhardt, and J. W. Sedat, "Subdiffraction multicolor imaging of the nuclear periphery with 3D structured illumination microscopy," *Science*, vol. 320, pp. 1332–1336, 2008.

[58] R. Fiolka, L. Shao, E. H. Rego, M. W. Davidson, and M. G. L. Gustafsson, "Time-lapse two-color 3D imaging of live cells with doubled resolution using structured illumination.," *Proceedings of the National Academy of Sciences of the United States of America*, vol. 109, pp. 5311–5, 2012.

[59] T. A. Planchon, L. Gao, D. E. Milkie, M. W. Davidson, J. a. Galbraith, C. G. Galbraith, and E. Betzig, "Rapid three-dimensional isotropic imaging of living cells using Bessel beam plane illumination.," *Nature methods*, vol. 8, no. 5, pp. 417–423, 2011.

[60] P. J. Keller, A. D. Schmidt, A. Santella, K. Khairy, Z. Bao, J. Wittbrodt, and E. H. K. Stelzer, "Fast, high-contrast imaging of animal development with scanned light sheet-based structured-illumination microscopy.," *Nature methods*, vol. 7, no. 8, pp. 637–642, 2010.

[61] L. Gao, L. Shao, C. D. Higgins, J. S. Poulton, M. Peifer, M. W. Davidson, X. Wu, B. Goldstein, and E. Betzig, "Noninvasive imaging beyond the diffraction limit of 3D dynamics in thickly fluorescent specimens," *Cell*, vol. 151, pp. 1370–1385, Dec. 2012.

[62] B.-C. Chen, W. R. Legant, K. Wang, L. Shao, D. E. Milkie, M. W. Davidson, C. Janetopoulos, X. S. Wu, J. A. Hammer, Z. Liu, B. P. English, Y. Mimori-Kiyosue, D. P. Romero, A. T. Ritter, J. Lippincott-Schwartz, L. Fritz-Laylin, R. D. Mullins, D. M. Mitchell, J. N. Bembenek, A.-C. Reymann, R. Bohme, S. W. Grill, J. T. Wang, G. Seydoux, U. S. Tulu, D. P. Kiehart, and E. Betzig, "Lattice light-sheet microscopy: Imaging molecules to embryos at high spatiotemporal resolution," *Science*, vol. 346, pp. 1257998–1257998, Oct. 2014.

[63] D. Li, L. Shao, B.-C. Chen, X. Zhang, M. Zhang, B. Moses, D. E. Milkie, J. R. Beach, J. A. Hammer, M. Pasham, T. Kirchhausen, M. A. Baird, M. W. Davidson, P. Xu, and E. Betzig, "Extended-resolution structured illumination imaging of endocytic and cytoskeletal dynamics.," *Science (New York, N.Y.)*, vol. 349, p. aab3500, 2015.

[64] L. B. Lucy, "An iterative technique for the rectification of observed distributions," *The Astronomical Journal*, vol. 79, p. 745, June 1974.

[65] W. H. RICHARDSON, "Bayesian-Based Iterative Method of Image Restoration," *Journal of the Optical Society of America*, vol. 62, p. 55, Jan. 1972.

[66] C. Vonesch and M. Unser, "A fast multilevel algorithm for wavelet-regularized image restoration.," *IEEE transactions on image processing : a publication of the IEEE Signal Processing Society*, vol. 18, pp. 509–23, Mar. 2009.

[67] M. V. Afonso, J. M. Bioucas-Dias, and M. a. T. Figueiredo, "Fast image recovery using variable splitting and constrained optimization.," *IEEE transactions on image processing : a publication of the IEEE Signal Processing Society*, vol. 19, pp. 2345–56, Sept. 2010.

[68] S. Osher, M. Burger, D. Goldfarb, J. Xu, and W. Yin, "An Iterative Regularization Method for Total Variation-Based Image Restoration," *Multiscale Modeling & Simulation*, vol. 4, pp. 460–489, Jan. 2005.

[69] T. Goldstein and S. Osher, "The Split Bregman Method for L1-Regularized Problems," *SIAM Journal on Imaging Sciences*, vol. 2, pp. 323–343, Jan. 2009.

[70] L. Rudin, S. Osher, and E. Fatemi, "Nonlinear total variation based noise removal algorithms," *Physica D: Nonlinear Phenomena*, vol. 60, pp. 259–268, 1992.

[71] S. H. Chan, R. Khoshabeh, K. B. Gibson, P. E. Gill, and T. Q. Nguyen, "An augmented Lagrangian method for total variation video restoration.," *IEEE transactions on image processing : a publication of the IEEE Signal Processing Society*, vol. 20, pp. 3097–111, Nov. 2011.

[72] F. Sroubek and P. Milanfar, "Robust multichannel blind deconvolution via fast alternating minimization.," *IEEE transactions on image processing : a publication of the IEEE Signal Processing Society*, vol. 21, pp. 1687–700, Apr. 2012.

[73] X. Liu and L. Huang, "Split Bregman iteration algorithm for total bounded variation regularization based image deblurring," *Journal of Mathematical Analysis and Applications*, vol. 372, pp. 486–495, Dec. 2010.

[74] T. Lukes, "SOFI Simulation Tool Project Website http://lob.epfl.ch/sofitool," 2016.

[75] G. T. Dempsey, J. C. Vaughan, K. H. Chen, M. Bates, and X. Zhuang, "Evaluation of fluorophores for optimal performance in localization-based super-resolution imaging," *Nature Methods*, vol. 8, pp. 1027–1036, 2011.

[76] B. Geiger, J. P. Spatz, and A. D. Bershadsky, "Environmental sensing through focal adhesions.," *Nature reviews. Molecular cell biology*, vol. 10, pp. 21–33, 2009.

[77] R. Zaidel-Bar, S. Itzkovitz, A. Ma'ayan, R. Iyengar, and B. Geiger, "Functional atlas of the integrin adhesome," *Nature Cell Biology*, vol. 9, pp. 858–867, 2007.

[78] C. M. Franz and D. J. Müller, "Analyzing focal adhesion structure by atomic force microscopy.," *Journal of cell science*, vol. 118, pp. 5315–5323, 2005.

[79] L. B. Smilenov, A. Mikhailov, R. J. Pelham, E. E. Marcantonio, and G. G. Gundersen, "Focal Adhesion Motility Revealed in Stationary Fibroblasts," *Science*, vol. 286, pp. 1172–1174, 1999.

[80] H. Shroff, C. G. Galbraith, J. A. Galbraith, and E. Betzig, "Live-cell photoactivated localization microscopy of nanoscale adhesion dynamics," *Nature methods*, vol. 5, pp. 417–423, 2008.

[81] O. Rossier, V. Octeau, J.-B. Sibarita, C. Leduc, B. Tessier, D. Nair, V. Gatterdam, O. Destaing, C. Albigès-Rizo, R. Tampé, L. Cognet, D. Choquet, B. Lounis, and G. Giannone, "Integrins β1 and β3 exhibit distinct dynamic nanoscale organizations inside focal adhesions," *Nature Cell Biology*, vol. 14, pp. 1057–1067, 2012.

[82] S. J. Stehbens, M. Paszek, H. Pemble, A. Ettinger, S. Gierke, and T. Wittmann, "CLASPs link focal-adhesion-associated microtubule capture to localized exocytosis and adhesion site turnover.," *Nature cell biology*, vol. 16, pp. 558–570, 2014.

[83] P. Annibale, S. Vanni, M. Scarselli, U. Rothlisberger, and A. Radenovic, "Quantitative Photo Activated Localization Microscopy: Unraveling the effects of photoblinking," *PLoS ONE*, vol. 6, 2011.

[84] S.-H. Lee, J. Y. Shin, A. Lee, and C. Bustamante, "Counting single photoactivatable fluorescent molecules by photoactivated localization microscopy (PALM).," *Proceedings of the National Academy of Sciences of the United States of America*, vol. 109, pp. 17436–41, 2012.

[85] M. Ovesný, P. Křížek, J. Borkovec, Z. Švindrych, and G. M. Hagen, "ThunderSTORM: A comprehensive ImageJ plug-in for PALM and STORM data analysis and super-resolution imaging," *Bioinformatics*, vol. 30, pp. 2389–2390, 2014.

[86] S. Wolter, A. Löschberger, T. Holm, S. Aufmkolk, M.-C. Dabauvalle, S. van de Linde, and M. Sauer, "rapidSTORM: accurate, fast open-source software for localization microscopy.," *Nature methods*, vol. 9, pp. 1040–1, 2012.

[87] R. Henriques, M. Lelek, E. F. Fornasiero, F. Valtorta, C. Zimmer, and M. M. Mhlanga, "QuickPALM: 3D real-time photoactivation nanoscopy image processing in ImageJ.," *Nature methods*, vol. 7, pp. 339–340, 2010.

[88] D. Sage, H. Kirshner, T. Pengo, N. Stuurman, J. Min, S. Manley, and M. Unser, "Quantitative evaluation of software packages for single-molecule localization microscopy.," *Nature Methods*, vol. 12, pp. 1–12, 2015.

[89] P. Sengupta, T. Jovanovic-Talisman, D. Skoko, M. Renz, S. L. Veatch, and J. Lippincott-Schwartz, "Probing protein heterogeneity in the plasma membrane using PALM and pair correlation analysis," *Nature methods*, vol. 8, pp. 969–975, 2011.

[90] S. L. Veatch, B. B. Machta, S. A. Shelby, E. N. Chiang, D. A. Holowka, and B. A. Baird, "Correlation functions quantify super-resolution images and estimate apparent clustering due to over-counting," *PLoS ONE*, vol. 7, 2012.

[91] D. M. Owen, C. Rentero, J. Rossy, A. Magenau, D. Williamson, M. Rodriguez, and K. Gaus, "PALM imaging and cluster analysis of protein heterogeneity at the cell surface," *Journal of Biophotonics*, vol. 3, pp. 446–454, 2010.

[92] X. A. Ester, M., Kriegel, H.-P., Sander, J., Xu, "A density-based algorithm for discovering clusters in large spatial databases with noise," *KDD*, vol. 96, pp. 226–231, 1996.

[93] M. Ankerst, M. Breunig, H. Kriegel, and J. Sander, "OPTICS: Ordering Points To Identify the Clustering Structure," *ACM SIGMOD international conference on Management of data*, vol. 28, no. 2, pp. 49–60, 1999.

[94] F. Levet, E. Hosy, A. Kechkar, C. Butler, A. Beghin, D. Choquet, and J.-B. Sibarita, "SR-Tesseler: a method to segment and quantify localization-based super-resolution microscopy data.," *Nature methods*, vol. 12, pp. 1065–71, 2015.

[95] P. Rubin-Delanchy, G. L. Burn, J. Griffié, D. J. Williamson, N. A. Heard, A. P. Cope, and D. M. Owen, "Bayesian cluster identification in single-molecule localization microscopy data," *Nature Methods*, vol. 12, pp. 1072–1076, 2015.

[96] P. Annibale, S. Vanni, M. Scarselli, U. Rothlisberger, and A. Radenovic, "Identification of clustering artifacts in photoactivated localization microscopy.," *Nature methods*, vol. 8, pp. 527–528, 2011.

[97] J. Sauvola and M. Pietikäinen, "Adaptive document image binarization," *Pattern Recognition*, vol. 33, no. 2, pp. 225–236, 2000.

[98] R. K. Neely, P. Dedecker, J.-i. Hotta, G. Urbanaviciute, S. Klimasauskas, and J. Hofkens, "DNA fluorocode: A single molecule, optical map of DNA with nanometre resolution," *Chemical Science*, vol. 1, p. 453, 2010.

[99] C. Vranken, J. Deen, L. Dirix, T. Stakenborg, W. Dehaen, V. Leen, J. Hofkens, and R. K. Neely, "Super-resolution optical DNA Mapping via DNA methyltransferase-directed click chemistry," *Nucleic Acids Research*, vol. 42, 2014.

[100] R. K. Neely, J. Deen, and J. Hofkens, "Optical mapping of DNA: Single-molecule-based methods for mapping genomes," 2011.

[101] J. Deen, W. Sempels, R. De Dier, J. Vermant, P. Dedecker, J. Hofkens, and R. K. Neely, "Combing of genomic DNA from droplets containing picograms of material," *ACS Nano*, vol. 9, pp. 809–816, 2015.

[102] N. Otsu, "A threshold selection method from Gray-level," *IEEE Transactions on Systems, Man, and Cybernetics*, vol. SMC-9, pp. 62–66, 1979.

[103] C. Harris and M. Stephens, "A Combined Corner and Edge Detector," *Proceedings of the 4th Alvey Vision Conference*, pp. 147–151, 1988.

[104] M. a. Fischler and R. C. Bolles, "Random sample consensus: a paradigm for model fitting with applications to image analysis and automated cartography," *Communications of the ACM*, vol. 24, pp. 381–395, 1981.

[105] M. J. Saxton and K. Jacobson, "Single-particle tracking: applications to membrane dynamics.," *Annual review of biophysics and biomolecular structure*, vol. 26, pp. 373–399, 1997.

[106] N. Chenouard, I. Smal, F. de Chaumont, M. Maška, I. F. Sbalzarini, Y. Gong, J. Cardinale, C. Carthel, S. Coraluppi, M. Winter, A. R. Cohen, W. J. Godinez, K. Rohr, Y. Kalaidzidis, L. Liang, J. Duncan, H. Shen, Y. Xu, K. E. G. Magnusson, J. Jaldén, H. M. Blau, P. Paul-Gilloteaux, P. Roudot, C. Kervrann, F. Waharte, J.-Y. Tinevez, S. L. Shorte, J. Willemse, K. Celler, G. P. van Wezel, H.-W. Dan, Y.-S. Tsai, C. Ortiz de Solórzano, J.-C. Olivo-Marin, and E. Meijering, "Objective comparison of particle tracking methods.," *Nature methods*, vol. 11, pp. 281–9, Mar. 2014.

[107] N. L. Andrews, K. A. Lidke, J. R. Pfeiffer, A. R. Burns, B. S. Wilson, J. M. Oliver, and D. S. Lidke, "Actin restricts FcepsilonRI diffusion and facilitates antigen-induced receptor immobilization," *Nat Cell Biol*, vol. 10, pp. 955–963, Aug. 2008.

[108] N. Banterle, K. H. Bui, E. A. Lemke, and M. Beck, "Fourier ring correlation as a resolution criterion for super-resolution microscopy," *Journal of Structural Biology*, vol. 183, pp. 363–367, 2013.

[109] R. P. J. Nieuwenhuizen, K. a. Lidke, M. Bates, D. L. Puig, D. Grünwald, S. Stallinga, and B. Rieger, "Measuring image resolution in optical nanoscopy.," *Nature methods*, vol. 10, pp. 557–62, 2013.

[110] N. B. Vicente, J. E. D. Zamboni, J. F. Adur, E. V. Paravani, and V. H. Casco, "Photobleaching correction in fluorescence microscopy images," *Journal of Physics: Conference Series*, vol. 90, no. 012068, 2007.

[111] P. Pollak, "Efficient and reliable measurement and simulation of noisy speech background," in *European Signal Processing Conference*, vol. 2015-March, pp. 1–4, IEEE, 2015.

[112] S.-C. Tai and S.-M. Yang, "A fast method for image noise estimation using Laplacian operator and adaptive edge detection," *2008 3rd International Symposium on Communications, Control and Signal Processing*, pp. 1077–1081, Mar. 2008.

Appendix

Microscope setups

Microscope setup used for image acquisition of the SIM images was designed and build by my colleagues from the Charles University in Prague Zdeněk Švindrych and Pavel Křížek led by Guy M. Hagen from the University of Colorado Colorado Springs. The setup is described in details in [37]. The pattern calibration procedure is described in [29]. The control of LCOS microdisplay is described in Supplementary of our paper devoted to SIMToolbox [55].

The multiplane SOFI setup used for 3D imaging was designed and build by my colleagues form EPFL Stefan Geissbuehler, Marcel Leutenneger, and Azat Sharipov led by Prof. Theo Lasser. Details about the multiplane SOFI setup can be find in [19] and about the 2D setup in [43, 48]. The new multiplane SOFI setup presented in Figure 4.2 contains a new image splitter. This single custom made optical component splits the fluorescence into eight channels and provides better stability compared to the previous solution with three 50:50 beam splitters shown in [19].

Samples

Samples related to SOFI imaging of Hela cells, MEF cells and DNA samples were prepared and kindly provided by my colleagues from EPFL. Hela cells were prepared by Azat Sharipov and Stefan Geissbuehler as described in [43]. MEF cells for imaging focal adhesions were prepared by Hendrik Deschout and Lely Feletti as described in [48] DNA samples were provided by Jochem Deen. Samples of T-cells for the investigation of CD4 protein organization were prepared and kindly provided by my colleagues from the Czech Academy of Sciences Daniela Glatzová, and Zuzana Kvíčalová under the super-vision of Marek Cebecauer. The LAMP1-GFP cells for live cell SIM experiments were provided by Viola Hausnerová and Christian Lanctôt from the Charles University.

Our papers [37, 43, 48, 55] which contain all the details about the microscopes, sample preparation and data processing are attached in the following part of the thesis.

List of publications

All listed publications are related to the topic of the thesis.

Journal papers (with IF)

H. Deschout* & **T. Lukeš***, A. Sharipov, D. Szlag, L. Feletti, W. Vandenberg, P. Dedecker, J. Hofkens, M. Leutenegger, T. Lasser, A. Radenovic, „Complementarity of PALM and SOFI for super-resolution live cell imaging of focal adhesions“, **Nature Comm.**, 2016

A. Girsault* & **T. Lukeš***, A. Sharipov, S. Geissbuehler, M. Leutenegger, W. Vandenberg, P. Dedecker, J. Hofkens, and T. Lasser, “SOFI Simulation Tool: A Software Package for Simulating and Testing Super-Resolution Optical Fluctuation Imaging,” **PLoS One**, vol. 11, p. e0161602, 2016.

P. Křížek, **T. Lukeš**, M. Ovesný, K. Fliegel, and G. M. Hagen, ”SIMToolbox: a MATLAB toolbox for structured illumination fluorescence microscopy,” **Bioinformatics**, vol. 15, p. btv576, 2015.

T. Lukeš , P. Křížek, Z. Švindrych, J. Benda, M. Ovesný, K. Fliegel, M. Klíma, and G. M. Hagen, ”Three-dimensional super-resolution structured illumination microscopy with maximum a posteriori probability image estimation,” **Optics Express**, vol. 22, no. 24, p. 29805, Nov. 2014.

D. Kekrt, **T. Lukeš**, M. Klŕna, and K. Fliegel,”2D Iterative MAP Detection: Principles and Applications in Image Restoration”, Radioengineering, vol. 23, no. 2, pp. 618–631, July 2014.

*Equal contribution

In preparation

T. Lukeš, J. Pospíšil, P. Křížek, Z. Švindrych, M. Ovesný, K. Fliegel, K. Spendier, and G. M. Hagen, “Imaging live cells with doubled resolution using Bayesian image reconstruction”

T Lukeš, D. Glatzová, Z. Kvíčalová, T. Brdička, T. Lasser & Marek Cebecauer "Determining protein densities in T-cells using super-resolution optical fluctuation imaging"

A. Sharipov, **T. Lukeš**, P. Sandoz, A. Nahas, M. Leutenegger, S. Geissbuehler, D. Szlag, G. van der Goot, T. Lasser "Live cell three-dimensional time-lapse super-resolution imaging"

Conference proceedings (listed in WoS)

T. Lukeš, D. Kekrt, K. Fliegel, M. Klíma,"Binarization of noisy microscopy images through signal reconstruction using iterative detection network ," International Conference on Image Processing ICIP 2014, 21th IEEE International Conference, October 2014

T. Lukeš, G. Hagen, P. Křížek, Z. Švindrych, K. Fliegel, and M. Klíma, "Comparison of image reconstruction methods for structured illumination microscopy" in Proc. SPIE 9129, Biophotonics, May 2014, vol. 9129, pp. 1–13.

T. Lukeš, K. Fliegel, M. Klíma,"Performance evaluation of image quality metrics with respect to their use for super-resolution enhancement," Quality of Multimedia Experience (QoMEX), 2013 Fifth International Workshop, pp. 42–43.

T. Lukeš, K. Fliegel, M. Klíma,"Objective image quality assessment of multiframe super-resolution methods" Radioelektronika, 2013 23rd International Conference, pp.267–272.

Other activities

Project assistance:

Supervision of a Master thesis:
Suppression of photobleaching in super-resolution optical fluctuation imaging using digital filtering, student Vojtěch Terš, CTU in Prague, 2016

Supervision of a Master thesis:
Super-resolution optical fluctuation imaging in life sciences, student Arik Girsault,
EPFL, Lausanne, 2015
Thesis was awarded by "Prize for the best Master Project in Neuroprosthetics of the Master Bioengineering" and "Grenier Prize"

Supervision of a Master project: Parallel processing for video super-resolution optical fluctuation imaging, student Vojtěch Terš, CTU in Prague, 2014

Journal paper reviews:

IEEE Transactions on Systems, Man, and Cybernetics: Systems
IET Biometrics
IET Computer Vision

Selected papers

nature COMMUNICATIONS

ARTICLE

Received 25 Apr 2016 | Accepted 25 Oct 2016 | Published 19 Dec 2016

DOI: 10.1038/ncomms13693 OPEN

Complementarity of PALM and SOFI for super-resolution live-cell imaging of focal adhesions

Hendrik Deschout[1,*], Tomas Lukes[1,2,*], Azat Sharipov[1], Daniel Szlag[1], Lely Feletti[1], Wim Vandenberg[3], Peter Dedecker[3], Johan Hofkens[3], Marcel Leutenegger[4], Theo Lasser[1] & Aleksandra Radenovic[1]

Live-cell imaging of focal adhesions requires a sufficiently high temporal resolution, which remains a challenge for super-resolution microscopy. Here we address this important issue by combining photoactivated localization microscopy (PALM) with super-resolution optical fluctuation imaging (SOFI). Using simulations and fixed-cell focal adhesion images, we investigate the complementarity between PALM and SOFI in terms of spatial and temporal resolution. This PALM-SOFI framework is used to image focal adhesions in living cells, while obtaining a temporal resolution below 10 s. We visualize the dynamics of focal adhesions, and reveal local mean velocities around 190 nm min^{-1}. The complementarity of PALM and SOFI is assessed in detail with a methodology that integrates a resolution and signal-to-noise metric. This PALM and SOFI concept provides an enlarged quantitative imaging framework, allowing unprecedented functional exploration of focal adhesions through the estimation of molecular parameters such as fluorophore densities and photoactivation or photoswitching kinetics.

[1] Laboratory of Nanoscale Biology & Laboratoire d'Optique Biomédicale, STI - IBI, Ecole Polytechnique Fédérale de Lausanne, Station 17, CH-1015 Lausanne, Switzerland. [2] Department of Radioelectronics, FEE, Czech Technical University in Prague, Technická 2, 166 27 Prague 6, Czech Republic. [3] Department of Chemistry, University of Leuven, Celestijnenlaan 200F, B-3001 Heverlee, Belgium. [4] Abteilung NanoBiophotonik, Max-Planck-Institut für biophysikalische Chemie, Am Fassberg 11, 37077 Göttingen, Germany. * These authors contributed equally to this work. Correspondence and requests for materials should be addressed to T.La (email: theo.lasser@epfl.ch) or to A.R. (email: aleksandra.radenovic@epfl.ch).

It is essential for cells to adhere to the extracellular matrix for carrying out fundamental tasks such as migration, proliferation and differentiation[1]. For all these processes, focal adhesions are essential. Focal adhesions rely on a concerted action of dense assemblies of hundreds of proteins[2] forming thin micron-sized plaques close to the cell membrane[3]. These protein assemblies contain transmembrane receptors, such as integrins, binding to the extracellular matrix and recruiting other proteins inside the cytoplasm, such as talin and paxillin. This entails the formation of small structures with an extent in the order of 100 nm, which either disassemble after a few seconds, or mature into larger focal adhesions that remain stable typically for tens of minutes. This underlying maturation process requires an ongoing recruitment of additional proteins, such as vinculin or α-actinin, which may be linked to actin filaments. Overall, focal adhesions can thus be seen as the anchor points of the cell onto the extracellular matrix, mediating interactions with the actin cytoskeleton. Most focal adhesion proteins have been identified. However, the observation of the spatial organization and dynamics of focal adhesions remains challenging.

Single-molecule localization microscopy (SMLM), based on localizing sparse sets of activatable or switchable fluorescent molecules with a precision of tens of nanometres, is considered to be a method of choice for this endeavour[4]. In 2006, Betzig *et al.*[5] used photoactivated localization microscopy (PALM) to image submicron patterns of vinculin in a fixed cell. However, focal adhesions are dynamic entities demanding fast live-cell imaging. This has been further investigated by using PALM to image the dynamic behaviour of paxillin[6], but elucidating the full cell adhesion process remains a challenging task for SMLM.

As shown by Shroff *et al.*[6], SMLM trades temporal resolution for spatial super-resolution, since using less raw images for individual SMLM images means less available single-molecule localizations. Several thousand raw images offer high spatial information of focal adhesions, but only a limited first glimpse into their dynamic behaviour. These focal adhesions not only evolve over time, they can also undergo translational movement. The mean velocity of focal adhesions in stationary fibroblasts has been reported to be in the order of 100 nm min^{-1} (ref. 7). This translates into a temporal resolution well below 1 min to capture the fundamental dynamic behaviour while avoiding motion blur, which would otherwise spoil the anticipated spatial resolution[6]. Although temporal resolutions in the order of seconds are possible using PALM[8], the SMLM method most often reported to achieve such a temporal resolution is (direct) stochastic optical reconstruction microscopy ((d)STORM)[9,10]. However, delivery of (d)STORM dyes to intracellular targets remains difficult[11]. PALM is well suited for live-cell imaging of focal adhesions since it uses genetically expressed fluorescent proteins known for being well tolerated in living cells.

PALM holds promise for obtaining information about the spatial composition and organization of proteins in focal adhesions. Indeed, assuming that each fluorescent protein is localized only once, their numbers would directly result in a fluorophore density map. However, fluorescent proteins are known to 'blink', that is, they can reversibly switch on and off for several times after being activated[12]. Blinking therefore results in an overcounting error. Several methods have been developed to account for this error, for instance, by combining localizations that are clustered in space and time[13,14] or by applying pair correlation analysis[15]. Undercounting errors can appear as well, not only by merging localizations of separate fluorophores in high-density samples, but also due to incomplete maturation and limited detection efficiency[16].

To address the need for quantitative and time-lapse super-resolution imaging of focal adhesions, we enlarge the scope of SMLM by merging PALM with super-resolution optical fluctuation imaging (SOFI)[17] applied to the same raw image sequence. SOFI exploits the correlated response of neighbouring image pixels based on a spatiotemporal cumulant analysis of image sequences[18]. This technique tolerates a significant overlap of single-molecule images and relaxes the requirements on the activation or switching rates when compared with classical SMLM concepts. This allows one to use fluorescent molecules with a higher activation or switching rate[19], resulting in an improved temporal resolution[20]. However, there is a common belief that SOFI cannot attain the spatial resolution achievable by known SMLM methods. In addition, balanced SOFI (bSOFI) can be used to determine the fluorophore on-time ratio, offering an estimation of the molecular density and molecular switching or activation rates[21].

In this paper, we investigate the complementarity of PALM and SOFI for imaging focal adhesions. By applying them both to the same data set, we obtain a better insight in the true structure of focal adhesions and their molecular parameters. We enhance bSOFI and achieve a substantial increase in spatial resolution, comparable to PALM. We also present a methodology for evaluating the super-resolution image quality, integrating a resolution and a signal-to-noise (SNR) metric. We demonstrate our PALM-SOFI framework by imaging moving focal adhesions in a living cell.

Results

Widefield super-resolution metrics. In Abbe's theory, microscopy imaging is conceived as low pass filtering with a cutoff frequency at 2NA/λ (with λ the wavelength of light and NA the numerical aperture of the microscope objective). Abbe's analysis established the generally adopted resolution metric for classical microscopy as a pure instrument parameter independent of the object. SMLM goes beyond the 'diffraction barrier' by exploiting to its best the precise localization of single fluorophores. Therefore, the final 'SMLM-resolution' is the accumulated information of localized fluorescent markers and is *de facto* sample dependent.

In recent publications[22,23], the concept of an optical resolution criterion was revisited with an extension to super-resolution imaging. However, as stated by Demmerle *et al.*[22], 'resolution in single-molecule imaging is especially challenging'. There is a manifold of sample dependent and difficult to master parameters like labelling density, bleaching and the sample structure itself, which have a difficult to assess impact on resolution. In view of merging different imaging modalities like PALM and SOFI, the need for a general resolution and SNR metric became mandatory.

An important step towards a resolution metric is the Fourier ring correlation (FRC)[24,25]. Essential to this metric is the correlation of the Fourier transform of two SMLM images obtained from two stochastically independent halves of the original image sequence (Supplementary Note 1). An extension of the FRC procedure applies also to SOFI, which we used for an objective assessment of PALM and SOFI. We imaged fixed mouse embryonic fibroblasts (MEFs) expressing paxillin labelled with mEos2 or psCFP2 (see Methods), and calculated the FRC metric as a function of the number of frames, as shown in Fig. 1. To improve the spatial resolution of SOFI, we introduced a novel linearization procedure for bSOFI to achieve higher orders of the cumulant analysis (Supplementary Note 2).

Figures 1a,b show that the individual adhesion footprints are structured into a specific pattern. As the FRC calculation involves circular path summing in frequency space with a constant radius, the FRC metric is almost insensitive to variations of the spatial frequency content along different directions (Supplementary Figs 1 and 2). In Fig. 1a,b, such a difference can readily be

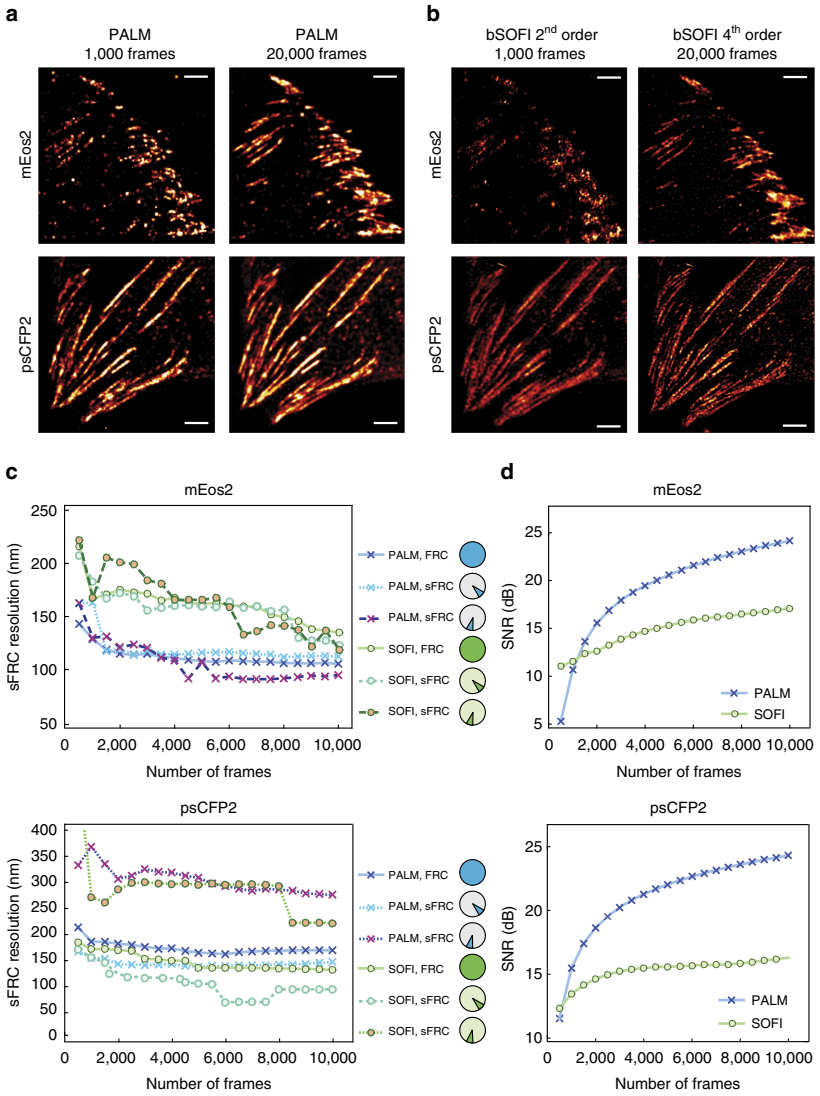

Figure 1 | Objective image quality assessment integrating a resolution metric and a SNR metric applied to PALM and SOFI images. (**a**) PALM images of fixed MEF cells expressing paxillin labelled with mEos2 or psCFP2, obtained from a full raw image sequence (20,000 frames) and the first 1,000 frames. The PALM images were rendered as probability maps (see Methods). (**b**) SOFI images obtained from the same raw image sequences as in **a**. (**c**) Resolution (sFRC) metric for SOFI and PALM as a function of the number of frames, obtained from subsequences of the same raw image sequences as in **a** and **b**. The circles indicate the sector used for the sFRC calculation, the sector with the lowest sFRC values provides the best description of the resolution. Note that the sFRC requires to split the number of frames in two halves to create two images. Therefore, 20,000 input frames allows one to calculate the sFRC corresponding to a super-resolved image reconstructed from 10,000 frames. (**d**) SNR metric for SOFI and PALM as a function of the number of frames, obtained from subsequences of the same raw image sequences as in **a** and **b**. Scale bar, 2 μm.

noticed for the psCFP2 marked cell image, where focal adhesions and elongated structures indicative of paxillin organized along actin filaments[26] can be seen. We therefore implemented a sectorial FRC (sFRC) metric (Supplementary Note 1) as already suggested by Nieuwenhuizen *et al.*[25] This sFRC metric shows a more nuanced picture: the measured values are varying around the classic FRC for different sectors as shown in Fig. 1c and Supplementary Fig. 3, reflecting the orientation dependence of the resolution metric. The resolution capabilities of the imaging technique are best described by the sector with the lowest sFRC value, indicating that a spatial resolution around 100 nm was obtained. Interestingly, the sFRC values indicate that SOFI resolves psCFP2-expressing cells better than PALM, while the opposite was observed for mEos2 labelling, despite the latter fluorescent protein being well known for its blinking properties. We attribute these results to a difference in activation rate and

emitter density, as indicated by the evolution of the number of localizations over time (Supplementary Fig. 4). The number of psCFP2 localizations is higher during the first several thousand frames, increasing the probability of overlapping psCFP2 images, which poses more difficulties for PALM than for SOFI.

Following these observations, we extended our PALM-SOFI framework to dual-colour imaging using both psCFP2 and mEos2. We imaged a fixed rat embryonic fibroblast (REF) expressing paxillin labelled with psCFP2 and integrin β3 labelled with mEos2 (see Methods). Calculating the sFRC metric in the two-colour channels for both SOFI and PALM shows that SOFI obtains the highest spatial resolution in the psCFP2 channel (that is, around 90 nm), while PALM gives the best resolution (that is, around 100 nm) in the mEos2 channel, in correspondence to our single colour results above. This suggests that an overlay of the SOFI (psCFP2) and PALM (mEos2) images results in an improved dual-colour image, as shown in Fig. 2.

Besides the image resolution, the image SNR should be characterized as well. We performed a pixel-wise SNR estimation based on a statistical approach known as jackknife resampling[27]. The jackknife method generates N data sets of N-1 camera frames, that is, each jackknife data set is obtained by 'cutting-out' just one single camera frame (Supplementary Note 3). The variance on the individual pixel values originating from each of these data sets is considered as an uncertainty measure, yielding an SNR value per pixel. This general approach applies to PALM as well as to SOFI and has been used as an objective comparison of SNR for our PALM and SOFI cell images, as shown in Fig. 1d. Except for a small number of frames (typically $<1{,}000$), PALM outperforms SOFI in terms of SNR. This is to be expected because the PALM images are reconstructed from fitted data.

In summary, our methodology for assessing the image quality integrates an objective evaluation of the resolution and the SNR for super-resolved images.

From spatial towards temporal resolution. Achieving a high temporal resolution in SMLM is truly a challenge. Bleaching, activation or switching rates, camera frame rates and last but not least the minimum number of frames limit the achievable temporal resolution. As stated before, spatial super-resolution comes at an expense of temporal resolution. As we intend to image the dynamics of focal adhesions, we are in need of characterizing the difficult balance between lowering spatial super-resolution while enhancing temporal resolution. To objectively characterize the spatiotemporal resolution of both SOFI and PALM for a broad range of controlled conditions, we performed resolution measurements using simulated data. In an attempt to stay close to classical resolution measurement concepts, we designed a test target adopted from charts used for modulation transfer function (MTF) analysis. The MTF allows one to extract the cutoff frequency and the visibility as a function of spatial frequency of an imaging system and is used as a metric for characterizing optical imaging instruments[28]. Our MTF analysis provides a resolution standard for simulated data and a control for the sFRC resolution estimates in our high-density conditions.

Our test target consists of progressively smaller bars randomly filled with point emitters at an *a priori* given density, providing an object of stochastically activated single emitters (Fig. 3a; Supplementary Note 4). To approximate the conditions of focal adhesions in a cell, we tested two emitter densities (that is, 800 and $1{,}200\,\mu m^{-2}$). Our simulation takes into account the photophysics of mEos2 and psCFP2 and parameters of the microscope set-up (Supplementary Note 4). On the basis of this test target, we determined the visibility for PALM and SOFI beyond the cutoff frequency f_c of classical widefield microscopy. From each simulated MTF, we extracted the cutoff frequency (Fig. 3b; Supplementary Note 4), resulting in a resolution measure related to the sFRC metric (Supplementary Fig. 5).

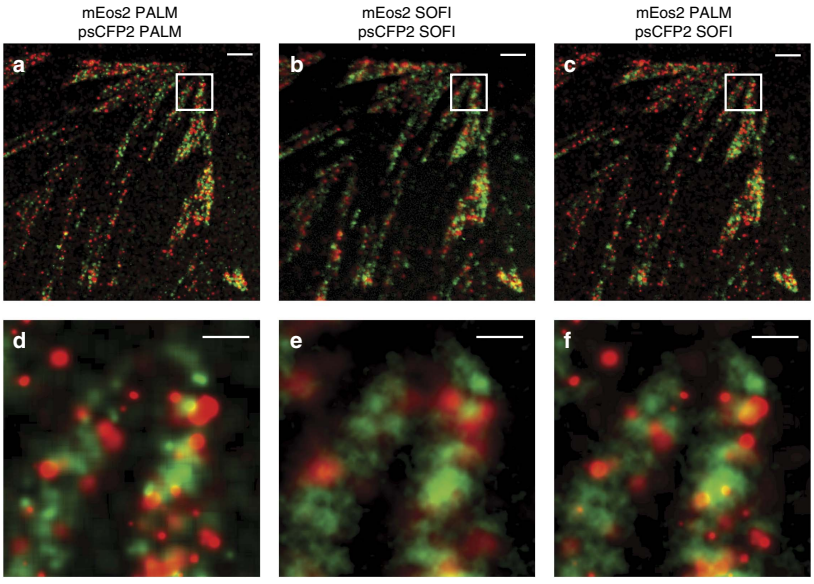

Figure 2 | Dual-colour imaging with PALM and SOFI. (**a**–**c**) Overlay of red and green images of a fixed REF cell expressing paxillin labelled with psCFP2 (green) and integrin β3 labelled with mEos2 (red) as obtained by (**a**) PALM in both colour channels, (**b**) SOFI in both colour channels, and (**c**) PALM in the red channel and SOFI in the green channel. (**d**–**f**) Corresponding zoom-ins for the images in **a**–**c**. The PALM images were rendered as probability maps (see Methods). Scale bar, 2 μm (**a**–**c**); 0.5 μm (**d**–**f**).

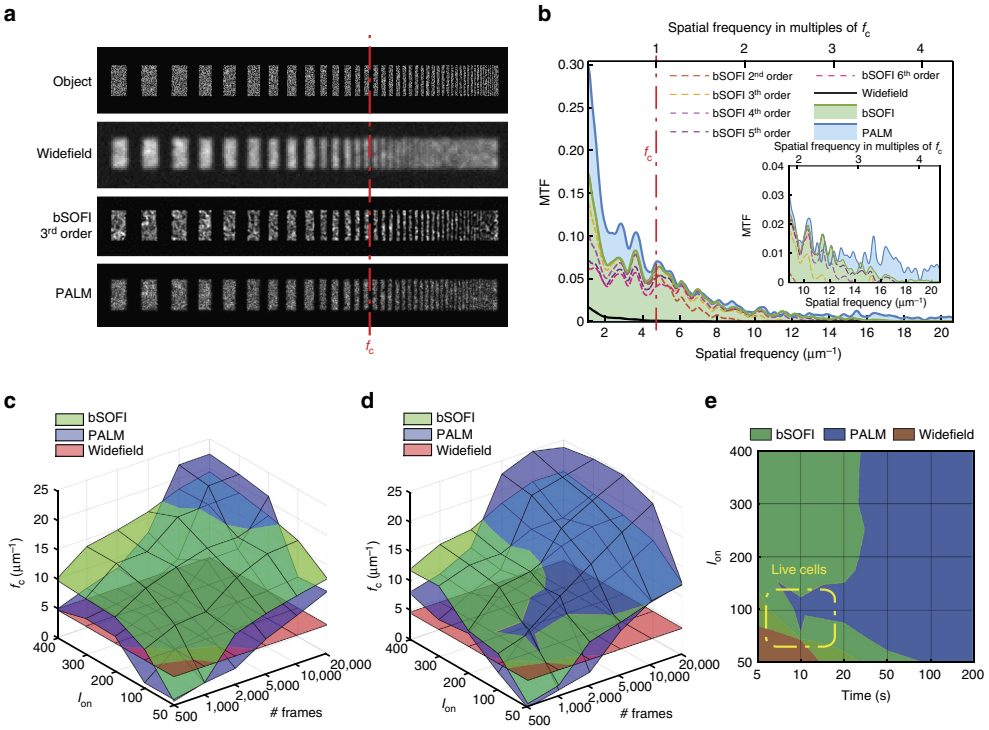

Figure 3 | MTF analysis on simulated PALM and SOFI images. (**a**) MTF test target consisting of single emitters randomly placed inside progressively thinner bars, together with resulting widefield, PALM and third order SOFI image (I_{on} = 100 photons and 20,000 frames). The red line indicates the cutoff frequency f_c for widefield imaging. The PALM images were rendered as localization number histograms (see Methods) with a pixel size equal to the SOFI pixel size. (**b**) MTF calculated from the simulated SOFI and PALM images in **a**. (**c**,**d**) Cutoff frequencies for PALM and SOFI as a function of I_{on} and the number of frames, with an emitter density of (**c**) 1,200 μm^{-2} and (**d**) 800 μm^{-2}. (**e**) Two-dimensional projection of the chart in **d**. The timescale assumes a frame rate equal to 100 Hz, which corresponds to the frame rate used for our live-cell measurements.

Figure 3c,d shows the simulated cutoff frequency maps for PALM and SOFI based on the same test target, as a function of the number of frames and the number of photons per emitter per frame in an on-state (that is, I_{on}). Figure 3c corresponds to an emitter density of 1,200 μm^{-2} and the psCFP2 case, whereas Fig. 3d corresponds to 800 μm^{-2} and the mEos2 case. The number of frames ranges from 500 to 20,000. At 20,000 frames, all emitters are detected and the structure of the test pattern is fully described. SOFI shows a slowly growing spatial resolution (that is an increase of cutoff frequency f_c) with increasing I_{on} and the number of frames. The PALM cutoff frequency grows faster, but only outperforms SOFI for a high number of frames (>10,000 for the higher density case and >5,000 for the lower density case). Note that SOFI requires at least 500 frames before 'super-resolution' can be achieved, while PALM needs even more frames (typically >1,000) and depends more strongly on the labelling density. For low frame numbers and low I_{on}, the number of localized emitters and the localization precision are too low for PALM to properly describe the test pattern, which results in low MTF values and a corresponding low resolution. Assuming a typical camera frame rate of 100 Hz, Fig. 3e shows the resolution sub-space where SOFI is dominant over PALM in terms of temporal/spatial resolution, and vice versa the sub-space where PALM outperforms SOFI. This indicates the parameter space where our PALM-SOFI imaging modality can be used for investigating the dynamics of focal adhesions as indicated in Fig. 3e.

Live-cell imaging. Imaging living cells requires a technique providing a sufficiently high temporal resolution and a compatibility with physiological conditions. Among the different SMLM methods, PALM meets the latter condition well, mainly due to genetically expressed fluorescent proteins acting as a label. However, the first condition is not perfectly met. PALM (like other SMLM techniques) makes the implicit assumption that the imaged structure stays stationary during the image acquisition, typically lasting for several minutes. Observing objects moving with a speed exceeding 10 nm min^{-1} (that is the typical localization precision) is almost incompatible with this stationarity condition. Focal adhesions are known to move at rates of about 100 nm min^{-1}, as mentioned before. Observing focal adhesions therefore demands PALM imaging cycles far below 1 min, to avoid significant motion blur. The obvious way to increase the temporal resolution is to shorten the imaging cycle by acquiring less raw images. However, this entails a decrease in spatial resolution as less localizations are contributing. Many attempts have therefore been undertaken in SMLM to improve the temporal resolution, while maintaining a sufficient number of localizations[8,29–31].

SOFI offers a large untapped potential for imaging living cells. Just like PALM, SOFI can be used with genetically expressed fluorescent proteins. However, it is also assumed that the sample is stationary during the acquisition of the raw images. This again asks for a tradeoff between spatial and temporal resolution, although SOFI images can be reconstructed with less images than

required in PALM. When comparing SOFI and PALM, the latter technique is generally perceived as providing a higher spatial resolution. SOFI, on the other hand, is assumed to feature a higher temporal resolution, allowing faster imaging of moving structures, which has indeed been suggested by Geissbuehler *et al.*[20].

When attempting to increase both temporal and spatial resolution, a PALM-SOFI approach based on an identical raw image sequence appears as an interesting imaging modality. We imaged living MEF cells expressing paxillin labelled with mEos2 and post-processed the data by both PALM and SOFI algorithms, as shown in Fig. 4a and Supplementary Video 1. We obtained a temporal resolution of 10 s, while maintaining an average spatial resolution of 157 nm for SOFI, as determined by the sFRC metric (Supplementary Fig. 6). PALM at this temporal resolution resulted in an average spatial resolution of 145 nm. We determined the mean velocity of one of the focal adhesions, obtained from a kymograph-based analysis[32,33] (Fig. 4b,c; Methods). PALM and SOFI show similar trends, indicating that the focal adhesion moved with a mean velocity of 190 nm min^{-1}. This mean velocity is in agreement with values reported and observed by others[7].

Quantitative imaging. Beyond qualitative imaging, SMLM methods such as PALM allow one to obtain quantitative molecular information, such as the number of localizations. This can be related to the number of fluorescent proteins. However, the relationship between both quantities is far from trivial, since most photoactivatable fluorescent proteins blink, that is they can reversibly go to a dark state. This may give rise to multiple localizations. Moreover, this blinking behaviour depends on the illumination intensity and the molecular environment of the fluorescent proteins. Simply counting the localizations usually results in an overestimation of the number of fluorescent proteins. Hence, several methods to correct this overcounting

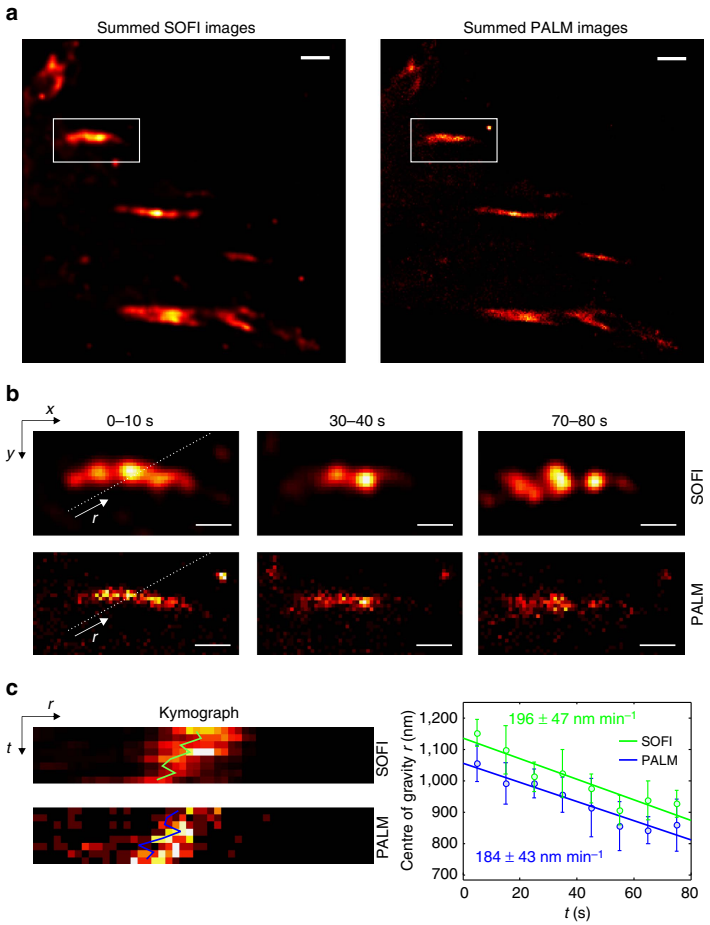

Figure 4 | Live-cell imaging with PALM and SOFI. (**a**) Sum of eight PALM and SOFI images of a living MEF cell expressing paxillin labelled with mEos2. Each image is reconstructed from 1,000 camera frames with 10 ms exposure time, resulting in a 10 s temporal resolution. The PALM images were rendered as localization number histograms (see Methods) with a pixel size equal to the SOFI pixel size. Scale bar, 1 µm. (**b**) Region of interest indicated in **a** showing a focal adhesion at different time points. Scale bar, 0.5 µm. (**c**) Kymographs along the direction of motion as indicated by the line in **b**. The focal adhesion mean velocity is determined by a linear fit to the centre of gravity *r* determined from the kymograph as a function of time (see Methods). The procedure was repeated five times for parallel kymographs, the error bar represents the s.d.

error have been developed for PALM, often based on merging localizations that are sufficiently close in time and space to be considered originating from the same blinking fluorescent protein[13,14]. As these methods require characterization of the blinking behaviour, for instance through the calculation of the average time between two emission bursts, they indirectly allow one to probe the molecular environment of the emitters.

Focal adhesions are dense assemblies of proteins, making it challenging to avoid merging localizations of different fluorescent proteins, which would lead to an under-counting error. Therefore, we have adapted the merging criterion of an earlier published work[13] to account for higher densities. Instead of using a fixed distance threshold of 1 raw image pixel as merging criterion, we assumed a threshold based on a statistical measure, called the Hellinger distance, which allows one to account for the varying localization precision (Supplementary Note 5). We applied this adapted method to our localization data (identical to those used for Fig. 1) of fixed MEF cells expressing paxillin labelled with mEos2 (Fig. 5a,b) and psCFP2 (Supplementary Fig. 7). The corrected localization number and the average time between two blinking events is shown as a function of different thresholds of the Hellinger distance, calculated for three areas with different emitter densities. We determined that a threshold value of 0.9 was a good compromise (Supplementary Note 5), but even around this value the number of localizations decreases with increasing threshold values for the densest areas (Fig. 5e). This indicates that the sample is too dense, which is corroborated by the average time between two blinking events being dependent on the area density (Fig. 5f).

SOFI is an interesting complement to PALM for quantitative imaging, since combining cumulant images of second, third and fourth order enables to extract molecular parameters such as the on-time ratio, the molecular brightness and the molecular density[21] (Supplementary Note 2). While PALM yields average values over the region of analysis, SOFI generates spatial maps of these parameters. Moreover, as SOFI is superior to PALM in imaging 'crowded' environments, this method is of great interest for quantitative imaging of focal adhesions. We used SOFI to determine the on-time ratio and density map of the same localization data used for PALM (Fig. 5c,d). As opposed to PALM, SOFI performs well in high-density areas. SOFI estimates the molecular parameters pixel-wise. This estimation is meaningless for areas that contain mostly background (SNR close to 1). Background areas therefore have to be removed by applying an intensity threshold or SNR based threshold. Since PALM is working well in these low-density areas, this again demonstrates the usefulness of our PALM-SOFI approach.

The molecular parameter estimation can be applied to living cells if the temporal resolution is sufficient for proper time sampling. Achieving fourth order SOFI images, required for molecular parameter estimation, is challenging in living cells since it requires high signals and generally a large number of frames. Given a high enough signal, 1,000 frames might be sufficient for the required fourth order. However, under our conditions in focal adhesions, 4,000–5,000 frames are necessary for high quality fourth order SOFI, which limits the temporal resolution of molecular parameter estimation. In the case of PALM, quantitative imaging requires a sufficient number of localizations, so the minimum number of frames will depend on the emitter density. On the other hand, if the density is too high, results will be biased. We therefore performed simulations to investigate SOFI and PALM-based molecular density estimation in function of the temporal resolution (that is, various numbers of frames) and the emitter density, see Fig. 5g and Supplementary Note 2. PALM-based density estimation performs well for low emitter densities (that is, $<400\,\mu m^{-2}$), regardless of the number of frames, while SOFI-based density estimation performs better than PALM for higher molecule densities, under the condition that enough frames are acquired (that is, $>5{,}000$), as can be seen in Fig. 5g.

Discussion

Our results indicate that PALM and SOFI are complementary techniques for the observation of focal adhesions in living cells. Such an imaging approach not only provides sufficient spatial resolution for their observation, it also grants access to their temporal dynamics. In view of the biological quest, we thoroughly investigated this imaging concept. Our simulations indicate a superior performance of SOFI when compared with PALM for low frame numbers (typically $<5{,}000$ frames), while PALM substantially outperforms SOFI for higher frame numbers. The onset of 'super-resolution' based on SOFI demands typically 500 frames, while PALM requires at least 1000 frames. Our PALM-SOFI framework applied to the same raw image sequences therefore opens the door for assessing the dynamics of 'not too fast' biological processes in the order of $100\,nm\,min^{-1}$.

Using both PALM and SOFI, we could image focal adhesions with a resolution better than 100 nm in fixed cells, whereas in living cells a resolution <150 nm was obtained, requiring <1000 raw images. These live-cell images were recorded at a frame rate of 100 Hz, which translates into a temporal resolution below 10 s. Such a temporal resolution is required to resolve the dynamics of the focal adhesions in more detail, as we observed 'focal adhesion velocities' around $190\,nm\,min^{-1}$.

Besides resolution, we also characterized the SNR for our PALM-SOFI framework. In general, PALM shows the highest SNR, up to 25 dB for large frame numbers for fixed-cell images. Only for small frame numbers (typically <500) SOFI showed a superior SNR. We attribute this difference to the different nature of PALM and SOFI images (that is rendered images based on localized emitters versus correlations of intensity fluctuations). Considering this difference, the ramp up towards the SNR plateau seems to be more important for our data than a comparison of absolute SNR values (Supplementary Fig. 8). The steeper onset of SNR is in favour of PALM whereas for SOFI the SNR plateau is reached at a lower frame number.

We used a generalized resolution metric named sFRC (adapted from the classical FRC metric) and a SNR metric based on statistical resampling for assessing the performance gain of the PALM-SOFI framework. Our simulations show that the sFRC metric is in agreement with the cutoff frequencies obtained from our MTF analysis (Supplementary Fig. 5). Under the tested conditions corresponding to focal adhesions, the (s)FRC values are slightly higher than expected. We attribute this to the fixed threshold used in the calculation of the (s)FRC metric. We would like to note that the sFRC by definition requires images with a rich spatial frequency content. When, for instance, a sparse structure in the presence of mostly background is imaged, the sFRC value is unreliable, and this metric is useful for qualitative comparison only.

Depending on the fluorophore properties, either PALM or SOFI yielded a better resolution. Using mEos2, PALM performed better, while SOFI outperformed PALM for psCFP2. We hypothesize that this is caused by a difference in activation rate, combined with a difference in fluorophore density. For mEos2, the localization number per frame was low and constant, which is in favour of PALM. psCFP2, on the other hand, showed a higher number of localizations during the beginning of the image acquisition, resulting in a better resolution for SOFI. This points to the interesting fact that difficult PALM data, caused by a 'crowded' environment, can still be evaluated by

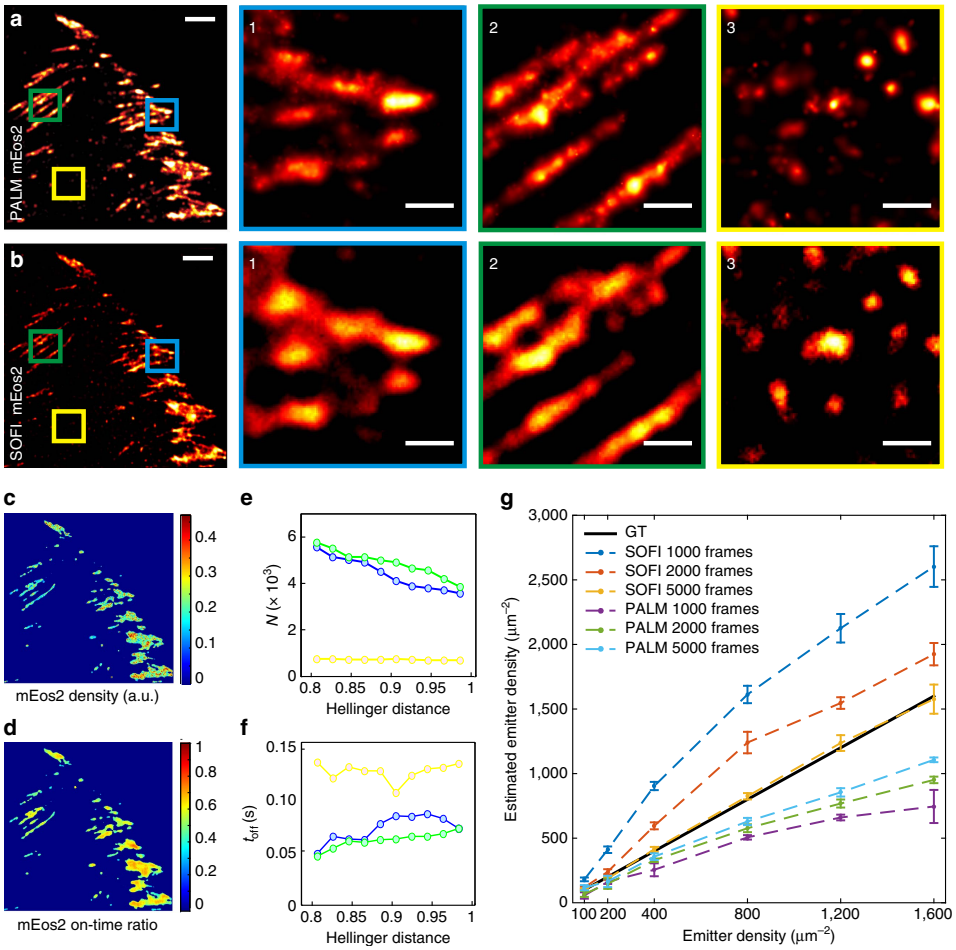

Figure 5 | Quantitative imaging with PALM and SOFI. (**a**,**b**) PALM and SOFI images of a fixed MEF cell expressing paxillin labelled with mEos2. Panels 1–3 are corresponding zoom-ins for the PALM or SOFI images. The PALM images were rendered as probability maps (see Methods). Scale bar, (**a**,**b**) 2 μm; (1–3) 0.5 μm. (**c**,**d**) SOFI analysis yields a fluorophore density and on-time ratio map. (**e**,**f**) Blinking events in PALM data can be detected by merging localizations that are sufficiently close in space and time. This analysis yields the blink corrected number of localizations N and the corresponding average off-time t_{off} between blinks, shown as a function of the Hellinger distance threshold for merging localizations. (**g**) SOFI and PALM-based quantitative analysis performed on simulated data (Supplementary Note 2). The emitter density estimated by PALM and SOFI is shown in function of the ground truth (GT) density for different numbers of simulated frames. The procedure was repeated 10 times, the error bars represent the s.d. The Hellinger distance threshold for the PALM-based estimation is 0.90 (Supplementary Note 5).

SOFI. In addition, our PALM-SOFI framework conveniently exploits these differences in fluorophore properties in order to improve on multicolour imaging, where one rarely has the luxury to choose an optimal combination of fluorescent proteins. As shown in Fig. 2, this allows to image both integrin β3 and paxillin in focal adhesions, without compromising the spatial resolution in one of the two-colour channels, which would be unavoidable when using only PALM or SOFI.

Another important benefit of this PALM-SOFI complementarity has been demonstrated by applying quantitative analysis on our focal adhesion data. PALM was shown to give reliable estimates of the blinking corrected localization numbers and the off-time between blinks in low-density areas of the cell sample. SOFI, on the other hand, was able to extract on-time ratios and number densities in high-density regions.

In summary, this PALM-SOFI imaging approach underlines the complementarity of both methods, enhanced by an additional gain in functional information. PALM imaging provides a high spatial resolution if enough frames can be acquired, while SOFI provides an interesting spatial resolution at lower frame numbers. The additional functional parameters provided by PALM and bSOFI post-processing add novel insights into cell biology without additional experimental effort.

Methods

Microscope set-up. Fixed-cell imaging was carried out on a custom built microscope[34]. Three continuous wave laser sources were used for excitation/activation: a 50 mW 405 nm laser beam (Cube, Coherent), a 100 mW 488 nm laser beam (Sapphire, Coherent), a 100 mW 561 nm laser beam (Excelsior, Spectra Physics). The 488 and 561 nm laser beams were combined using a dichroic mirror (T495lpxr, Chroma) and sent through an acousto-optic tunable filter

(AOTFnC-VIS-TN, AA Opto Electronic). Both laser beams were combined with the 405 nm laser beam using a dichroic mirror (405 nm laser BrightLine, Semrock). The three laser beams were focused by a lens into the back focal plane of the objective mounted on an inverted optical microscope (IX71, Olympus). We used a $\times 100$ objective (UApo N $\times 100$, Olympus) with a numerical aperture of 1.49 configured for total internal reflection fluorescence microscopy. The fluorescence light collected by the objective was filtered to suppress the residual illumination light using a combination of a dichroic mirror (493/574 nm BrightLine, Semrock) and an emission filter (405/488/568 nm StopLine, Semrock). The fluorescence light was detected by an EMCCD camera (iXon DU-897, Andor). The back-projected pixel size was 105 nm. An adaptive optics system (Micao 3D-SR, Imagine Optics) and an optical system (DV2, Photometrics) equipped with a dichroic mirror (617/73 nm BrightLine, Semrock) were placed in front of the EMCCD camera. The Micao 3D-SR system was used to compensate for aberrations and the DV2 system was used to split the fluorescence light into a green and red-colour channel that were each sent to a separate half of the camera chip.

Live-cell imaging was carried out on a custom built microscope equipped with a temperature and CO_2 controlled incubator for live-cell imaging[20]. Three continuous wave laser sources were used for excitation/activation: a 120 mW 405 nm laser beam (iBeam smart, Toptica), a 200 mW 488 nm laser beam (iBeam smart, Toptica), a 800 mW 532 nm laser beam (MLL-FN-532, Roithner Lasertechnik). The 488 and 532 nm laser beams were combined using a dichroic mirror (T495LP, Chroma), and both laser beams were combined with the 405 nm laser beam using a dichroic mirror (T425LPXR, Chroma). All three laser beams were focused by a lens into the back focal plane of the objective. We used a $\times 60$ objective (Apo N $\times 60$, Olympus) with a numerical aperture of 1.49 configured for total internal reflection fluorescence illumination. The fluorescence light collected by the objective was filtered to suppress the residual illumination light using a combination of a dichroic mirror (Z488/532/633RPC, Chroma) and an emission filter (ZET405/488/532/640 m, Chroma). The fluorescence light was detected by an EMCCD camera (iXon DU-897, Andor). The back-projected pixel size was 96 nm.

Sample preparation. The MEF cells (kindly provided by Dr Luca Scorrano) and REFs (CRL-1213, ATCC) were grown in DMEM supplemented with 10% fetal bovine serum, 1% penicillin–streptomycin, 1% non-essential amino acids and 1% glutamine, at 37 °C with 5% CO_2. The cells were transfected by electroporation (Neon Transfection System, Invitrogen), which was performed on 600,000–800,000 cells using 1 pulse of 1,350 V lasting for 35 ms. The amount of DNA used for the transfection was 2 µg for the mEos2-paxillin-22 vector, 3 µg for the mEos2-Integrin-β3-N-18 vector, and 5 µg for the psCFP2-paxillin-22 vector.

For fixed-cell experiments, a 25 mm diameter microscope cover slip (#1.5 Micro Coverglass, Electron Microscopy Sciences) was prepared by first cleaning with an oxygen plasma for 5 min and then incubated with PBS containing 50 µg ml^{-1} fibronectin (Bovine Plasma Fibronectin, Invitrogen) for 30 min at 37 °C. To remove the excess of fibronectin, the cover slip was washed with PBS. The transfected cells were seeded on the cover slip and grown in DMEM supplemented with 10% fetal bovine serum, 1% non-essential amino acids and 1% glutamine, at 37 °C with 5% CO_2. The cells were washed with PBS around 24 h after transfection, and then incubated in PBS with 4% paraformaldehyde at 37 °C for 30 min. After removing the fixative, the cells were again washed with PBS, and the cover slip was placed into a custom made holder.

For live-cell imaging, the transfected cells were seeded in a chambered cover slip system (Lab-Tek II Chambered Coverglass System, Thermo Scientific) and grown in DMEM supplemented with 10% fetal bovine serum, 1% non-essential amino acids and 1% glutamine, at 37 °C with 5% CO_2. Finally, the cells were washed with PBS around 24 h after transfection.

Imaging procedure. Fixed cells were imaged in PBS at room temperature. Before imaging, 100 nm gold nanospheres (C-AU-0.100, Corpuscular) had been added to the sample for lateral drift monitoring. Axial drift correction was ensured by a nanometre positioning stage (Nano-Drive, Mad City Labs) driven by an optical feedback system[34]. Excitation of mEos2 was done at 561 nm with ~15 mW power (as measured in the back focal plane of the objective). Imaging of psCFP2 was performed using 488 nm laser light with ~15 mW power. Both fluorescent labels were gently activated by 405 nm laser light with ~5 µW power in case of single colour imaging, while ~1.5 mW power was used for dual-colour imaging. The gain of the EMCCD camera was set at 100 and the exposure time to 50 ms. For each single colour experiment, at least 20,000 camera frames were recorded. Dual-colour imaging was performed similarly to a procedure published elsewhere[34]. First, at least 10,000 camera frames in the red channel were acquired in order to image mEos2, and subsequently the remaining population of mEos2 in the off-state was photobleached using 488 nm laser light. Finally, at least 10,000 camera frames were recorded in the green channel to image psCFP2. In addition, gold nanospheres visible in both the red and green channel were imaged to co-register the two colour channels *a posteriori*.

The live cells were imaged in DMEM with low fluorescence background (FluoroBrite DMEM, Thermo Scientific) at 37 °C with 5% CO_2. Before imaging, 100 nm gold nanospheres (C-AU-0.100, Corpuscular) were added to the sample for lateral drift correction. mEos2 was excited at 532 nm with ~8.5 mW power and activated by 405 nm laser light with ~0.6 mW power. The gain of the EMCCD camera was set at 150 and the exposure time to 10 ms. For each experiment at least 8,000 camera frames were recorded.

PALM data analysis. The recorded images were analysed by a custom written algorithm (Matlab, The Mathworks) that was adapted from an algorithm that was published elsewhere[5]. First, peaks were identified in each camera frame by filtering the frames and applying an intensity threshold. Only peaks with an intensity of at least 4 times the background were considered to be fluorescent labels or gold nanospheres. Subsequently, the peaks were fitted by maximum likelihood estimation of a 2D Gaussian point spread function (PSF)[35]. Drift was corrected in each frame by subtracting the average position of the gold nanospheres from the positions of the fluorescent labels that were localized in that frame. Co-registration of the two-colour channels was done using a second order polynomial transformation that was derived from the localizations of the gold nanospheres visible in both colour channels, using the Matlab function *cp2tform*. The theoretical localization precision for each fluorescent label was obtained from the Cramér-Rao lower bound of the maximum likelihood procedure[36]. This value was multiplied with the square root of 2 in order to account for the degradation of the localization precision caused by the electron multiplication process in the EMCCD camera[35]. The PALM images were generated either as a 2D localization number histogram or as a probability map by plotting a 2D Gaussian PSF centred on each fitted position with a standard deviation equal to the corresponding localization precision. Only positions with a localization precision between 1 and 50 nm were plotted.

SOFI data analysis. For the SOFI calculation, we adapted and enhanced the bSOFI algorithm[21] (Supplementary Note 2; Supplementary Figs 9–12). The whole input image sequence was divided into subsequences of 500 frames each. The subsequences were chosen sufficiently short to minimize the influence of photobleaching. As SOFI assumes the sample to be stationary over the investigated image subsequence, drift has to be corrected before the bSOFI processing. Tracking the positions of the gold nanospheres provides translational motion vectors in between consecutive frames. Drift was then corrected by registering the frames with sub-pixel precision using a bilinear interpolation. Co-registration of two-colour channels was done by applying the second order polynomical transform that was derived for PALM to the SOFI images. The linearization step of the bSOFI algorithm was replaced by an adaptive linearization, which takes into account blinking properties of the sample and thus enables more effective use of the available dynamic range and SNR for high-order SOFI analysis (Supplementary Fig. 9).

Simulations. For each fluorophore, a time trace was modelled, describing the number of photons emitted by a given fluorophore over time. The simulation assumed photokinetics typical for fluorescent proteins in PALM experiments (Supplementary Note 4; Supplementary Fig. 13). The intensity of a pixel at a certain time point was given by an integration of brightness from all fluorophores with a PSF that extends to that pixel at that time point. The number of photo-electrons was simulated by a Poisson distributed random number with an average value equal to the pixel value multiplied by the detection efficiency and added to the thermal noise (dark current). Gain noise and read-out noise were modelled as additive Gaussian noise. The parameters of the optical system and the camera used for simulations matched the properties of the microscope set-up. We tested two emitter densities: 800 and 1200 µm^{-2}, leading to two different scenarios (Fig. 3c,d). For each scenario, the number of photons per emitter per frame (that is, I_{on}) varied from 50 to 400 and the number of frames ranged from 500 to 20,000. In total, we generated and analysed 60 image stacks. Each image sequence was processed by a SMLM and a bSOFI algorithm. For SMLM processing, we used the FALCON algorithm[37] with the settings tuned for high densities. Using the bSOFI algorithm, images of second to sixth order were calculated. The cutoff frequency f_c was measured for every bSOFI order. With increasing order of the bSOFI analysis, the resolution increases, but the image SNR decreases which limits the highest achievable resolution. The output SOFI cutoff frequencies shown in Fig. 3c,d represent the highest cutoff frequency achieved from the measured orders of the bSOFI analysis.

Measuring the cutoff frequency. An average line profile was calculated from each simulated super-resolved output image. The one-dimensional MTF (Supplementary Note 4) was calculated as the modulus of the discrete Fourier transform of the average line profile. Each MTF curve was smoothed by a moving average filter with a window length equal to 3 to suppress fluctuations and provide a more robust estimate of the cutoff frequency. To eliminate small non-zero MTF values that are caused mostly by noise and do not contain relevant information, we subtracted a constant 0.5 from each MTF curve before normalization. Each MTF curve was normalized using the MTF corresponding to the 20,000 frames test case as a reference. The cutoff frequency is the spatial frequency where the normalized MTF curve falls below a threshold (that is a small positive constant close to zero). The threshold was determined as the value of the widefield MTF, which occurs at the theoretical cutoff frequency of a noiseless diffraction-limited imaging system given by Abbe's resolution limit.

sFRC calculation. We used the sFRC metric for analysing the images shown in Fig. 1a,b. The full raw image sequence (20,000 frames) was split into 40 subsequences of 500 frames each (Supplementary Note 1; Supplementary Fig. 14). For bSOFI, images up to the sixth order were calculated for each subsequence. These images were split into two groups and averaged within each group to generate two SOFI images. The splitting procedure is described in Supplementary Note 1. For PALM, the localizations corresponding to the selected 500 frame subsequences were pooled and used to render two independent PALM images as 2D histograms with a pixel size that is $\sim$1/6 of the real pixel size, matching the sixth order bSOFI pixel size. To minimize the effect of photobleaching during the image sequence, the recombination into two independent PALM/SOFI images was done in an alternating way, and an extra correction was applied in case of SOFI, see Supplementary Note 1. To observe the evolution of the sFRC with increasing number of frames, the calculation was repeated using an increasing amount of frames, going from 1,000 to 20,000 frames with an increment of 1,000 frames in each step. The sFRC was calculated in separate sectors with an angular extent of $\pi/12$. The results for all sectors are shown in Supplementary Fig. 3. Two selected sectors are shown in Fig. 1c.

SNR calculation. We calculated the pixel-wise SNR using a statistical approach, that is, jackknife resampling (Supplementary Note 3; Supplementary Fig. 15) on the data shown in Fig. 1a,b. For an objective comparison, PALM images were rendered as histograms with a pixel size of 105 nm (that is, the pixel size in the raw images) and SOFI images were binned on an equal pixel size before the SNR estimation. To observe the evolution of the SNR throughout the raw image sequence (20,000 frames), the calculation was repeated for an increasing number of frames, starting with 1,000 frames and adding the next 1,000 frames in each step. The SNR values as function of the number of frames are shown in Fig. 1d.

Kymograph-based analysis. The kymograph shown in Fig. 4c along the line indicated in Fig. 4b was obtained using ImageJ (National Institutes of Health). For each time point, the centre position of the focal adhesion was calculated as the centre of gravity r along the corresponding line in the kymograph, with the PALM/SOFI pixel values as weights. The focal adhesion mean velocity was determined as the slope of a linear fit to these centre positions, as a function of the time points. This procedure was repeated for four other lines parallel to the one shown in Fig. 4b. The reported focal adhesion mean velocity is the average, and the error bar represents the corresponding s.d. The direction of the kymograph was chosen as the direction of the focal adhesion mean velocity, which was determined by applying the above procedure to the x- and y-direction separately (Supplementary Fig. 16).

Data availability. All data and code are available from the corresponding author upon request.

References

1. Geiger, B., Spatz, J. P. & Bershadsky, A. D. Environmental sensing through focal adhesions. *Nat. Rev. Mol. Cell Biol.* **10,** 21–33 (2009).
2. Zaidel-Bar, R., Itzkovitz, S., Ma'ayan, A., Iyengar, R. & Geiger, B. Functional atlas of the integrin adhesome. *Nat. Cell Biol.* **9,** 858–868 (2007).
3. Franz, C. M. & Muller, D. J. Analyzing focal adhesion structure by atomic force microscopy. *J. Cell Sci.* **118,** 5315–5323 (2005).
4. Tabarin, T. *et al.* Insights into adhesion biology using single-molecule localization microscopy. *Chemphyschem* **15,** 606–618 (2014).
5. Betzig, E. *et al.* Imaging intracellular fluorescent proteins at nanometer resolution. *Science* **313,** 1642–1645 (2006).
6. Shroff, H., Galbraith, C. G., Galbraith, J. A. & Betzig, E. Live-cell photoactivated localization microscopy of nanoscale adhesion dynamics. *Nat. Methods* **5,** 417–423 (2008).
7. Smilenov, L. B., Mikhailov, A., Pelham, R. J., Marcantonio, E. E. & Gundersen, G. G. Focal adhesion motility revealed in stationary fibroblasts. *Science* **286,** 1172–1174 (1999).
8. Huang, F. *et al.* Video-rate nanoscopy using sCMOS camera-specific single-molecule localization algorithms. *Nat. Methods* **10,** 653–658 (2013).
9. Carlini, L. & Manley, S. Live intracellular super-resolution imaging using site-specific stains. *ACS Chem. Biol.* **8,** 2643–2648 (2013).
10. Shim, S. H. *et al.* Super-resolution fluorescence imaging of organelles in live cells with photoswitchable membrane probes. *Proc. Natl Acad. Sci. USA* **109,** 13978–13983 (2012).
11. Hennig, S. *et al.* Instant live-cell super-resolution imaging of cellular structures by nanoinjection of fluorescent probes. *Nano Lett* **15,** 1374–1381 (2015).
12. Annibale, P., Vanni, S., Scarselli, M., Rothlisberger, U. & Radenovic, A. Identification of clustering artifacts in photoactivated localization microscopy. *Nat. Methods* **8,** 527–528 (2011).
13. Annibale, P., Vanni, S., Scarselli, M., Rothlisberger, U. & Radenovic, A. Quantitative photo activated localization microscopy: unraveling the effects of photoblinking. *PLoS ONE* **6,** e22678 (2011).
14. Lee, S. H., Shin, J. Y., Lee, A. & Bustamante, C. Counting single photoactivatable fluorescent molecules by photoactivated localization microscopy (PALM). *Proc. Natl Acad. Sci. USA* **109,** 17436–17441 (2012).
15. Sengupta, P. & Lippincott-Schwartz, J. Quantitative analysis of photoactivated localization microscopy (PALM) datasets using pair-correlation analysis. *Bioessays* **34,** 396–405 (2012).
16. Durisic, N., Laparra-Cuervo, L., Sandoval-Alvarez, A., Borbely, J. S. & Lakadamyali, M. Single-molecule evaluation of fluorescent protein photoactivation efficiency using an in vivo nanotemplate. *Nat. Methods* **11,** 156–162 (2014).
17. Vandenberg, W., Leutenegger, M., Lasser, T., Hofkens, J. & Dedecker, P. Diffraction-unlimited imaging: from pretty pictures to hard numbers. *Cell Tissue Res.* **360,** 151–178 (2015).
18. Dertinger, T., Colyer, R., Iyer, G., Weiss, S. & Enderlein, J. Fast, background-free, 3D super-resolution optical fluctuation imaging (SOFI). *Proc. Natl Acad. Sci. USA* **106,** 22287–22292 (2009).
19. Geissbuehler, S., Dellagiacoma, C. & Lasser, T. Comparison between SOFI and STORM. *Biomed Opt. Express* **2,** 408–420 (2011).
20. Geissbuehler, S. *et al.* Live-cell multiplane three-dimensional super-resolution optical fluctuation imaging. *Nat. Commun.* **5,** 5830 (2014).
21. Geissbuehler, S. *et al.* Mapping molecular statistics with balanced super-resolution optical fluctuation imaging (bSOFI). *Opt. Nanosc.* **1,** 4 (2012).
22. Demmerle, J., Wegel, E., Schermelleh, L. & Dobbie, I. M. Assessing resolution in super-resolution imaging. *Methods* **88,** 3–10 (2015).
23. Li, D. *et al.* Extended-resolution structured illumination imaging of endocytic and cytoskeletal dynamics. *Science* **349,** aab3500 (2015).
24. Banterle, N., Bui, K. H., Lemke, E. A. & Beck, M. Fourier ring correlation as a resolution criterion for super-resolution microscopy. *J. Struct. Biol.* **183,** 363–367 (2013).
25. Nieuwenhuizen, R. P. J. *et al.* Measuring image resolution in optical nanoscopy. *Nat. Methods* **10,** 557–562 (2013).
26. Shroff, H. *et al.* Dual-color superresolution imaging of genetically expressed probes within individual adhesion complexes. *Proc. Natl Acad. Sci. USA* **104,** 20308–20313 (2007).
27. Vandenberg, W. *et al.* Model-free uncertainty estimation in stochastical optical fluctuation imaging (SOFI) leads to a doubled temporal resolution. *Biomed. Opt. Express* **7,** 467–480 (2016).
28. Gross, H., Zügge, H., Peschka, M. & Blechinger, F. *Handbook of Optical Systems, Volume 3, Aberration Theory and Correction of Optical Systems* (Wiley, 2006).
29. Cox, S. *et al.* Bayesian localization microscopy reveals nanoscale podosome dynamics. *Nat. Methods* **9,** 195–200 (2012).
30. Ovesny, M., Krizek, P., Svindrych, Z. & Hagen, G. M. High density 3D localization microscopy using sparse support recovery. *Opt. Express* **22,** 31263–31276 (2014).
31. Wang, Y., Quan, T. W., Zeng, S. Q. & Huang, Z. L. PALMER: a method capable of parallel localization of multiple emitters for high-density localization microscopy. *Opt. Express* **20,** 16039–16049 (2012).
32. Rossier, O. *et al.* Integrins beta(1) and beta(3) exhibit distinct dynamic nanoscale organizations inside focal adhesions. *Nat. Cell Biol.* **14,** 1057–1067 (2012).
33. Stehbens, S. J. *et al.* CLASPs link focal-adhesion-associated microtubule capture to localized exocytosis and adhesion site turnover. *Nat. Cell Biol.* **16,** 558–570 (2014).
34. Annibale, P., Scarselli, M., Greco, M. & Radenovic, A. Identification of the factors affecting co-localization precision for quantitative multicolor localization microscopy. *Opt. Nanosc.* **1,** 9 (2012).
35. Mortensen, K. I., Churchman, L. S., Spudich, J. A. & Flyvbjerg, H. Optimized localization analysis for single-molecule tracking and super-resolution microscopy. *Nat. Methods* **7,** 377–381 (2010).
36. Ober, R. J., Ram, S. & Ward, E. S. Localization accuracy in single-molecule microscopy. *Biophys. J.* **86,** 1185–1200 (2004).
37. Min, J. H. *et al.* FALCON: fast and unbiased reconstruction of high-density super-resolution microscopy data. *Sci. Rep.* **4,** 4577 (2014).

Acknowledgements

The MEF cells were kindly provided by Dr Luca Scorrano. The mEos2-paxillin-22, mEos2-Integrin-β3-N-18, and psCFP2-paxillin-22 vectors were kindly provided by Dr Michael Davidson. H.D. and A.R. acknowledge the support of the Max Planck-EPFL Center for Molecular Nanoscience and Technology. A.R. and T.La. acknowledge the support of the Horizon 2020 project AD Gut (SEFRI 16.0047). We highly appreciate the partial funding by the Swiss National Science Foundation (SNSF, http://www.snf.ch/) under grants 200020-159945 and 205321-138305. T.Lu. acknowledges a SCIEX scholarship (13.183) and a Czech Technical University student grant (SGS16/167/OHK3/2T/13).

Author contributions

H.D., T.Lu., T.La. and A.R. conceived the study. T.Lu., T.La. and D.S. developed the MTF analysis. T.Lu. performed the simulations. H.D. and L.F. prepared the samples.

H.D. performed the fixed-cell experiments, H.D. and A.S. performed the live-cell experiments. T.Lu. developed the enhanced bSOFI algorithm. T.Lu. and H.D. analysed the data. W.V., M.L. developed the Jackknife code. D.S., W.V., P.D., J.H. and M.L. provided research advice. H.D., T.Lu., T.La. and A.R. wrote the paper. All authors reviewed and approved the manuscript.

Additional information

Supplementary Information accompanies this paper at http://www.nature.com/naturecommunications

Competing financial interests: The authors declare no competing financial interests.

Reprints and permission information is available online at http://npg.nature.com/reprintsandpermissions/

How to cite this article: Deschout, H. *et al.* Complementarity of PALM and SOFI for super-resolution live-cell imaging of focal adhesions. *Nat. Commun.* **7**, 13693 doi: 10.1038/ncomms13693 (2016).

Publisher's note: Springer Nature remains neutral with regard to jurisdictional claims in published maps and institutional affiliations.

PLOS ONE

RESEARCH ARTICLE

SOFI Simulation Tool: A Software Package for Simulating and Testing Super-Resolution Optical Fluctuation Imaging

Arik Girsault[1☯], Tomas Lukes[1,3☯], Azat Sharipov[1], Stefan Geissbuehler[1], Marcel Leutenegger[1¤], Wim Vandenberg[2], Peter Dedecker[2], Johan Hofkens[2], Theo Lasser[1]*

1 Laboratoire d'Optique Biomédicale, Ecole Polytechnique Fédérale de Lausanne, Lausanne, Switzerland, **2** Department of Chemistry, University of Leuven, Celestijnenlaan, Heverlee, Belgium, **3** Department of Radioelectronics, Faculty of Electrical Engineering, Czech Technical University in Prague, Prague, Czech Republic

☯ These authors contributed equally to this work.
¤ Current address: Abteilung NanoBiophotonik, Max-Planck-Institut für biophysikalische Chemie, Göttingen, Germany
* theo.lasser@epfl.ch

OPEN ACCESS

Citation: Girsault A, Lukes T, Sharipov A, Geissbuehler S, Leutenegger M, Vandenberg W, et al. (2016) SOFI Simulation Tool: A Software Package for Simulating and Testing Super-Resolution Optical Fluctuation Imaging. PLoS ONE 11(9): e0161602. doi:10.1371/journal.pone.0161602

Editor: Vadim E. Degtyar, University of California Berkeley, UNITED STATES

Received: May 19, 2016

Accepted: August 8, 2016

Published: September 1, 2016

Data Availability Statement: Software package and a user guide are freely available at http://lob.epfl.ch/sofitool/. The software is now freely available also at GitHub public repository according to Plos One recommendation for software sharing. https://github.com/lob-epfl/sofitool.

Funding: This research was supported by the Swiss National Science Foundation (SNSF, http://www.snf.ch/en) under grants 200020-159945/1 and 205321-138305/1. Tomas Lukes acknowledges a SCIEX scholarship (13.183).

Abstract

Super-resolution optical fluctuation imaging (SOFI) allows one to perform sub-diffraction fluorescence microscopy of living cells. By analyzing the acquired image sequence with an advanced correlation method, i.e. a high-order cross-cumulant analysis, super-resolution in all three spatial dimensions can be achieved. Here we introduce a software tool for a simple qualitative comparison of SOFI images under simulated conditions considering parameters of the microscope setup and essential properties of the biological sample. This tool incorporates SOFI and STORM algorithms, displays and describes the SOFI image processing steps in a tutorial-like fashion. Fast testing of various parameters simplifies the parameter optimization prior to experimental work. The performance of the simulation tool is demonstrated by comparing simulated results with experimentally acquired data.

Introduction

The emergence of sub-diffraction fluorescence microscopy [1–5] has opened the door for novel insights in the life sciences by imaging features well beyond the diffraction limit [6]. Super-resolved single molecule localization methods such as photoactivation localization microscopy (PALM) [7] and stochastic optical reconstruction microscopy (STORM) [8] rely on stochastic emissions of photon bursts produced by independently blinking emitters. PALM and STORM analyze a sequence of image frames showing sparse sub-sets of emitting labels such that the emitters can be localized individually. The emitter localizations are then combined into a spatially super-resolved image of the sample.

In contrast to this frame-by-frame localization, super-resolution optical fluctuation imaging (SOFI) [9, 10] exploits the image sequence as a whole by using higher order statistics, i.e. higher

Competing Interests: The authors have declared that no competing interests exist.

order cross-cumulants to analyze the temporal fluctuations of blinking emitters for generating super-resolved images. The resolution enhancement increases with the growing cumulant order in all three spatial dimensions [11]. Balanced SOFI (bSOFI), an extension of SOFI, combines the information content of different cumulant orders further and allows one to extract physically meaningful parameters like density, brightness and blinking frequency of the observed blinking emitters [12].

Sample preparation for super-resolution imaging and an optimized choice of image acquisition parameters is often a tedious process requiring experience and several trials before a suitable parameter set is found. This work attempts to shorten this task by providing a simulation tool allowing a qualitative assessment of SOFI under various conditions and to assist the user to better understand the full chain of processing steps for SOFI. The simulator can be used for optimizing various experimental parameters such as blinking rate, labeling density, as well as system parameters of the microscope and camera prior the final imaging.

The SOFI principle

SOFI applies high order nonlinear statistics to exploit the temporal blinking sequence of fluorescent emitters [9, 10]. More precisely, SOFI is based on calculating spatio-temporal cross-cumulants to obtain a 3D super-resolved, background-free and noise-reduced image using a conventional widefield microscope. As stated in the work initiated by J. Enderlein [9], the fluctuating emitters should fulfill the following conditions:

1. The markers should switch between at least two optically distinguishable states, e.g. a dark and a bright state.
2. Each emitter switches between the states repeatedly and independently in a stochastic manner.
3. The point-spread image of each emitter has to extend over several camera pixels.

The image intensity of a randomly blinking emitter is spatio-temporally correlated with itself but uncorrelated with neighboring signals. Images of stochastically blinking emitters are recorded such that the PSF is spread over several camera pixels. As a consequence, the intensities recorded by each camera pixel over which the PSF spreads are likewise spatio-temporally correlated.

Fig 1 displays the general SOFI principle. By acquiring a stack of images, a time trace for each pixel is obtained. These pixel time traces contain all intensity contributions of each stochastically blinking emitter.

$$I(\mathbf{r}, t) = \sum_{k=1}^{M} \epsilon_k U(\mathbf{r} - \mathbf{r}_k) s_k(t) + b(\mathbf{r}) \tag{1}$$

where $I(\mathbf{r}, t)$ denotes the intensity time trace at position $\mathbf{r}$, ϵ_k the brightness, $\mathbf{r}_k$ the position and $s_k(t)$ normalized temporal fluctuations of the k^{th}-emitter. $U(\mathbf{r})$ is the PSF and b represents a stationary background. For each pixel, the n^{th} order cumulant is calculated for a better discrimination of emitters inside the PSF volume. Cumulants provide a correlative measure exhibiting the fundamental additivity property stating that the cumulant of the sum is the sum of cumulants, i.e. the cumulant analysis disentangles the emission patterns of closely spaced emitters [13]. By

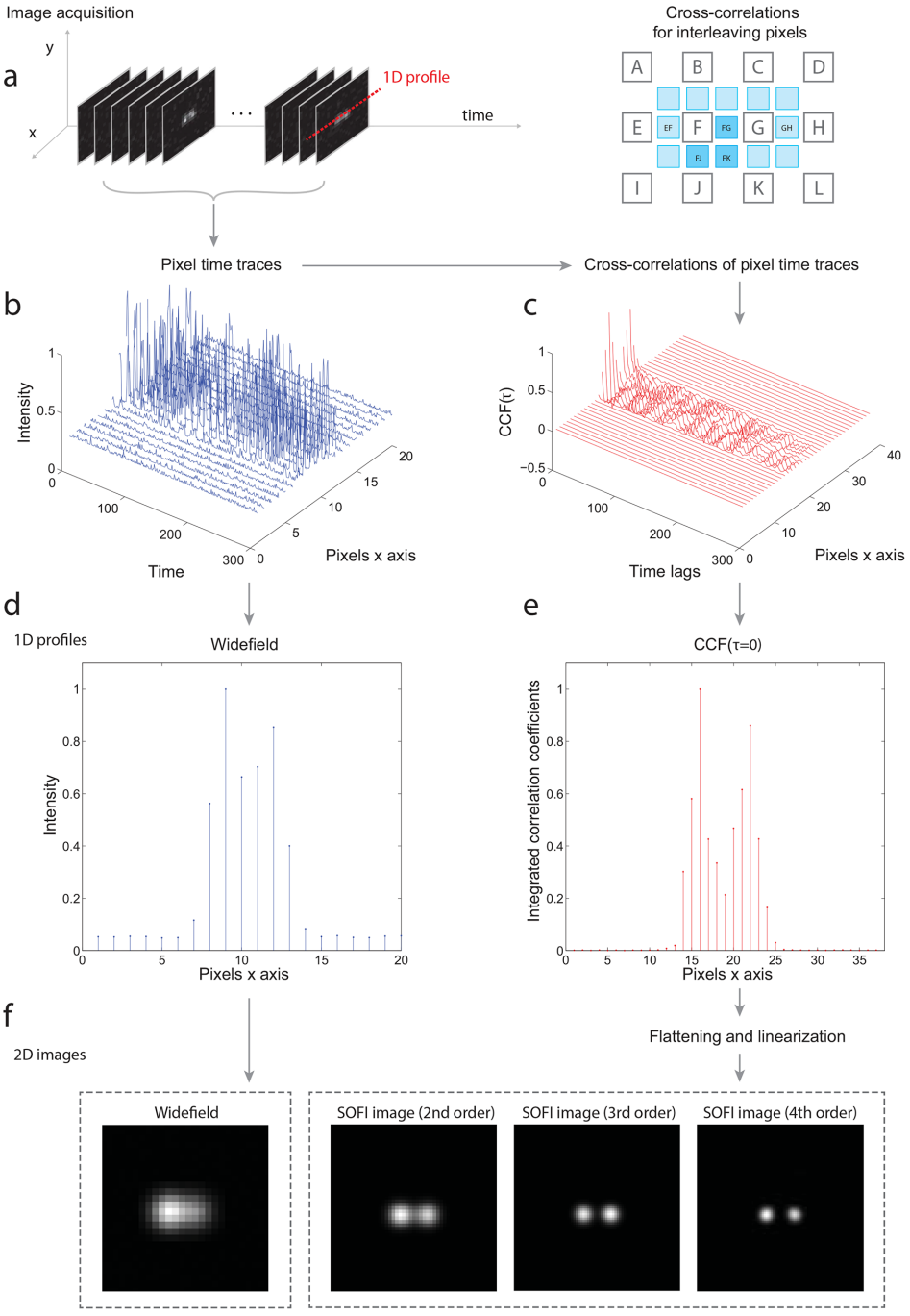
Image acquisition
a
y
x
1D profile
time
Cross-correlations
for interleaving pixels
A
B
C
D
E
EF
F
FG
G
GH
H
FJ
FK
I
J
K
L
Pixel time traces
Cross-correlations of pixel time traces
b
Intensity
Time
Pixels x axis
c
CCF(τ)
Time lags
Pixels x axis
d
1D profiles
Widefield
Intensity
Pixels x axis
e
CCF(τ=0)
Integrated correlation coefficients
Pixels x axis
Flattening and linearization
f
2D images
Widefield
SOFI image (2nd order)
SOFI image (3rd order)
SOFI image (4th order)

Fig 1. The SOFI principle in a one dimensional example. (a) 1D profile is taken from the input image sequence of two blinking emitters. (b) Corresponding 1D intensity time traces. (c) 2^{nd} order cross-cumulants calculated from the intensity time traces for all time lags. In practice, mainly the zero-time lag ($\tau = 0$) is used. Using cross-cumulants, the interleaving pixels are also calculated. Note that the 2^{nd} order cross-cumulant is equivalent to cross-correlation. (d) The widefield image (the temporal average of intensity time traces). (e) The 2^{nd} order cross-cumulants for $\tau = 0$. (f) The resulting 2D SOFI images up to the 4th cumulant order after flattening and linearization.

doi:10.1371/journal.pone.0161602.g001

applying the n^{th} order cumulant to the Eq (1), we obtain

$$\begin{aligned}\kappa_n\{I(\mathbf{r},t)\}(\tau) &= \kappa_n\left\{\sum_{k=1}^{M}\epsilon_k U(\mathbf{r}-\mathbf{r}_k)s_k(t)+b(\mathbf{r})\right\}(\tau)\\ &= \sum_{k=1}^{M}\kappa_n\{\epsilon_k U(\mathbf{r}-\mathbf{r}_k)s_k(t)\}(\tau)+\kappa_n\{b(\mathbf{r})\}(\tau)\\ &= \sum_{k=1}^{M}\epsilon_k^n U^n(\mathbf{r}-\mathbf{r}_k)\kappa_n\{s_k(t)\}(\tau).\end{aligned} \quad (2)$$

For an n^{th} order cumulant, the PSF is raised to the n^{th} power. In consequence, the spatial resolution is improved by a factor of $\sqrt{n}$ [9]. Therefore, increasing the cumulant order yields an image with an enhanced spatial resolution. Since a multiplication in the spatial domain corresponds to a convolution in the spatial frequency domain, the cut-off frequency of $U^n(\mathbf{r})$ is in principle n-times higher than that of $U(\mathbf{r})$. Consequently, by applying deconvolution and a subsequent rescaling, the cumulant image exhibits up to an n-fold resolution improvement [10].

An n^{th} order cumulant does not contain lower order correlation contributions which would hamper the resolution enhancement [9]. As an additional characteristic of cumulants, any non-fluctuating background is strongly suppressed. Additionally, SOFI processing, which relies on cross-cumulants, reduces uncorrelated noise [9, 10].

Materials and Methods

Sample preparation

Prior to transfection, HeLa [14] cells (American Type Culture Collection, ATCC CCL2) were incubated at 37°C with 5% CO_2 using Minimum Essential Medium with Earles salts, L-glutamine, sodium bicarbonate complemented with 10% fetal bovine serum, 1× penicilin-streptomycin, 1× GlutaMAX, 1× MEM Non-Essential Amino Acids Solution (LifeTechnologies products). 4-well Nunc Lab-Tek II Chambered Coverglass (Thermo Fisher Scientific) was used as a chamber for the HeLa cells. Live HeLa cells were transfected with a pMD-Vim-Dreiklang plasmid using FuGENE 6 transfection reagent (Promega) and images were acquired at room temperature.

Microscope setup

The microscope setup comprised a 60× water-immersion objective with a numerical aperture of 1.2 (UPLSAPO 60XW, Olympus), a green DPSS laser (MLL-FN-532, 800mW, Roithner Lasertechnik) for excitation and a 405nm diode laser (iBeam smart, 405 120mW, Toptica) for reactivation and tuning the blinking rate. 3D multiplane imaging was performed with a custom-built microscope setup presented in [11]. We used three 50:50 beam splitters (BS013, Thorlabs) and two sCMOS cameras (ORCA Flash 4.0, Hamamatsu). For 2D imaging, we used

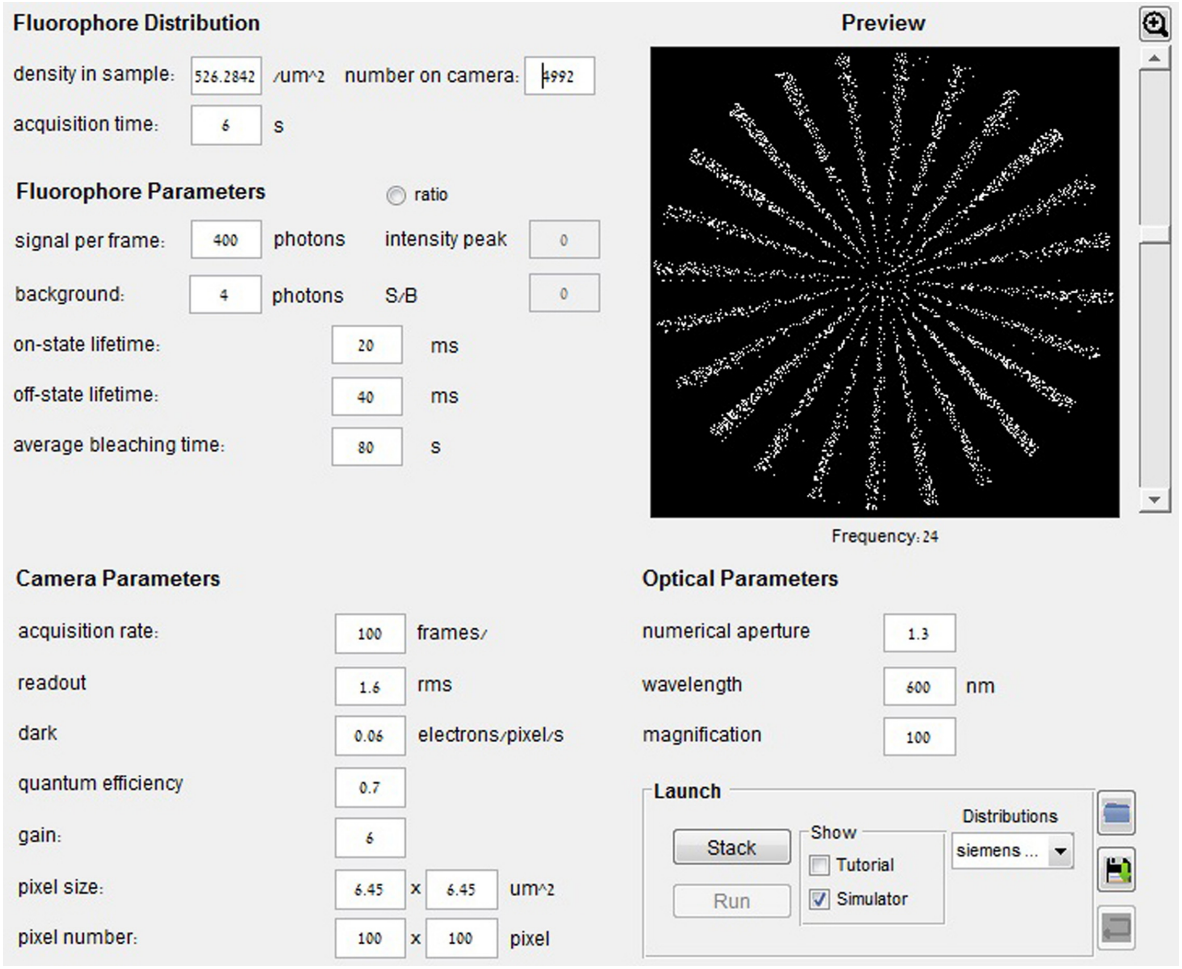

Fig 2. Screenshot of the main menu of the SOFI simulation tool. The user can specify the fluorophore distribution, various parameters of the fluorophores, camera and optics. For more details, see S1 Appendix.

doi:10.1371/journal.pone.0161602.g002

an additional 365nm illumination from a LED to tune the switching kinetics of the fluorescent protein Dreiklang [15] and an EMCCD camera (Andor iXon DU 897).

Results

The SOFI simulation tool

We developed an simulation tool equipped with a graphical user interface (GUI). The microscope settings and the fluorescent sample can be investigated prior the experimental work. For more details about the GUI in Fig 2, please refer to the S1 Appendix. The software written in MATLAB is freely available together with a user manual at the website [16].

Simulated data sets

The simulation starts by generating randomly placed emitters given by user-defined parameters such as the spatial density and spatial distributions. For each emitter, the blinking behaviour is modelled as a time-continuous Markovian process with an average blinking rate of $k = \frac{1}{\tau_{on}+\tau_{off}}$. For the experiments, we further describe the blinking rate by the on-time ratio defined as

$$\rho_{on} = \frac{\tau_{on}}{\tau_{off}} \tag{3}$$

The contribution $\nu(x, y)$ of each fluorophore is given as [17]

$$\nu(x, y|\hat{x}, \hat{y}, \hat{\sigma}_{xy}) = I_x I_y \tag{4}$$

$$\begin{aligned} I_x &= \frac{1}{2}\mathrm{erf}\left(\frac{x-\hat{x}+\frac{1}{2}}{\sqrt{2}\hat{\sigma}_{xy}}\right) - \frac{1}{2}\mathrm{erf}\left(\frac{x-\hat{x}-\frac{1}{2}}{\sqrt{2}\hat{\sigma}_{xy}}\right) \\ I_y &= \frac{1}{2}\mathrm{erf}\left(\frac{y-\hat{y}+\frac{1}{2}}{\sqrt{2}\hat{\sigma}_{xy}}\right) - \frac{1}{2}\mathrm{erf}\left(\frac{y-\hat{y}-\frac{1}{2}}{\sqrt{2}\hat{\sigma}_{xy}}\right) \end{aligned}$$

where $(\hat{x}, \hat{y})$ describe the position related to the discrete pixel grid, i.e. within a circle of radius $3\hat{\sigma}_{xy}$. The PSF is assumed to be a symmetric 2D Gaussian with a standard deviation $\hat{\sigma}_{xy}$ determined by user-defined parameters (numerical aperture, camera pixel size and wavelength). The time varying brightness is generated for each blinking fluorophore. The signal per frame is obtained by summing contributions of all fluorophores at that time point. This procedure is performed frame by frame for simulating an acquired image stack. The simulation allows to add a background. Each pixel intensity is subjected to an additive Poissonian noise contribution. The light intensity per pixel is converted to an electric charge according to the quantum efficiency and gain of the camera setting. This electrical charge is modelled by a Gamma distribution $\Gamma(k, g)$. Its shape k is given by the number of photons registered by each camera pixel and g is the camera gain. Finally, Gaussian noise with a standard deviation related to dark noise is added.

The program also includes a parameter which sets the characteristic time during which the fluorophore stays emissive before bleaching (the average bleaching time). The simulation models overall bleaching composed of switching fatigue and classical bleaching via excited states. Under constant illumination, as typically applied in SOFI, photo-switching and fluorescence excitation are proportional, such that our model describes the photo-bleaching satisfactorily well. The average bleaching time can be estimated from an experiment by an exponential fit to the plotted average fluorescence per frame. In contrast to the simulation, an initial transient can be present in a measurement until the fluorophores reached the dynamic switching equilibrium. The average fluorescence should then fade approximately exponentially towards an eventual background value.

In the simulation, all emitters exhibit the same on-state lifetime τ_{on} and off-state lifetime τ_{off}. However in practice, the blinking statistics may spatially vary across the biological sample in a sample dependent yet uncontrollable manner.

Implemented algorithms

The simulation tool incorporates SOFI and bSOFI algorithms [12]. Fig 3 shows the principle of the calculation of spatio-temporal cross-cumulants. By using spatial cross-cumulants, virtual

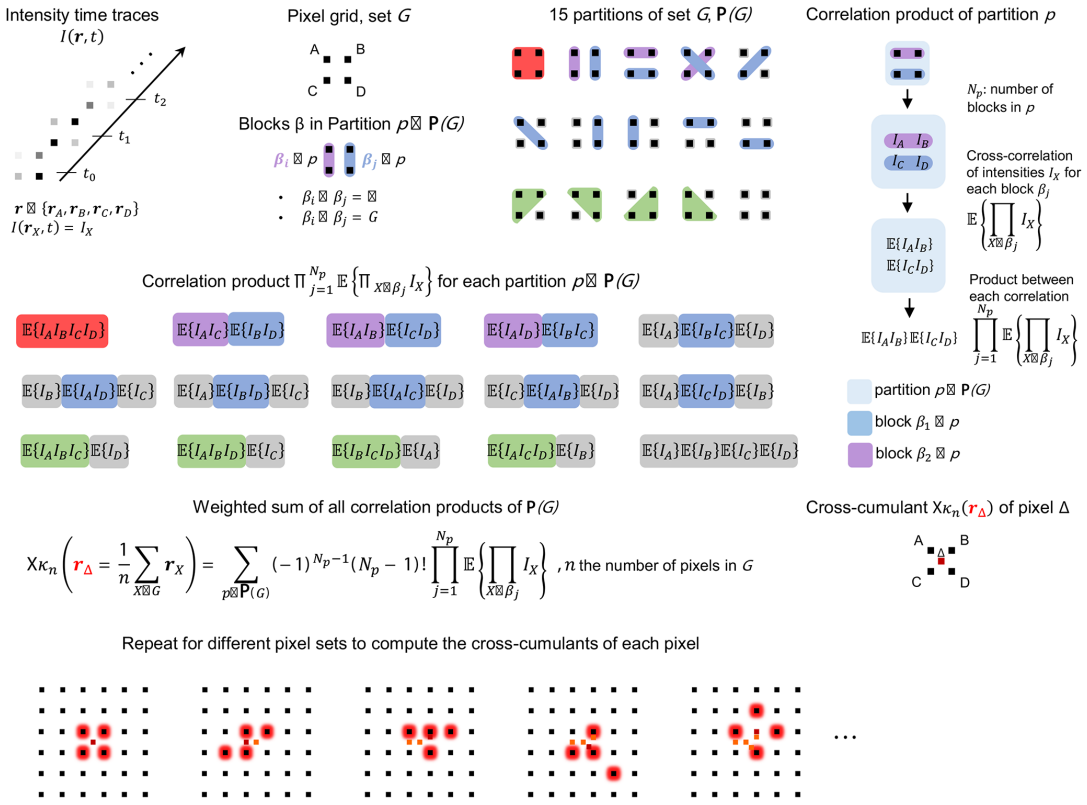

Fig 3. SOFI algorithm, cross-cumulant calculation. The n^{th} order cross-cumulant κ_n of a pixel δ is calculated as a weighted sum over all partitions of a set G of n pixels. The position of pixel δ is given by the geometrical mean of the n pixels within G. By using different sets of n pixels, the n^{th} order cross-cumulant of an arbitrary large pixel grid can be calculated. Formulas are shown for any n and sketches for $n = 4$.

doi:10.1371/journal.pone.0161602.g003

pixels can be calculated in between the physical camera pixels leading to an image with a finer sampling grid [10]. A subsequent flattening operation corrects for differences in brightness between the physical pixels and virtual pixels of raw cumulants. The cumulant analysis leads to a nonlinear response to the brightness of fluorophores. The bSOFI algorithm introduces a linearization step for rescaling and linearizing the brightness response.

The simulation tool also incorporates a basic STORM algorithm [18] consisting of segmentation of each frame and subsequent localization of single molecules using Gaussian fitting methods. The image segments of a frame are generated by first applying a Laplacian of a Gaussian filter in order to reduce noise and to enhance the single emitter pattern (including a background subtraction). Once the image is segmented, a fitting procedure is performed on the raw data. An unweighted least-squares optimization based on the Levenberg-Marquardt algorithm estimates the amplitude, position, width, and background signal for each molecule. The initial position used to initialize Gaussian fit is determined by estimating the center of gravity of each image segment. Finally, estimates of width and amplitude deviating significantly from their

expected values are discarded and a super-resolved STORM image is generated. The simulation tool also provides FALCON [19], an algorithm for STORM which combines a sparsity-promoting formulation with a Taylor approximation of the PSF for high-density imaging.

Simulation examples

We simulated various specific situations: standard conditions (i.e. conditions under which STORM is able to resolve individual emitters), short acquisition time, short off-state lifetime of the emitters, low signal-to-noise ratio (SNR), and high-labelling density. Reversibly photoswitchable fluorescent proteins have on-off duty cycles in the order of 0.1 in contrast to organic dyes with on-off duty cycles much smaller ($\lesssim 0.01$) [20]. Fig 4 shows the results for widefield, bSOFI, and FALCON STORM. For these simulations, we assumed fluorescent proteins and we set the on-time ratio to 0.1. Regarding the various conditions, bSOFI gave reliable results and seems to be well suited for photoswitchable proteins. The dark-state lifetime does not need to exceed the on-state lifetime and only needs to be on the order of the frame exposure time, which is in agreement with previous findings [18].

Fig 5 shows simulated structures such as filaments labelled with a relatively high density of emitters of $1000/\mu m^2$. In the case of a sufficiently long off-state life time of the emitters (on-time ratio $\lesssim 0.01$), strong signals, and high number of frames ($\approx$10000), STORM provides a high resolution enhancement, whereas SOFI can be useful even if these conditions are not met. The simulations reveal a good performance for bSOFI even in the case of a short off state lifetime of the blinking molecules and a relatively short acquisition time.

The deconvolution step in bSOFI helps to exploit the maximum potential resolution improvement given by the order of the cumulant analysis, but it comes at the price of introducing common deconvolution artifacts. Deconvolution may cause ringing artifacts due to conversion of a discontinuous signal into Fourier space. These ringing artifacts appear mostly along sharp edges or points. For sufficiently high signals (SNR approx. 20dB), the artifacts have very low values and can be neglected. With increasing order of the SOFI analysis, resolution improvement also increases, but the SNR of super-resolved images decreases. This effect limits the highest resolution achievable in practice. The short acquisition case represents unfavorable conditions for the 7th order bSOFI shown in Fig 4. In that case, it is better to use a lower order SOFI analysis. Fig 6 shows bSOFI images of different orders. For lower order bSOFI images, the ringing artifacts are less pronounced and the two points in the top right corner are properly separated. Both STORM and SOFI have a range of optimal conditions. Our simulation tool can be used to quickly check various conditions and the effect on the output super-resolved images.

Experimentally acquired images of live HeLa cells compared to simulations

We performed an experiment comparing simulated data to experimentally acquired data. Parameters of the experimentally acquired images were measured and used to set the simulation parameters in the GUI. The measured parameters (shown in Fig 7) were the peak signal (I_{peak}), the peak signal to background ratio (S/B), molecular on-time ratio Eq (3) of Dreiklang fluorescent protein, and molecular density.

Fig 7a, 7b and 7c shows experimentally acquired images of Dreiklang-labelled vimentin networks in HeLa cells. By decreasing the 405nm illumination intensity, and increasing the 365nm intensity at the same time, the on-time ratios of Dreiklang can be tuned. The estimated on-time ratios in the acquired image sequences were 0.02, 0.05, and 0.2 accordingly. On-time ratios of Dreiklang were measured in live cells using a procedure described in [11]. An average image from each acquired image stack was calculated and thresholded by an iterative threshold

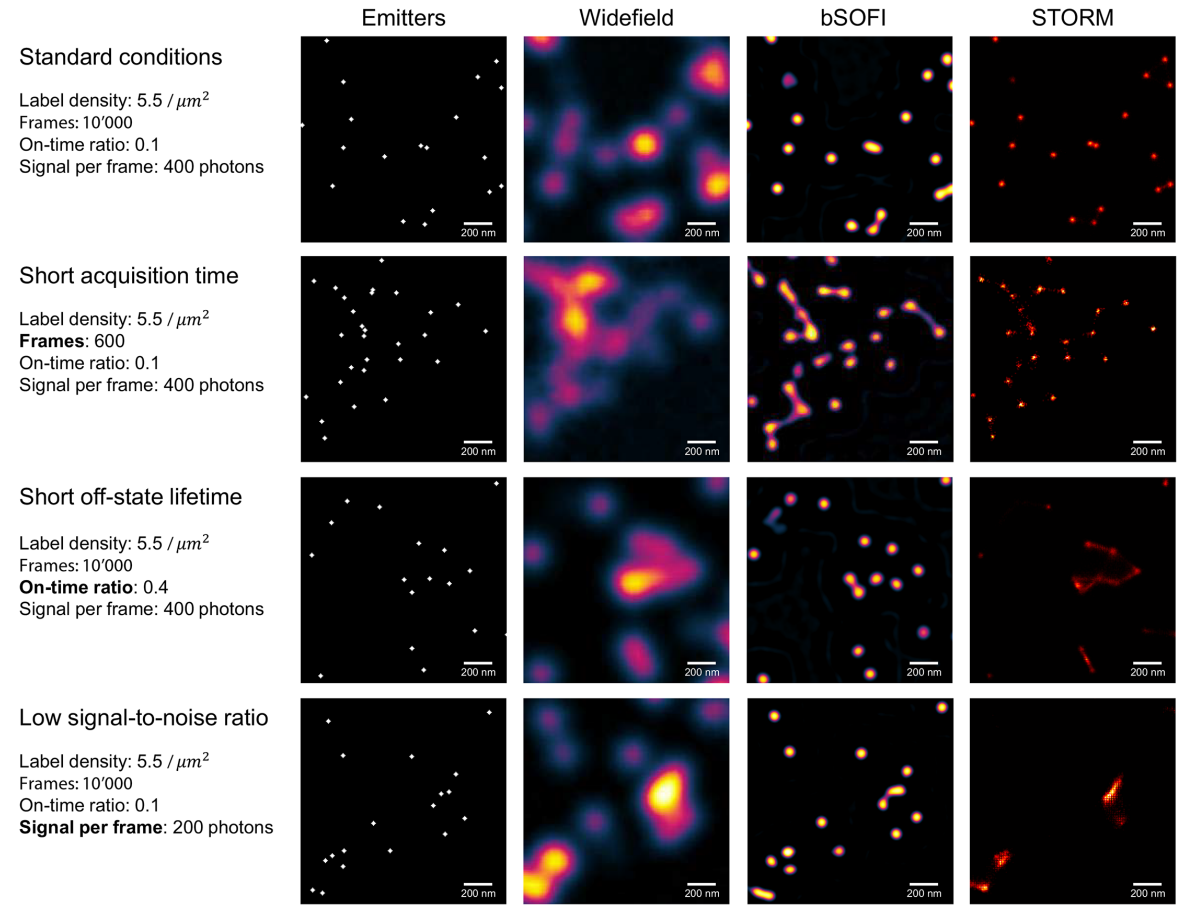

Fig 4. Simulation examples. Widefield, SOFI and FALCON STORM images with the generated emitter distributions for different imaging conditions. *Standard conditions* represent a scenario in which the simulator displays comparable performance for FALCON and SOFI in terms of resolution enhancement. All following experimental scenarios deviate from the standard conditions as follows: *Short off-state lifetime*, the sample is composed of emitters with fast off-switching kinetics; *Short acquisition time*, the super-resolution images are generated from an image sequence of only 600 frames; *low SNR*, the number of photons emitted per switching event per emitter is low which results in low signal-to-noise ratios (8 dB). Emitters shown in the left column are enlarged for the visualization purposes. All parameters of the standard conditions can be found in the S1 Appendix and on our project website [16].

doi:10.1371/journal.pone.0161602.g004

selection method [21] in order to generate signal and background masks. The estimated SNRs and signal-to-background ratios (S/Bs) were measured from the average images according to the procedure described in [22] and used as simulation parameters. Under normal conditions in cells, we assume a few hundreds to thousand Dreiklang per micrometer of fiber length. For this simulation example, we set the density to 600 fluorescent proteins per micrometer. Number of frames of the simulated image sequence was set to 1000. Fig 7a, 7b, 7d and 7e shows two situations which lead to high quality images, and Fig 7c and 7f shows a situation which resulted in low quality images.

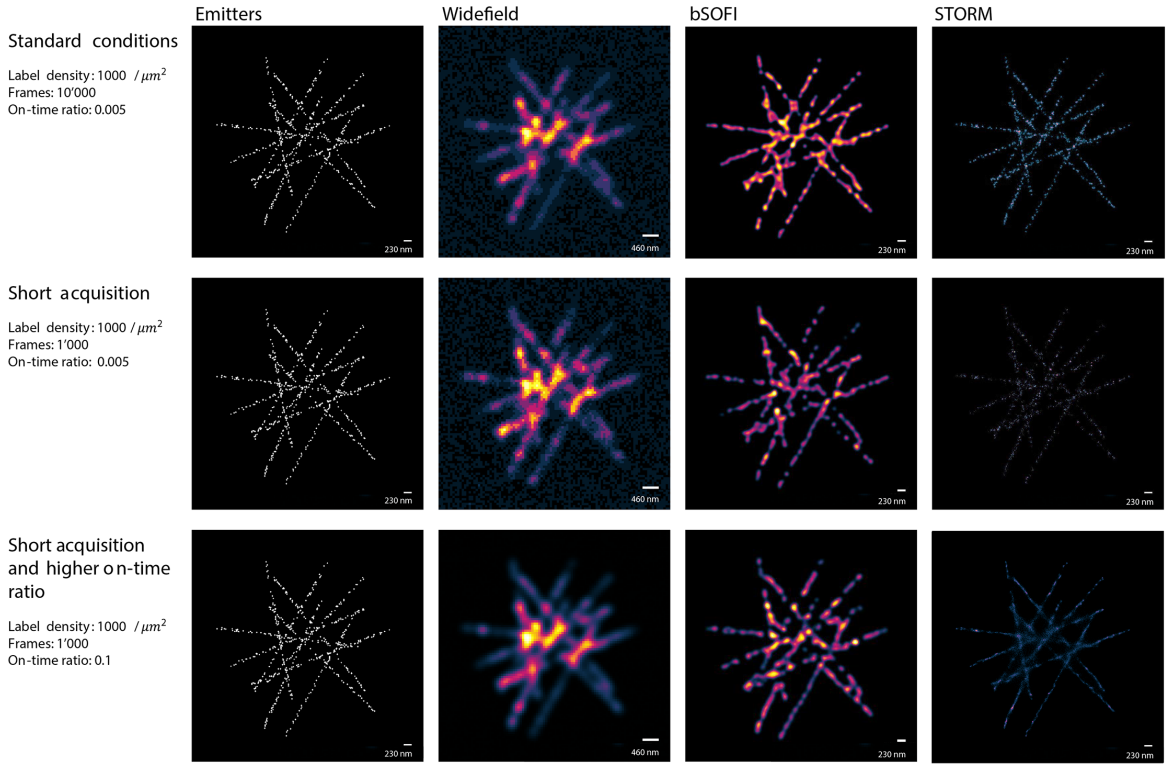

Fig 5. High-labelling density simulations. Widefield, SOFI and FALCON STORM images of the simulated structures labelled with a relatively high density of emitters (1000/μm^2) *Standard conditions* represent a scenario well suited for STORM. in the case of *Short acquisition time*, the super-resolution images are generated from an image sequence of only 1000 frames. *Short acquisition time and higher on-time ratio* represent a situation with very high density of activated emitters per frame which makes it challenging for STORM algorithms. Emitters shown in the left column are enlarged for the visualization purposes. All parameters of the standard conditions can be found in the S1 Appendix and on our project website [16].

doi:10.1371/journal.pone.0161602.g005

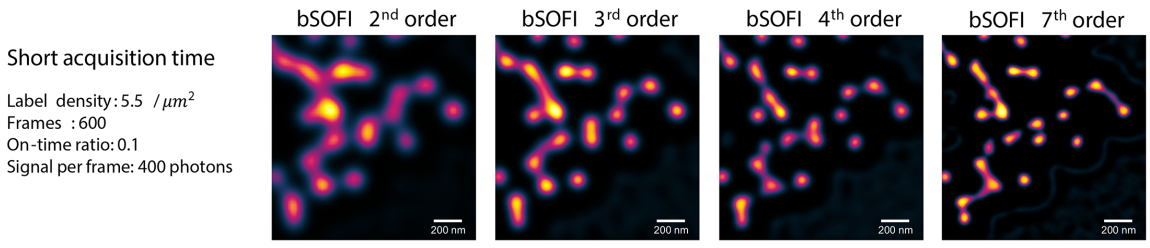

Fig 6. Balanced SOFI (bSOFI) images of different orders for the test case with only 600 input frames. With increasing order of the SOFI analysis, resolution improvement also increases, but higher orders generally require more input frames in order to avoid apparent artifacts.

doi:10.1371/journal.pone.0161602.g006

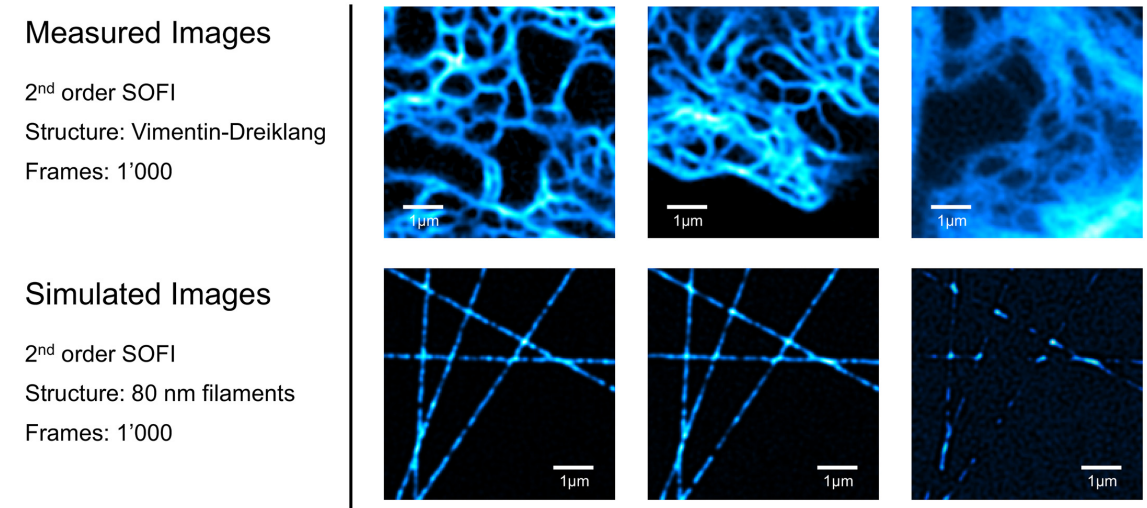

On-time ratio	0.02	0.05	0.2
SNR[dB]	13.2	15	9.5
S/B	2.2	2.4	1.8
Ipeak	9876	9134	4325

Fig 7. Experimental data compared to simulations. (a)-(d) 2^{nd} order bSOFI images computed from experimental data. (e)-(h) 2^{nd} order bSOFI images computed from simulated data. Table below the figure shows the parameters estimated from experimental data and used for the simulations. S/B and Ipeak denote respectively the signal-to-background ratio and the intensity peak of the average images. Density for simulation was set to 600 fluorescent proteins per micrometer.

doi:10.1371/journal.pone.0161602.g007

Conclusions

We developed a novel software for modeling the imaging procedure of super-resolution optical fluctuation imaging. The software is equipped with a user friendly graphical interface which allows the user to generate simulated image stacks and calculate SOFI and STORM super-resolution images. The processing steps of SOFI are visualized and explained in a tutorial-like way. We compared simulated results with experimentally acquired data of living HeLa cells expressing vimentin-Dreiklang. We demonstrated that the software is able to predict, through simulation, the image quality. The software allows the user to quickly test numerous image acquisition settings prior to experimental work. For more information about the software, see S1 Appendix.

Supporting Information

S1 Appendix. User Manual. Documentation for installing and using the software.
(PDF)

S2 Appendix. Software package. Zip file which includes the software package. The software is written in MATLAB, equipped with graphical user interface and freely available together with a user manual also at [16].
(ZIP)

Acknowledgments

We thank Stefan Jakobs for kindly providing the Vimentin plasmids and Gisou van der Goot for kindly providing the HeLa cells.

Author Contributions

Conceptualization: T. Lasser.

Data curation: AG AS.

Formal analysis: SG ML.

Funding acquisition: T. Lasser.

Investigation: AG T. Lukes AS.

Methodology: AG T. Lukes T. Lasser.

Project administration: T. Lasser JH.

Resources: AS T. Lasser.

Software: AG T. Lukes ML.

Supervision: T. Lasser.

Validation: AG T. Lukes WV PD.

Visualization: AG T. Lukes T. Lasser.

Writing original draft: AG T. Lukes T. Lasser.

Writing review & editing: AG T. Lukes T. Lasser PD JH.

References

1. Hell SW, Wichmann J. Breaking the diffraction resolution limit by stimulated emission: stimulated-emission-depletion fluorescence microscopy. Optics letters. 1994; 19(11):780–782. doi: 10.1364/OL.19.000780 PMID: 19844443
2. Huang B, Bates M, Zhuang X. Super resolution fluorescence microscopy. Annual Review of Biochemistry. 2010; 78:993–1016. doi: 10.1146/annurev.biochem.77.061906.092014
3. Patterson G, Davidson M, Manley S, Lippincott-Schwartz J. Superresolution Imaging using Single-Molecule Localization. Amnu Rev Phys Chem. 2013;(3):345–367.
4. Schermelleh L, Heintzmann R, Leonhardt H. A guide to super-resolution fluorescence microscopy. Journal of Cell Biology. 2010; 190(2):165–175. doi: 10.1083/jcb.201002018 PMID: 20643879
5. Vandenberg W, Leutenegger M, Lasser T, Hofkens J, Dedecker P. Diffraction-unlimited imaging: from pretty pictures to hard numbers. Cell and Tissue Research. 2015; doi: 10.1007/s00441-014-2109-0 PMID: 25722085
6. Abbe E. Beitrage zur Theorie des Mikroskops und der mikroskopischen Wahrnehmung. Archiv für mikroskopische Anatomie. 1873; 9(1):413–418. doi: 10.1007/BF02956173
7. Betzig E, Patterson GH, Sougrat R, Lindwasser OW, Olenych S, Bonifacino JS, et al. Imaging intracellular fluorescent proteins at nanometer resolution. Science (New York, NY). 2006; 313(September):1642–1645. doi: 10.1126/science.1127344

8. Rust MJ, Bates M, Zhuang X. Sub-diffraction-limit imaging by stochastic optical reconstruction microscopy (STORM). Nature methods. 2006; 3(10):793–795. doi: 10.1038/nmeth929 PMID: 16896339
9. Dertinger T, Colyer R, Iyer G, Weiss S, Enderlein J. Fast, background-free, 3D super-resolution optical fluctuation imaging (SOFI). Proceedings of the National Academy of Sciences of the United States of America. 2009; 106(52):22287–22292. doi: 10.1073/pnas.0907866106 PMID: 20018714
10. Dertinger T, Colyer R, Vogel R, Enderlein J, Weiss S. Achieving increased resolution and more pixels with Superresolution Optical Fluctuation Imaging (SOFI). Optics express. 2010; 18(18):18875–18885. doi: 10.1364/OE.18.018875 PMID: 20940780
11. Geissbuehler S, Sharipov A, Godinat A, Bocchio NL, Sandoz PA, Huss A, et al. Live-cell multiplane three-dimensional super-resolution optical fluctuation imaging. Nature Communications. 2014; 5:5830. doi: 10.1038/ncomms6830 PMID: 25518894
12. Geissbuehler S, Bocchio NL, Dellagiacoma C, Berclaz C, Leutenegger M, Lasser T. Mapping molecular statistics with balanced super-resolution optical fluctuation imaging (bSOFI). Optical Nanoscopy. 2012; 1:4. doi: 10.1186/2192-2853-1-4
13. Mendel JM. Tutorial on higher-order statistics (spectra) in signal processing and system theory: theoretical results and some applications. Proceedings of the IEEE. 1991; 79(3):278–305. doi: 10.1109/5.75086
14. Scherer WF, Syverton JT, Gey GO. Studies on the propagation in vitro of poliomyelitis viruses. IV. Viral multiplication in a stable strain of human malignant epithelial cells (strain HeLa) derived from an epidermoid carcinoma of the cervix. The Journal of experimental medicine. 1953; 97:695–710 doi: 10.1084/jem.97.5.695 PMID: 13052828
15. Brakemann T, Stiel AC, Weber G, Andresen M, Testa I, Grotjohann T, et al. A reversibly photoswitchable GFP-like protein with fluorescence excitation decoupled from switching. Nature Biotechnology. 2011; 29(10):942–947. doi: 10.1038/nbt.1952 PMID: 21909082
16. Girsault A, Lukes T. MATLAB codes for SOFI optimization tool; 2016. http://lob.epfl.ch/sofitool/
17. Ovesný M, Křížek P, Borkovec J, Švindrych Z, Hagen GM. ThunderSTORM: a comprehensive ImageJ plug-in for PALM and STORM data analysis and super-resolution imaging. Bioinformatics (Oxford, England). 2014; 30(16):2389–2390. doi: 10.1093/bioinformatics/btu202
18. Geissbuehler S, Dellagiacoma C, Lasser T. Comparison between SOFI and STORM. Biomedical optics express. 2011; 2(3):408–420. doi: 10.1364/BOE.2.000408 PMID: 21412447
19. Min J, Vonesch C, Kirshner H, Carlini L, Olivier N, Holden S, et al. FALCON: fast and unbiased reconstruction of high-density super-resolution microscopy data_ SI. Scientific reports. 2014; 4:4577. doi: 10.1038/srep04577 PMID: 24694686
20. Dempsey GT, Vaughan JC, Chen KH, Bates M, Zhuang X. Evaluation of fluorophores for optimal performance in localization-based super-resolution imaging. Nature Methods. 2011; 8(12):1027–1036. doi: 10.1038/nmeth.1768 PMID: 22056676
21. Šonka M, Hlaváč V, Boyle R. Image Processing Analysis and Machine Vision. 2nd ed. PWS Publishing. 1998;
22. Lukeš T, Hagen GM, Křížek P, Švindrych Z, Fliegel K, Klíma M. Comparison of image reconstruction methods for structured illumination microscopy. Proc SPIE 9129. 2014;

Three-dimensional super-resolution structured illumination microscopy with maximum a posteriori probability image estimation

Tomáš Lukeš,[1,2] Pavel Křížek,[3] Zdeněk Švindrych,[3] Jakub Benda,[4] Martin Ovesný,[3] Karel Fliegel,[1] Miloš Klíma,[1] and Guy M. Hagen[3*]

[1]*Dept. of Radioelectronics, Faculty of Electrical Engineering, Czech Technical University in Prague, Technická 2, 166 27 Prague 6, Czech Republic;*
[2]*Laboratoire d'Optique Biomédicale LOB, École Polytechnique Fédérale de Lausanne, CH-1015 Lausanne, Switzerland*
[3]*Institute of Cellular Biology and Pathology, First Faculty of Medicine, Charles University in Prague, Albertov 4, 128 01 Prague 2, Czech Republic*
[4]*Institute of Theoretical Physics, Faculty of Mathematics and Physics, Charles University in Prague, V Holešovičkách 2, 180 00 Prague 8, Czech Republic*
[*]*Guy.Hagen@lf1.cuni.cz*

Abstract: We introduce and demonstrate a new high performance image reconstruction method for super-resolution structured illumination microscopy based on maximum a posteriori probability estimation (MAP-SIM). Imaging performance is demonstrated on a variety of fluorescent samples of different thickness, labeling density and noise levels. The method provides good suppression of out of focus light, improves spatial resolution, and allows reconstruction of both 2D and 3D images of cells even in the case of weak signals. The method can be used to process both optical sectioning and super-resolution structured illumination microscopy data to create high quality super-resolution images.

OCIS codes: (180.2520) Fluorescence microscopy; (230.6120) Spatial light modulators; (100.3010) Image reconstruction techniques; (100.6640) Superresolution.

References and links

1. S. W. Hell and J. Wichmann, "Breaking the diffraction resolution limit by stimulated emission: stimulated-emission-depletion fluorescence microscopy," Opt. Lett. **19**(11), 780–782 (1994).
2. E. Betzig, G. H. Patterson, R. Sougrat, O. W. Lindwasser, S. Olenych, J. S. Bonifacino, M. W. Davidson, J. Lippincott-Schwartz, and H. F. Hess, "Imaging intracellular fluorescent proteins at nanometer resolution," Science **313**(5793), 1642–1645 (2006).
3. S. T. Hess, T. P. K. Girirajan, and M. D. Mason, "Ultra-high resolution imaging by fluorescence photoactivation localization microscopy," Biophys. J. **91**(11), 4258–4272 (2006).
4. M. J. Rust, M. Bates, and X. Zhuang, "Sub-diffraction-limit imaging by stochastic optical reconstruction microscopy (STORM)," Nat. Methods **3**(10), 793–796 (2006).
5. T. Dertinger, R. Colyer, G. Iyer, S. Weiss, and J. Enderlein, "Fast, background-free, 3D super-resolution optical fluctuation imaging (SOFI)," Proc. Natl. Acad. Sci. U.S.A. **106**(52), 22287–22292 (2009).
6. S. Geissbuehler, C. Dellagiacoma, and T. Lasser, "Comparison between SOFI and STORM," Biomed. Opt. Express **2**(3), 408–420 (2011).
7. S. Geissbuehler, N. L. Bocchio, C. Dellagiacoma, C. Berclaz, M. Leutenegger, and T. Lasser, "Mapping molecular statistics with balanced super-resolution optical fluctuation imaging (bSOFI)," Opt. Nanoscopy **1**(1), 4 (2012).
8. R. Heintzmann and C. Cremer, "Laterally modulated excitation microscopy: improvement of resolution by using a diffraction grating," Proc. SPIE **3568**, 185–196 (1999).
9. M. G. L. Gustafsson, "Surpassing the lateral resolution limit by a factor of two using structured illumination microscopy," J. Microsc. **198**(2), 82–87 (2000).
10. M. G. L. Gustafsson, "Nonlinear structured-illumination microscopy: Wide-field fluorescence imaging with theoretically unlimited resolution," Proc. Natl. Acad. Sci. U.S.A. **102**(37), 13081–13086 (2005).
11. P. Kner, B. B. Chhun, E. R. Griffis, L. Winoto, and M. G. L. Gustafsson, "Super-resolution video microscopy of live cells by structured illumination," Nat. Methods **6**(5), 339–342 (2009).

#222375 - $15.00 USD Received 2 Sep 2014; revised 17 Oct 2014; accepted 18 Oct 2014; published 20 Nov 2014

12. L. M. Hirvonen, K. Wicker, O. Mandula, and R. Heintzmann, "Structured illumination microscopy of a living cell," Eur. Biophys. J. **38**(6), 807–812 (2009).
13. M. G. L. Gustafsson, L. Shao, P. M. Carlton, C. J. R. Wang, I. N. Golubovskaya, W. Z. Cande, D. A. Agard, and J. W. Sedat, "Three-dimensional resolution doubling in wide-field fluorescence microscopy by structured illumination," Biophys. J. **94**(12), 4957–4970 (2008).
14. L. Shao, P. Kner, E. H. Rego, and M. G. L. Gustafsson, "Super-resolution 3D microscopy of live whole cells using structured illumination," Nat. Methods **8**(12), 1044–1046 (2011).
15. M. A. A. Neil, R. Juškaitis, and T. Wilson, "Method of obtaining optical sectioning by using structured light in a conventional microscope," Opt. Lett. **22**(24), 1905–1907 (1997).
16. R. Heintzmann, "Structured illumination methods," in *Handbook of Biological Confocal Microscopy*, J. B. Pawley, ed., 3rd ed. (Springer, 2006), pp. 265–279.
17. F. Chasles, B. Dubertret, and A. C. Boccara, "Optimization and characterization of a structured illumination microscope," Opt. Express **15**(24), 16130–16140 (2007).
18. P. Křížek, I. Raška, and G. M. Hagen, "Flexible structured illumination microscope with a programmable illumination array," Opt. Express **20**(22), 24585–24599 (2012).
19. K. O'Holleran and M. Shaw, "Optimized approaches for optical sectioning and resolution enhancement in 2D structured illumination microscopy," Biomed. Opt. Express **5**(8), 2580–2590 (2014).
20. E. Mudry, K. Belkebir, J. Girard, J. Savatier, E. Le Moal, C. Nicoletti, M. Allain, and A. Sentenac, "Structured illumination microscopy using unknown speckle patterns," Nat. Photonics **6**(5), 312–315 (2012).
21. F. Orieux, E. Sepulveda, V. Loriette, B. Dubertret, and J.-C. Olivo-Marin, "Bayesian estimation for optimized structured illumination microscopy," IEEE Trans. Image Process. **21**(2), 601–614 (2012).
22. T. Lukeš, G. M. Hagen, P. Křížek, Z. Švindrych, K. Fliegel, and M. Klíma, "Comparison of image reconstruction methods for structured illumination microscopy," in *Proc. SPIE 9129, Biophotonics: Photonic Solutions for Better Health Care IV, 91293J (May 8, 2014)* (2014), Vol. 9129, pp. 1–13.
23. G. M. P. Van Kempen, L. J. Van Vliet, P. J. Verveer, and H. T. M. Van Der Voort, "A quantitative comparison of image restoration methods for confocal microscopy," J. Microsc. **185**(3), 354–365 (1997).
24. P. Sarder and A. Nehorai, "Deconvolution methods for 3-D fluorescence microscopy images," IEEE Signal Process. Mag. **23**(3), 32–45 (2006).
25. P. J. Verveer and T. M. Jovin, "Efficient superresolution restoration algorithms using maximum a posteriori estimations with application to fluorescence microscopy," J. Opt. Soc. Am. A **14**(8), 1696–1706 (1997).
26. P. J. Verveer, M. J. Gemkow, and T. M. Jovin, "A comparison of image restoration approaches applied to three-dimensional confocal and wide-field fluorescence microscopy," J. Microsc. **193**(1), 50–61 (1999).
27. P. Milanfar, ed., *Super-Resolution Imaging* (CRC Press, 2011), p. 490.
28. S. Chaudhuri, *Super-Resolution Imaging* (Kluwer Academic Publishers, 2000), p. 279.
29. J. W. Goodman, *Introduction to Fourier Optics*, 2nd ed. (McGraw-HIll Int., 1996).
30. G. M. Hagen, W. Caarls, K. A. Lidke, A. H. B. De Vries, C. Fritsch, B. G. Barisas, D. J. Arndt-Jovin, and T. M. Jovin, "Fluorescence recovery after photobleaching and photoconversion in multiple arbitrary regions of interest using a programmable array microscope," Microsc. Res. Tech. **72**(6), 431–440 (2009).
31. Z. Cvačková, M. Mašata, D. Staněk, H. Fidlerová, and I. Raška, "Chromatin position in human HepG2 cells: although being non-random, significantly changed in daughter cells," J. Struct. Biol. **165**(2), 107–117 (2009).
32. J. Barzilai and J. M. Borwein, "Two-point step size gradient methods," IMA J. Numer. Anal. **8**(1), 141–148 (1988).
33. M. Geissbuehler and T. Lasser, "How to display data by color schemes compatible with red-green color perception deficiencies," Opt. Express **21**(8), 9862–9874 (2013).
34. B. Thomas, M. Momany, and P. Kner, "Optical sectioning structured illumination microscopy with enhanced sensitivity," J. Opt. **15**(9), 094004 (2013).

1. Introduction

Recently, new methods have been developed which circumvent the diffraction limit of optical microscopes. These include stimulated emission depletion microscopy [1] (STED), photoactivated localization microscopy [2,3] (PALM, FPALM), stochastic optical reconstruction microscopy [4] (STORM), super-resolution optical fluctuation imaging [5–7] (SOFI), and super-resolution structured illumination microscopy (SR-SIM) [8–10]. SR-SIM offers high photon efficiency, potentially high imaging rates, relatively low hardware requirements, and compatibility with most dyes and fluorescent proteins, making it an attractive method for a broad range of studies in cell biology.

SR-SIM uses illumination patterns with high spatial frequency (close to the resolution limit of the microscope) to illuminate the sample. High frequency information contained in the sample is encoded, through aliasing, into the acquired images. By acquiring multiple images with illumination patterns of different phases and orientations, aliased components can be separated and a high-resolution image reconstructed [8,9]. Two-dimensional SR-SIM

#222375 - $15.00 USD Received 2 Sep 2014; revised 17 Oct 2014; accepted 18 Oct 2014; published 20 Nov 2014

enables a twofold resolution improvement in the lateral dimension [9,11,12], but does not provide optical sectioning. If a three-dimensional illumination pattern is used, resolution can also be improved in the axial direction [13,14].

Structured illumination microscopy has also been used for optical sectioning, but without lateral resolution enhancement (OS-SIM) [15]. Optically sectioned images can be calculated by taking the root mean square of the differences of the acquired images (square-law method), or by a form of homodyne detection [15]. Several other methods are also possible [16]. When combined with optimized illumination patterns, OS-SIM can achieve an axial resolution of ~300 nm [17,18]. This is about two to three fold better than is achievable in confocal laser scanning microscopy (CLSM) and is comparable to the axial resolution reported in 3D SR-SIM [13].

Recently, new concepts in structured illumination have appeared such as combining OS-SIM and SR-SIM by weighting Fourier space image components [19], or use of random speckle patterns for illumination the sample (blind-SIM) [20]. Orieux et al. suggested a framework for SR-SIM based on Bayesian estimation for 2D image reconstruction [21], and we previously showed that Bayesian estimation methods have several advantages over the square-law method and can achieve a performance comparable to SR-SIM methods [22].

Here we propose an image reconstruction method for SIM which provides resolution improvement in all three dimensions using two-dimensional illumination patterns. Our method, maximum a posteriori probability SIM (MAP-SIM) is based on combining, via spectral merging in the frequency domain, maximum a posteriori probability estimation (for resolution improvement) and homodyne detection (for optical sectioning). We used a microscope setup in which the illumination pattern is generated by a spatial light modulator (SLM) together with incoherent illumination. MAP-SIM does not require precise knowledge of the point spread function (PSF) which must be carefully measured in most SR-SIM approaches. Additionally, MAP-SIM does not require precise knowledge of the pattern positions in each acquired image.

2. Theory

2.1 Maximum a posteriori probability estimation

An image acquired by the microscope can be modeled as a convolution of an ideal image of a real sample with the point spread function (PSF) of the microscope. The additional noise is composed of different noise sources (e.g., photon noise, read out noise) and can be modeled by additive Gaussian noise with zero mean [23,24]. Image acquisition in structured illumination microscopy can then be described as

$$\boldsymbol{y}_k = HM_k\boldsymbol{x} + \boldsymbol{n}_k\,, \tag{1}$$

where $k = 1,\ldots,K$ indexes the sequence of illumination patterns, $\boldsymbol{y}_k$ denotes a vectorized (matrix converted into a column vector by stacking the columns of the matrix on top of each other), diffraction limited low-resolution (LR) image acquired by the camera using the *k*-th illumination pattern, $\boldsymbol{x}$ represents an unknown, vectorized high-resolution (HR) image, and $\boldsymbol{n}_k$ is a vectorized image containing additive noise; all of these vectors contain m elements. Toeplitz matrix H is an $m\times m$ matrix which models the convolution between the HR image and the PSF of the system, and M_k is an $m\times m$ diagonal matrix in which the elements represent the *k*-th illumination pattern. We model the PSF of the microscope as an Airy function, see Section 2.2.

The reconstruction of the HR image $\boldsymbol{x}$ can be performed using a Bayesian approach [21,25,26]. The maximum a posteriori estimator of $\boldsymbol{x}$ is given by maximizing the probability of the HR image represented by the observed LR images

#222375 - $15.00 USD Received 2 Sep 2014; revised 17 Oct 2014; accepted 18 Oct 2014; published 20 Nov 2014

$$\hat{\boldsymbol{x}} = \arg\max_{\mathrm{x}} \left[P\left(\boldsymbol{x} \mid \boldsymbol{y}_1, \boldsymbol{y}_2, \ldots, \boldsymbol{y}_K \right) \right]. \tag{2}$$

Applying Bayes' theorem to the conditional probability in Eq. (2) and by taking the logarithm, we obtain

$$\hat{\boldsymbol{x}} = \arg\max_{\mathrm{x}} \left[\log P\left(\boldsymbol{y}_1, \boldsymbol{y}_2, \ldots, \boldsymbol{y}_K \mid \boldsymbol{x} \right) + \log P\left(\boldsymbol{x} \right) \right]. \tag{3}$$

Because the LR images $\boldsymbol{y}_k$ are independent measurements, we can write

$$P\left(\boldsymbol{y}_1, \boldsymbol{y}_2, \ldots, \boldsymbol{y}_K \mid \boldsymbol{x} \right) = \prod_{k=1}^{K} P\left(\boldsymbol{y}_k \mid \boldsymbol{x} \right). \tag{4}$$

The additive noise $\boldsymbol{n}_k$ in Eq. (1) is modeled as white Gaussian noise with a mean of zero and variance σ^2. The density function in Eq. (4) can be expressed as

$$P\left(\boldsymbol{y}_k \mid \boldsymbol{x} \right) \propto \exp\left(-\frac{\left\| \boldsymbol{y}_k - HM_k \boldsymbol{x} \right\|^2}{2\sigma^2} \right). \tag{5}$$

Because of the presence of noise, the inversion of Eq. (1) is an ill-posed problem and some form of regularization is needed to ensure uniqueness of the solution. The regularization term in Eq. (3), provided by the density function $P\left(\boldsymbol{x} \right)$, reflects prior knowledge about the HR image, such as a positivity constraint and image smoothness. Several kinds of priors and regularization techniques have been proposed within the Bayesian framework [27]. To impose a smoothness condition and to ensure that a cost function is simple to minimize, we have adopted a term composed of finite difference approximations of the first order derivatives at each pixel location [28].

$$\log P\left(\boldsymbol{x} \right) = \Gamma\left(\boldsymbol{x} \right) = \sum_{i} \left[\left(\Delta_h \boldsymbol{x} \right)_i^2 + \left(\Delta_v \boldsymbol{x} \right)_i^2 \right]. \tag{6}$$

Here Δ_h and Δ_v are the finite difference operators along the horizontal and vertical direction of an image, and $\left(\cdot \right)_i$ denotes the *i*-th element of a vector.

Substituting Eqs. (5) and (6) into Eq. (3), the image reconstruction can be expressed as a minimization of the following cost function

$$\hat{\boldsymbol{x}} = \arg\min_{\mathrm{x}} \left[\sum_{k=1}^{K} \left\| \boldsymbol{y}_{\boldsymbol{k}} - HM_k \boldsymbol{x} \right\|^2 + \lambda \Gamma\left(\boldsymbol{x} \right) \right]. \tag{7}$$

The cost function in Eq. (7) consists of two terms. The first term describes the mean square error between the estimated HR image and the observed LR images. The second term is the regularization term. Its contribution is controlled by the parameter λ, which is a small positive constant proportional to the noise variance σ^2, and which defines the strength of the regularization. Equation (7) is minimized by gradient descent optimization methods and the estimate of the unknown image $\boldsymbol{x}$ at the $\left(n+1 \right)^{\text{th}}$ iteration is obtained as

$$\boldsymbol{x}^{(n+1)} = \boldsymbol{x}^{(n)} - \alpha^{(n)} \boldsymbol{g}^{(n)}. \tag{8}$$

Here $\alpha^{(n)}$ is the step size, $\boldsymbol{g}^{(n)}$ is the gradient of the cost function, and $n = 0, 1, 2, \ldots$ is an iteration step. Computation iteratively continues until $\left\| \alpha^{(n+1)} \boldsymbol{g}^{(n+1)} \right\| / \left\| \alpha^{(n)} \boldsymbol{g}^{(n)} \right\| < \varepsilon$, where $\varepsilon > 0$ is a user-defined stopping criterion. This enables one to stop the algorithm very quickly after only a few aggressive steps towards the minimum.

#222375 - $15.00 USD Received 2 Sep 2014; revised 17 Oct 2014; accepted 18 Oct 2014; published 20 Nov 2014

1 December 2014 | Vol. 22, No. 24 | DOI:10.1364/OE.22.029805 | OPTICS EXPRESS 29808

2.2 OTF modeling

The spatial frequency f_c at which the optical transfer function (OTF) reaches zero determines the achievable resolution of a microscope, see Fig. 1(a). We model the PSF as an Airy disk [29] which in Fourier space leads to an OTF

$$\mathrm{OTF}(\boldsymbol{f}) = \frac{1}{\pi}\left[2\cos^{-1}\left(\frac{|\boldsymbol{f}|}{f_c}\right) - \sin\left(2\cos^{-1}\left(\frac{|\boldsymbol{f}|}{f_c}\right)\right)\right], \tag{9}$$

where $\boldsymbol{f}$ is the spatial frequency. The cut off frequency f_c is estimated by calculating the radial average of the power spectral density (PSD) of a widefield image, see Fig. 1(b).

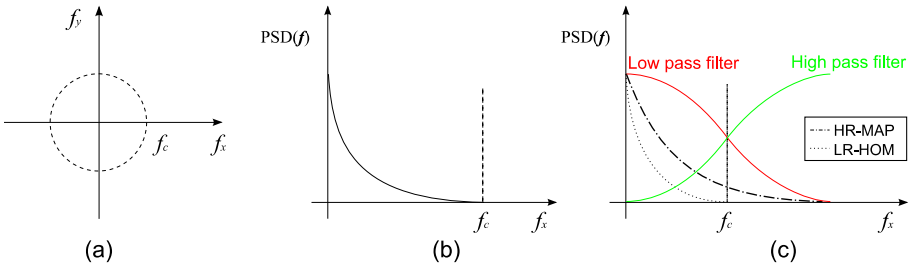

Fig. 1. Schematic of spectral merging (a) Spatial frequencies in Fourier space, where f_c is the cut off frequency. (b) Power spectral density (PSD) in relation to the spatial frequency. (c) Blending frequency spectra of HR-MAP estimation and LR homodyne detection using low and high pass filters.

2.3 Spectral merging

MAP estimation of a high resolution image obtained with structured illumination microscopy enables reconstruction of images (HR-MAP) with details unresolvable in a widefield microscope. However, MAP estimation as described here does not suppress the out of focus light. On the other hand, the homodyne detection method

$$\boldsymbol{x}_{\text{LR-HOM}} = \left|\sum_{k=1}^{K} \mathrm{y}_k \exp\left(2\pi \mathrm{i}\frac{k}{K}\right)\right| \tag{10}$$

used in OS-SIM [15] provides images (LR-HOM) with optical sectioning but without resolution improvement. Noting that the unwanted out of focus light is dominantly present at low spatial frequencies, we merge both LR-HOM and HR-MAP images in the frequency domain, see Fig. 1(c), to obtain the final HR image (MAP-SIM). Low pass filtering is applied to the LR-HOM image and a complementary high pass filter is applied to the HR-MAP image. O'Holleran and Shaw [19] used Gaussian weights with empirically adjusted standard deviations for weighting frequency components obtained by SR-SIM. We verified that Gaussian functions are well suited for our case, and we applied a weighting scheme based on linear combination of both merged components to preserve the total signal power

$$\boldsymbol{x}_{\text{MAP-SIM}} = \mathcal{F}^{-1}\left\{(1-\beta)\mathcal{F}\{\boldsymbol{x}_{\text{LR-HOM}}\}\exp\left(-\frac{\boldsymbol{f}^2}{2\rho^2}\right) + \beta\mathcal{F}\{\boldsymbol{x}_{\text{HR-MAP}}\}\left(1-\exp\left(-\frac{\boldsymbol{f}^2}{2\rho^2}\right)\right)\right\}, \tag{11}$$

where $\mathcal{F}, \mathcal{F}^{-1}$ denotes Fourier transform operator and its inverse, respectively, $\boldsymbol{f}$ is the spatial frequency, ρ is the standard deviation of the Gaussian filter, and β is a positive

#222375 - $15.00 USD Received 2 Sep 2014; revised 17 Oct 2014; accepted 18 Oct 2014; published 20 Nov 2014

weighting coefficient. The use of these variables and application of Eq. (11) are described in more detail in Section 3.4.

3. Methods

3.1 Microscope setup and acquisition

Our setup is based on an IX71 microscope equipped with UPLSAPO 100 × /1.40 NA and 60 × /1.35 NA oil immersion objectives (Olympus, Hamburg, Germany) [18], see Fig. 2. We used a NEO sCMOS camera (pixel size 6.5 μm). Focus was adjusted using a piezo-Z stage (resolution 1.5 nm, NanoScan-Z, Prior, Cambridge, UK). The desired illumination patterns were produced by a high speed ferroelectric liquid crystal on silicon (LCOS) microdisplay (SXGA-3DM, Forth Dimension Displays, Dalgety Bay, Scotland; 1280 × 1024 pixels, 13.62 μm pixel pitch). Similar LCOS microdisplays have been used previously in SIM [14,18], and in other fast optical sectioning systems such as programmable array microscopy (PAM) [30]. The display was illuminated by a home-built, three channel LED system based on high power LEDs (PT-54, Luminous Devices, Sunnyvale, California) with emission maxima at 460 nm, 525 nm, and 623 nm. The output of each LED was filtered with a band pass filter (450–490 nm, 505–555 nm, 633–653 nm, resp., Chroma, Bellows Falls, Vermont), and the three wavelengths were combined with appropriate dichroic mirrors. The light was then vertically polarized with a linear polarizer (Edmund Optics, Barrington, NJ). We imaged the microdisplay into the microscope using a 180 mm focal length tube lens (U-TLU, Olympus) and polarizing beam splitter cube (Newport, Irvine, California). When using a 100 × objective, single microdisplay pixels are imaged into the sample with a nominal size of 136.2 nm, thus as diffraction-limited spots. Sample fluorescence was isolated with a dual band filter set appropriate for Cy3 and Cy5, or a single band set for GFP (Chroma).

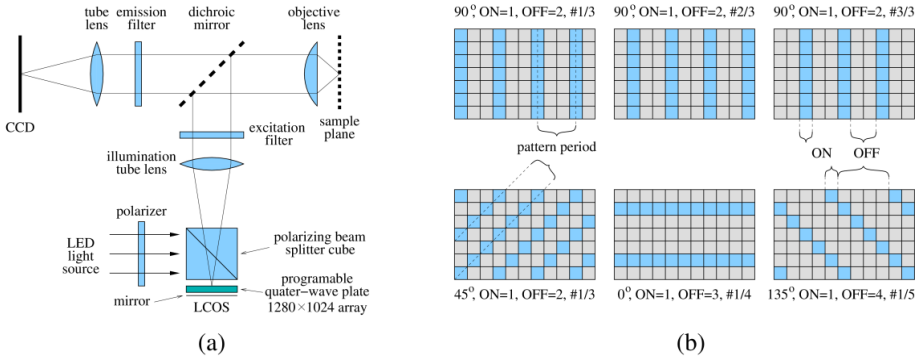

Fig. 2. Structured illumination microscope: (a) the microscope setup, (b) examples of line grid illumination patterns. Top row shows a pattern sequence which creates homogenous illumination. Bottom row shows several line grid patterns in different orientations. Blue are "on" pixels creating the illumination, gray are "off" pixels.

3.2. Illumination patterns

Most strategies in structured illumination microscopy assume that a set of illumination patterns required for image reconstruction consists of K equal movements of the same pattern such that the sum of all of the patterns results in homogenous illumination. In our experiments, the illumination patterns created by the microdisplay consisted of a regular grid of lines. The lines were one microdisplay pixel thick (diffraction limited in the sample when using a 100 × objective) with a gap of several "off" pixels in between. The line grid was shifted by one pixel between each image acquisition to obtain a new illumination mask, see Fig. 2(b). Changing the spacing between the "on" pixels allows one to vary the spatial

#222375 - $15.00 USD Received 2 Sep 2014; revised 17 Oct 2014; accepted 18 Oct 2014; published 20 Nov 2014

1 December 2014 | Vol. 22, No. 24 | DOI:10.1364/OE.22.029805 | OPTICS EXPRESS 29810

frequency of the pattern in the sample which influences signal to noise ratio of the result, imaging depth, and optical sectioning ability [18]. This spacing can be adjusted experimentally based on the sample, for example, when imaging deep into the sample, a lower pattern frequency may be required. In most experiments, we used pattern sequences with several orientations of the line grid pattern (0°, 90°, 45° and 135°) in order to achieve isotropic resolution improvement. Note that due to square shape of the microdisplay pixels, more patterns are required in the diagonal direction to equally cover the whole image while keeping the spatial frequency of the pattern approximately the same.

3.3 Samples

HepG2 cells expressing the labeled histone H4-dendra2 [31] were maintained in DMEM supplemented with 10 % FCS, 100 U/ml penicillin, and 100 U/ml streptomycin (all from Invitrogen, Carlsbad, CA, USA) at 37 °C, 5% CO_2, and 100 % humidity. Mowiol containing 1,4-diazabicyclo[2.2.2]octane (DABCO) was from Fluka (St. Louis, Missouri). Cells were grown on high precision #1.5 coverslips (Zeiss, Jena, Germany). Before imaging, cells were first washed with PBS, then fixed with 2 % paraformaldehyde for 15 minutes at 4 °C. For imaging of actin, we permeabilized fixed cells with 0.1 % Triton X-100 for 15 minutes at 4 °C, then labeled the cells with 2 nM Atto565-phalloidin (Atto-Tec Siegen, Germany) for 30 minutes at room temperature. We then mounted the coverslips in mowiol and sealed them onto clean slides with clear nail polish.

To illustrate the versatility of MAP-SIM, we imaged *Drosophila* salivary gland chromosomes (type 30-9066, Carolina Biological, Burlington, North Carolina), and pollen grains (type 30-4264, Carolina Biological). We also imaged mitochondria in bovine pulmonary artery endothelial (BPAE) cells labeled with MitoTracker Red CMXRos (FluoCells prepared slide #1, Invitrogen). The PSF of the microscope was measured using 100 nm tetraspeck beads (Invitrogen).

3.4 Image processing

The input data were first normalized into the range [0, 1] according to their bit depth. To obtain a HR-MAP image, we minimized Eq. (7) using a gradient descent algorithm. The speed of convergence is strongly influenced by the iteration step size $\alpha^{(n)}$. In the case of a fixed value ($\alpha = 0.5$), the algorithm converges in approximately 14 iterations, see Fig. 3(a). In order to speed up the convergence, we used the Barzilai-Borwein method [32], which is a variation of a standard gradient descent algorithm but with a step size which is adapted in every iteration based on the changes of the image estimate and the gradient of the cost function between consecutive iterations. This accelerates the convergence rate substantially. A good initial guess $\boldsymbol{x}^{(0)}$ of the HR-MAP image is also important for fast convergence. For this initial guess we used the sum of the acquired SIM images, which corresponds to a widefield image. Regularization of the problem in Eq. (7) is controlled by a small positive constant λ, which can be adjusted according to the noise conditions. If the noise increases, λ should also increase. The value $\lambda = 0.001$ worked well for all tested samples. Setting the regularization parameter to a small value prevents oversmoothing of the image and potential loss of high frequency information. We found that a stopping criterion $\varepsilon = 0.01$ was a reasonable value. With these settings, good results are obtained in about four iterations, see Figs. 3(a)-3(b). The frequency spectrum of the estimated image was then apodized with a cosine bell function and transformed into the real space to obtain the HR-MAP image. Note that the convolution step $H\boldsymbol{x}$ in Eq. (7) was performed in the frequency domain in order to achieve fast execution and memory efficiency.

The optically sectioned LR-HOM image and the super-resolution HR-MAP image are merged in the frequency domain by combining their Fourier spectra using Eq. (11), see the flowchart in Fig. 4. The balance between LR-HOM and HR-MAP images is controlled by the

#222375 - $15.00 USD Received 2 Sep 2014; revised 17 Oct 2014; accepted 18 Oct 2014; published 20 Nov 2014

coefficient β. To maximally exploit image details, it is preferred to put more emphasis on HR-MAP image. We experimentally determined that $\beta = 0.8$ provides good results across the range of the samples we imaged. The standard deviation of the Gaussian weighting function is related to the normalized frequency f_c, see Fig. 1(c).

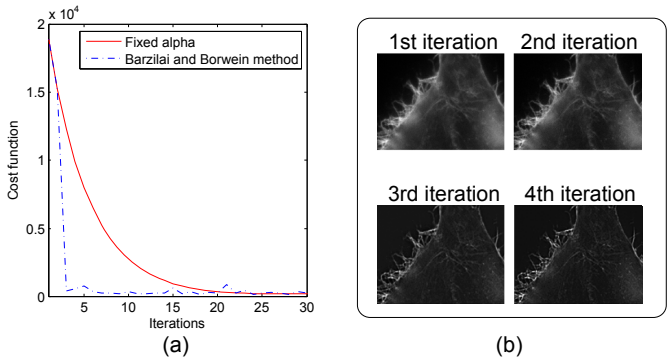

Fig. 3. Choice of the iteration step size (coefficient alpha) and its influence on the convergence of the algorithm. (a) Cost function vs. number of iterations. Fixed step size (red) and step size given by the Barzilai-Borwein method (blue). (b) Region of interest from a test sample (phalloidin-labeled actin in a HepG2 cell). Shown are the first 4 iterations of the algorithm, where the step size was determined using the Barzilai-Borwein method.

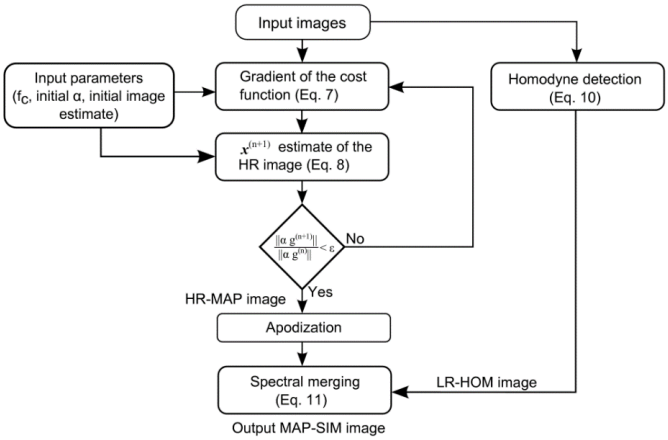

Fig. 4. Flowchart of the MAP-SIM algorithm.

4. Results

4.1 Spatial resolution measurements

Spatial resolution was determined by averaging measurements from fifty individual 100 nm fluorescent beads. We used a 100 × /1.40 NA oil immersion objective and 460 nm LED excitation (emission 500 - 550 nm). Fourteen images were acquired at each z-plane (pattern orientation: 0°, 90°; number of shifts: 3; pattern period imaged in the sample: 409 nm; and orientation: 45°, 135°; shifts: 4; period: 385 nm). A region of interest (ROI) around every bead position (19 × 19 pixels) was extracted from both the widefield and MAP-SIM images. In order to align the position of the beads in each ROI, we registered the ROIs with sub-pixel accuracy using standard normalized cross-correlation methods. Intensity values were then fit with a Gaussian function and the full width at half maximum (FWHM) was determined in the

#222375 - $15.00 USD Received 2 Sep 2014; revised 17 Oct 2014; accepted 18 Oct 2014; published 20 Nov 2014

1 December 2014 | Vol. 22, No. 24 | DOI:10.1364/OE.22.029805 | OPTICS EXPRESS 29812

axial and lateral directions. Figure 5 shows the resulting averaged FWHM values and PSF cross-sections.

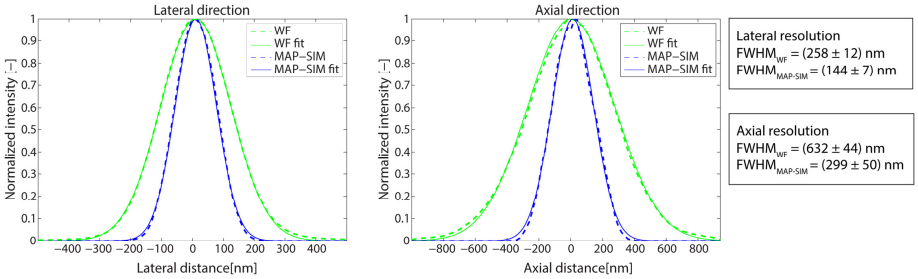

Fig. 5. Measurements of the spatial resolution on a sample of fluorescent beads. Cross-sections of the PSF are obtained by averaging measurements over 50 beads along (a) lateral and (b) axial directions.

4.2 2D MAP-SIM

To demonstrate the lateral resolution improvement of MAP-SIM in a thin sample, we imaged a *Drosophila* salivary gland chromosome preparation. The images were acquired using 623 nm LED illumination and a 100 × /1.40 NA oil immersion objective. Forty eight images were acquired at each z-plane (orientation: 0°, 90°; shifts: 10; period: 1.36 μm; and orientation: 45°, 135°; shifts: 14; period: 1.35 μm). The chromosome sample is quite thin (~1.5 μm), producing little out of focus light. Figure 6 demonstrates how MAP-SIM performs when compared to widefield and square-law methods in terms of contrast and lateral resolution. Plotting the intensity profile across the widefield, square-law and MAP-SIM images revealed many more fine details in MAP-SIM, see Fig. 6(g). We also plotted the normalized power spectral density vs. reduced spatial frequency, see Fig. 6(h). The reduced spatial frequency was normalized in the interval [0, 1] according to the maximum spatial frequency in the MAP-SIM image.

4.3 3D MAP-SIM

To demonstrate the optical sectioning characteristics of MAP-SIM, we imaged a relatively thick biological sample, a fluorescent pollen grain about 50 μm thick, see Fig. 7. The images were acquired using a 60 × /1.35 NA oil immersion objective. In this case a SIM pattern with a single orientation was used (orientation: 0°; number of shifts: 10; period: 2.27 μm). Ninety planes along the z-axis were scanned with a spacing of 500 nm. Lateral and axial cross sections of the pollen grain image in Fig. 7(c) reveal that MAP-SIM provides increased lateral and axial resolution compared to the widefield image. We also imaged Atto-532 phalloidin labeled actin in a HepG2 cell using the same illumination patterns as the pollen grain sample, see Fig. 8. Depth color coding was applied to the image using the isolum color map [33]. Maximum intensity projections of the color coded 3D MAP-SIM images are shown in Fig. 8(a)-8(c).

In our microscope set-up, the illumination pattern contrast is lower at high spatial frequencies compared to SR-SIM using coherent illumination. Despite this, we compared MAP-SIM and SR-SIM processing methods in images of HepG2 cells expressing the labeled histone H4-dendra2. In this sample we also labeled actin using Atto-532 phalloidin. The images were acquired using a 460 nm LED (H4-dendra2) and 525 nm LED (atto-532 phalloidin) with a 100 × /1.40 NA oil immersion objective. In total, 24 patterned images were acquired for each z-plane Twenty four images were acquired at each z-plane (orientation: 0°, 90°; shifts: 5; period: 681 nm; and orientation: 45°, 135°; shifts: 7; period: 674 nm). Figure 9(a)-9(c) shows a maximum intensity projection of 23 Z-planes. Figure 9(f)-9(g) shows

#222375 - $15.00 USD Received 2 Sep 2014; revised 17 Oct 2014; accepted 18 Oct 2014; published 20 Nov 2014

results for a single optical section. To process the data using SR-SIM methods, we followed the approach of Gustafsson, et al. [13]. We located peaks in the Fourier spectrum using a spatial calibration method derived from our previous work [18].

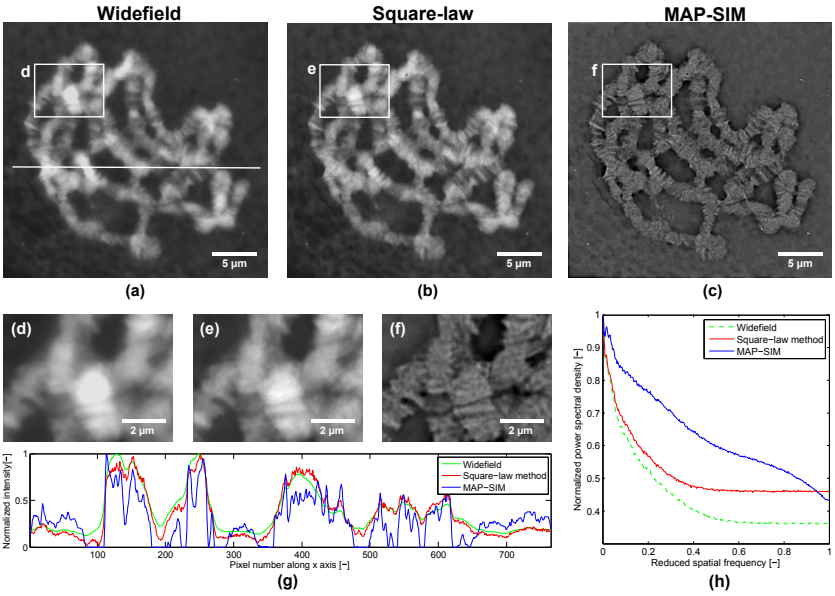

Fig. 6. Comparison of different imaging methods. *Drosophila* salivary gland chromosome sample. (a, d) Widefield image and region of interest. (b, e) Square-law method and ROI. (c, f) MAP-SIM and ROI. (g) Line profile of the images, indicated by the white line in (a). (h) Plot of normalized power spectral density vs. reduced spatial frequency for widefield, square law, and MAP-SIM approaches.

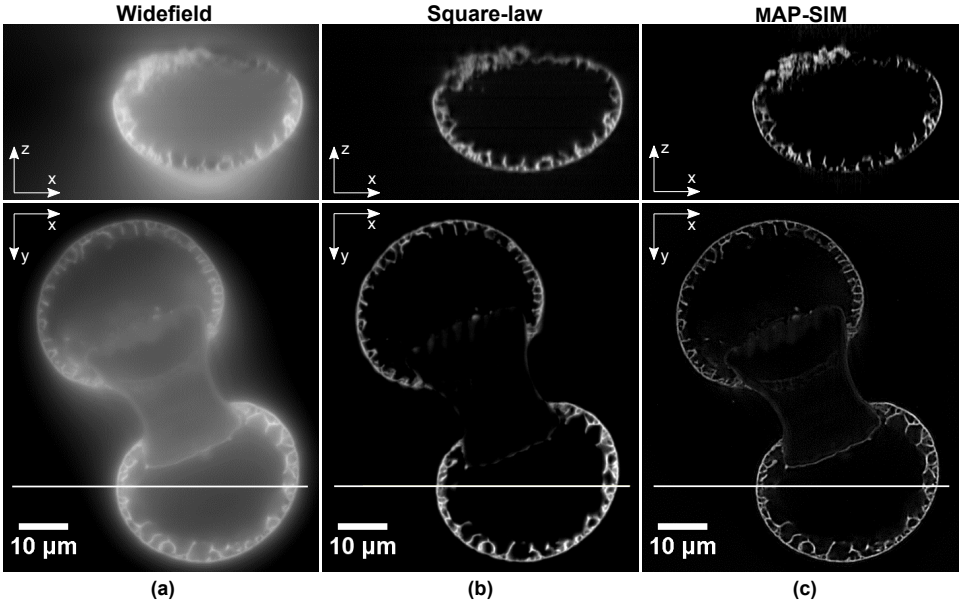

Fig. 7. Image of an autofluorescent pollen grain acquired using a 60 × /1.35 NA oil immersion objective. (a) Widefield image. (b) square-law method. (c) MAP-SIM. Shown are also XZ projections taken along the pixel row indicated by the white line.

#222375 - $15.00 USD Received 2 Sep 2014; revised 17 Oct 2014; accepted 18 Oct 2014; published 20 Nov 2014

1 December 2014 | Vol. 22, No. 24 | DOI:10.1364/OE.22.029805 | OPTICS EXPRESS 29814

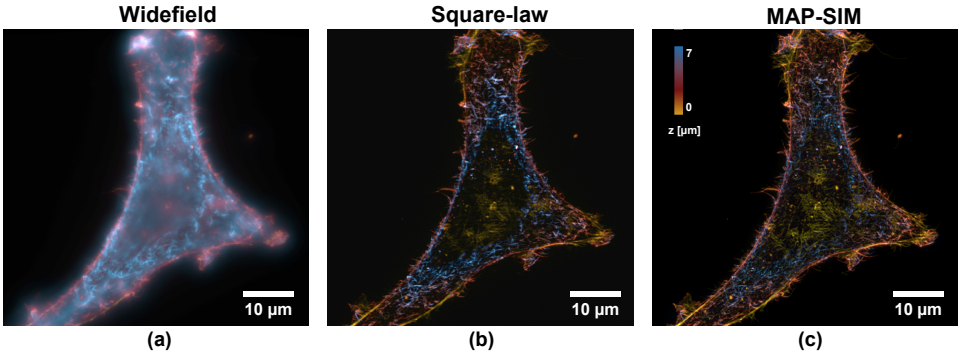

Fig. 8. Atto-532 Phalloidin labeled actin in a HepG2 cell. Maximum intensity projections of the 3D stack. (a) widefield, (b) square-law method, (c) MAP-SIM. Thickness of the sample is 7 µm. The look up table isolum [33] was used for depth color coding.

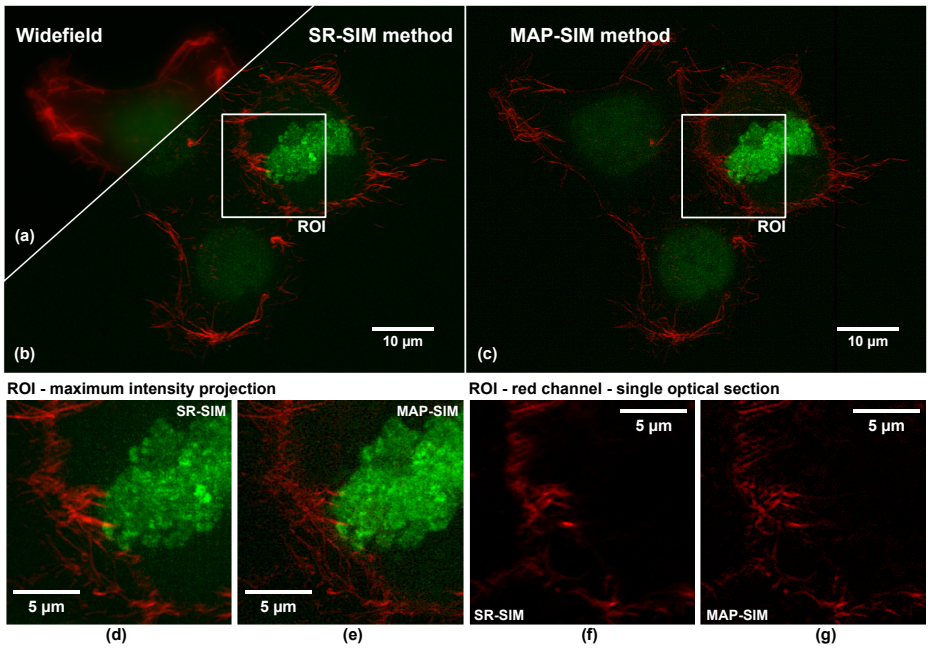

Fig. 9. Comparison between SR-SIM processing and MAP-SIM. Maximum intensity projection of 23 Z-planes in each of two color channels (red, green) for (a) widefield, (b) SR-SIM, (c) MAP-SIM. (d, e) Regions of interest indicated in (b, c). (f, g) Single optical section in the red channel.

#222375 - $15.00 USD Received 2 Sep 2014; revised 17 Oct 2014; accepted 18 Oct 2014; published 20 Nov 2014

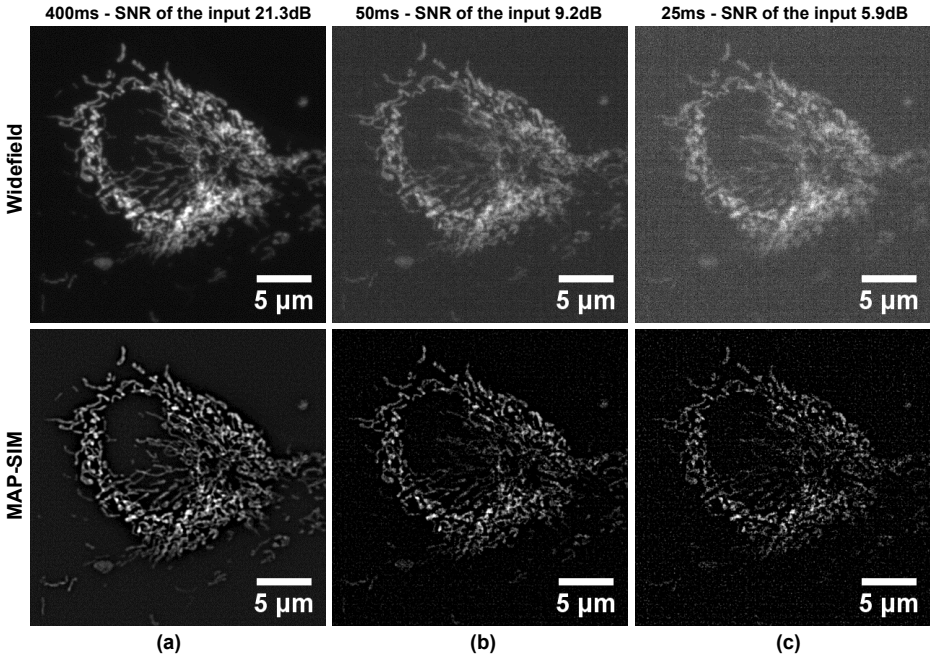

Fig. 10. Performance of the proposed MAP-SIM method under various noise conditions in comparison to the widefield image. Data acquisition times are 400 ms, 50 ms and 25 ms respectively. Images are of mitochondria labelled with Mitotracker in BPAE cells.

4.4 SNR analysis and acquisition times

When using typical SR-SIM processing methods [13], high noise levels in the raw data can lead to inaccuracies when determining the shifts of the spectral components and thereby degrade the final super-resolution image. Thomas et al. examined the performance of SIM image reconstruction methods at low signal levels [34]. They showed an image reconstruction for a sample where the SNR of an equivalent widefield image was estimated as 12 dB.

We evaluated the performance of MAP-SIM under various noise conditions. Using a 100 × /1.40 NA oil immersion objective, images of MitoTracker-labeled mitochondria in BPAE cells were acquired with 525 nm LED excitation and acquisition times (for one SIM pattern position) ranging from 10 ms to 400 ms. Under these conditions the SNR of equivalent widefield images ranged from 2.7 dB to 21.3 dB. We found that MAP-SIM reconstruction was successful down to a SNR of about 5.9 dB. The SNR was measured in widefield images based on manually selected regions in areas containing signal or background respectively and the results are shown in Fig. 10.

5. Discussion

There are several advantages to the use of an incoherent illumination approach such as the one presented here. One is that we do not require a pupil plane mask to block the unwanted diffraction orders that are generated when using coherent illumination based on two-beam or three-beam laser interference. Such masks can be tricky to implement because different wavelength lasers are focused to different locations in the (reconstructed) pupil plane. This then requires numerous holes in the mask which must be precisely positioned. On the other hand, the contrast of our patterns is lower when compared to coherent interference patterns

#222375 - $15.00 USD Received 2 Sep 2014; revised 17 Oct 2014; accepted 18 Oct 2014; published 20 Nov 2014

1 December 2014 | Vol. 22, No. 24 | DOI:10.1364/OE.22.029805 | OPTICS EXPRESS 29816

and we achieved a slightly lower resolution improvement than that typically reported in SR-SIM with coherent illumination.

The LCOS microdisplay used here can be configured with a variety of timing schemes which are supplied with the device. With the timing program that we used, the microdisplay can display an illumination pattern and switch to the next pattern in the sequence in 1.14 ms. Given a bright enough light source, fast enough camera, and appropriate sample, acquisition of raw SIM images at rates exceeding 800 Hz would therefore be possible. However, specifying the fastest possible acquisition rate, as is sometimes reported in SIM, is rather meaningless without consideration of the illumination power density, microscope objective, nature of the sample labeling, and other factors. The SNR analysis shown in Fig. 10 thus reflects an attempt to determine the relevant parameters based on measured quantities.

So far the MATLAB implementation of the MAP-SIM algorithm was not optimized for speed. The reconstruction of the 765 × 735 pixel image shown in Fig. 6, employing 48 patterned illumination images, took about 15 seconds using a conventional PC (Intel Core i7, 2.1 GHz, 8 GB RAM). We attribute the fast processing speeds to the frequency domain convolution we applied when solving Eq. (7), and to the Barzilai-Borwein method which ensures fast convergence. Processing each 2D plane separately also reduces the required CPU time and suggests parallel processing of individual planes, which would significantly speed up reconstruction of 3D samples.

6. Conclusion

We introduced a fast and efficient MAP-SIM algorithm, which is suitable for processing data acquired by both optical sectioning and super-resolution structured illumination microscopy. The proposed algorithm creates high quality super-resolution images. The measured resolution was (144 ± 7) nm in the lateral direction and (299 ± 50) nm axially. The reconstruction of super-resolution images was successful even in the presence of high noise levels, where the SNR of the corresponding widefield images was about 5.9 dB. Image acquisition and data processing are both very fast, revealing an interesting potential for live cell imaging. The microscope setup uses a relatively inexpensive microdisplay with no moving parts together with low cost LED illumination and is a simple add-on to conventional widefield fluorescence microscopes. MAP-SIM processing should also prove useful for other illumination strategies such as TIRF-SIM or emerging combinations of SIM and light sheet microscopy.

Acknowledgments

T.L. thanks Prof. Theo Lasser for his kind help and valuable advice. G.H. thanks Lubomír Kováčik for useful discussions. This work was supported by the Czech Science Foundation (P102/10/1320, P302/12/G157, 14-15272P, P205/12/P392), by Charles University in Prague (PRVOUK P27/LF1/1 and UNCE 204022), by OPPK CZ.2.16/3.1.00/24010 and OPVK CZ.1.07/2.3.00/30.0030, by COST CZ LD12018, by Czech Technical University in Prague (SGS14/148/OHK3/2T/13), and by the Biotechnology and Biomedicine Center of the Academy of Sciences and Charles University in Vestec. T.L. acknowledges a SCIEX scholarship (project code 13.183).

#222375 - $15.00 USD Received 2 Sep 2014; revised 17 Oct 2014; accepted 18 Oct 2014; published 20 Nov 2014

Bioinformatics Advance Access published October 24, 2015

Bioinformatics, 2015, 1–3
doi: 10.1093/bioinformatics/btv576
Advance Access Publication Date: 6 October 2015
Applications Note

Bioimage informatics

SIMToolbox: a MATLAB toolbox for structured illumination fluorescence microscopy

Pavel Křížek[1], Tomáš Lukeš[2,3], Martin Ovesný[1], Karel Fliegel[2] and Guy M. Hagen[4,*]

[1]First Faculty of Medicine, Charles University in Prague, Prague 12800, Czech Republic, [2]Department of Radioelectronics, Faculty of Electrical Engineering, Czech Technical University in Prague, Prague 16627, Czech Republic, [3]Laboratoire d'Optique Biomédicale, École Polytechnique Fédérale de Lausanne, Lausanne CH-1015, Switzerland and [4]UCCS center for the BioFrontiers Institute, University of Colorado at Colorado Springs, Colorado Springs, CO 80918, USA

* To whom correspondence should be addressed.
Associate Editor: Robert Murphy

Received on July 22, 2015; revised on September 28, 2015; accepted on September 30, 2015

Abstract

Summary: SIMToolbox is an open-source, modular set of functions for MATLAB equipped with a user-friendly graphical interface and designed for processing two-dimensional and three-dimensional data acquired by structured illumination microscopy (SIM). Both optical sectioning and super-resolution applications are supported. The software is also capable of maximum *a posteriori* probability image estimation (MAP-SIM), an alternative method for reconstruction of structured illumination images. MAP-SIM can potentially reduce reconstruction artifacts, which commonly occur due to refractive index mismatch within the sample and to imperfections in the illumination.
Availability and implementation: SIMToolbox, example data and the online documentation are freely accessible at http://mmtg.fel.cvut.cz/SIMToolbox.
Contact: ghagen@uccs.edu
Supplementary information: Supplementary data are available at *Bioinformatics* online.

1 Introduction

In structured illumination microscopy (SIM), a sequence of images is acquired, each taken with a different position of an illumination pattern in a fluorescence microscope but without a mask in the detection path (Heintzmann, 2006). Subsequent processing of the raw data is required to reconstruct the final image. Current SIM methods include optical sectioning microscopy (OS-SIM) (Křížek *et al.*, 2012; Neil *et al.*, 1997; Wilson, 2011) and super-resolution SIM (SR-SIM) (Gustafsson, 2000; Gustafsson *et al.*, 2008; Heintzmann and Cremer, 1998).

Several different algorithms can be used to process SIM data (Heintzmann, 2006). SIMToolbox offers a set of MATLAB functions for processing both OS-SIM and SR-SIM data according to a variety of methods. SIMToolbox can also apply an alternative method for processing the data, maximum *a posteriori* probability estimation (MAP-SIM) (Lukeš *et al.*, 2014). The tools can be accessed from a user-friendly graphical user interface.

Our goal is to offer a collection of processing methods, which were developed based on extensive testing with real data. The software can be used to process data acquired by commercial SIM systems; however, some of the tools and documentation provided are meant for researchers developing their own systems. In addition to the software, we provide example data, a user's guide and a detailed description of the implemented methods and algorithms. Please refer to the Supplementary Note for further details.

2 Features and methods

2.1 OS-SIM

SIMToolbox can process OS-SIM data using homodyne detection (Křížek *et al.*, 2012; Neil *et al.*, 1997), maximum–minimum projection (Heintzmann, 2006) or several forms of scaled subtraction (Heintzmann, 2006; Křížek *et al.*, 2012). When using scaled subtraction, it is necessary to have knowledge of the illumination pattern positions

in the camera image. We accomplish this by spatial calibration using an alignment pattern (Křížek *et al.*, 2012). Residual stripes are corrected using a method introduced by Cole *et al.* (2001).

2.2 SR-SIM

SIMToolbox can process SR-SIM data using the Heintzmann–Gustafsson method (Gustafsson, 2000; Gustafsson *et al.*, 2008; Heintzmann and Cremer, 1998). Briefly, the image processing steps are as follows:

1. Forward fast Fourier transformation (FFT) of the raw data.
2. Identification of peaks in the frequency spectrum. The software can accomplish this with high accuracy using spatial calibration methods (Křížek *et al.*, 2012) or using spot detection methods (Ovesný *et al.*, 2014).
3. Shifting of spectral components in frequency space.
4. Apodizing the frequency spectrum according to one of several possible functions. SIMToolbox offers several apodizing functions including a standard incoherent model, cosine bell, Butterworth, triangle and application of the Lukosz bound (Righolt *et al.*, 2013).
5. Inverse FFT with an adjustable inverse filter parameter to recover an image with resolution beyond the conventional limit.

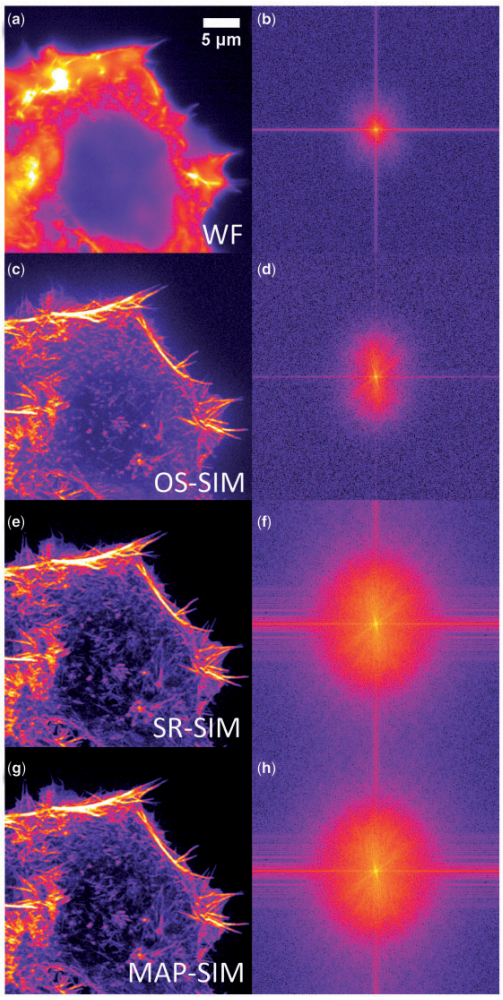

Fig. 1. Widefield (WF) image and OS-SIM, SR-SIM and MAP-SIM reconstructions of images of a HEP-G2 cell in which the actin cytoskeleton has been labeled with Atto565-phalloidin. (**a**) WF. (**b**) FFT of WF. (**c**) OS-SIM, homodyne method. (**d**) FFT of OS-SIM image. (**e**) SR-SIM processing. (**f**) FFT of SR-SIM. (**g**) MAP-SIM. (**h**) FFT of MAP-SIM. Images are maximum intensity projections of 31 axial sections and have been individually brightness adjusted for presentation

2.3 MAP-SIM

An alternative method for processing SR-SIM data is the MAP-SIM method introduced by our group (Lukeš *et al.*, 2014a, b). Here, image details beyond the diffraction limit are estimated by maximum *a posteriori* restoration methods, and optically sectioned, conventional resolution image information is processed by homodyne detection. The two components are then combined by spectral merging in the frequency domain. The result is then apodized, and an inverse FFT is performed to recover the final image.

Our experience has been that MAP-SIM can, in some cases, produce super-resolution images with fewer artifacts than the Heintzmann–Gustafsson method. Such artifacts seem to be primarily caused by problems with the sample, especially refractive index mismatch between the mounting medium and immersion fluid. Reconstruction artifacts can also be caused by high noise levels, by poor SIM pattern contrast or other imperfections in the illumination or by the use of inappropriate parameters in the reconstruction process. For example, we have found that the choice of apodizing and inverse filter parameters (SR-SIM steps 4 and 5 above) have a large impact on the results.

Figure 1 shows a comparison of some of the various methods supported by SIMToolbox, acquired using the methods introduced by our group (Křížek *et al.*, 2012). Please see the Supplementary Note for more details about this SIM experiment.

3 Summary

SIMToolbox is open-source software for processing SIM data. This allows researchers building their own systems to process their data using a unique set of tools and concepts. The software also offers features not currently present in commercially available software, making it a useful choice for reconstructing super-resolution images acquired with commercial equipment.

Funding

This work was supported by the UCCS center for the BioFrontiers Institute and by the CTU (SGS14/148/OHK3/2T/13). T.L. acknowledges a SCIEX fellowship (project code 13.183).

Conflict of Interest: none declared.

References

Cole,M.J. *et al.* (2001) Time-domain whole-field fluorescence lifetime imaging with optical sectioning. *J. Microsc.*, **203**, 246–257.

Gustafsson,M.G.L. (2000) Surpassing the lateral resolution limit by a factor of two using structured illumination microscopy. *J. Microsc.*, **198**, 82–87.

Gustafsson,M.G.L. *et al.* (2008) Three-dimensional resolution doubling in widefield fluorescence microscopy by structured illumination. *Biophys. J.*, **94**, 4957–4970.

Heintzmann,R. (2006) Structured illumination methods. In: Pawley,J.B. (ed.) *Handbook of Biological Confocal Microscopy*. Springer, New York, pp. 265–279.

Heintzmann,R. and Cremer,C. (1998) Laterally modulated excitation microscopy: improvement of resolution by using a diffraction grating. *Proc. SPIE*, **3568**, 185–196.

Křížek,P. *et al*. (2012) Flexible structured illumination microscope with a programmable illumination array. *Opt. Express*, **20**, 24585–24599.

Lukeš,T. *et al*. (2014a) Comparison of image reconstruction methods for structured illumination microscopy. In: Popp,J. *et al*. (eds.) *SPIE Photonics Europe*. International Society for Optics and Photonics, Bellingham, WA, p. 91293J.

Lukeš,T. *et al*. (2014b) Three-dimensional super-resolution structured illumination microscopy with maximum a posteriori probability image estimation. *Opt. Express*, **22**, 29805–29817.

Neil,M.A.A. *et al*. (1997) Method of obtaining optical sectioning by using structured light in a conventional microscope. *Opt. Lett.*, **22**, 1905–1907.

Ovesný,M. *et al*. (2014) ThunderSTORM: a comprehensive ImageJ plug-in for PALM and STORM data analysis and super-resolution imaging. *Bioinformatics*, **30**, 2389–2390.

Righolt,C.H. *et al*. (2013) Image filtering in structured illumination microscopy using the Lukosz bound. *Opt. Express*, **21**, 24431–24451.

Wilson,T. (2011) Optical sectioning in fluorescence microscopy. *J. Microsc.*, **242**, 111–116.